Institute of Fundamental Technological Research Polish Academy of Sciences

A thesis presented for the degree of Doctor of Philosophy

Advancing Understanding of Dislocation Dynamics in Metals Through Machine Learning-Enabled Analysis

By

Amirhossein D. Naghdi

Doctoral thesis supervisor
Stefanos Papanikolaou

Warsaw, 2024

Acknowledgments

This research was conducted at NOMATEN Center of Excellence, with financial support from the European Union Horizon 2020 Research and Innovation Program under grant agreement no. 857470, and the European Regional Development Fund via the Foundation for Polish Science International Research Agenda PLUS program (grant no. MAB PLUS/2018/8). These resources were fundamental to the successful completion of this work.

I would like to extend my heartfelt gratitude to my supervisor, Stefanos Papanikolaou, for his invaluable guidance, patience, and encouragement throughout my doctoral studies. His expertise has been instrumental in shaping both this thesis and my growth as a researcher.

A special thanks goes to my wife, Shima, whose unwavering patience and support have been my greatest source of strength. She stood by me through every stage of this work, tolerating the demands it placed on our lives with remarkable grace.

I also want to express my profound gratitude to my family, especially my mother, whose love and encouragement helped me persevere through difficult times.

Finally, I am deeply grateful to my best friend during my PhD journey, Dario Massa, for the countless hours we spent discussing research and life during challenging moments. Your support and friendship have been a cornerstone of this experience.

Contents

Abstract

Defects in crystalline materials are essential to advancing materials design, particularly extended defects like dislocations, which play a crucial role in determining mechanical properties. Understanding these defects enables researchers to synthesize improved materials, as dislocations govern how materials respond to external stress. For instance, when stress is applied to a functional material, dislocations nucleate and move within the crystal to prevent abrupt fracture. The dynamics of dislocations, along with their interactions with obstacles such as grain boundaries, voids, and precipitates, provide critical insights into tuning material properties like hardness, toughness, and ductility.

This PhD thesis explores the dynamics of dislocations and extended defects in crystalline materials and multi-component alloys using a combination of machine learning, molecular dynamics, Monte Carlo simulations, and density functional theory. Specifically, it investigates the behavior of dislocations in medium-entropy alloys and their interactions with nano-scale chemical short-range ordering of constituent atoms. Additionally, nano-mechanical tests, such as nano-indentation simulations, were conducted to examine the manipulation of short range ordering. To further enhance simulation tools for dislocation-related experiments, machine-learned interatomic potentials were developed, focusing on the dynamics of dislocations and open surface nano-mechanical applications.

This thesis is presented as a collection of four publications, each advancing the understanding of defect dynamics from different angles. The author is the lead author in three of these works and contributes as a co-author in the remaining one. The publications are grouped into two major themes. The first set centers on the development of machine learning force fields, utilizing first-principles data, to enable more accurate molecular dynamics simulations of dislocation behavior and nano-mechanical experiments. The second set study the intricate dynamics of dislocations and their interactions in complex alloys, with a focus on nano-mechanical testing and the role of atomic-level short range ordering, explored through molecular dynamics simulations. Together, these works offer valuable insights into computational materials science, particularly in understanding and simulating dislocation dynamics in crystalline materials.

The research begins with study of dislocation dynamics through simulating nano-indentation experiments on single crystalline tungsten matrices at various temperatures and loading rates using molecular dynamics. Both empirical and machine-learned approaches were utilized for this study. The simulations aimed to investigate plastic deformation mechanisms of this material. While similarities were observed in load-displacement curves and dislocation densities across different interatomic potentials and crystal orien-

tations at lower temperatures, key differences emerged in the elastic-to-plastic transition stages, specifically at higher temperatures. These variations suggest the need for the development of more accurate computational methods for plastic deformation in crystalline materials. In this case study, machine learning force fields proved to have the most accurate results in alignment with density functional theory calculations and experimental data.

The research continues with the development of machine learning force fields for nano-mechanical molecular dynamics simulations. Recognizing that interatomic potentials are critical tools for simulating nano-mechanical behavior, a robust neural network interatomic potential was developed for single crystalline Molybdenum and applied to molecular dynamics nano-indentation simulations. Ab initio configurations, including generalized stacking fault structures and high-temperature configurations, were carefully selected to capture the behavior of the indented sample. Inclusion of dislocation nucleation mechanisms and accurate stacking fault energy curves allowed the neural network interatomic potential to provide detailed surface energy landscapes during indentation. Comparisons with existing potentials revealed the neural network interatomic potential improved accuracy in predicting shear stress and dislocation dynamics, aligning closely with experimental results for reduced Youngs modulus and slip traces.

The research then investigates dislocation dynamics in multi-component NiCoCr medium-entropy alloys using hybrid molecular dynamics and monte carlo simulations to explore how short range ordering forms under thermal treatments such as annealing and aging. Two different interatomic potentials, Li-Sheng-Ma (LSM) and Farkas-Caro (FC), are employed, with LSM effectively capturing short range ordering linked to experimental observations. By analyzing short range ordering within stacking faults, the study shows that short range ordering enhances dislocation depinning and dynamics resistance, thereby strengthening the alloy. This work provides key insights into how nanoscopic short range ordering influences the dislocation dynamics in complex alloys.

The final part of the research focuses on exploring nano-mechanical tests, such as nano-indentation, to manipulate short range ordering in multi-component equiatomic NiCoCr alloys. Through atomic-scale modeling, it is demonstrated that nano-indentation can be used not only as a mechanical probe but also as a tool for reorganizing local atomic ordering. Specific nano-indentation protocols at room temperature are shown to induce local reorganization of atoms under the indenter tip, forming distinct density-wave stripe patterns. These patterns arise from the intrinsic interelemental energetics and are directly linked to the stress fields caused by the nano-indentation probe. The findings suggest that such manipulations of short range ordering could be validated experimentally through nano-indentation, as a size effect correlated to the indenter radius is observed.

The thesis concludes by addressing the limitations and potential improvements of the methods and interatomic potentials used in the simulations. While the developed neural network interatomic potential and other potentials demonstrated significant accuracy in predicting dislocation behavior and mechanical properties, challenges remain in capturing complex atomic interactions at high strain rates and extreme temperatures. Additionally,

the transferability of these potentials across different materials and loading conditions is an area for future research. Further work, such as machine learning interatomic potential development for dislocation dynamics study in multi-component alloys by employing advanced methods such as active learning and accurate machine learning models, is required in this research area.

Streszczenie (Abstract in Polish)

Defekty w materiaach krystalicznych odgrywaj kluczow rol w projektowaniu nowoczesnych materiaów, szczególnie defekty rozszerzone, takie jak dyslokacje, które w duym stopniu determinuj ich waciwoci mechaniczne. Zrozumienie tych defektów umoliwia naukowcom tworzenie ulepszonych materiaów, poniewa dyslokacje decyduj o sposobie, w jaki materiay reaguj na naprenia zewntrzne. Na przykad, pod wpywem naprenia w materiale funkcjonalnym, dyslokacje inicjuj si i przemieszczaj w krysztale, zapobiegajc nagemu pkniciu. Dynamika dyslokacji, a take ich interakcje z przeszkodami, takimi jak granice ziaren, pory i wydzielenia, dostarczaj istotnych informacji potrzebnych do modyfikowania waciwoci materiaów, takich jak twardo, wytrzymao i plastyczno.

Niniejsza rozprawa doktorska bada dynamik dyslokacji i defektów rozszerzonych w materiaach krystalicznych i stopach wieloskadnikowych, wykorzystujc poczenie metod uczenia maszynowego, dynamiki molekularnej, symulacji Monte Carlo oraz teorii funkcjonau gstoci. W szczególnoci analizuje zachowanie dyslokacji w stopach rednio-entropyjnych oraz ich interakcje z nanoskaliowym uporzdkowaniem chemicznym atomów. Dodatkowo przeprowadzono testy nanomechaniczne, takie jak symulacje nanoindentacji, w celu zbadania moliwoci manipulacji uporzdkowaniem krótkiego zasigu. Aby dalej ulepszy narzdzia symulacyjne stosowane w badaniach dyslokacji, opracowano interatomowe potencjay oparte na uczeniu maszynowym, koncentrujc si na dynamice dyslokacji oraz zastosowaniach nanomechanicznych na otwartych powierzchniach.

Praca ta skada si z czterech publikacji, z których kada rozwija zrozumienie dynamiki defektów z innej perspektywy. Autor jest pierwszym autorem w trzech z tych prac, a w czwartej wystpuje jako wspóautor. Publikacje te podzielono na dwa gówne tematy. Pierwszy z nich koncentruje si na opracowaniu pól si opartych na uczeniu maszynowym, które wykorzystuj dane z pierwszych zasad do umoliwienia bardziej precyzyjnych symulacji dynamiki molekularnej zachowania dyslokacji i eksperymentów nanomechanicznych. Drugi temat obejmuje szczegóowe badania dynamiki dyslokacji oraz ich interakcji w zoonych stopach, z naciskiem na testy nanomechaniczne i rol uporzdkowania atomowego krótkiego zasigu, analizowan za pomoc symulacji dynamiki molekularnej. cznie prace te dostarczaj cennych informacji w dziedzinie komputerowej nauki o materiaach, szczególnie w kontekcie modelowania i symulacji dynamiki dyslokacji w materiaach krystalicznych.

Badania rozpoczynaj si od analizy dynamiki dyslokacji poprzez symulacje eksperymentów nanoindentacji w monokrysztaach wolframu w rónych temperaturach i przy rónych prdkociach obcienia, przy uyciu dynamiki molekularnej. W tym celu zastosowano zarówno empiryczne, jak i oparte na uczeniu maszynowym podejcia. Celem symulacji

byo zbadanie mechanizmów odksztace plastycznych tego materiau. Podczas gdy na niszych temperaturach zaobserwowano podobiestwa w krzywych obcienie-przemieszczenie i gstociach dyslokacji dla rónych potencjaów interatomowych i orientacji krystalicznych, kluczowe rónice pojawiy si w etapach przejcia od stanu sprystego do plastycznego, szczególnie w wyszych temperaturach. Rónice te sugeruj konieczno opracowania bardziej precyzyjnych metod obliczeniowych dla mechanizmów odksztace plastycznych w materiaach krystalicznych. W tym badaniu potencjay si oparte na uczeniu maszynowym okazay si najbardziej precyzyjne, wykazujc zgodno z wynikami teorii funkcjonau gstoci oraz danych eksperymentalnych.

Kolejnym krokiem w badaniach byo opracowanie potencjaów si opartych na uczeniu maszynowym do symulacji nanomechanicznych metod dynamiki molekularnej. W uznaniu, e potencjay interatomowe s kluczowymi narzdziami w symulacjach zachowania nanomechanicznego, opracowano solidny potencja midzyatomowy oparty na sieciach neuronowych dla monokryształu molibdenu i zastosowano go do symulacji nanoindentacji metod dynamiki molekularnej. Konfiguracje ab initio, w tym struktury ogólnych bdów polizgu oraz konfiguracje wysokotemperaturowe, zostay starannie dobrane, aby uchwyci zachowanie próbki poddanej wgnieceniu. Uwzgldnienie mechanizmów nukleacji dyslokacji oraz dokadnych krzywych energii bdów polizgu pozwolio potencjaowi neuronowemu precyzyjnie odwzorowa powierzchniowe krajobrazy energetyczne podczas wgniecenia. Porównania z istniejcymi potencjaami wykazay, e potencja neuronowy poprawi dokadno w przewidywaniu napre cinajcych i dynamiki dyslokacji, wykazujc zgodno z wynikami eksperymentalnymi dla zredukowanego moduu Younga i ladów polizgu.

Nastpnie badania zajy si analiz dynamiki dyslokacji w wieloskadnikowych stopach NiCoCr rednio-entropyjnych, wykorzystujc hybrydowe symulacje dynamiki molekularnej i Monte Carlo w celu zbadania formowania si uporzdkowania krótkiego zasigu pod wpywem obróbki cieplnej, takiej jak wyarzanie i starzenie. Zastosowano dwa róne potencjay interatomowe: Li-Sheng-Ma (LSM) i Farkas-Caro (FC). Potencja LSM skutecznie uchwyci uporzdkowanie krótkiego zasigu powizane z obserwacjami eksperymentalnymi. Analizujc uporzdkowanie krótkiego zasigu w obrbie bdów polizgu, badanie wykazao, e uporzdkowanie krótkiego zasigu zwiksza odporno na odpinanie dyslokacji, co skutkuje wzmocnieniem stopu. Praca ta dostarcza kluczowych informacji o wpywie nanoskaliowego uporzdkowania krótkiego zasigu na dynamik dyslokacji w zoonych stopach.

Ostatnia cz bada koncentruje si na eksploracji testów nanomechanicznych, takich jak nanoindentacja, w celu manipulowania uporzdkowaniem krótkiego zasigu w wieloskadnikowych stopach NiCoCr. Modelowanie w skali atomowej wykazao, e nanoindentacj mona wykorzysta nie tylko jako sond mechaniczn, ale take jako narzdzie do reorganizacji lokalnego uporzdkowania atomowego. Specyficzne protokoy nanoindentacji w temperaturze pokojowej pokazano jako indukujce lokaln reorganizacj atomów pod kocówk wgbnika, prowadzc do powstawania wyranych pasm fal gstoci. Wzorce te wynikaj z wewntrznych waciwoci energetycznych pomidzy pierwiastkami i s bezporednio zwizane z polami napre generowanymi przez próbk nanoindentacyjn. Wyniki sugeruj, e takie manipulacje uporzdkowaniem krótkiego zasigu mona zweryfikowa eksperymentalnie za pomoc nanoindentacji,

gdy zaobserwowano efekt rozmiarowy zwizany z promieniem wgbnika.

Praca koczy si omówieniem ogranicze i potencjalnych usprawnie metod oraz potencjaów midzyatomowych stosowanych w symulacjach. Chocia opracowany potencja midzyatomowy oparty na sieciach neuronowych oraz inne potencjay wykazay znaczn dokadno w przewidywaniu zachowania dyslokacji i waciwoci mechanicznych, wci istniej wyzwania zwizane z odwzorowaniem zoonych interakcji atomowych przy wysokich szybkociach odksztace i ekstremalnych temperaturach. Ponadto, poprawa transferowalnoci tych potencjaów midzy rónymi materiaami i warunkami obcienia pozostaje kluczowym zagadnieniem do dalszych bada. Dalsze postpy w tej dziedzinie mog obejmowa rozwój potencjaów midzyatomowych opartych na uczeniu maszynowym, ukierunkowanych na badanie dynamiki dyslokacji w stopach wieloskadnikowych, z wykorzystaniem zaawansowanych metod, takich jak aktywne uczenie si oraz bardziej precyzyjne modele uczenia maszynowego.

Cycle of Publications

This Ph.D. thesis is presented as a series of research publications. It includes the following cycle of published research articles:

- F. Javier Dominguez–Gutierrez, Petr Grigorev, Amirhossein D. Naghdi, Jesper Byggmästar, G. Y. Wei, Thomas D Swinburne, Stefanos Papanikolaou Mikko Alava
  Nanoindentation of tungsten: From interatomic potentials to dislocation plasticity mechanisms
  Physical Review Materials, Vol. 7(4), 043603, 2023.

  Impact factor (2023): 3.1

- Amirhossein D. Naghdi, Franco Pellegrini, Emine Kücükbenli, Dario Massa, F. Javier Dominguez–Gutierrez, Efthimios Kaxiras, Stefanos Papanikolaou
  Neural network interatomic potentials for open surface nano-mechanics applications
  Acta Materialia, Vol. 277, 120200. 1359-6454, 2024.

  Impact factor (2023): 8.3

- Amirhossein D. Naghdi, Kamran Karimi, Axel E Poisvert, Amin Esfandiarpour, Rene Alvarez, Pawel Sobkowicz, Mikko Alava, Stefanos Papanikolaou
  Dislocation plasticity in equiatomic NiCoCr alloys: Effect of short-range order
  Physical Review B, Vol. 107(9), 094109, 2023.

  Impact factor (2023): 3.2

- Amirhossein D. Naghdi F. Javier Dominguez–Gutierrez, Wenyi Huo, Kamran. Karimi, Stefanos Papanikolaou
  Dynamic Nanoindentation and Short-Range Order in Equiatomic NiCoCr Medium-Entropy Alloy Lead to Novel Density Wave Ordering
  Physical Review Letters, Vol. 132, 116101, 2024.

  Impact factor (2023): 8.1

Motivation

The field of materials science is continually evolving, driven by the need for advanced materials that can withstand extreme conditions. This quest for innovative materials often requires a deep understanding of their atomic-level behavior, particularly concerning dislocation dynamics and the mechanisms of plastic deformation. The motivation for this thesis arises from the recognition that traditional methods for studying these phenomena often fall short in capturing the intricate interactions at the atomic scale. By exploiting advanced computational techniques, this work aims to bridge the gap between theoretical predictions and experimental observations and enhance our ability to design materials with tailored properties.

The exploration of dislocation dynamics, presents a unique challenge. Dislocations play a critical role in determining the mechanical properties of materials, and their behavior is influenced by various factors, including short-range order and the presence of nano-precipitates. In this research, I also investigated the reorganization of short-range order in conjunction with nano-mechanical tests, providing deeper insights into how these factors interplay during mechanical deformation. Understanding these interactions is crucial for developing materials that can endure high-stress applications, such as aerospace and automotive components. The motivation behind this thesis is to provide insights into the fundamental mechanisms governing dislocation dynamics. This leads to facilitating the design of materials with improved performance and reliability

This thesis addresses the important aspect of dislocation dynamics in nano-indentation, particularly in Tungsten. As a material known for its exceptional hardness and strength, Tungsten is widely used in various applications. However, accurately modeling its mechanical behavior during indentation remains a challenge. By employing tailored interatomic potentials, this work aims to provide a more comprehensive understanding of the nano-indentation process and its implications for the material's performance. This motivation stems from the need to develop reliable predictive models that can inform the design of materials with enhanced mechanical properties.

Finally, the development of neural network interatomic potentials for nano-mechanical applications is explained. The motivation for creating a neural network interatomic potentials, specifically for Molybdenum in this thesis, lies in the potential to overcome the limitations of traditional potentials and provide more accurate predictions of atomic-scale dislocation dynamics mechanisms. By achieving this, the thesis not only contributes to a deeper understanding of Molybdenum's mechanical properties but also paves the way for future studies on complex materials.

Background

2.1 Fundamentals of Dislocation Dynamics

Dislocations are one-dimensional defects that govern plastic deformation in crystalline materials. The core of a dislocation spans a width of only a few atoms radius, where the atomic positions deviate significantly from the perfect lattice sites. This intrinsic "lattice distortion" generates a localized stress within the crystal and makes dislocations a primary source of internal stress in crystalline materials [1–3]. Dislocations have a length dimension which this distortion extends along and is referred to as the "dislocation line". The orientation and geometry of a dislocation determine its type, which influences its response to external forces and its impact on the material's mechanical properties. Dislocations are emergent defects in crystalline materials which makes their observation and measurement particularly challenging.

Geometrically, dislocations are broadly classified into two main types: edge and screw dislocations. Edge dislocations are a type of dislocation characterized by the addition of an extra half-plane of atoms to the lattice structure of the crystal [4–7]. On the other hand, screw dislocations are formed due to shear distortion within the crystal structure [8–10] and facilitate plastic flow by twisting the atomic planes around the dislocation line. In addition to their geometry, the differences of these types expand into their dynamics in response to external force. While edge dislocations allow the plastic flow by "glide" along specific slip planes, the plastic deformation through screw dislocations is mainly due to atomic planes gliding past one another along helical paths [11]. Dislocations in face-centered cubic materials split into two "partial dislocations" and create a stacking fault region in the material, while this is not the case for body-centered cubic crystals. Dislocations can exhibit edge or screw characteristics along different segments of the dislocation line, known as "mixed dislocations", which combines the properties of both types [1].

The magnitude and direction of the lattice distortion caused by a dislocation, is defined by its Burgers vector ($\vec{b}$) [1, 12]. The Burger's vector direction in edge dislocation is parallel to the dislocation line, while it is perpendicular to the dislocation line for screw dislocations. For a perfect dislocation, an applied force in the direction of $\vec{b}$ leads into the dislocation's glide and motion within the material. The magnitude of the Burgers vector is the shortest lattice translation distance [1]. Thus, for face-centered cubic crystals the Burgers vector $\vec{b} = \frac{1}{2}\langle 110 \rangle$ with a magnitude of $|b| = \frac{a}{\sqrt{2}}$, while for body-centered cubic

crystals $\vec{b} = \frac{1}{2}\langle 111 \rangle$ with the magnitude of $|b| = \frac{a\sqrt{3}}{2}$. Here, "$a$" is the lattice constant. The direction and magnitude of the Burgers vector are useful for determining certain mechanical properties of crystals [1].

Dislocation motion is driven by the application of external stress to the material. The external stress field acting on the material exerts a force on the dislocation, a concept first quantified by Peach and Koehler [13]. The Peach- Koehler force drives the dynamics of dislocations, which can occur through two primary mechanisms: glide motion and climb motion [1]. Glide refers to the motion of a dislocation within a plane (the "slip plane") containing both the Burgers vector and the dislocation line, while climb occurs when the dislocation moves normal to its Burgers vector and leaves the slip plane. At low temperatures and in perfect crystals, dislocations primarily exhibit glide motion. However, at higher temperatures and under applied forces, climb motion can occur as an additional mechanism for dislocation movement [1]. Another type of dislocation motion in crystals occurs when dislocations change their slip planes, a process known as "cross-slip" [1]. For instance, screw dislocations in face-centered cubic crystals primarily slip in the $\{111\}$ family of planes but can transition to another plane within this family. The activation energy for this phenomenon was first quantified experimentally by Bonneville and Escaig [14]. Nucleation and interaction of dislocations with each other and other defects, i.e. vacancies and Interstitials, results into formation of dislocation junctions and loops, with characteristics of both edge and screw dislocation.

Dislocation junctions and loops are formed because a dislocation should either end on a surface of a material or fork into other dislocations [1]. Junctions – regions where three or more dislocations meet – happen due to nucleation, propagation and finally interaction of dislocations in extreme environments or during mechanical tests [15, 16]. The Burgers vectors of a junction's constituent dislocations should be conserved ($\sum \vec{b} = 0$). This leads into increase in the total length of the dislocations per unit volume, know as "dislocation density". Loops, on the other hand, happen when a dislocation closes upon itself [17, 18]. Loops are classified into "prismatic" and "glissile" types. While the Burgers vector of the former is perpendicular to the loop plane, that of the latter is parallel to the glide plane [1]. In general, forces acting on the dislocations govern the plastic flow in crystals and form complex hardening mechanisms in materials. The complex mechanisms underlying these dynamics are collectively referred to as "crystal plasticity" or "work hardening". Without a thorough understanding of these processes, theoretical models fail to be descriptive, particularly under extreme conditions and temperatures.

Dynamics of dislocations under external forces determine a material's mechanical properties, such as ductility and strength. Materials with low dislocation density or limited dislocation mobility tend to be brittle, whereas those with higher dislocation density and greater mobility are generally more ductile [22, 23]. On the other hand, the strengthening of materials depends on limiting dislocation motion. Various strengthening mechanisms, such as solid solution strengthening [24] and precipitate strengthening [25] occur in alloys. In solid solution strengthening, dislocation motion is hindered by local atomic misfits, while in precipitate strengthening, precipitates act as obstacles to dislocation movement.

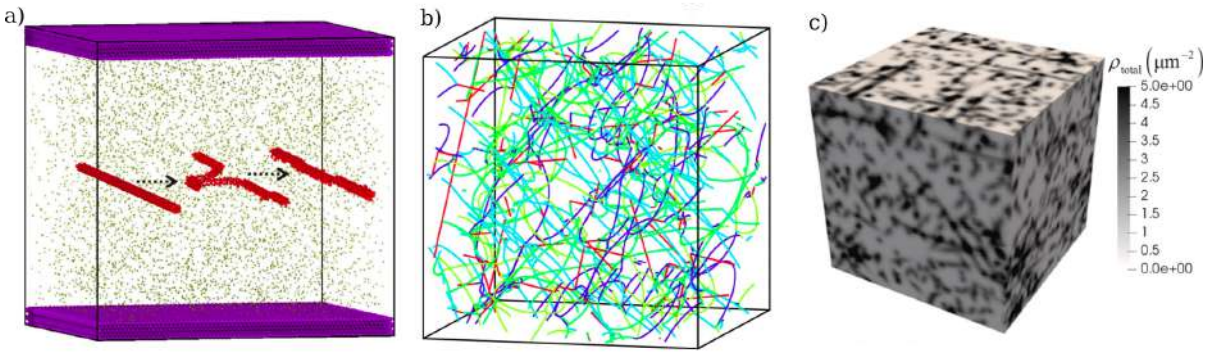

Figure 2.1: Demonstration of dislocations in computational methods in **(a)** molecular dynamics simulations in a gallium nitride [19]. Here, the specific motion of dislocations (red atoms) within this material is demonstrated. **(b)** Discrete dislocation dynamics simulations. In this example, colors represent different slip systems in a copper crystal [20]. **(c)** Continuum dislocation dynamics modeling for a AISI 316L steel [21], where collective dynamics of dislocations is modeled using continuum fields. Here, the contrasts in the image demonstrate the dislocation density.

The "Peierls stress" [26, 27] – the minimum stress required to initiate dislocation motion without thermal assistance – is a useful parameter to quantify this resistance. Finally, volume defect such as solutes in alloys, where a secondary atom (B) is added in excess to the primary atomic structure (A), are another source of strengthening. When the concentration of B atoms exceeds solubility limits, they precipitate, forming clusters that impede dislocation motion and enhance the material's strength [28–31].

Computational methods, such as molecular dynamics and discrete dislocation dynamics, are essential tools for investigating dislocation behavior, particularly when experimental approaches face significant challenges. Molecular dynamics techniques give atomic-scale insights into dynamics of dislocation [32–39]. Properties such as mobility coefficient, cross slip energy barriers, interaction of dislocations with themselves and other defects could be studied with molecular dynamics methods. The output parameters of molecular dynamics simulation are often used to do large scale dislocation dynamics modeling within discrete dislocation methods [40–44]. Two snapshots of dislocations studied by these methods are shown in Fig. 2.1(a-b). In discrete dislocation dynamics methods, each dislocation is considered as a line that interacts with other lines (dislocations), which make the study of their interaction possible. In contrast, continuum dislocation dynamics methods [21, 45, 46] simulates the compound behavior of dislocations within a material using continuum fields (Fig. 2.1(c)), opposed to tracking each dislocation as a line.

2.2 Experimental Insights into Dislocations

2.2.1 Observation of Dislocation Dynamics

The direct observation of dislocations became possible only in the 1950s. The presence of dislocations in materials was first hypothesized due to the discrepancy between the theoretical and experimental shear stress values required for plastic deformation [1]. Frenkel's

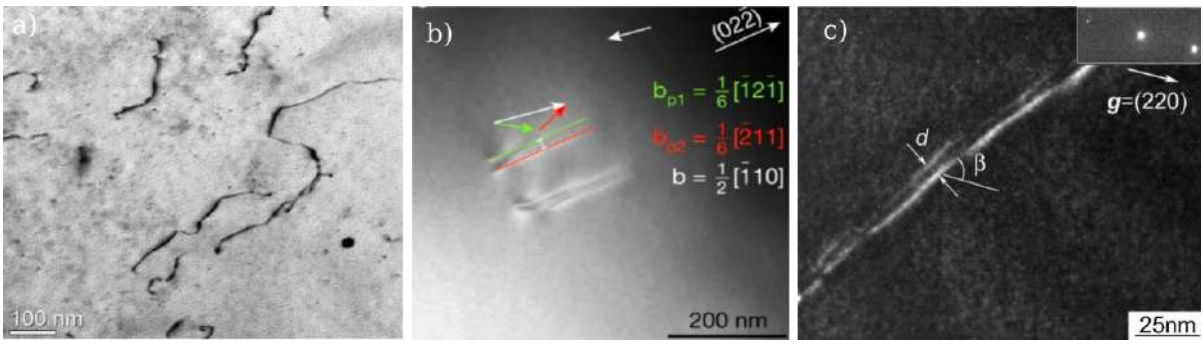

Figure 2.2: Examples of trnsmission electron microscopy images. **(a)** Bright-field image of a Fe-Ni-based superalloy after a creep test at a temperature of 750°C. Image credit: [53]. **(b)** Low angle annular dark-field image of NiCoCr medium entropy alloy: Copyright 2020, Springer Nature [54]. **(c)** Weak-beam dark-field images of dislocations in $FeCoNiCrAl_{0.1}$, image credit: [55].

theoretical work [47] first estimated the shear stress required for plastic deformation in a crystal, where revealed a value orders of magnitude higher than experimental measurements. Experimental measurements of this value for nearly perfect crystal nanowires or nanopillars, devoid of dislocations, aligned with theoretical predictions [48, 49]. This confirmed that defects were responsible for the previously observed discrepancy [1]. A second indication of the presence of dislocations in materials arose from crystal growth theory, where the growth of a crystal in vapor required a lower supersaturation percentage than theoretically predicted [1, 50]. In this case, it was found that the presence of dislocations ease the crystal growth by orders of magnitude less supersaturation required in the vapor.

The Emergence of advanced experimental methods, such as transmission electron microscopy, made the direct observation of dislocations possible. Various experimental techniques are employed to measure dislocation properties, including dislocation density, spatial distribution, and arrangement within different material types [51, 52]. Transmission electron microscopy creates images of dislocations by utilizing the contrast generated from strain fields within the material. More recently, high-resolution transmission electron microscopy techniques have enabled imaging at the atomic scale when very thin specimens are studied. Transmission electron microscopy images are created by directing a beam of electrons at a thin specimen of the material. Electrons that pass through the sample form "bright-field images", while those diffracted by the sample are used to create "dark-field images" [1].

Transmission electron microscopy techniques facilitate detailed study of dislocation types, core structures, and interactions with other defects by producing high-resolution images of dislocations. Transmission electron microscopy techniques also reveal dislocation line orientations and Burgers vector characteristics and allow for precise mapping of dislocation structures and measurement of related properties [56–58]. For instance, fine structure details of dislocations are studied through weak-beam dark-field imaging by minimizing unwanted contrast from nearby crystal features [59–61]. A second example is the use of high-angle annular dark-field scanning transmission electron microscopy that enables atomic-scale imaging of dislocations [62–64]. This technique enables detailed

study of dislocation interactions and individual atomic types, as image contrast directly reflects the material's composition.

Three examples of transmission electron microscopy imaging of dislocations are illustrated in Fig. 2.2. In Fig. 2.2 (a), a bright-field image of a Fe-Ni-based superalloy after a creep test at a temperature of 750°C is shown [53]. In such images, dislocations appear as dark lines within the material. Bright-field images allow observation of slip systems, dislocation density, core structures, and various other dislocation properties. A low-angle annular dark-field image of a NiCoCr alloy [54] is shown in Fig. 2.2(b). This image demonstrates that the direction of the Burgers vector can be identified within such images. Finally, weak-beam dark-field images, such as the one shown in Fig. 2.2(c), provide a detailed visualization of dislocations [55]. These images allow precise measurements of properties such as the distance between dislocations, known as stacking fault width, which can be used to calculate stacking fault energy – a crucial parameter for understanding material behavior.

Other techniques, besides transmission electron microscopy, include X-ray diffraction topography [66, 67], scanning electron microscopy [68, 69], and field ion microscopy [70], which are also used to observe dislocations. The X-ray diffraction topography technique provides lower resolution images ($1\mu m$) compared to transmission electron microscopy. However, it is advantageous because it allows for the examination of much larger samples [1]. in contrast, field ion microscopy and atom probe field ion microscopy provide atomic-level resolution to the dislocations which enables the study of their interaction with point

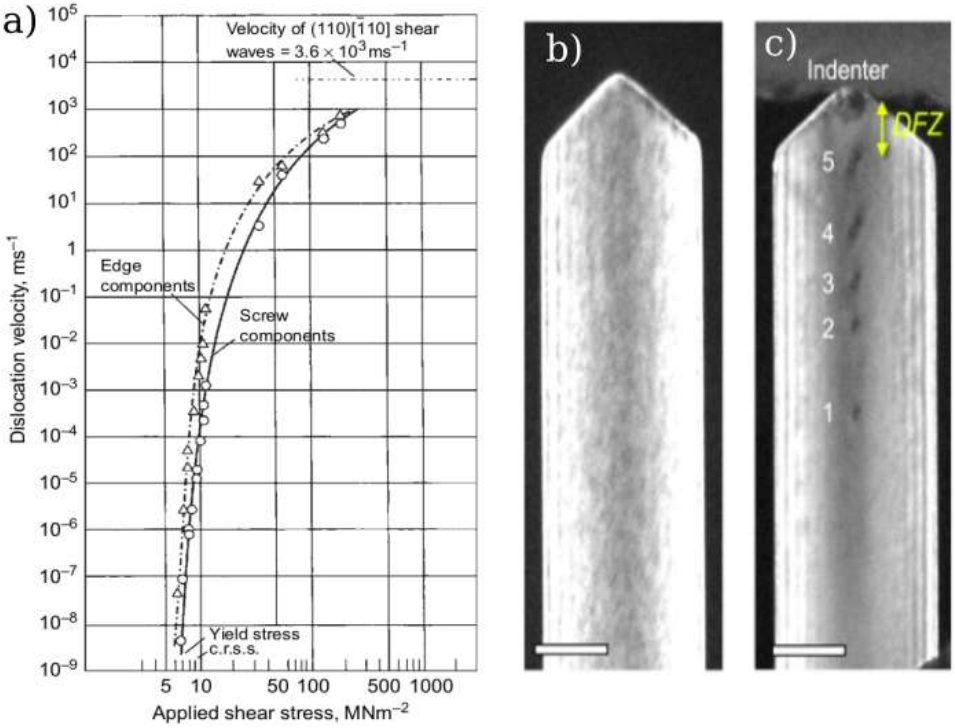

Figure 2.3: **(a)** Dislocation velocity versus applied shear stress in lithium fluoride [65], image credit [1]. **(b-c)** Bright-field in-situ transmission electron microscopy images of dislocation cross-slip in $FeCoNiCrAl_{0.1}$, image credit: [55].

defects such as vacancies and interstitials in applications like the study of radiation damage [1]. Experimental techniques, such as scanning electron microscopy, allow the study of dislocations at the surface of a material. Dislocations often nucleate and propagate from the surface, and techniques like scanning electron microscopy can provide valuable insights into tracking these movements on the surface of a material [1].

Early studies of the dynamic properties of dislocations became possible once researchers developed methods to directly observe dislocations and prepare crystals in specific orientations, enabling controlled dislocation motion [14, 71]. The motion of dislocations within a crystal, including properties such as dislocation velocity, cross-slip energy barriers, and climb mechanisms, plays a critical role in determining a material's mechanical properties [1]. These properties were initially quantified through x-ray micrographs [71]. These methods are more advanced today, as in-situ transmission electron microscopy methods allow for real-time observation of dislocation dynamics and movements including climb, cross-slip, and responses to external stimuli that is beneficial for clarity in understanding dislocation behavior under varying conditions [72–76].

The velocity of dislocations can be measured using X-ray diffraction and in-situ transmission electron microscopy techniques. This velocity depends on the type of dislocations, purity of the material, temperature and the applied shear stress [1]. One method for measuring dislocation velocity involves preparing a crystal in a specific crystallographic orientation and inducing dislocations from the surface of the material. Upon applying shear stress, the positions of the dislocations are tracked over time using X-ray diffraction topography [71]. This technique has been successfully employed to determine the stress dependence of dislocation velocity in copper [71] and other materials, such as lithium fluoride [65], as shown in Fig.2.3(a). A More advanced technique is the calculation of the velocity of the dislocation through in-situ transmission electron microscopy [77, 78]. Fig.2.3(b-c) show a gold nanowire before and after application of external stress, where dislocation loops are observable through in-situ observation. In these methods, the positions of dislocations are directly measured using the output from a transmission electron microscope while external stress is applied to the material. From the linear portions of the stress-velocity curves, the mobility coefficient n can be calculated using the expression $v = v_0 \left(\frac{\tau}{\tau_0}\right)^n$, where v and v_0 are the dislocation velocities at corresponding applied shear stress of τ and τ_0, respectively.

Cross-slip properties of dislocations is also studied widely during past years [9, 55, 79]. Escaig and Bonneville [14] studied cross-slip by first predeforming a large single-crystal pure copper sample, which induced the nucleation of several dislocations within the material. Subsequently, new samples were cut from the predeformed specimen in specific crystallographic orientations to ensure that the applied stress selectively facilitated dislocation movement through cross-slip. This new technique allowed for quantifying of related properties such as cross-slip activation volume, activation energy and dislocation cross-slip rate. In-situ transmission electron microscopy also allows for study of cross slip in crystalline materials. This is possible due to the fact that the rate of the cross-slip could be calculated over time and makes quantification of related propertied achievable.

2.2.2 Dislocation Dynamics in Complex alloys

Development of advanced alloy materials is central to modern technological advancements, particularly for applications requiring materials that can withstand extreme conditions [80, 81]. Recently, concentrated solid solution alloys have gained attention for their promising mechanical properties. Take the example of equiatomic NiCoCr alloy, which has exceptional strength, ductility, fracture toughness, and hardness with a rather simple composition [80]. This remarkable performance is believed to root into specific chemical and structural characteristics within the alloy, particularly the presence of nanoscale (1 nanometer) short-range ordering, which is influenced by thermomechanical processing and affects dislocation behavior and stacking fault widths [82–85]. Additionally, lattice distortions and atomic misfits, which appear due to differences in atomic radii, are thought to contribute to the alloy's enhanced mechanical behavior [86, 87]. However, the exact role of short-range ordering in upgrading these properties remains under investigation.

Characterizing dislocation behavior in complex alloys is crucial, as the observation of these defects in multi-component alloys differs significantly from that in single-element crystals [54, 55, 82, 88–90]. The observation of dislocations in complex alloys is particularly challenging due to factors such as their chemical complexity, nanoscale short-range ordering effects on dislocation motion, and the intricate dynamic evolution of dislocations [55, 88, 89]. Additionally, transmission electron microscopy proves difficult, as overlapping strain fields from dislocations and local misfit distortions (Known as the Cottrell

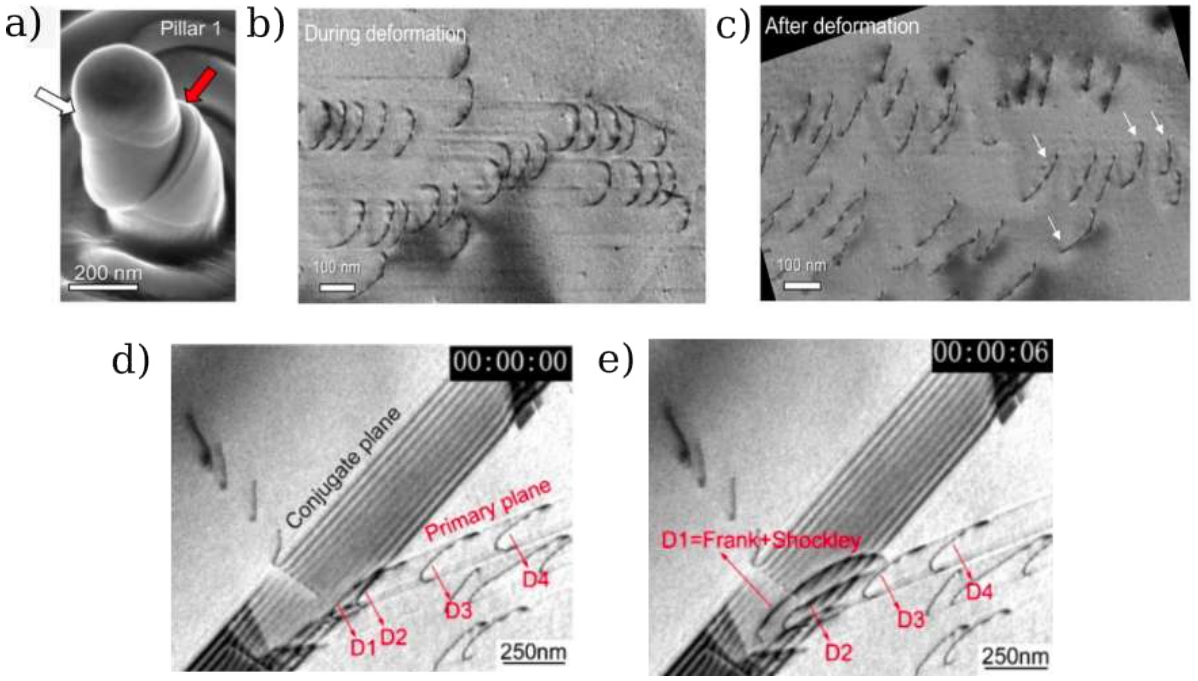

Figure 2.4: Dislocation dynamics study in high entropy alloys, image credit: [55, 88]. **(a-c)** In-situ transmission electron microscopy was utilized to study the nano-pillars of a FeCoCrMnNi high entropy alloy during and after deformation. **(c-d)** Dislocation cross-slip study of a $FeCoNiCrAl_{0.1}$ high entropy alloy through in-situ transmission electron microscopy.

atmosphere [91, 92]), or the overall complexity of strain fields, hinder clear visualization. Thus, nanowires or nanoscale pillars are used for imaging, as dislocation dynamics can be more effectively controlled at the nanoscale [88]. Fig.2.4(a) shows a nano-pillar of a FeCoCrMnNi high-entropy alloy. In-situ transmission electron microscopy allows for study of dislocation motion during the deformation of the this alloy as shown in Fig.2.4(b). It has also been observed that dislocations appear straighter after load removal Fig.2.4(c), though the origin of this phenomenon remains unknown. Atomic-scale observation of short-range ordering and other effects is crucial to understanding this behavior. In-situ techniques were also used to study the cross-slip of dislocations in $FeCoNiCrAl_{0.1}$ high-entropy alloys [55]. As shown in Fig.2.4(d-e), in-situ methods allow for observing dislocations motion from one slip plane to another slip plane family.

Molecular dynamics simulations can aid in understanding dislocation dynamics in multi-component alloys [32–39]. This is because molecular dynamics provides atomic-scale insights into dislocations, enabling the study of numerous dislocation-related properties that are challenging or impossible to investigate using experimental methods. The emergence of machine learning force fields [93–97] has further enhanced the atomic-scale precision in studying dislocations. Machine learning force fields, trained on density functional theory data, allow the molecular dynamics study of dislocations with near-quantum accuracy. These recent advancements could address many unanswered questions about dislocation dynamics in complex alloys, which are challenging to investigate experimentally. An example is the significant differences discovered in pillar compression of body-centered and face-centered crystal structures [98]. Molecular dynamics simulations have shown that plastic deformation and dislocation nucleation and multiplication in these crystal structures are fundamentally different.

2.3 Machine Learning Force Fields in Dislocation Dynamics Modeling

A variety of computational approaches are used in modeling nanomechanical testing and each of them offer distinct advantages and limitations. Finite element methods [99, 100], for instance, approximate material behavior by solving numerical solutions to differential equations and predicts materials properties under various conditions. This technique is particularly useful for capturing macroscopic material responses as the model relies on continuum mechanics. Thus, it falls short of atomic-level precision and its accuracy in nanoscale contexts is limited. Discrete dislocation dynamics methods [40–44], another commonly used approach, model dislocations and their interactions but remain limited in atomic resolution. Discrete dislocation dynamics can effectively simulate dislocation behaviors within crystal structures, though it still cannot capture individual atomic movements or the effects of atomic-scale irregularities.

In contrast, molecular dynamics simulations can offer insights into dislocation dynamics at an atomic scale by using interatomic potentials carefully tuned for nanomechanical

applications [32–39]. This atomic-level modeling capability allows molecular dynamics to reveal detailed behaviors in materials under stress, such as dislocation nucleation and propagation [101–104]. Despite the higher computational costs, molecular dynamics's precision makes it indispensable for studying nanoscale mechanical properties and behaviors and bridges the gap left by finite element methods and discrete dislocation dynamics. Together, these methods complement one another and provide a multi-scale view of material behavior under various conditions.

Over the past five years, numerous data-driven models, leveraging machine learning, have been developed to create interatomic force fields. Among the earliest of these models are potentials based on Behler-Parrinello symmetry functions [93–97], Smooth Overlap of Atomic Positions (SOAP) [105–111], and moment tensor potentials [112–116]. These atomic-scale descriptor frameworks have been used alongside Gaussian processes and neural networks and allow models to learn a material's potential energy surface directly from quantum-accurate data, such as density functional theory calculations. These methods are exceptionally powerful and accurate in supporting multi-scale modeling of materials at scales beyond traditional first-principle calculations. Thus, these models could simulate systems of thousands of atoms for diverse applications.

The next generation of these methods is built upon atomic cluster expansion potentials [117], initially introduced by Drautz [118]. Using this formalism, several highly accurate interatomic potentials have been developed [119]. Additionally, a high- performance C++ implementation of atomic cluster expansion has been created to support large-scale simulations with improved efficiency [120]. Variants of atomic cluster expansion include the Message Passing Graph Neural Networks (MACE) [121–123] and the Graph Atomic Cluster Expansion for Semilocal Interactions beyond Equivariant Message Passing (GRACE) [124]. MACE, in particular, utilizes neural networks with Euclidean symmetry and is one of the most accurate models available for molecular dynamics simulations at near-quantum accuracy.

In addition to the models discussed above, active learning techniques have been employed to improve the development of interatomic potentials [109, 125, 126]. These techniques operate by assessing uncertainties in a sparse Gaussian process kernel and capacitates the on-the-fly selection of configurations during ab-initio molecular dynamics simulations. By focusing on configurations with high uncertainty, these methods ensure that the training dataset captures a comprehensive range of the potential energy surface, which is crucial for constructing accurate interatomic potentials [127]. This approach has proven effective across various materials science applications. Furthermore, active learning facilitates the efficient generation of training data and reduces computational cost and improves the robustness of the resulting potential models [128].

Several studies on machine learning force fields in the context of defects in crystalline materials is done up to date. Study of smaller scale defects such as point defects and maybe their dynamics are straight forward with density functional theory accuracy as the dimension of supercell needed does not exceed a few hundred of atoms [129–132]. However, for bigger dimensional defects such as interfaces, grain boundaries an dislocations, larger

scale simulation with density functional theory accuracy is desired [133–136]. Several types of defects are studied for crystalline defects ranging from point defects such as vacancies and self-interestitials, grain boundaries, dislocations, stacking faults, surfaces and solidliquid interfaces with machine learning interatomic potentials. Also, a variety of methods such as gaussian approximation potentials, moment tensor potentials and neural network interatomic potentials were employed for these studies.

For machine learning force fields to accurately model dislocations, it is essential that they first capture the correct elastic properties of materials. This is because plastic deformation due to dislocations is largely governed by their long-range elastic fields [1, 2]. machine learning force fields have consistently demonstrated impressive accuracy in predicting elastic properties, matching the precision of density functional theory and experimental data. However, while crucial, elastic accuracy alone does not make an machine learning force fields ideal for modeling dislocations [32].

A critical aspect in dislocation modeling is the accurate representation of dislocation cores regions in a machine learning force fields training dataset, where atoms deviate from the lattice structure over a few lattice spacings [32, 137]. These configurations are challenging to investigate through density functional theory due to the large supercell sizes and complex periodic boundary conditions. Instead, generalized stacking fault configurations, which exhibit similar properties to dislocation cores, can be included in machine learning force fields training datasets to improve model reliability for dislocations [138]. machine learning force fields excel over many classical force fields by accurately predicting generalized stacking fault energies and Peierls stress. These properties are critical for modeling dislocation behavior and defects in materials. This capability makes machine learning force fields a strong choice for simulating dislocation dynamics and defect properties in diverse crystalline materials [139].

As shown elsewhere [110], although GSF configurations can greatly aid in modeling dislocations in metals, including the actual dislocation core structure in the training dataset can yield even more accurate results. This may be feasible for body-centered cubic materials since their dislocation cores are non-degenerate, meaning they do not typically split into two partial dislocations. Consequently, their dimensionality is manageable enough to be captured through density functional theory calculations. However, dislocations also exhibit varied properties depending on their line length. For instance, in body-centered cubic materials, dislocation propagation often occurs through the movement of kink formations [140]. Incorporating kinked crystal configurations into machine learning force fields training datasets remains challenging due to the larger length scale required. Despite these challenges, studies so far demonstrate that machine learning force fields provide valuable insights into dislocation behavior, even though further investigation is necessary to refine their accuracy in this complex area.

Finally, it is essential to note that developing machine learning force fields for face-centered cubic and hexagonal close-packed materials presents greater challenges than for body-centered cubic materials. This is due to the dislocation core being degenerate and often splitting into two partial dislocations with a more energetically favorable state.

In addition, these materials contain a larger number of unique dislocation slip systems. However, advanced machine learning force fields development methods, such as active learning, using frameworks like FLARE [126], offer promising approaches for tackling these complexities.

In summary, computational methods in materials science, particularly in modeling complex defects in crystals, are advancing rapidly and they offer unprecedented accuracy and predictive power. The development of machine learning force fields has significantly improved our ability to simulate atomic-scale phenomena, including dislocation behavior, stacking fault energies, and cross-slip, with near-quantum accuracy across larger length scales. As these models continue to evolve, they offer the ability to bridge the gap between quantum-level simulations and macroscopic materials properties. Ultimately, these methods could expand the applications of computational materials science to real-world engineering challenges.

Aims and thesis

The thesis builds upon the following studies from the selected published work:

i. **Investigation of Extended Dislocation Dynamics:** Explores the behavior of dislocations in multi-component alloys with and without chemical short-range ordering, using molecular dynamics and Monte Carlo simulations with various classical interatomic potentials.

ii. **Development of neural network interatomic potentials:** Focuses on evaluating existing machine learning force fields designed for dislocations and creating neural network interatomic potentials for capturing dislocation dynamics in crystalline materials.

iii. **Dwell Nano-Indentation in Multi-Component Alloys:** Examines nano-indentation phenomena through molecular dynamics and Monte Carlo simulations, focusing on the capabilities of interatomic potentials to influence short range ordering.

In more detail, the thesis addresses the following key points:

- Interatomic potentials found in the literature are highly diverse and often show varying properties for the same material.
- For NiCoCr medium entropy alloys, some potentials exhibit short range ordering that aligns with experimental data, while others show a random distribution of the constituent atoms.
- These variations in interatomic potentials influence the mechanical properties and dislocation dynamics predicted by computational methods.
- Further studies indicate that using the correct interatomic potentials in dwell nano-indentation simulations can manipulate the underlying short range ordering in NiCoCr alloys and facilitates experimental measurements.
- This body of work emphasizes the significant role of interatomic potentials in atomistic simulations involving dislocation dynamics in nanomechanics and the importance of developing accurate potentials for nanomechanical applications in crystalline materials.

- Even in single-element materials like tungsten, classical interatomic potentials produce varied results in nano-mechanical simulations, demonstrating inconsistencies.
- The thesis proposes effective methods for developing interatomic potentials tailored to nano-mechanical simulations and ensures better coverage of dislocation dynamics representation and the associated energy landscape.

Aligned with the objectives of this research, I have formulated the following central thesis:

Computational material science methods are critical in determining the accuracy of atomistic simulations, particularly in predicting dislocation dynamics in multi-component alloys and single-element materials. By effectively leveraging computational tools, such as interatomic potentials, one can improve the predictive power of molecular dynamics methods for dislocations modeling. My work centers on enhancing the utilization of existing interatomic potentials and development of machine learning potentials to more accurately capture dislocation dynamics in a manner that aligns with experimental results and hence facilitates materials design.

Methodology

This chapter presents the comprehensive methodologies employed to investigate the dislocation dynamics and mechanical properties of NiCoCr alloys, along with the development of neural network interatomic potentials (NNIPs) for single element crystals. I begin by exploring dislocation dynamics simulations, which utilizes molecular dynamics (MD) and hybrid molecular dynamics-Monte Carlo (MD-MC) techniques for the annealing of NiCoCr alloys. The focus then shifts to nano-indentation simulations, where I explain the MD setup and the specific approach taken for dwell nano-indentation experiments tailored to NiCoCr materials. Finally, I discuss the development of NNIPs, including the use of Behler-Parrinello descriptors, strategies for neural network training, the creation of datasets through density functional theory (DFT), and methods for similarity measurement. Each section is designed to provide a clear understanding of the techniques and parameters that underpin this thesis.

4.1 Dislocation Dynamics in NiCoCr Alloys

4.1.1 MD Setup and Dislocation Dynamics Simulations

The investigation of edge dislocation dynamics was conducted in both the presence and absence of chemical short-range ordering (CSRO). MD simulations were performed using LAMMPS [141], focusing on atomistic models of sizes ranging from 500,000 to 1,700,000 atoms, all contained within three-dimensional periodic cells. To explore the properties of CSRO without the influence of dislocations, cubic samples with dimensions of 10 nm along the $x[100]$, $y[010]$, and $z[001]$ axes were constructed.

Simulations were carried out under the NPT ensemble and utilized a Nose-Hoover thermostat and barostat with relaxation times set to $\tau_{\text{therm}} = 10\,\text{fs}$ for thermal control and $\tau_{\text{bar}} = 100\,\text{fs}$ for pressure stabilization and the discretization time was fixed at $\Delta t = 1.0\,\text{fs}$. Initial configurations were achieved through energy minimization at $T = 0\,\text{K}$ at a constant volume and then equilibration of the sample at varying temperatures at a constant pressure of $P = 0\,\text{bar}$.

Two commonly employed embedded-atom method (EAM) potentials were utilized for modeling interatomic forces within the context of NiCoCr solid solution alloys. The first potential, known as the Li-Sheng-Ma potential [142], has been integral in recent studies addressing SRO phenomena, dislocation nucleation, glide dynamics [143, 144], and nanoindentation tests [145]. The second potential, the EAM FarkasCaro potential

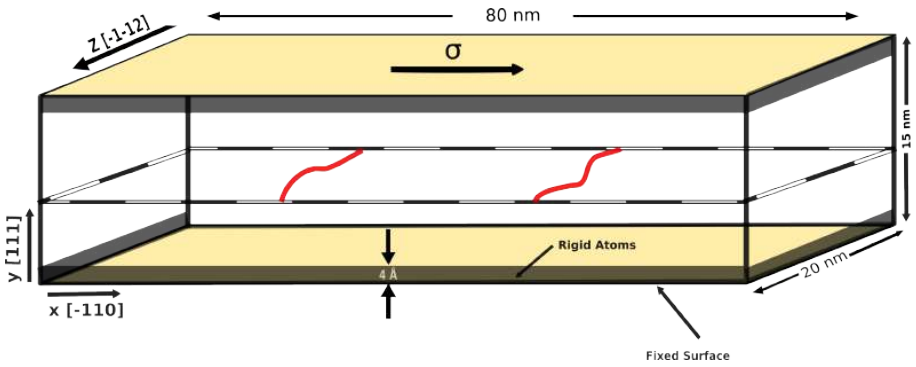

Figure 4.1: A schematic of the shear setup, illustrating the partial dislocations, is provided. Periodic boundary conditions are applied along both the dislocation lines and the glide direction (in the x and z dimensions, respectively), while fixed boundaries are enforced along the y direction using rigid slabs (shown in gray). During shearing, atoms in the bottom surface remain fixed (with zero displacement), while shear stress σ is applied to the rigid top plane.

[146], was originally designed for high-entropy FeNiCoCrCu alloys and was leveraged here to confirm the consistency of SRO formation across different potential frameworks.

In addition to the SRO analysis, the dynamics of a edge dislocations were explored. This dislocation undergoes dissociation into two partial dislocations with an accompanying stacking fault when subjected to external perturbations in face-centered cubic (FCC) crystals. For this study, a simulation cell was constructed with dimensions $L_x = 80\,\text{nm}$, $L_y = 20\,\text{nm}$, and $L_z = 15\,\text{nm}$, as illustrated in Fig. 4.1. The alloy was annealed at a specified temperature T_a, followed by equilibration at a low temperature of $T = 5$ K and zero pressure ($P = 0\,\text{bar}$) for 100 ps.

To effectively introduce the edge dislocation into the aged sample, the periodic array of dislocation model, as proposed in Ref. [147], was implemented to ensure proper periodicity along the Burgers vector $x[110]$ and the dislocation line $z[1\bar{1}2]$. Following this, the dislocated sample underwent further relaxation using the NPT framework with $P_{xx} = P_{zz} = 0$ at $T = 5$ K for an additional 100 ps, leading to the dislocation's dissociation into two Shockley partials.

To assess the effects of local lattice distortion and CSRO on yield properties, shear tests were executed at $T = 5$, K. These tests were conducted in a stress-controlled manner within the NVT ensemble, where additional forces were applied to the top surface (normal to the y direction), while the bottom layer, approximately 4 Å thick, was held fixed. The applied stress was gradually increased from $\sigma = 50$ MPa in a quasi-static manner, surpassing the critical depinning stress to facilitate the movement of the partial dislocations.

4.1.2 Hybrid Molecular Dynamics - Monte Carlo Simulations

To obtain the annealed configurations, hybrid MD-MC simulations, specifically using the variance constrained semigrand-canonical (VCSGC) ensemble [148] were employed. This method was implemented across an annealing temperature range of $T_a = 400\,\text{K}$ to $1300\,\text{K}$.

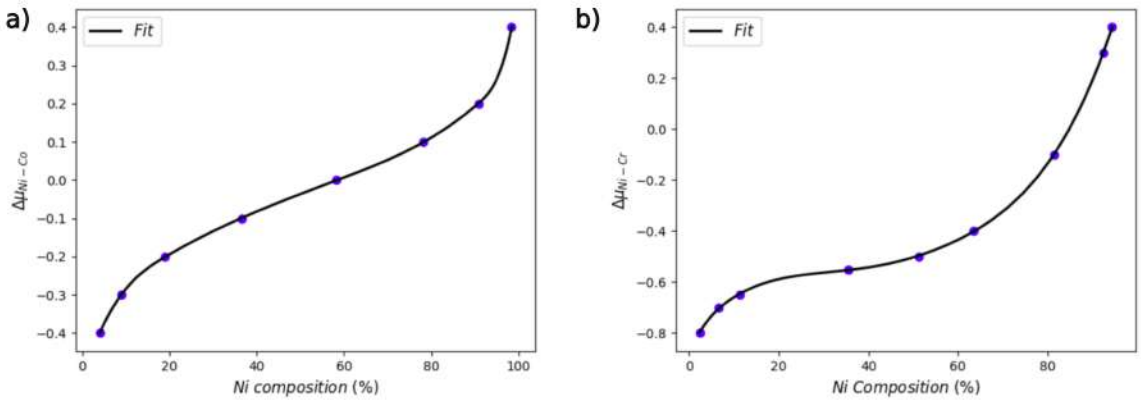

Figure 4.2: Chemical potential differences for a) Ni-Co and b) Ni-Cr pairs used for variance constrained semi-grand canonical (VCSGC) ensemble.

The combination of MD and MC facilitates further relaxation of the system, effectively overcoming the extended relaxation times associated with purely MD simulations.

To determine the chemical potential differences, composition errors were minimized by conducting a series of semi-grand-canonical simulations at a temperature of $T = 1500\,\mathrm{K}$. The chemical potential difference between two species, represented as $\Delta\mu_{X_1X_2} = \mu_{X_1} - \mu_{X_2}$, was calculated based on the equation:

$$\mu(X_1, P, T) = T \ln\left(\frac{X_1}{1 - X_1}\right) + \sum_{i=0}^{n} A_i X_1^i \tag{4.1}$$

where X_1 denotes the reference element (in this case, Ni) and A_i are the fitting parameters derived from the simulations (see Fig. 4.2).

The hybrid MD-MC approach employed a fixed target composition throughout the annealing process. During the MC steps, one complete cycle comprising $N/2$ attempts of atomic transmutation in every 20 MD steps was conducted. This enables the effective interchange of species to achieve a more thermodynamically stable configuration. In total, $800,000$ MC cycles at all annealing temperatures were performed to ensure that the system reached thermal equilibrium. This extensive sampling enabled the structures to achieve statistical independence in terms of the CSRO characteristics being investigated.

4.2 Nano-indentation Simulations

4.2.1 Simulation Setup and Boundary Conditions

To simulate the nanoindentation process and accurately capture the deformation behavior of materials in this thesis, specific boundary conditions were meticulously designed (Fig. 4.3). The sample was divided into three distinct regions along the z-axis. First, a frozen section, covering approximately $0.02 \times dz$, was established at the base to ensure numerical stability during the indentation process. Here, dz is the hight of the sample. Above this, a thermostatic region, approximately $0.08 \times dz$, was included to dissipate the heat generated

during nanoindentation. This region maintains the thermal equilibrium during the nanoindentation simulations [149, 150]. The primary deformation occur in the dynamic atoms section, where interactions between the rigid indenter tip and the sample surface alters the atomic structure of the material and results in plastic deformation.

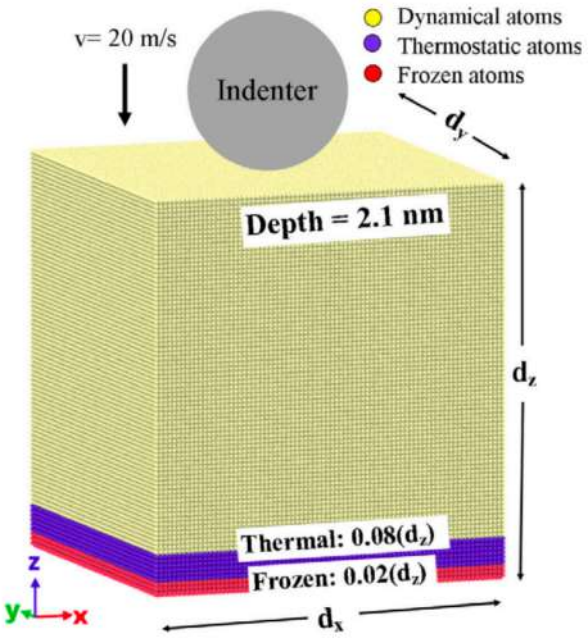

Figure 4.3: Schematic of the typical setup for MD simulations of nanoindentation. The sample is divided into three distinct regions to account for boundary conditions, and a non-atomic repulsive spherical indenter is employed [150].

A vacuum region of 5 nm was added above the surface to simulate an open boundary. This region prevents stress reflections and allows realistic surface deformation. This open boundary condition ensures that the indentation could proceed without artificial constraints on the samples surface response [150]. A schematic of the simulation setup is illustrated in Fig. 4.3.

The indenter tip was represented as a repulsive imaginary (RI) rigid sphere, modeled to interact with the surface using the following force potential:

$$F(t) = K(\vec{r}(t) - R)^2 \tag{4.2}$$

where $K = 236$ eV/Å^3, equal to 37.8 GPa, is the force constant, while $\vec{r}(t)$ represented the position of the indenter's center over time, and $R = 3$ nm is the radius of the indenter tip.

Following the equilibration of the sample at a intended temperature within a NPT ensemble, nanoindentation simulations are performed within the NVE ensemble. This ensures that the number of atoms, system volume, and energy remains constant throughout the simulation. The velocity Verlet algorithm is applied for time integration and enables accurate position and velocity updates for all atoms. Periodic boundary conditions were imposed along the x- and y-axes to mimic an infinite surface, while a fixed

boundary was applied at the base of the z-axis, with the top surface free to deform. The chosen parameters guarantees that the nanoindentation process could be simulated under realistic experimental conditions [150].

In these simulations, the trajectory of the indenter tip is expressed as:

$$\vec{r}(t) = x_0\hat{x} + y_0\hat{y} + (z_0 \pm vt)\hat{z} \tag{4.3}$$

where x_0 and y_0 represented the coordinates of the center of the sample surface on the xy plane. Also, z_0 defined the initial gap between the indenter and the sample surface. The indenter tip velocity and the time step in nanoindentation simulations are set to $v = 20\,\mathrm{m/s}$ and $\Delta t = 1\,\mathrm{fs}$, respectively.

4.2.2 Nanomechanical Response Measurements

The elastic behavior of the material during the initial loading process of nano-indentation is assessed using a Hertzian contact model, which defines the elastic load P_{H} as a function of the contact between a spherical indenter and a flat surface. This relationship is characterized by the following equation [149, 151]:

$$P_{\mathrm{H}} = \frac{4}{3} E_{\mathrm{Hertz}} R^{1/2} h^{3/2} \tag{4.4}$$

Here, R is the radius of the indenter, h is the depth of indentation, and E_{Hertz} represents the effective Young's modulus of the material in the contact region. The Hertzian contact model assumes purely elastic behavior without any plastic deformation. This analysis helps the analysis of the mechanical response of the material in the elastic region.

In addition to P_{H}, the contact pressure P at the indenter interface is computed based on linear elastic contact mechanics, which is expressed as [152]:

$$P = 2\pi \left[24p \left(\frac{E_{\mathrm{Y}} R}{1-\nu^2} \right)^2 \right]^{1/3} \tag{4.5}$$

In this equation, E_{Y} denotes the Young's modulus of the material, p refers to the applied load during the simulation, R is the radius of the indenter, and ν represents Poisson's ratio. The contact radius, $\mathrm{a}(h)$, is then obtained using a geometric relationship that connects the indentation depth to the size of the contact area. This radius is given by [152]:

$$\mathrm{a}(h) = \left[\frac{3PR(1-\nu^2)}{8E_{\mathrm{Y}}} \right]^{1/3} \tag{4.6}$$

The contact radius $\mathrm{a}(h)$ corresponds to the region at the interface where plastic deformation initiates and defects such as dislocations nucleate [152]. The relationship between the applied pressure and the contact radius is essential for understanding the material's resistance to indentation-induced plasticity. In particular, it provides insight into how far the material can withstand applied stress before yielding occurs.

A universal linear relationship between P/E_{Y} and $a(h)/R_i$ is found, which is expressed as:

$$\frac{P}{E_{\mathrm{Y}}} = \frac{0.844}{1-\nu^2}\frac{a(h)}{R_i} \tag{4.7}$$

where $a(h)/R_i$ can be considered a dimensionless measure of the nanoindentation strain, a parameter that quantifies how the material deforms elastically and plastically under load. This provides a key insight into how different materials, particularly those with varying elastic moduli, respond to contact forces during nanoindentation experiments.

To investigate the material's mechanical stability and strength under compressive stress, the principal stress component in the z-direction (σ_{zz}) was calculated as follows [153]:

$$\sigma_{zz} = -\mathcal{S}\left[\left(1 - \frac{\arctan(\alpha)}{\alpha}\right)(1+\nu) - \frac{1}{2(1+1/\alpha^2)}\right] \tag{4.8}$$

The parameters $\mathcal{S}$ and α are defined as:

$$\mathcal{S} = \frac{3P_{\mathrm{ave}}}{2\pi \mathrm{a}(h)^2}, \quad \alpha = \frac{\mathrm{a}(h)}{h} \tag{4.9}$$

This expression for σ_{zz} accounts for both the applied pressure and the Poissons ratio and provides a detailed understanding of how the material responds to compressive forces applied normal to its surface.

The stress components parallel to the surface of the indented sample in the x and y directions were calculated as:

$$\sigma_{xx} = \sigma_{yy} = -\frac{\mathcal{S}}{1+1/\alpha^2} \tag{4.10}$$

These stresses represent the forces acting tangentially to the surface during indentation, and they contribute to the nucleation and movement of dislocations within the material.

The maximum shear stress $\tau_{\max}$, which is responsible for initiating plastic deformation, is evaluated using the difference between the principal stress components as:

$$\tau_{\max} = \frac{1}{2}(\sigma_{zz} - \sigma_{xx}) \tag{4.11}$$

This shear stress provides a critical measure of the materials strength, as it defines the stress level at which the material begins to yield and plastically deform. The normalized shear stress, when divided by the applied pressure, yields a dimensionless parameter that characterizes the onset of plasticity as a function of the applied load. Finally, the normalized depth at which maximum shear occurs is also an important factor, as it indicates the location beneath the surface where dislocation nucleation is most likely to begin, typically near the indenter contact zone.

4.2.3 Defect Analysis

The identification and classification of defects formed during nanoindentation simulations of body-centered cubic (BCC) crystals (as is the case in this thesis) are critical for understanding how a material responds to mechanical stress at the atomic level. For this purpose, the BCC Defect Analysis (BDA) method developed by Möller and Biztek [154] was employed. This method is chosen as simulation of BCC Molybdenum (Mo) and Tungsten (W) crystals are performed in this thesis. This comprehensive technique integrates three powerful tools (coordination number (CN), centrosymmetry parameter (CSP), and common neighbor analysis (CNA)) to detect and characterize common defects in BCC crystal structures. These methods allow for the precise identification of defects, including surfaces, vacancies, dislocations, and planar faults, which are essential for determining how the material's structure deforms under indentation.

The first step in defect analysis involves calculating the CN, CSP, and CNA values for every atom within the simulated crystal. This is achieved by setting a cutoff radius of $(1+\sqrt{2})/2a_0$, where a_0 denotes the lattice constant of considered material. The chosen cutoff ensures that the six next-nearest neighbors of a perfect BCC atom, typically present in the crystal structure, fall within the defined radius. Under these conditions, the coordination number of perfect BCC atoms increases from 8 to 14, effectively capturing any deviations from the ideal structure. This change is vital in detecting structural imperfections or regions where defects may arise.

Once the CN values have been established, the CSP is computed for each atom to further assess local symmetry. The centrosymmetry parameter quantifies the deviation from perfect BCC symmetry, with higher CSP values indicating atoms that have moved away from their ideal lattice sites due to mechanical deformation.

After computing CN and CSP, common neighbor analysis (CNA) is applied to classify the local atomic environments. CNA assigns each atom a structural identity based on its bonding configuration with neighboring atoms. This method compares the local atomic arrangement to a reference structure (in this case, the perfect BCC lattice). This allows for atoms to be categorized based on their surrounding neighborhood. Atoms that do not conform to the BCC structure (CNA $\neq$ BCC) and have a CN $\neq$ 14 are flagged as potentially defective and require further classification.

4.3 Neural Network Interatomic Potentials

Recently, machine learning force fields (MLFFs) trained on first-principles data have gained popularity due to their ability to achieve near-quantum accuracy. These methods employ atomic-level descriptor features to predict energies, forces, and stresses. While these approaches are reliable, it is crucial to carefully construct the training dataset to ensure that the model parameters encompass the energetic landscape required for large-scale simulations. This thesis will describe the NNIP developed in this work, along with an explanation of the descriptor model employed. Additionally, the thesis will detail

how these descriptors are used to develop a similarity measurement method that aids in creating reliable datasets for targeted simulations.

4.3.1 Behler-Parrinello Descriptors

In this investigation, the interatomic potential is constructed using PANNA (Properties from Artificial Neural Network Architectures) [155, 156]. This innovative framework employs Tensorflow [157] to facilitate the training and evaluation of fully-connected feed-forward NNIPs. A modified version of the Behler-Parrinello (mBP) descriptors [93, 158] is specifically selected to accurately represent the atomic environments essential for simulating the interactions within materials.

The mBP representation generates a fixed-size vector, referred to as the G-vector, for each atom in a given configuration within the dataset. Each G-vector encapsulates the surrounding atomic environment of the corresponding atom up to a specified cutoff radius R_c. While a higher-dimensional G-vector can lead to a more precise approximation of the potential energy surface, it also incurs a significant increase in computational cost during MD simulations.

To effectively calculate the G-vectors, the radial and angular components are derived from the distances R_{ij} and R_{ik} between atom i and its neighboring atoms j and k, as well as the angle θ_{ijk} formed by those distances. The mathematical expressions for the radial and angular G-vectors are given by:

$$G_i^{rad}[s] = \sum_{i \neq j} e^{-\eta(R_{ij}-R_s)^2} f_c(R_{ij}), \tag{4.12}$$

$$\begin{aligned} G_i^{ang}[s] = 2^{1-\zeta} \sum_{j,k \neq i} &[1 + cos(\theta_{ijk} - \theta_s)]^{\zeta} \\ &\times e^{-\eta[\frac{1}{2}(R_{ij}+R_{ik})-R_s]^2} f_c(R_{ij}) f_c(R_{ik}). \end{aligned} \tag{4.13}$$

The smooth cutoff function, which defines the range of interaction, is expressed as:

$$f_c(R_{ij}) = \begin{cases} \frac{1}{2}\left[\cos\left(\frac{\pi R_{ij}}{R_c}\right) + 1\right], & R_{ij} \leq R_c \\ 0, & R_{ij} > R_c \end{cases} \tag{4.14}$$

Here, the parameters η, ζ, θ_s, and R_s are distinct for the radial and angular components, providing flexibility in modeling the local atomic environments. The choice of R_c was made to encompass the first three nearest neighbors in BCC Mo, where the lattice constant is $a = 3.17$ Å, making the distance to the third nearest neighbor approximately $a \times \sqrt{2} = 4.48$ Å.

For a single-element system, the total length of the G-vector can be formulated as follows:

$$|G_i[s]| = (R_s^{ang} \times \theta_s) + R_s^{rad}, \tag{4.15}$$

This results in a G-vector length of 152, as outlined in Table 4.1. The specific parameters selected for this study are crucial for ensuring that the NNIPs accurately capture the interatomic interactions while maintaining computational efficiency.

Descriptor parameter	Symbol	Value
Radial component:		
Radial exponent ($Å^{-2}$)	η^{rad}	32
cutoff (Å)	R_c^{rad}	5
Number of R_s radial	R_s^{rad}	24
Angular component:		
Radial exponent ($Å^{-2}$)	η^{ang}	16
cutoff (Å)	R_c^{ang}	5
Number of R_s angular	R_s^{ang}	8
Angular exponent	ζ	128
Number of θ_s	θ_s	16

Table 4.1: Values of the parameters that appear in the definition of the radial and angular G-vectors, Eq.s (4.12), (4.13), (4.14). Where a number of components is given, the values are equispaced.

4.3.2 Similarity Measurement

A distance-based criterion, inspired by methodologies described in [111, 159] is employed, to quantitatively assess the similarity between two distinct atomic configurations. This approach is further generalized to evaluate how closely two datasets correspond to one another.

To illustrate this method, lets consider two configurations, designated as α and β, which contain n and m atoms per supercell, respectively. For these two configurations, a distance matrix is constructed, which is denoted as $\mathbf{D}^{\alpha\beta}$, that has dimensions of $n \times m$. Each entry in this matrix represents the Euclidean distance between atom i in configuration α and atom j in configuration β, formulated as follows:

$$D_{i,j}^{\alpha\beta} = \|G_i^{\alpha}[s] - G_j^{\beta}[s]\|_2, \tag{4.16}$$

where i ranges over $\{1, 2, \ldots, n\}$ and j ranges over $\{1, 2, \ldots, m\}$. Each vector $G[s]$ is a 152-dimensional representation, as previously discussed.

With this distance matrix established, one can determine the minimum distance from each atom i in configuration α to any atom j in configuration β. A similarity measure from α to β as the maximum of these minimum distances is defined, expressed mathematically as:

$$D^{\alpha\beta} = \max_i \min_j D_{i,j}^{\alpha\beta}. \tag{4.17}$$

It is important to note that this derived quantity, $D^{\alpha\beta}$, does not satisfy the properties of a conventional distance metric; rather, it is a non-symmetric measure that serves as the "similarity measure" in this thesis.

Moreover, one can utilize this similarity measure to explore innovative configurations, especially concerning the scenario of an indented supercell. For example, by computing the average of all $D^{\alpha\beta}$ values between atoms from two distinct datasets or configuration types, an indication of the degree of (dis)similarity between these datasets is obtained. This approach can be similarly applied to assess how closely a dataset aligns with a target simulation, which, in this thesis, is represented by an indented sample.

4.3.3 Neural Network Training

Within the PANNA framework, environmental descriptors corresponding to each atom serve as inputs to a fully connected neural network architecture. This architecture comprises two hidden layers, featuring 256 and 128 nodes in the first and second layers, respectively. Both hidden layers employ a Gaussian activation function, while the output layer consists of a single node with linear activation. The atomic environment is encapsulated in a descriptor vector comprising 152 components, resulting in a network characterized by a total of 71,808 weights and 385 biases.

For the training process, a batch size of 10 is utilized, with the model initialized using random weights. A constant learning rate of 10^{-4} is maintained throughout the training iterations. The energy of a configuration containing N atoms is articulated as the summation of individual atomic energy contributions:

$$E = \sum_{i=1}^{N} E_i(G_i), \tag{4.18}$$

where E_i denotes the energy associated with atom i characterized by its corresponding G-vector G_i.

The force acting on atom i, located at position $\vec{R}_i$, can be expressed as:

$$\vec{F}_i = -\sum_j \sum_\mu \frac{\partial E_j}{\partial G_{j\mu}} \frac{\partial G_{j\mu}}{\partial \vec{R}_i} \tag{4.19}$$

where j identifies the atoms within the cutoff distance from atom i, and μ indexes the components of the descriptor.

To optimize the networks weight and bias parameters, the Adam optimization algorithm [160] is employed to calculate gradients from randomly chosen batches of the training dataset. The loss function, denoted as $\mathcal{L}(W)$, is designed to facilitate the optimization of the network weights W and comprises two components: one addressing the energy, $\mathcal{L}_E(W)$, and the other concerning the forces, $\mathcal{L}_F(W)$:

$$\mathcal{L}(W) = \mathcal{L}_E(W) + \mathcal{L}_F(W). \tag{4.20}$$

The energy contribution is computed as follows:

$$\mathcal{L}_E(W) = \sum_{s \in \text{batch}} \left[E_s^{\text{DFT}} - E_s(W)\right]^2 \tag{4.21}$$

where s indicates the atomic configuration, E_s^{DFT} represents the total energy derived from DFT (the target value), and $E_s(W)$ is the predicted total energy from the NNIP.

The force contribution is expressed as:

$$\mathcal{L}_F(W) = \lambda_F \sum_{s\in\text{batch}} \sum_{i=1}^{N_s} \left| \vec{F}_{i;s}^{\text{DFT}} - \vec{F}_{i;s}(W) \right|^2 \tag{4.22}$$

where $\vec{F}_{i;s}^{\text{DFT}}$ denotes the force derived from DFT, and $\vec{F}_{i;s}$ indicates the force obtained from the NNIP for atom i in configuration s. Here, N_s denotes the total number of atoms present in configuration s. The parameter λ_F modulates the relative influence of the force component, and in this case, it is set to $\lambda_F = 0.5$.

4.3.4 Dataset Creation with Density Functional Theory

The DFT calculations were carried out using the Quantum Espresso package [161, 162]. To ensure accurate representation of the electronic structure, the norm-conserving PBEsol exchange-correlation functional was employed [163–165], which is particularly well-suited for solid-state calculations. A total of 14 valence electrons were considered for Mo.

The Brillouin zone was sampled using the Monkhorst-Pack method [166], which divides the reciprocal space into a grid of k-points for integration. Based on a thorough convergence analysis, the k-point mesh for the Mo unit-cell was determined to be $8 \times 8 \times 8$, while the plane-wave cutoff energy was set at 60 Ry. These parameters were carefully chosen to balance computational efficiency and accuracy. For supercell calculations, the k-point grid was appropriately scaled according to the size of the supercell. For instance, a $2\times2\times2$ grid was used for $4\times4\times4$ conventional supercells, and for larger configurations, the grid was reduced to $1 \times 1 \times 1$ to maintain consistency across different scales.

To aid in the convergence of the calculations, the Methfessel-Paxton smearing technique [167] was applied, using a smearing width of 0.00735 Ry (equivalent to 0.1 eV). This approach helps smooth out discontinuities in the electron occupancy near the Fermi level, particularly useful for metals like Mo, improving both the numerical stability and the accuracy of the energy calculations.

Overview of Results

In this chapter, an overview of the entire thesis is presented in a coherent and structured manner. The results are organized to demonstrate the significant impact of interatomic potentials on dislocation dynamics studies and to illustrate how a well-constructed interatomic potential can enhance the understanding of crystalline materials.

The order of this chapter is as follows: First, discrepancies in interatomic potentials for nano-mechanical applications in single-element metals like W and Mo are discussed. Significant errors and inconsistencies are observed in empirical interatomic potentials when modeling processes like dislocation dynamics, generalized stacking fault energy (GSFE), and other dislocation-related phenomena. This highlights the necessity for advanced methods to develop interatomic potentials with quantum-level accuracy for modeling dislocation dynamics. Next, the focus shifts to the development of accurate interatomic potentials for Mo, demonstrating their utility in studying nano-mechanical properties such as dislocation dynamics and surface interactions.

Subsequently, the study examines the interplay of dislocation dynamics and CSRO in NiCoCr alloys, emphasizing the importance of accurate interatomic potentials for capturing nanoscale ordering. The mechanical properties of these materials, including dislocation dynamics, are analyzed in relation to CSRO. Finally, the manipulation and reorganization of CSRO through dwell nano-indentation techniques are explored, showcasing how advanced interatomic potentials enable a deeper understanding of these phenomena. A novel method based on distance measurements is also proposed to guide the development of NNIPs for targeted simulations.

5.1 The Role of Interatomic Potentials in Dislocation Dynamics of Tungsten

Understanding dislocation dynamics in nano-mechanical simulations and ensuring they align with experimental data requires advanced modeling techniques. This thesis investigates the nano-indentation of tungsten and explores how various interatomic potentials influence dislocation plasticity. Specifically, the early stages of the elastic-to-plastic transition at different temperatures are examined. The study evaluates the performance of EAM [168, 169], modified (MEAM) [170], analytic bond-order potential (ABOP) [171], and MLFFs (tabGAP) [172] in modeling tungstens response to nano-indentation. It highlights how these different potentials affect dislocation nucleation and the formation of the

plastic zone beneath the indenter tip. While each potential exhibits distinct mechanisms for dislocation nucleation and dynamics during loading, particularly at elevated temperatures, tabGAP demonstrates better agreement with both DFT [168] and experimental results [173, 174], making it the most accurate in capturing the behavior of tungsten during nano-mechanical processes.

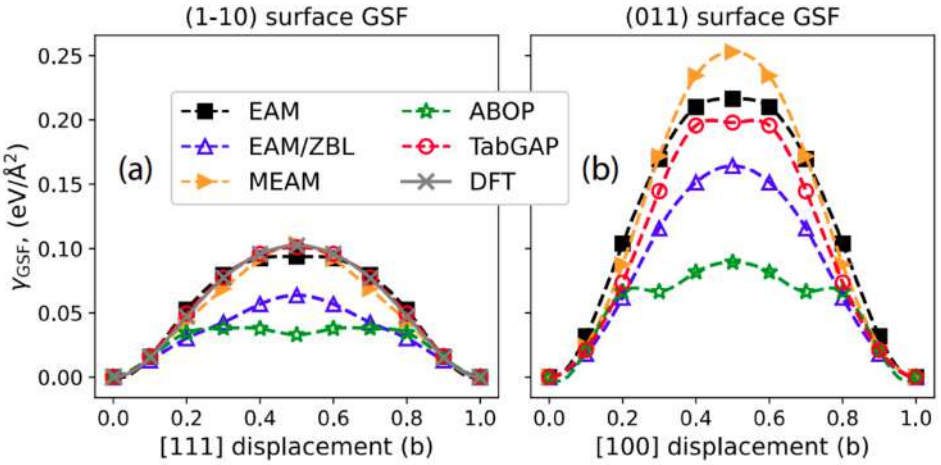

Figure 5.1: Generalized stacking fault energies for $\langle 111\rangle\{110\}$ in (a) and $\langle 100\rangle\{011\}$ in (b), calculated using various methods. The $\langle 111\rangle\{110\}$ data are compared with DFT results from [168].

One of the most critical factors to consider when evaluating the accuracy of interatomic potentials for dislocation modeling is their ability to reliably capture static dislocation-related properties, such as GSFE. Fig. 5.1 presents the GSFE for two slip systems, $\langle 111\rangle\{110\}$ and $\langle 100\rangle\{011\}$, calculated using various MD potentials. These results are compared with DFT [168] data, demonstrating that while most potentials provide reasonable estimates, the EAM/ZBL [169] potentials tend to underestimate stacking fault energies. This underestimation explains their failure to predict the formation of twinned regions. In contrast, tabGAP [172] and MEAM [170] potentials show strong agreement with DFT results, making them more reliable for modeling dislocation glide energies and plasticity in tungsten.

Experimental images and measurements from transmission electron microscopy (TEM) and scanning electron microscopy (SEM) can be directly compared to simulation results, making the nucleation and dynamics of dislocations in nano-mechanical applications, such as nano-indentation, critically important. For example, in nano-indentation simulations, strain maps on the surface and beneath the indenter tip can be compared with SEM and TEM images. These strain maps are directly connected to the nucleation and propagation of the dislocations inside the material during the nano-indentation. Fig. 5.2 shows the nucleation and evolution of dislocations at the maximum indentation depth for W, with results obtained from different methods at both 77 K and 300 K. The figure highlights the formation of shear dislocation loops during loading, which play a crucial role in the transition from elastic to plastic deformation. In BCC materials, prismatic loops evolve

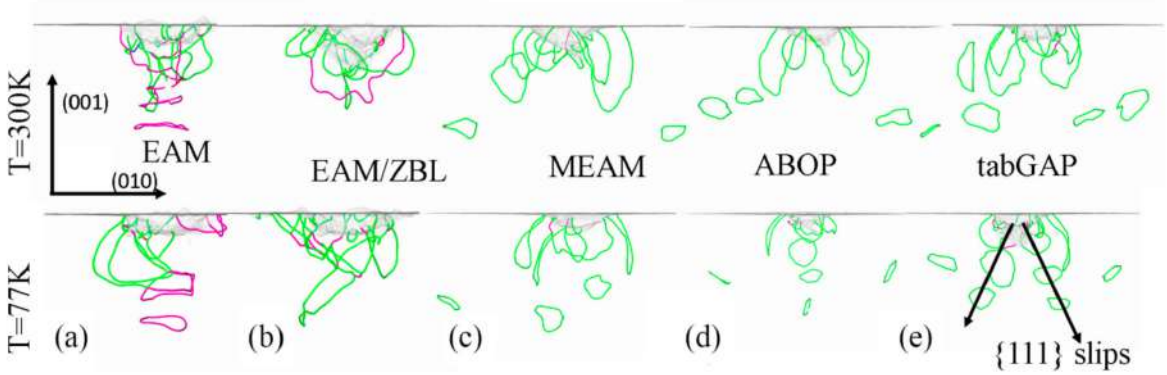

Figure 5.2: Nano-indentation induced dislocation nucleation and dynamics in W with different interatomic potentials at two different temperatures.

as shear loops propagate along ⟨111⟩ slip directions, with limited cross-slip. This visualization demonstrates that tabGAP provides the most accurate representation of these mechanisms, and it closely matches experimental observations [173, 174].

The accuracy of tabGAP as a MLFF, developed based on DFT data, suggests that machine learning methods could benefit dislocation dynamics modeling in material science. A detailed explanation of this study, including the analysis of indentation elastic modulus, twinning mechanisms, pileup patterns, dislocation densities, and other key aspects, can be found in [149].

5.2 NNIPs for Modeling of Dislocation Dynamics

As demonstrated in the previous study on W, MLFFs based on first-principles data can achieve near-quantum accuracy in capturing the energetics of dislocations. Consequently, this thesis focuses on designing a dataset for the nano-mechanical application of Mo single crystals, along with the further development of a NNIP and its validation.

Initially, an EAM potential [175] was employed to obtain indented configurations of Mo samples. Additionally, a dataset from the literature [176] was utilized alongside similarity measurement techniques (described in the methodology section) to assess the "closeness" of the dataset to the indented samples. This measure of "closeness" is crucial for ensuring that the final NNIP effectively captures the energetics of atoms in the sample, from dislocation cores to surface atoms, enabling comparisons of strain images with scanning electron microscopy experimental measurements.

In Fig. 5.3, the average minimum distances between different configuration types are illustrated and also highlights their proximity to the configurations of the indented sample. This measurement is essential for verifying that the dataset adequately represents the critical atomic environments of interest, particularly those located at the indenter tip and dislocation cores.

Further investigations, as detailed in [32], indicate that the dataset requires enhancements for atoms located at the dislocation cores, surface atoms, and atoms under the indenter tip. For each of these regions, novel configurations were incorporated into the

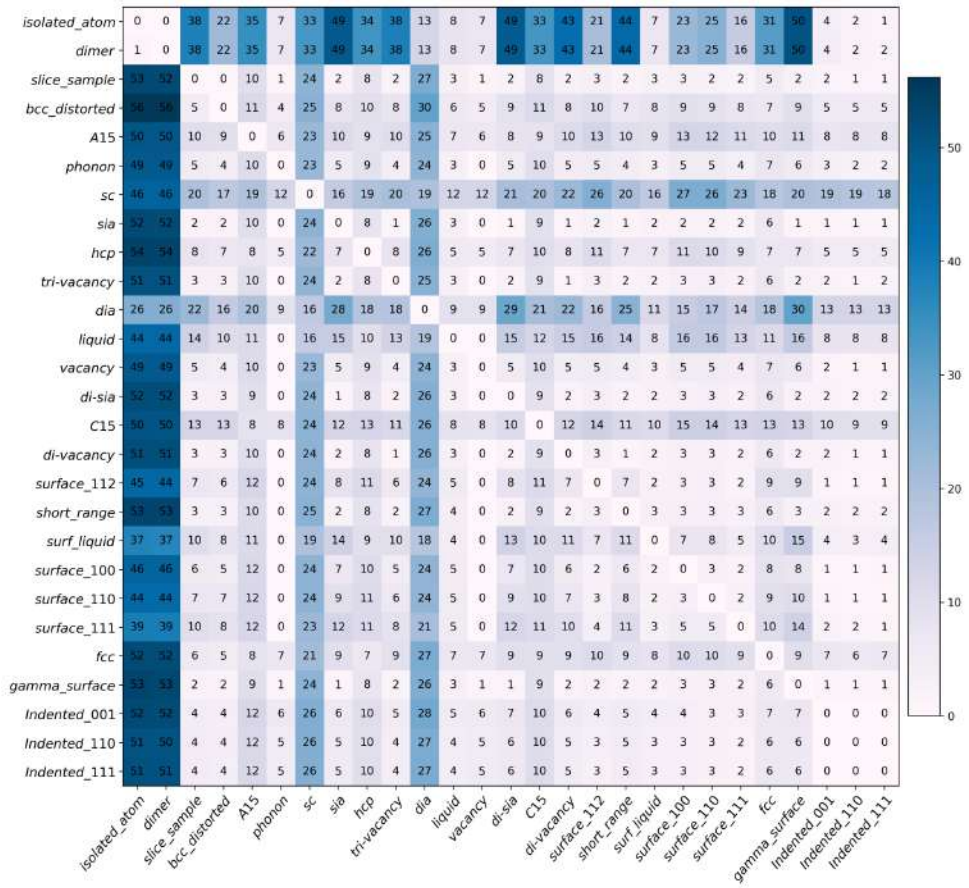

Figure 5.3: Average of minimum distances between different configuration types as well as with the indented samples.

dataset that are in close proximity to the desired atoms. For instance, in Fig. 5.4, it is shown that the distances (color-coded for each atom) are initially high; however, after adding GSFE configurations with a dumbbell self-interstitial, the distances to the atoms on the dislocation core decrease. Consequently, DFT energies derived from these configurations align with the energetics of the atoms in the dislocation core and makes the final NNIP suitable for nano-mechanical applications.

The first validation of the trained NNIP focuses on comparing its GSFE predictions with those obtained from DFT. Fig. 5.5 presents the results for Mo in the two most critical slip planes: the $\{110\}\langle 111\rangle$ and $\{121\}\langle 111\rangle$ families, where NNIP is compared against DFT, along with EAM [175], GAP [176], and TabGAP potentials [172]. Since the $\{110\}\langle 111\rangle$ GSF configurations with a $\langle 111\rangle$ dumbbell interstitial are key for accurately capturing the energetics of dislocations, the GSFE for these configurations was also examined.

Fig. 5.5 demonstrates that all potentials predict the GSFE with high accuracy for both slip systems and pure crystals. However, the EAM/FS potential exhibits significant errors, about 50% for the $\{110\}\langle 111\rangle$ slip family and 32% for the $\{121\}\langle 111\rangle$ family, particularly at the peak of the GSFE curve. These configurations are critical as they represent the atomic arrangements on the slip plane of an indented sample, as shown and explained in Fig. 5.4. While accurate GSFE prediction is essential for reliable dislocation modeling, it

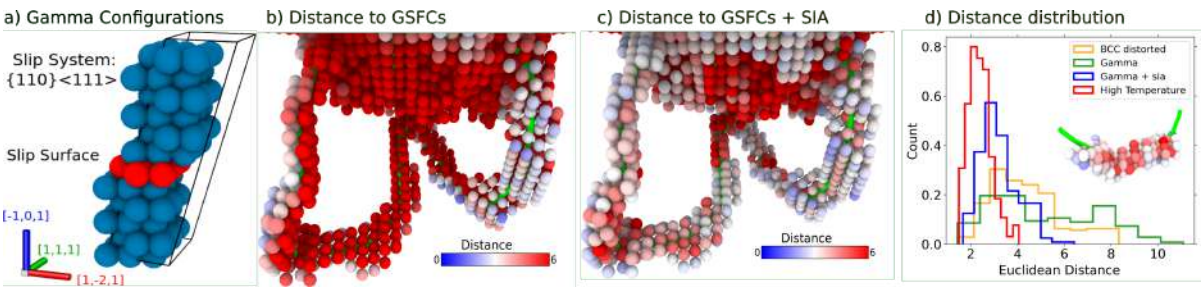

Figure 5.4: The influence of incorporating GSFE configurations on the atomic distances in dislocation cores from the dataset. **(a)** Schematic illustration of GSFE configurations integrated into the dataset. **(b)** The inclusion of GSFE configurations leads to a reduction in the distances of atoms located on the slip plane of dislocation cores. **(c)** Adding a self-interstitial atom to the surface of GSFCs allows for comprehensive coverage of all atoms within the dislocation cores. **(d)** The distribution of atomic distances in dislocation cores indicates that GSFE configurations with the self-interstitial atom can effectively encompass the dislocation cores.

is equally important for a potential to accurately capture the energies and forces within dislocation cores. To address this, I also calculated the GSFE curve for configurations containing a $\langle 111 \rangle$ dumbbell interstitial on the surface. As illustrated in Fig. 5.5(c), NNIP is the most accurate in predicting these energies, indicating its reliability in simulating dislocation dynamics during nanoindentation. In contrast, the GAP and EAM potentials exhibited errors of 40%, and TabGAP showed a 20% deviation from DFT results. This suggests their limitations in accurately predicting these configurations. This is discussed further in the following section.

The elastic-to-plastic transition is crucial for comparing simulation results with experimental data. Accurate modeling of the elastic regimes energetics is essential for interatomic potentials to capture material behavior during nanoindentation. In these simulations, the forces between the indenter tip and the top atomic layers significantly influence the material's response. In Fig. 5.6, the normalized maximum shear stress ($\tau_{\max}/P$), a dimensionless quantity, is presented as a function of displacement for three main crystal orientations: [001], [011], and [111]. The calculation of this parameter is detailed in the Methods section. Fig. 5.6 suggests that GAP simulations accurately capture the interaction between the indenter tip and the top surface layers for the [001] and [011] orientations, but they face limitations with the [111] orientation due to the absence of relevant atomic configurations in the training data. This gap restricts the ability to model

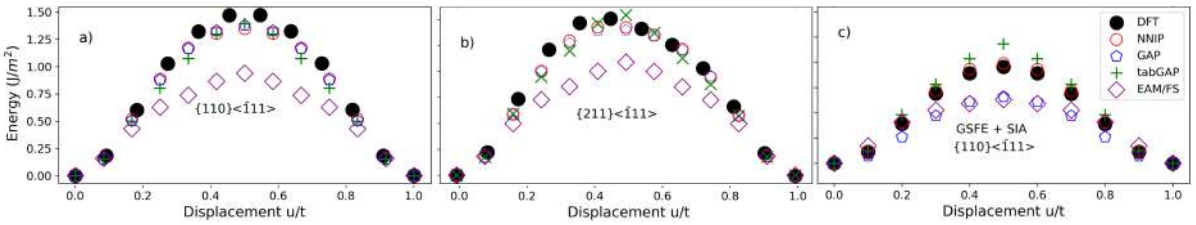

Figure 5.5: GSFE for single-crystalline molybdenum: **(a)** for $\{110\}\langle 111 \rangle$ and **(b)** for $\{211\}\langle 111 \rangle$. **(c)** GSFE curve for the configurations involving self-interstitial atoms.

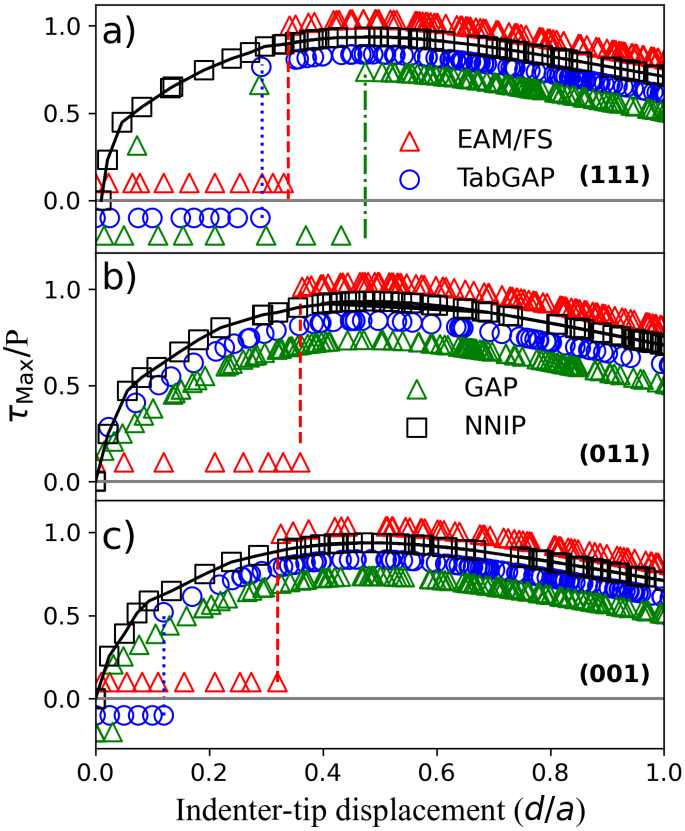

Figure 5.6: Hertzian calculation of the normalized maximum shear stress, $\frac{\tau_{\max}}{P}$, as a function of normalized depth for the primary crystal orientations. Surface information is essential in the interatomic potentials to accurately model nanoindentation-induced plasticity within the range of 0.0 to 0.475$\frac{d}{a}$. To facilitate the interpretation of the results, the values for EAM/FS were adjusted by -0.1, those for GAP were adjusted by $+0.2$, and the values for tabGAP were adjusted by $+0.1$ (all values expressed in units of $\frac{\tau_{\max}}{P}$).

nanoindentation before the yield point. In contrast, the NNIP simulations incorporate detailed surface structure information. This accurate early-stage modeling is essential for understanding the critical load for plasticity initiation, which NNIP predicts with a high degree of consistency with experimental observations.

Accurate development of NNIPs makes it possible to compare surface pile-up patterns in nanoindentation experiments with computational methods. In Fig. 5.7, a comparison is made between the results from NNIP simulations and experimental observations obtained through SEM coupled with EBSD [177]. The experiments involved indenting a (001) Mo grain using a Berkovich tip, with the computational models incorporating the tip's roundness, which typically ranges from 50 to 100 nm, to facilitate an accurate comparison during the initial stages of nanoindentation.

Upon evaluating the MD simulation results generated with various potentials against the experimental data, it was found that the slip trace propagation along the [-110] direction closely mirrors the four-folded rosette pattern captured by NNIP potentials. Notably, the NNIP simulations excelled in depicting the formation of pile-ups at this crystal orientation. In contrast, the TabGAP and EAM potentials displayed limitations in

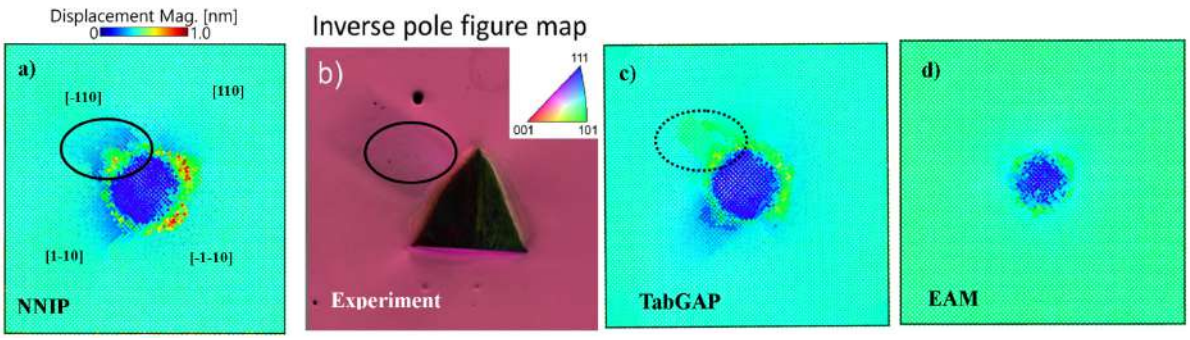

Figure 5.7: Slip traces and pileup of [001] molybdenum at the maximum indentation depth for NNIP in **(a)**, TabGAP in **(c)**, and EAM in **(d)**, compared to an experimental SEM observation presented in Ref. [177] **(b)**. The four-fold rosette is accurately represented by NNIP, where the slip trace propagates along the $[-110]$ and $[1-10]$ planes, demonstrating strong qualitative agreement with the experimental findings [177].

accurately representing the pile-up formation around the indenter tip. The insights drawn from the results in Fig. 5.7 highlight the limitations of various interatomic potentials in modeling plastic deformation mechanisms across different crystal orientations.

The developed NNIP in this thesis also captures the stages of dislocation nucleation effectively. Fig. 5.8 presents the defects identified using the BCC Defect Analysis (BDA) method [154] (see Methods) within a (111) Mo sample at varying depths. The nanoindentation simulations conducted with NNIP during the early stages of loading significantly improve the understanding of the interactions between the indenter tip and the surface atoms (see Fig. 5.8(a)). In this scenario, several Mo atoms at the topmost surface layer are classified as surface defects. Additionally, Mo atoms located just beneath these defects start to merge, resulting in the formation of edge dislocations that may develop into shear loops, a mechanism that remains unrecognized in simulations using other interatomic potentials.

The NNIP simulations are expected to provide an accurate representation of the nucleation and propagation of shear loops on {112} planes, which aligns with experimental findings in BCC materials [152, 153]. Moreover, NNIP captures the nucleation of loops through a lasso mechanism. This contrasts with the behavior observed in GAP and tabGAP simulations, where multiple loops form, as illustrated in Fig. 5.8(c) at a depth of 1.45 nm. At maximum indentation depth, the surface of the sample clearly shows that displaced atoms align with the slip planes, forming a distinctive three-folded rosette pattern typical of BCC materials in the (111) orientation (Fig. 5.8(d)), characterized by the $\{1\bar{1}2\}$, $\{1\bar{0}1\}$, and $\{0\bar{1}1\}$ planes. In contrast, GAP, tabGAP, and EAM fail to accurately represent this behavior, largely due to their insufficient modeling of pileup formations.

The differences in dislocation and loop nucleation across the various potentials can be attributed to two key factors: (1) the predictions of the GSFE curve (Fig. 5.5(c)) differ among the potentials, and (2) the indentation surface energy as a function of depth varies across these potentials, which is explained in detail in [32].

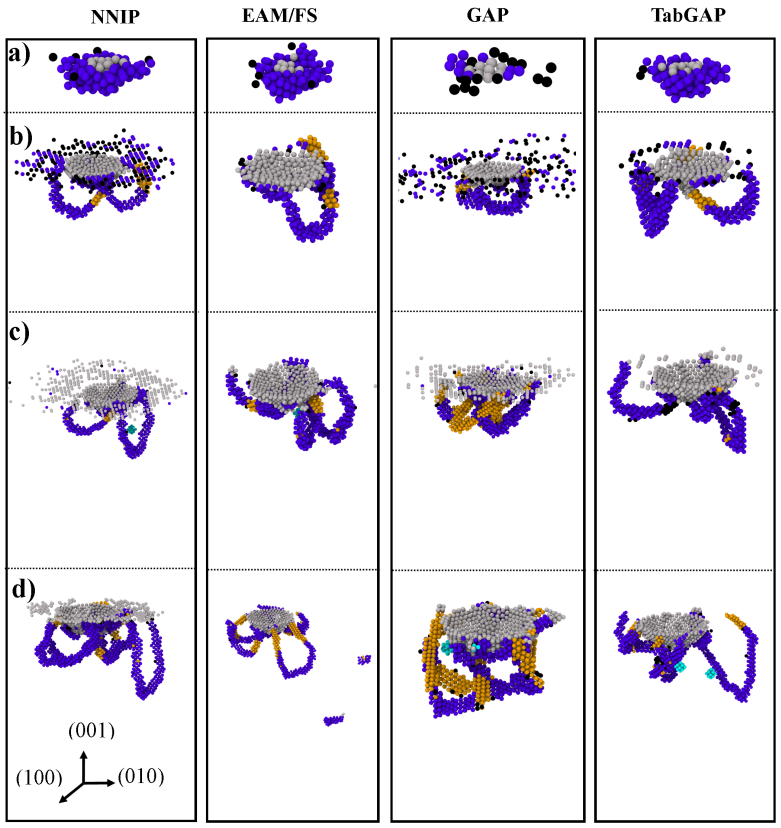

Figure 5.8: Defects identified in indented (111) molybdenum samples at various depths using the BDA method with NNIP, EAM, TabGAP, and GAP approaches. Different defect types are represented by specific colors: gray spheres indicate surface atoms in direct contact with the indenter tip, blue spheres denote edge dislocations, light-blue spheres mark atoms near vacancies, yellow spheres signify twin/screw dislocations, and black spheres highlight unidentified defect atoms. Edge dislocations nucleate and propagate along the {111} slip planes, eventually forming prismatic loops. Additionally, NNIP simulations effectively model the characteristic three-fold symmetric rosette at depths below 1.45 nm, formed by slip traces and pile-ups along the $[11\bar{1}]$, $[\bar{1}01]$, and $[0\bar{1}1]$ planes.

5.3 Dislocation Dynamics in Complex alloys

Equiatomic NiCoCr random solid solutions (RSS) have recently been shown through both experiments and atomistic simulations to exhibit outstanding mechanical properties [142]. However, the underlying microstructural mechanisms responsible for these properties remain under debate [86, 90, 178]. A potential explanation involves the presence of nanometer-scale SRO, which emerges from specific thermal treatments and has significant effects on dislocation pinning and stacking fault widths. In the first part of this section, two distinct interatomic potentials, alongside sample annealing at different temperatures, are compared to demonstrate how they influence the formation of SRO in NiCoCr alloys.

The two potentials studied are the Li-Sheng-Ma (LSM) potential [142] and the Farkas-Caro (FC) potential [146]. The LSM potential leads to pronounced SRO during aging, while the FC potential, under identical thermal conditions, produces a chemical/structural state that closely resembles a RSS. The LSM potential, in particular, reveals the formation

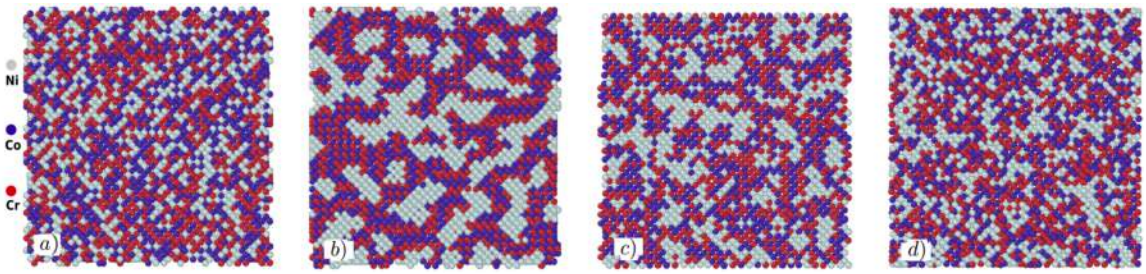

Figure 5.9: Images of NiCoCr samples showing: a) a randomly solid solution (RSS) equilibrated at T = 400 K, b) annealed at **(a)** $T_a = 400K$, **(b)** annealed at $T_a = 400K$, **(c)** annealed at $T_a = 800K$, **(d)** annealed at $T_a = 1400K$.

of Ni-rich nanoprecipitates and inhomogeneities in the annealed NiCoCr matrix, which has been suggested to influence the stacking fault width, ultimately contributing to alloy strengthening [142, 179].

Fig. 5.9 displays snapshots of NiCoCr samples annealed at various temperatures (T_a) using the LSM potential. The ordering and segregation of Ni, along with the precipitation of Co-Cr, are clearly visible, with the extent of segregation depending on the annealing temperature. This observation aligns with experimental findings where SRO is also detected in NiCoCr alloys [85].

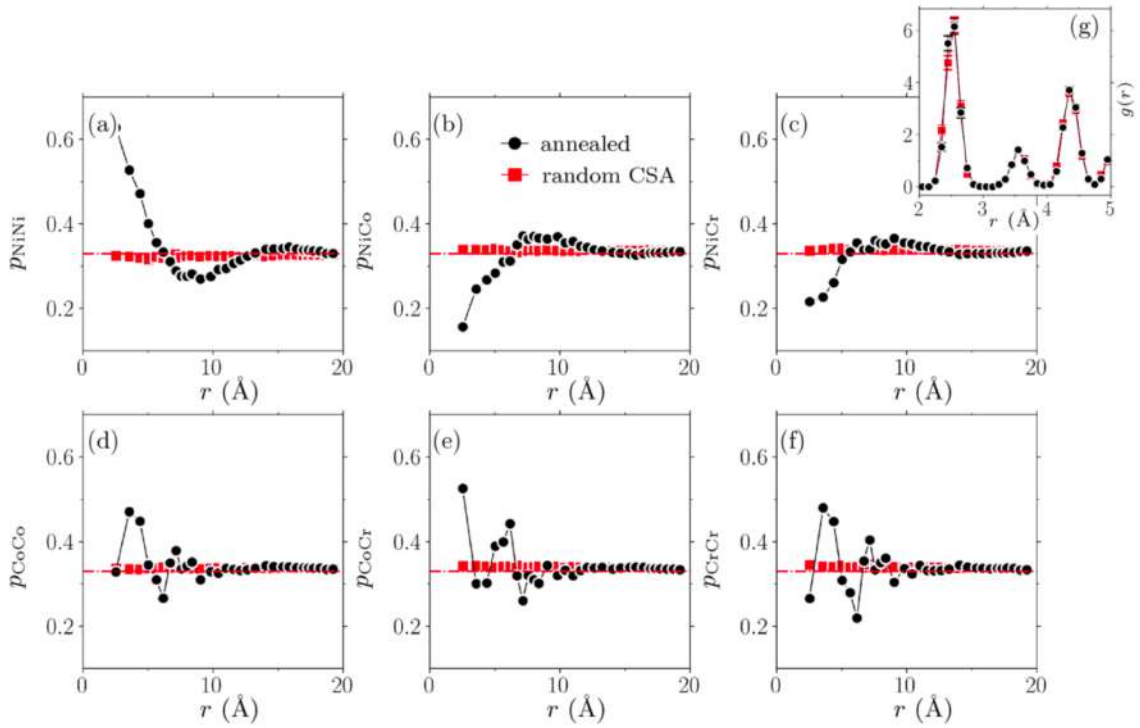

Figure 5.10: Short-range ordering in annealed NiCoCr CSAs using the Li-Sheng-Ma potential. WarrenCowley SRO parameters are displayed for **(a)** p_{NiNi}, **(b)** p_{NiCo}, **(c)** p_{NiCr}, **(d)** p_{CoCo}, **(e)** p_{CoCr}, **(f)** p_{CrCr} plotted against distance r at $T_a = 400K$. **(g)** Pair correlation function $g(r)$ at $T_a = 400K$. The base (red) dash-dotted line indicates the random concentration.

SRO refers to compositional deviations from the statistically random arrangement of atoms in a solution matrix, i.e a RSS. To quantify this, the WarrenCowley SRO param-

eters, $p_{ab}(r)$, were analyzed, probing the concentration variations of type-b atoms at a distance r from a center type-a atom. In an equimolar random NiCoCr solid solution, the expected value of $p_{ab}(r)$ is 0.33 at any distance r, which remains constant, as observed in the pair correlation function $g(r)$ [180]. These parameters can also be evaluated locally for individual atoms, highlighting potential fluctuations in the presence of SRO. The averaged WarrenCowley parameters are useful for capturing the overall statistical homogeneity of the system beyond the typical SRO size.

Fig. 5.10(a-f) reveal deviations in p_{ab} from random values after annealing at $400K$. Notably, an excess of Ni-Ni pairs persists up to approximately 5 Å, consistent with the SRO size observed in segregation maps [142, 181, 182]. Beyond this, the Ni-Ni pairs exhibit a broad peak around 15 Å before eventually reaching the RSS baseline. Similar trends, but in the opposite direction, are observed for Ni-Co and Ni-Cr pairs, since their values must sum to unity. In contrast, Co-Co and Cr-Cr pairs show weaker ordering patterns, with possible anti-ordering at near-neighbor distances. Additionally, strong bonding between Co and Cr is notable at the first-nearest-neighbor distance, as shown in Fig. 5.10(e). Interestingly, the pair correlation function $g(r)$ does not reveal structural differences between annealed and random solid solutions.

The interaction between dislocations and SRO is also analyzed to determine whether SRO is more prominent between partial dislocations. Fig. 5.11 presents a comparison of SRO structures within the dislocation dissociation boundaries and in dislocation-free regions of aged NiCoCr at a temperature of $600K$. In Fig. 5.11(a), the higher concentration of SROs within the stacking fault is visibly noticeable when compared to the

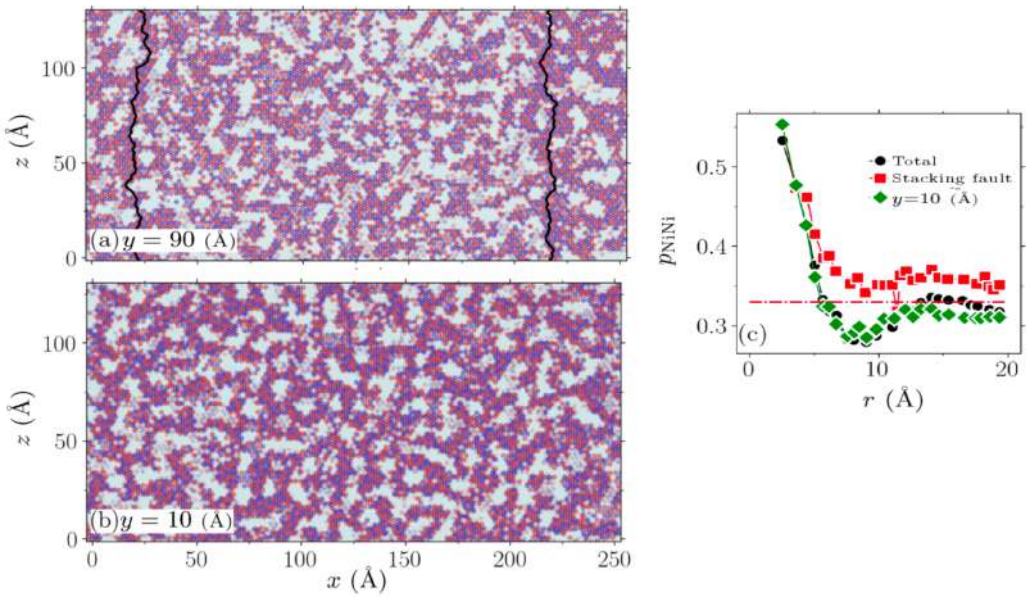

Figure 5.11: SRO microstructure with partial dislocations in aged NiCoCr at $T_a = 600\,\mathrm{K}$. **(a)** Cross-section containing the stacking fault. **(b)** Cross-section at $y = 10\,\text{Å}$. **(c)** SRO parameter p_{NiNi} as a function of pairwise distance r, with curves representing the full configuration as well as the two-dimensional slices shown in **(a)** and **(b)**. Black segments indicate dislocation lines, and the red dash-dotted line represents RSS. In **(a)**, the stacking fault region spans approximately from $x \simeq 25\,\text{Å}$ to $x \simeq 220\,\text{Å}$.

two-dimensional stack without dislocations, shown in Fig. 5.11(b) at $y = 10$Å. This trend is quantitatively confirmed in Fig. 5.11(c), where the SRO parameter p_{NiNi} for atoms inside the stacking fault region demonstrates a slower decay than that observed for atoms outside the fault plane. This significant increase in chemical ordering within the stacking fault has not been reported in previous studies.

One possible explanation for this phenomenon is that the long-range elastic strain field associated with the dislocations could influence atomic arrangements within the fault region, promoting chemical ordering. Fig. 5.11(c) shows the p_{NiNi} as a function of pairwise distance r, with distinct curves for the entire configuration and the specific regions highlighted in Fig. 5.11(a-b). The black segments mark the dislocation lines, and the red dash-dotted line indicates the RSS baseline. The stacking fault region, displayed in Fig. 5.11(a), extends between x = 25 and 220 Å.

The concept of "plastic flow" in solute strengthening theories is directly linked to the idea of a critical friction stress, denoted as σ_c. This represents the threshold stress beyond which dislocations can move more easily, maintaining a noticeable average velocity v [127, 183]. When the applied shear stress σ exceeds σ_c, dislocations glide smoothly, contributing to material deformation.

In contrast, when the applied stress is below σ_c, dislocation movement in concentrated solid solution alloys (CSAs) with their highly irregular energy landscapes becomes erratic. Under these conditions, dislocations exhibit long periods of quiescence (i.e., $v \approx 0$) interrupted by sudden, brief bursts of motion. This phenomenon is referred to as "intermittent" migration [183].

Without thermal activation, this transition to continuous dislocation motion is phenomenologically described by:

$$v \propto (\sigma - \sigma_c)^{1/\beta} \tag{5.23}$$

where $\beta \approx 1$ indicates a sharp change at the critical stress σ_c. Below σ_c, the average velocity v remains zero, meaning that dislocations do not move unless the applied stress exceeds σ_c. Here, σ represents the applied shear stress resolved on the glide plane.

To determine the critical shear stress σ_c, atomistic simulations were conducted to investigate the behavior of dislocations in FCC NiCoCr CSAs. Specifically, the dynamics of edge dislocations oriented along the [110][111] direction were analyzed, focusing on their dissociation into two mixed partial dislocations and a stacking fault under applied external stress.

Fig. 5.12(a-b) present configurations of dislocations, both frozen and in an annealed NiCoCr matrix, as well as in a NiCoCr RSS under varying loads that remain below the depinning transition threshold ($\sigma < \sigma_c$). The local curvatures of the dislocation segments depicted in Fig. 5.12(a) suggest coherent pinning effects, which appear to correlate with the spatial distribution of SRO regions. While similar features may be observed in RSSs, as illustrated in Fig. 5.12(b), their spatial extent is notably limited. The positive local curvature of the dislocation lines, in relation to the glide direction, may serve as an

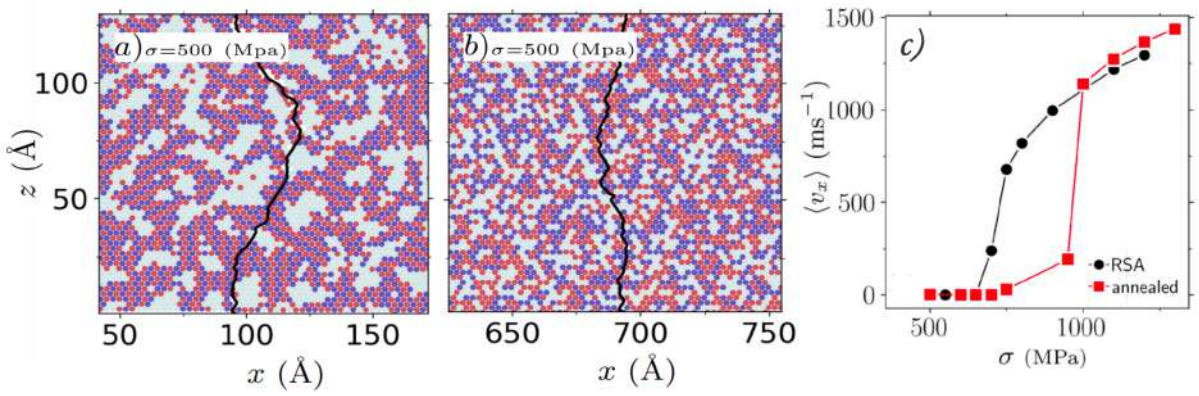

Figure 5.12: Realizations of *immobile* partial edge dislocations in an **(a)** annealed NiCoCr and **(b)** a RSS NiCoCr subject to the shear stress $\sigma = 500$. **(c)** mean dislocation velocity as a function of applied stress for annealed and RSS NiCoCr samples.

indicator of the effectiveness of pinning due to SROs or local atomic misalignments.

Fig. 5.12(c) displays the relationship between shear stress and the average dislocation velocity. The behavior of the dislocation velocity v_x as a function of σ at σ_c illustrates the transition from pinning to depinning, aligning well with the anticipated generic behavior around this critical point. This transition appears largely unaffected by the annealing process, apart from a significant shift of σ_c toward higher values. The estimated critical shear stresses were found to be approximately $\sigma_c \approx 950\,\text{MPa}$ for aged samples and $\sigma_c \approx 650\,\text{MPa}$ for RSS. This emphasizes the strengthening effects of SRO on NiCoCr CSAs. A detailed explanation of this work can be found in Naghdi et al. [183].

5.4 Complex Dislocation Dynamics: Plastic Deformation and SRO Manipulation

Having established the importance of interatomic potentials as vital tools for investigating plastic deformation in crystalline materials, it is equally important to acknowledge their potential to uncover novel physical phenomena within materials science. A key research component of this thesis explores the possibility of manipulating and reorganizing SRO. If this capability is validated, it could make possible for innovative methodologies to more accurately characterize SRO in multi-component alloys. This would be particularly groundbreaking, as the experimental detection and quantification of SRO at the nanoscale is notoriously difficult and pose significant challenges to traditional techniques [85].

To accomplish this, I employed dwell nanoindentation within molecular simulations to explore the potential of nanomechanical probes, to actively manipulate SRO. This approach provides a robust framework for validation. By utilizing advanced interatomic potentials, MD and MC simulations at room temperature are performed to demonstrate that specific dwell nanoindentation strategies, when paired with thermal MC equilibration, lead to a localized reconfiguration beneath the indenter tip. This reorganization manifests as highly anisotropic density-wave stripe patterns, which arise from nanoindentation-induced

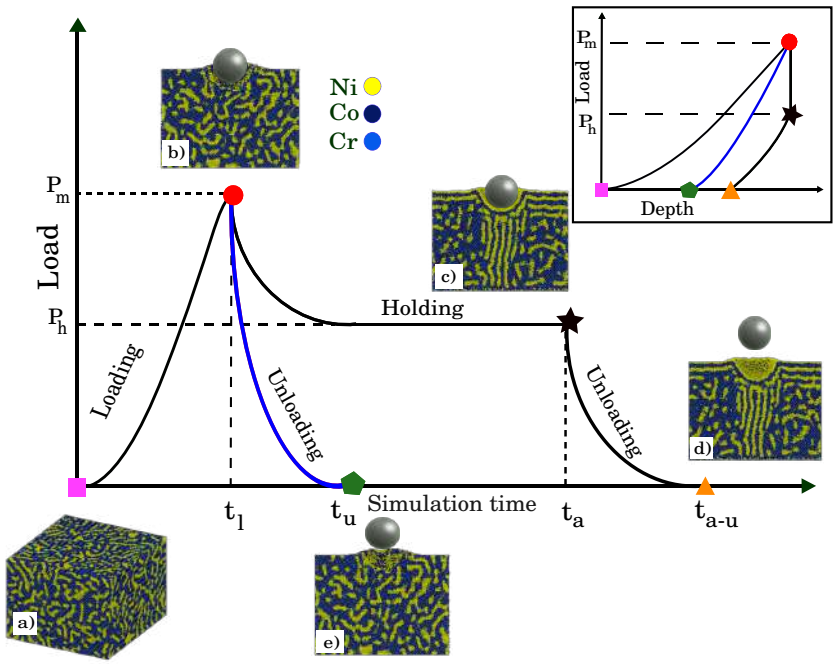

Figure 5.13: Nanoindentation protocol illustrating SRO reorganization in equiatomic NiCoCr alloys. The process begins with the indentation of an aged NiCoCr sample **(a)** to a specified depth **(b)**. At this point, the indenter's velocity is set to zero, initiating a hybrid MD-MC process that rearranges atomic distributions, leading to segregation of Ni and Co-Cr and the formation of stripe patterns beneath the indenter tip **(c)**. This reorganized pattern remains stable even after the indenter is withdrawn from the sample **(d)**. In contrast, such a pattern does not emerge during standard loading-unloading nanoindentation simulations, as shown by the blue line **(e)**. The inset shows corresponding load-depth behavior, with symbol types indicating the loading path.

stress fields and are directly influenced by intrinsic interelemental energetics. These newly discovered patterns not only align with the stress distribution within the incipient plastic zone beneath the indenter but also exhibit consistent scaling behavior. This suggests the possibility of observing SRO at experimentally attainable nanoindentation depths.

Fig. 5.13 illustrates the protocol used to study CSRO in equiatomic NiCoCr. In this process, NiCoCr (which has been observed to display Ni-rich SRO patterns [85, 142]) is subjected to a sequence of indentation, holding, and unloading steps. Initially, in the "loading" step, the sample is indented to a specific depth. However, significant changes in the CSRO occur only during the "holding" phase, where the indenter remains in place while thermomechanical relaxation is performed using a combination of MC and MD simulations at room temperature. This holding phase typically leads to a reduction in the load, where the force on the indenter decreases from a maximum value, P_m, at time t_l, to a lower value, P_h, at time t_a.

In the subsequent "unloading" step, the applied load is fully removed, and the sample undergoes further relaxation through MC-MD simulations. After the unloading process, a distinct density-wave oscillation (DWO) pattern emerges, which, as shown in Fig. 5.13, would not have appeared without the holding stage. The entire protocol is also captured in the load-depth plot presented in the inset of Fig. 5.13, which visualizes the relationship

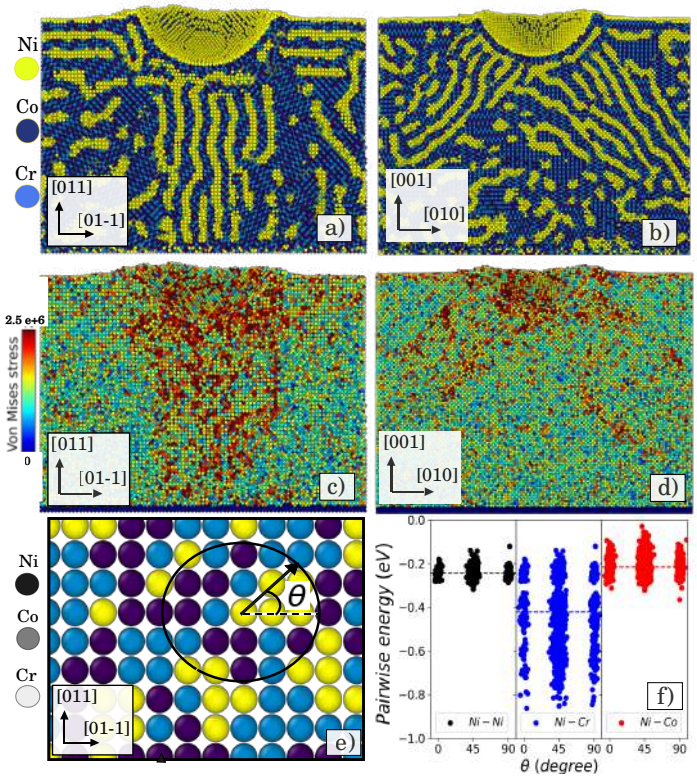

Figure 5.14: Mechanism of nanoindentation-induced SRO reconfiguration. **(a-b)** illustrate SRO patterns observed along the z[011] and z[001] directions. In **(c)** and **(d)**, the alignment of the stripe patterns shown in **(a)** and **(b)** is compared with the von Mises stress distribution. **(e)** presents interaction energies between pairs of Ni-Ni, Ni-Cr, and Ni-Co atoms within neighboring atomic regions, displayed in the same plane as in **(a)**, but separated for Ni, Ni-Cr, and Ni-Co configurations. **(f)** shows the relationship between these pairwise energies and the in-plane angle, indicating that Ni-Cr pairs have substantially lower average energies than Ni-Ni and Ni-Co pairs.

between the applied load and the indentation depth throughout the experiment.

The origin and characteristics of the emerging DWO were further explored by considering how crystal orientation affects this behavior. For crystals oriented along $x = [100]$, $y = [010]$, and $z = [001]$ (Fig. 5.14(b)), the DWO pattern displayed a significant deviation from the behavior observed in the original orientation (Fig. 5.14(a)), with the DWO orientation being notably tilted. However, upon closer examination, it is found that the DWO consistently forms along the $z = [011]$ direction and maintains the same alignment relative to the crystal structure (Fig. 5.14(b)). Additionally, the DWO pattern aligns with regions of maximum von Mises stress and principal stress accumulated in the [011] planes (Fig. 5.14(c-d)), suggesting that material anisotropy plays a critical role.

To further understand this phenomenon, the pairwise potential energy for atomic pairs (Ni-Ni, Ni-Cr, and Ni-Co) in a RSS crystal, oriented along $x = [100]$, $y = [011]$, and $z = [011]$ (Fig. 5.14(f)) was estimated. These calculations were carried out for each atom, considering only the first nearest neighbors defined by the first peak of the pair correlation function $g(r)$ at approximately 3 Å (Fig. 5.14(e)). This suggests that the emergence of the DWO is closely tied to the energetic properties of the interatomic

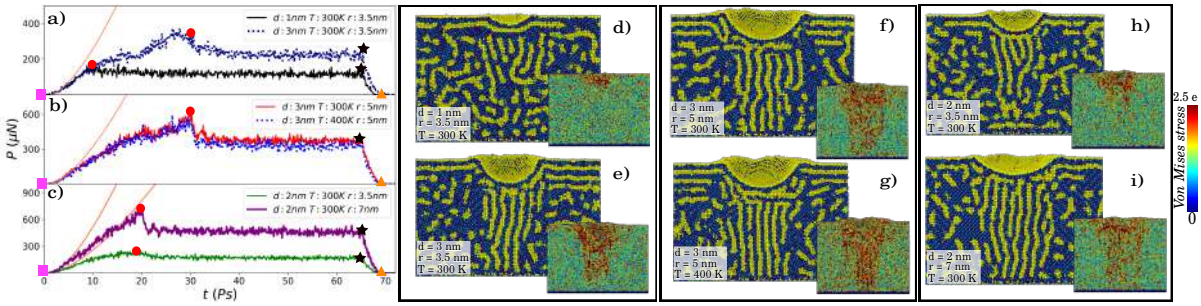

Figure 5.15: Influence of size and temperature on nanoindentation-induced reorganization of SRO. **(a)** presents load-time (P-t) curves for nanoindentation at varying holding depths, showing that greater holding depths produce more distinct stripe patterns, as observed in **(d)** and **(e)**. Inset snapshots in **(d)(i)** display von Mises stress values (in GPa), which correlate with the stripe formations. Panel **(b)** illustrates that raising the temperature by 100 K enhances stripe pattern organization, seen in **(f)** and **(g)**, due to increased von Mises stress (indicated by more red areas in the inset). Panel **(c)** demonstrates that a larger indenter radius causes a more significant load drop, which also affects pattern size, as shown in **(h)** and **(i)**.

potential, which also underlies the formation of SRO in equiatomic NiCoCr. The observed behavior in the simulations resembles nanometer-scale experimental observations of SRO made possible by advanced characterization techniques [85, 184]. For verification, the results were compared with those obtained using an alternative interatomic potential developed by Farkas et al. [146]. In that case, no SRO was observed either during aging or after the nanoindentation protocol employed in this study.

The emergence of the DWO patterns exhibits pronounced size effects, which depend on both the indentation depth and the radius of the indenter tip, as a function of temperature (Fig. 5.15). In the displacement-controlled tests performed in this study, the load-time (P-t) curves (Figs. 5.15(a-c)) show a more significant load drop during the holding phase as the depth or tip radius increases and leads to the spatial extension of the DWO. This spatial expansion of the DWO is reminiscent of the growing size of the plastic zone surrounding the indentation site.

While load-controlled tests were not specifically investigated in this study, it is anticipated that strain bursts, which are size-dependent, would also be observed in such scenarios. The protocol depicted in Fig. 5.13 was applied for two distinct indenter depths (1 nm and 3 nm), while the temperature was maintained at 300 K, and the indenter tip radii were fixed at 3.5 nm (Figs. 5.15(d-e)). As the indenter radius was increased from 2 nm to 7 nm, the resulting plastic zone expanded, which in turn generated a larger DWO pattern (Figs. 5.15(h-i)). This correlation is further supported by the more substantial load drops observed in the P-t curves for larger indenter radii (Fig. 5.15(c)).

Interestingly, when the temperature was raised from 300 K to 400 K, while the indenter depth and radius remained constant, a more organized DWO pattern emerged (Figs. 5.15(f-g)). However, at higher temperatures, the pronounced size effects observed at lower temperatures diminished, as evidenced by the lack of a corresponding reduction in

the load drop (Fig. 5.15(b)). This shows that both the indentation depth and indenter radius play significant roles in the formation and spatial extension of the DWO, while the temperature modifies the organization of these patterns, yet reduces the size-related variations.

Conclusions

This thesis presents a comprehensive study of various atomic-level phenomena and emphasizes the importance of computational methods to validate experimental measurements. The primary focus is on dislocation dynamics, nano-indentation, interplay of dislocations and SRO, and development of NNIPs for nano-mechanical applications. The methods employed were designed to accurately capture the underlying physical mechanisms and guarantee that the simulations align closely with experimental observations.

The first part of the thesis focuses on dislocation dynamics in tungsten, where the tabGAP MLFF proved particularly effective. The thesis examines how nanoindentation tests on tungsten crystals using MD simulations reveal critical insights into the materials hardness and elastic-plastic transitions. The tabGAP potential, specifically developed for tungsten, demonstrated excellent performance in capturing pileup formation, dislocation nucleation, and indentation depth correlations. This section emphasizes the importance of having tailored MLFFs to achieve accurate and reliable simulation results for tungstens mechanical properties.

The second major contribution is the development of a NNIP specifically for Mo. Mo, as a BCC metal, presents unique challenges in simulating its dislocation behavior and plastic deformation accurately. The NNIP developed in this thesis addresses several limitations inherent in traditional and machine-learned potentials, offering precise predictions of dislocation nucleation, dislocation dynamics, and surface effects during nanoindentation. This potential was particularly successful in modeling the atomic-scale mechanisms governing the early stages of plasticity in Mo. This advancement underscores the potential of NNIPs in improving the modeling of complex mechanical behaviors in crystalline materials.

The thesis then explores the dislocation dynamics in NiCoCr alloys, a class of medium-entropy alloys. Using MD simulations, it investigates the interaction of dislocations with nanoscale CSRO and Ni-rich nanoprecipitates. The results, derived from two interatomic potentials, Li-Sheng-Ma and Farkas-Caro, reveal significant differences in dislocation behavior. The LSM potential effectively captures SRO effects and the formation of Ni-rich nanoprecipitates, while the FC potential models a random solid solution. These findings enhance the understanding of how nanoscale ordering influences the mechanical behavior of multi-component alloys like NiCoCr.

Finally, the manipulation and reorganization of SRO in NiCoCr through nanoindentation are examined. Accurate interatomic potentials, such as LSM, enable simulations of ordering phenomena in alloys, providing insights into their mechanical stability and po-

tential applications in structural materials. The work demonstrates that tailored nanoindentation protocols can reorganize local atomic ordering, forming distinct density-wave stripe patterns linked to stress fields under the indenter tip. This phenomenon offers opportunities for experimental validation and the design of materials with customized properties, advancing the understanding of density wave ordering in multi-component alloys.

Despite the significant achievements of this thesis, several challenges and limitations must be acknowledged. While NNIPs have shown tremendous potential in improving the accuracy of MD simulations, their development requires large datasets, which can be time-consuming and computationally expensive to generate. Furthermore, while NNIPs have been successfully trained for Mo, their generalizability to other materials systems and more complex deformation mechanisms remains a challenge that warrants further research. The limitations of classical potentials like EAM and GAP have also been noted in this thesis, particularly in their inability to capture certain dislocation behaviors and surface interactions accurately. These findings underscore the need for continued development of MLFFs that can address these gaps.

Looking ahead, the work presented in this thesis opens up several promising avenues for future research. First, the expansion of NNIPs to other materials, especially high-entropy alloys and multi-component systems, could provide more accurate predictions of mechanical properties across a wider range of materials. Additionally, the integration of hybrid simulation techniques that combine NNIPs with quantum-mechanical methods, such as DFT, could offer even greater accuracy in modeling complex physical phenomena. Moreover, advancements in data-driven approaches, including the use of active learning and generative models, may further enhance the efficiency and scalability of NNIP development, allowing for faster and more accurate simulations across diverse materials systems.

In conclusion, this thesis has contributed significantly to the understanding of plastic deformation mechanisms in BCC and FCC materials through the development and validation of force fields. The findings not only validate NNIPs as a powerful tool for modeling dislocation dynamics and nanoindentation but also highlight their potential for future advancements in materials science. By addressing current limitations and exploring new directions for research, this work lays the foundation for more accurate and efficient computational methods, ultimately driving innovation in the field of materials design and mechanical behavior prediction.

Bibliography

[1] Derek Hull and David J Bacon. *Introduction to dislocations*. Vol. 37. Elsevier, 2011.

[2] Peter M Anderson, John P Hirth, and Jens Lothe. *Theory of dislocations*. Cambridge University Press, 2017.

[3] Frank RN Nabarro and Mike S Duesbery. *Dislocations in solids*. Vol. 11. Elsevier, 2002.

[4] Yu N Osetsky and D J Bacon. "An atomic-level model for studying the dynamics of edge dislocations in metals." In: *Modelling and Simulation in Materials Science and Engineering* 11.4 (May 2003), p. 427. DOI: 10.1088/0965-0393/11/4/302. URL: https://dx.doi.org/10.1088/0965-0393/11/4/302.

[5] A.S. Argon and W.C. Moffatt. "Climb of extended edge dislocations." In: *Acta Metallurgica* 29.2 (1981), pp. 293–299. ISSN: 0001-6160. DOI: https://doi.org/10.1016/0001-6160(81)90156-5.

[6] Chanho Lee et al. "Strength can be controlled by edge dislocations in refractory high-entropy alloys." In: *Nature Communications* 12.1 (Sept. 2021), p. 5474. ISSN: 2041-1723. DOI: 10.1038/s41467-021-25807-w. URL: https://doi.org/10.1038/s41467-021-25807-w.

[7] Dale F. Stein and Jr. Low J. R. "Mobility of Edge Dislocations in SiliconIron Crystals." In: *Journal of Applied Physics* 31.2 (Feb. 1960), pp. 362–369. ISSN: 0021-8979. DOI: 10.1063/1.1735574.

[8] V. Celli and N. Flytzanis. "Motion of a Screw Dislocation in a Crystal." In: *Journal of Applied Physics* 41.11 (Oct. 1970), pp. 4443–4447. ISSN: 0021-8979. DOI: 10.1063/1.1658479.

[9] T. Vegge et al. "Determination of the of Rate Cross Slip of Screw Dislocations." In: *Phys. Rev. Lett.* 85 (18 Oct. 2000), pp. 3866–3869. DOI: 10.1103/PhysRevLett.85.3866.

[10] Xinran Zhou, Sicong He, and Jaime Marian. "Cross-kinks control screw dislocation strength in equiatomic bcc refractory alloys." In: *Acta Materialia* 211 (2021), p. 116875. ISSN: 1359-6454. DOI: https://doi.org/10.1016/j.actamat.2021.116875.

[11] Erik Bitzek and Peter Gumbsch. "Dynamic aspects of dislocation motion: atomistic simulations." In: *Materials Science and Engineering: A* 400-401 (2005). Dislocations 2004, pp. 40–44. ISSN: 0921-5093. DOI: https://doi.org/10.1016/j.msea.2005.03.047.

[12] Vlado A. Lubarda. "Dislocation Burgers vector and the PeachKoehler force: a review." In: *Journal of Materials Research and Technology* 8.1 (2019), pp. 1550–1565. ISSN: 2238-7854. DOI: https://doi.org/10.1016/j.jmrt.2018.08.014.

[13] M. Peach and J. S. Koehler. "The Forces Exerted on Dislocations and the Stress Fields Produced by Them." In: *Phys. Rev.* 80 (3 Nov. 1950), pp. 436–439. DOI: 10.1103/PhysRev.80.436. URL: https://link.aps.org/doi/10.1103/PhysRev.80.436.

[14] J Bonneville and B Escaig. "Cross-slipping process and the stress-orientation dependence in pure copper." In: *Acta Metallurgica* 27.9 (1979), pp. 1477–1486. ISSN: 0001-6160. DOI: https://doi.org/10.1016/0001-6160(79)90170-6. URL: https://www.sciencedirect.com/science/article/pii/0001616079901706.

[15] R. Madec, B. Devincre, and L. P. Kubin. "From Dislocation Junctions to Forest Hardening." In: *Phys. Rev. Lett.* 89 (25 Dec. 2002), p. 255508. DOI: 10.1103/PhysRevLett.89.255508. URL: https://link.aps.org/doi/10.1103/PhysRevLett.89.255508.

[16] Vasily V. Bulatov et al. "Dislocation multi-junctions and strain hardening." In: *Nature* 440.7088 (Apr. 2006), pp. 1174–1178. ISSN: 1476-4687. DOI: 10.1038/nature04658. URL: https://doi.org/10.1038/nature04658.

[17] K. Arakawa et al. "Observation of the One-Dimensional Diffusion of Nanometer-Sized Dislocation Loops." In: *Science* 318.5852 (2007), pp. 956–959. DOI: 10.1126/science.1145386. eprint: https://www.science.org/doi/pdf/10.1126/science.1145386.

[18] Yu.N Osetsky et al. "Stability and mobility of defect clusters and dislocation loops in metals." In: *Journal of Nuclear Materials* 276.1 (2000), pp. 65–77. ISSN: 0022-3115. DOI: https://doi.org/10.1016/S0022-3115(99)00170-1.

[19] Cheng Chen et al. "Effect of indium doping on motions of a-prismatic edge dislocations in wurtzite gallium nitride." In: *Journal of Physics: Condensed Matter* 31.31 (May 2019), p. 315701. DOI: 10.1088/1361-648X/ab1bf3. URL: https://dx.doi.org/10.1088/1361-648X/ab1bf3.

[20] Haidong Fan et al. "Strain rate dependency of dislocation plasticity." In: *Nature Communications* 12.1 (Mar. 2021), p. 1845. ISSN: 2041-1723. DOI: 10.1038/s41467-021-21939-1.

[21] Peng Lin et al. “On the computational solution of vector-density based continuum dislocation dynamics models: A comparison of two plastic distortion and stress update algorithms.” In: *International Journal of Plasticity* 138 (2021), p. 102943. ISSN: 0749-6419. DOI: https://doi.org/10.1016/j.ijplas.2021.102943. URL: https://www.sciencedirect.com/science/article/pii/S0749641921000188.

[22] B. B. He et al. “High dislocation densityinduced large ductility in deformed and partitioned steels.” In: *Science* 357.6355 (2017), pp. 1029–1032. DOI: 10.1126/science.aan0177. URL: https://www.science.org/doi/abs/10.1126/science.aan0177.

[23] Yongkun Mu et al. “A high-entropy alloy with dislocation-precipitate skeleton for ultrastrength and ductility.” In: *Acta Materialia* 232 (2022), p. 117975. ISSN: 1359-6454. DOI: https://doi.org/10.1016/j.actamat.2022.117975.

[24] Seok Su Sohn et al. “Ultrastrong medium-entropy single-phase alloys designed via severe lattice distortion.” In: *Advanced Materials* 31.8 (2019), p. 1807142.

[25] Kaisheng Ming, Xiaofang Bi, and Jian Wang. “Precipitation strengthening of ductile Cr15Fe20Co35Ni20Mo10 alloys.” In: *Scripta Materialia* 137 (2017), pp. 88–93. ISSN: 1359-6462. DOI: https://doi.org/10.1016/j.scriptamat.2017.05.019.

[26] F.R.N. Nabarro. “Fifty-year study of the Peierls-Nabarro stress.” In: *Materials Science and Engineering: A* 234-236 (1997), pp. 67–76. ISSN: 0921-5093. DOI: https://doi.org/10.1016/S0921-5093(97)00184-6.

[27] Xiaowang Wang et al. “Generalized stacking fault energies and Peierls stresses in refractory body-centered cubic metals from machine learning-based interatomic potentials.” In: *Computational Materials Science* 192 (2021), p. 110364. ISSN: 0927-0256. DOI: https://doi.org/10.1016/j.commatsci.2021.110364.

[28] Paraskevas Kontis. “Interactions of solutes with crystal defects: A new dynamic design parameter for advanced alloys.” In: *Scripta Materialia* 194 (2021), p. 113626. ISSN: 1359-6462. DOI: https://doi.org/10.1016/j.scriptamat.2020.11.011.

[29] Shankha Nag and William A. Curtin. “Effect of solute-solute interactions on strengthening of random alloys from dilute to high entropy alloys.” In: *Acta Materialia* 200 (2020), pp. 659–673. ISSN: 1359-6454. DOI: https://doi.org/10.1016/j.actamat.2020.08.011.

[30] Qiang Li et al. “Coupled solute effects enable anomalous high-temperature strength and stability in nanotwinned Al alloys.” In: *Acta Materialia* 200 (2020), pp. 378–388. ISSN: 1359-6454. DOI: https://doi.org/10.1016/j.actamat.2020.08.059.

[31] S.I. Rao et al. “Theory of solid solution strengthening of BCC Chemically Complex Alloys.” In: *Acta Materialia* 209 (2021), p. 116758. ISSN: 1359-6454. DOI: https://doi.org/10.1016/j.actamat.2021.116758.

[32] Amirhossein D. Naghdi et al. “Neural network interatomic potentials for open surface nano-mechanics applications.” In: *Acta Materialia* 277 (2024), p. 120200. ISSN: 1359-6454. DOI: https://doi.org/10.1016/j.actamat.2024.120200.

[33] Daniel Marchand et al. “Machine learning for metallurgy I. A neural-network potential for Al-Cu.” In: *Phys. Rev. Mater.* 4 (10 Oct. 2020), p. 103601. DOI: 10.1103/PhysRevMaterials.4.103601. URL: https://link.aps.org/doi/10.1103/PhysRevMaterials.4.103601.

[34] Y. Mishin. “Machine-learning interatomic potentials for materials science.” In: *Acta Materialia* 214 (2021), p. 116980. ISSN: 1359-6454. DOI: https://doi.org/10.1016/j.actamat.2021.116980. URL: https://www.sciencedirect.com/science/article/pii/S1359645421003608.

[35] Markus Stricker et al. “Machine learning for metallurgy II. A neural-network potential for magnesium.” In: *Phys. Rev. Mater.* 4 (10 Oct. 2020), p. 103602. DOI: 10.1103/PhysRevMaterials.4.103602.

[36] Abhinav C. P. Jain et al. “Machine learning for metallurgy III: A neural network potential for Al-Mg-Si.” In: *Phys. Rev. Mater.* 5 (5 May 2021), p. 053805. DOI: 10.1103/PhysRevMaterials.5.053805. URL: https://link.aps.org/doi/10.1103/PhysRevMaterials.5.053805.

[37] Daniel Marchand and W. A. Curtin. “Machine learning for metallurgy IV: A neural network potential for Al-Cu-Mg and Al-Cu-Mg-Zn.” In: *Phys. Rev. Mater.* 6 (5 May 2022), p. 053803. DOI: 10.1103/PhysRevMaterials.6.053803. URL: https://link.aps.org/doi/10.1103/PhysRevMaterials.6.053803.

[38] Manura Liyanage et al. “Machine learning for metallurgy V: A neural-network potential for zirconium.” In: *Phys. Rev. Mater.* 6 (6 June 2022), p. 063804. DOI: 10.1103/PhysRevMaterials.6.063804. URL: https://link.aps.org/doi/10.1103/PhysRevMaterials.6.063804.

[39] Wei Yu et al. “Machine-learning-based interatomic potentials for advanced manufacturing.” In: *International Journal of Mechanical System Dynamics* 1.2 (2021), pp. 159–172. DOI: https://doi.org/10.1002/msd2.12021. URL: https://onlinelibrary.wiley.com/doi/abs/10.1002/msd2.12021.

[40] Caizhi Zhou, S. Bulent Biner, and Richard LeSar. “Discrete dislocation dynamics simulations of plasticity at small scales.” In: *Acta Materialia* 58.5 (2010), pp. 1565–1577. ISSN: 1359-6454. DOI: https://doi.org/10.1016/j.actamat.2009.11.001. URL: https://www.sciencedirect.com/science/article/pii/S1359645409007678.

[41] C. Motz et al. “Micro-bending tests: A comparison between three-dimensional discrete dislocation dynamics simulations and experiments.” In: *Acta Materialia* 56.9 (2008), pp. 1942–1955. ISSN: 1359-6454. DOI: https://doi.org/10.1016/j.actamat.2007.12.053. URL: https://www.sciencedirect.com/science/article/pii/S1359645408000062.

[42] H. Song et al. “Discrete dislocation dynamics simulations of nanoindentation with pre-stress: Hardness and statistics of abrupt plastic events.” In: *Journal of the Mechanics and Physics of Solids* 123 (2019). The N.A. Fleck 60th Anniversary Volume, pp. 332–347. ISSN: 0022-5096. DOI: https://doi.org/10.1016/j.jmps.2018.09.005. URL: https://www.sciencedirect.com/science/article/pii/S0022509618305027.

[43] Giacomo Po et al. “Recent Progress in Discrete Dislocation Dynamics and Its Applications to Micro Plasticity.” In: *JOM* 66.10 (Oct. 2014), pp. 2108–2120. ISSN: 1543-1851. DOI: 10.1007/s11837-014-1153-2. URL: https://doi.org/10.1007/s11837-014-1153-2.

[44] R. Santos-Güemes et al. “Discrete dislocation dynamics simulations of dislocation-θ' precipitate interaction in Al-Cu alloys.” In: *Journal of the Mechanics and Physics of Solids* 118 (2018), pp. 228–244. ISSN: 0022-5096. DOI: https://doi.org/10.1016/j.jmps.2018.05.015. URL: https://www.sciencedirect.com/science/article/pii/S0022509617310037.

[45] Thomas Hochrainer et al. “Continuum dislocation dynamics: Towards a physical theory of crystal plasticity.” In: *Journal of the Mechanics and Physics of Solids* 63 (2014), pp. 167–178. ISSN: 0022-5096. DOI: https://doi.org/10.1016/j.jmps.2013.09.012. URL: https://www.sciencedirect.com/science/article/pii/S0022509613001877.

[46] Thomas Hochrainer. “Thermodynamically consistent continuum dislocation dynamics.” In: *Journal of the Mechanics and Physics of Solids* 88 (2016), pp. 12–22. ISSN: 0022-5096. DOI: https://doi.org/10.1016/j.jmps.2015.12.015. URL: https://www.sciencedirect.com/science/article/pii/S002250961530048X.

[47] J. Frenkel. “Über die Wärmebewegung in festen und flüssigen Körpern.” In: *Zeitschrift für Physik* 35.8 (Aug. 1926), pp. 652–669. ISSN: 0044-3328. DOI: 10.1007/BF01379812. URL: https://doi.org/10.1007/BF01379812.

[48] E. Orowan. “Zur Kristallplastizität. III.” In: *Zeitschrift für Physik* 89.9 (Sept. 1934), pp. 634–659. ISSN: 0044-3328. DOI: 10.1007/BF01341480. URL: https://doi.org/10.1007/BF01341480.

[49] Geoffrey Ingram Taylor. “The mechanism of plastic deformation of crystals. Part I.Theoretical.” In: *Proceedings of the Royal Society of London. Series A, Containing Papers of a Mathematical and Physical Character* 145.855 (1934), pp. 362–387. DOI: 10.1098/rspa.1934.0106. URL: https://royalsocietypublishing.org/doi/abs/10.1098/rspa.1934.0106.

[50] Fi C Frank. “The influence of dislocations on crystal growth.” In: *Discussions of the Faraday Society* 5 (1949), pp. 48–54.

[51] P. Shanthraj and M.A. Zikry. “Dislocation density evolution and interactions in crystalline materials.” In: *Acta Materialia* 59.20 (2011), pp. 7695–7702. ISSN: 1359-6454. DOI: https://doi.org/10.1016/j.actamat.2011.08.041.

[52] P Gay, P.B Hirsch, and A Kelly. "The estimation of dislocation densities in metals from X-ray data." In: *Acta Metallurgica* 1.3 (1953), pp. 315–319. ISSN: 0001-6160. DOI: https://doi.org/10.1016/0001-6160(53)90106-0.

[53] L.L Wei et al. "Microstructure evolution and creep-rupture behaviour of a low-cost Fe-Ni-based superalloy." In: *Materials Technology* 38.1 (2023), p. 2270865. DOI: 10.1080/10667857.2023.2270865.

[54] Ruopeng Zhang et al. "Short-range order and its impact on the CrCoNi medium-entropy alloy." In: *Nature* 581.7808 (May 2020), pp. 283–287. ISSN: 1476-4687. DOI: 10.1038/s41586-020-2275-z. URL: https://doi.org/10.1038/s41586-020-2275-z.

[55] Jiabin Liu et al. "Deformation twinning behaviors of the low stacking fault energy high-entropy alloy: An in-situ TEM study." In: *Scripta Materialia* 137 (2017), pp. 9–12. ISSN: 1359-6462. DOI: https://doi.org/10.1016/j.scriptamat.2017.05.001. URL: https://www.sciencedirect.com/science/article/pii/S1359646217302336.

[56] F. A. Ponce et al. "Characterization of dislocations in GaN by transmission electron diffraction and microscopy techniques." In: *Applied Physics Letters* 69.6 (Aug. 1996), pp. 770–772. ISSN: 0003-6951. DOI: 10.1063/1.117886.

[57] X.D. Xu et al. "Transmission electron microscopy characterization of dislocation structure in a face-centered cubic high-entropy alloy Al0.1CoCrFeNi." In: *Acta Materialia* 144 (2018), pp. 107–115. ISSN: 1359-6454. DOI: https://doi.org/10.1016/j.actamat.2017.10.050.

[58] S. R. Agnew, J. A. Horton, and M. H. Yoo. "Transmission electron microscopy investigation of ⟨c+a⟩ dislocations in Mg and α-solid solution Mg-Li alloys." In: *Metallurgical and Materials Transactions A* 33.3 (Mar. 2002), pp. 851–858. ISSN: 1543-1940. DOI: 10.1007/s11661-002-0154-x.

[59] J. Miao et al. "Dislocation Characterization using Weak Beam Dark Field STEM Imaging." In: *Microscopy and Microanalysis* 24.S1 (2018), pp. 2202–2203. DOI: 10.1017/S1431927618011492.

[60] Yan-Ru Lin et al. "Application of Weak-Beam Dark-Field STEM for Dislocation Loop Analysis." In: *Microscopy and Microanalysis* 30.4 (July 2024), pp. 681–691. ISSN: 1431-9276. DOI: 10.1093/mam/ozae067.

[61] J. R. Tong J. S. Barnard J. Sharp and P. A. Midgley. "Three-dimensional analysis of dislocation networks in GaN using weak-beam dark-field electron tomography." In: *Philosophical Magazine* 86.29-31 (2006), pp. 4901–4922. DOI: 10.1080/14786430600798839.

[62] D.D. Perovic, C.J. Rossouw, and A. Howie. "Imaging elastic strains in high-angle annular dark field scanning transmission electron microscopy." In: *Ultramicroscopy* 52.3 (1993), pp. 353–359. ISSN: 0304-3991. DOI: https://doi.org/10.1016/0304-3991(93)90046-Z.

[63] A. Howie D. D. Perovic and C. J. Rossouw. "On the image contrast from dislocations in high-angle annular dark-field scanning transmission electron microscopy." In: *Philosophical Magazine Letters* 67.4 (1993), pp. 261–272. DOI: 10.1080/09500839308240938.

[64] A. Amali, P. Rez, and J.M. Cowley. "High angle annular dark field imaging of stacking faults." In: *Micron* 28.2 (1997), pp. 89–94. ISSN: 0968-4328. DOI: https://doi.org/10.1016/S0968-4328(97)00001-2. URL: https://www.sciencedirect.com/science/article/pii/S0968432897000012.

[65] W. G. Johnston and J. J. Gilman. "Dislocation Velocities, Dislocation Densities, and Plastic Flow in Lithium Fluoride Crystals." In: *Journal of Applied Physics* 30.2 (Feb. 1959), pp. 129–144. ISSN: 0021-8979. DOI: 10.1063/1.1735121. eprint: https://pubs.aip.org/aip/jap/article-pdf/30/2/129/18319171/129_1_online.pdf. URL: https://doi.org/10.1063/1.1735121.

[66] Brian Keith Tanner. *X-ray diffraction topography: international series in the science of the solid state*. Vol. 10. Elsevier, 2013.

[67] T. Ohno et al. "Direct observation of dislocations propagated from 4HSiC substrate to epitaxial layer by X-ray topography." In: *Journal of Crystal Growth* 260.1 (2004), pp. 209–216. ISSN: 0022-0248. DOI: https://doi.org/10.1016/j.jcrysgro.2003.08.065. URL: https://www.sciencedirect.com/science/article/pii/S0022024803017330.

[68] Martin A. Crimp. "Scanning electron microscopy imaging of dislocations in bulk materials, using electron channeling contrast." In: *Microscopy Research and Technique* 69.5 (2006), pp. 374–381. DOI: https://doi.org/10.1002/jemt.20293. eprint: https://analyticalsciencejournals.onlinelibrary.wiley.com/doi/pdf/10.1002/jemt.20293. URL: https://analyticalsciencejournals.onlinelibrary.wiley.com/doi/abs/10.1002/jemt.20293.

[69] I. Gutierrez-Urrutia, S. Zaefferer, and D. Raabe. "Coupling of Electron Channeling with EBSD: Toward the Quantitative Characterization of Deformation Structures in the SEM." In: *JOM* 65.9 (Sept. 2013), pp. 1229–1236. ISSN: 1543-1851. DOI: 10.1007/s11837-013-0678-0. URL: https://doi.org/10.1007/s11837-013-0678-0.

[70] P.D. Styman G.D.W. Smith D. Hudson and C.A. Williams. "Studies of dislocations by field ion microscopy and atom probe tomography." In: *Philosophical Magazine* 93.28-30 (2013), pp. 3726–3740. DOI: 10.1080/14786435.2013.818257.

[71] K. M. Jassby and T. Vreeland Jr. "An experimental study of the mobility of edge dislocations in pure copper single crystals." In: *The Philosophical Magazine: A Journal of Theoretical Experimental and Applied Physics* 21.174 (1970), pp. 1147–1168. DOI: 10.1080/14786437008238500.

[72] Benjamin Galy et al. “Glide and mixed climb dislocation velocity in gamma-TiAl investigated by in-situ transmission electron microscopy.” In: *Scripta Materialia* 228 (2023), p. 115333. ISSN: 1359-6462. DOI: https://doi.org/10.1016/j.scriptamat.2023.115333.

[73] Quan Li et al. “In-situ TEM characterization of basal dislocations between nano-spaced long-period stacking ordered phases in MgYZn alloy.” In: *Scripta Materialia* 235 (2023), p. 115601. ISSN: 1359-6462. DOI: https://doi.org/10.1016/j.scriptamat.2023.115601.

[74] Dewang Cui et al. “Effect of dose rate on the characteristics of dislocation loops in palladium: In-situ TEM analysis during 30 keV H2+ irradiation.” In: *Journal of Materials Science & Technology* 150 (2023), pp. 86–95. ISSN: 1005-0302. DOI: https://doi.org/10.1016/j.jmst.2022.12.013.

[75] Bo Gao et al. “In-situ TEM investigation on deformation mechanisms of a fine-grained 316L stainless steel.” In: *Scripta Materialia* 234 (2023), p. 115538. ISSN: 1359-6462. DOI: https://doi.org/10.1016/j.scriptamat.2023.115538.

[76] M. Larranaga et al. “High temperature plasticity at twin boundary in Al: An in-situ TEM perspective.” In: *Acta Materialia* 251 (2023), p. 118877. ISSN: 1359-6454. DOI: https://doi.org/10.1016/j.actamat.2023.118877.

[77] Louchet, F. et al. “In situ TEM study of dislocation mobility in semiconducting materials.” In: *Microsc. Microanal. Microstruct.* 4 (1993), pp. 199–210. DOI: 10.1051/mmm:0199300402-3019900. URL: https://doi.org/10.1051/mmm:0199300402-3019900.

[78] Daniel Caillard, Martin Rautenberg, and Xavier Feaugas. “Dislocation mechanisms in a zirconium alloy in the high-temperature regime: An in situ TEM investigation.” In: *Acta Materialia* 87 (2015), pp. 283–292. ISSN: 1359-6454. DOI: https://doi.org/10.1016/j.actamat.2015.01.016. URL: https://www.sciencedirect.com/science/article/pii/S1359645415000208.

[79] W. Püschl. “Models for dislocation cross-slip in close-packed crystal structures: a critical review.” In: *Progress in Materials Science* 47.4 (2002), pp. 415–461. ISSN: 0079-6425. DOI: https://doi.org/10.1016/S0079-6425(01)00003-2. URL: https://www.sciencedirect.com/science/article/pii/S0079642501000032.

[80] Zezhou Li et al. “Mechanical properties of high-entropy alloys with emphasis on face-centered cubic alloys.” In: *Progress in Materials Science* 102 (2019), pp. 296–345.

[81] Yuanyuan Shang et al. “Mechanical Behavior of High-Entropy Alloys: A Review.” In: *High-Entropy Materials: Theory, Experiments, and Applications*. Ed. by Jamieson Brechtl and Peter K. Liaw. Cham: Springer International Publishing, 2021, pp. 435–522. ISBN: 978-3-030-77641-1. DOI: 10.1007/978-3-030-77641-1_10.

[82] Ruopeng Zhang et al. “Short-range order and its impact on the CrCoNi medium-entropy alloy.” In: *Nature* 581.7808 (2020), pp. 283–287.

[83] Yuan Wu et al. “Short-range ordering and its effects on mechanical properties of high-entropy alloys.” In: *Journal of Materials Science & Technology* 62 (2021), pp. 214–220.

[84] Lingling Zhou et al. “Atomic-scale evidence of chemical short-range order in CrCoNi medium-entropy alloy.” In: *Acta Materialia* 224 (2022), p. 117490.

[85] Xuefei Chen et al. “Direct observation of chemical short-range order in a medium-entropy alloy.” In: *Nature* 592.7856 (2021), pp. 712–716.

[86] Binglun Yin et al. “Yield strength and misfit volumes of NiCoCr and implications for short-range-order.” In: *Nature Communications* 11.1 (2020), pp. 1–7.

[87] Wolfram Georg Noehring and WA Curtin. “Correlation of microdistortions with misfit volumes in high entropy alloys.” In: *Scripta Materialia* 168 (2019), pp. 119–123.

[88] Subin Lee et al. “Dislocation plasticity in FeCoCrMnNi high-entropy alloy: quantitative insights from in situ transmission electron microscopy deformation.” In: *Materials Research Letters* 8.6 (2020), pp. 216–224. DOI: 10.1080/21663831.2020.1741469.

[89] Evan Ma. “Unusual dislocation behavior in high-entropy alloys.” In: *Scripta Materialia* 181 (2020), pp. 127–133. ISSN: 1359-6462. DOI: https://doi.org/10.1016/j.scriptamat.2020.02.021. URL: https://www.sciencedirect.com/science/article/pii/S135964622030097X.

[90] FX Zhang et al. “Local structure and short-range order in a NiCoCr solid solution alloy.” In: *Physical review letters* 118.20 (2017), p. 205501.

[91] Y. Mishin and J.W. Cahn. “Thermodynamics of Cottrell atmospheres tested by atomistic simulations.” In: *Acta Materialia* 117 (2016), pp. 197–206. ISSN: 1359-6454. DOI: https://doi.org/10.1016/j.actamat.2016.07.013. URL: https://www.sciencedirect.com/science/article/pii/S1359645416305092.

[92] Yong Zhang, Jun-wei Qiao, and Peter K. Liaw. “A Brief Review of High Entropy Alloys and Serration Behavior and Flow Units.” In: *Journal of Iron and Steel Research International* 23.1 (Jan. 2016), pp. 2–6. ISSN: 2210-3988. DOI: 10.1016/S1006-706X(16)30002-4. URL: https://doi.org/10.1016/S1006-706X(16)30002-4.

[93] Jörg Behler and Michele Parrinello. “Generalized Neural-Network Representation of High-Dimensional Potential-Energy Surfaces.” In: *Phys. Rev. Lett.* 98 (14 Apr. 2007), p. 146401. DOI: 10.1103/PhysRevLett.98.146401. URL: https://link.aps.org/doi/10.1103/PhysRevLett.98.146401.

[94] Mingjie Liu and John R. Kitchin. "SingleNN: Modified Behler–Parrinello Neural Network with Shared Weights for Atomistic Simulations with Transferability." In: *The Journal of Physical Chemistry C* 124.32 (Aug. 2020), pp. 17811–17818. ISSN: 1932-7447. DOI: 10.1021/acs.jpcc.0c04225. URL: https://doi.org/10.1021/acs.jpcc.0c04225.

[95] T. van der Heide et al. "Fortnet, a software package for training Behler-Parrinello neural networks." In: *Computer Physics Communications* 284 (2023), p. 108580. ISSN: 0010-4655. DOI: https://doi.org/10.1016/j.cpc.2022.108580.

[96] Yuki Nagai, Masahiko Okumura, and Akinori Tanaka. "Self-learning Monte Carlo method with Behler-Parrinello neural networks." In: *Phys. Rev. B* 101 (11 Mar. 2020), p. 115111. DOI: 10.1103/PhysRevB.101.115111.

[97] Pablo Montero de Hijes et al. "Comparing machine learning potentials for water: Kernel-based regression and BehlerParrinello neural networks." In: *The Journal of Chemical Physics* 160.11 (Mar. 2024), p. 114107. ISSN: 0021-9606. DOI: 10.1063/5.0197105.

[98] Christopher R. Weinberger and Wei Cai. "Surface-controlled dislocation multiplication in metal micropillars." In: *Proceedings of the National Academy of Sciences* 105.38 (2008), pp. 14304–14307. DOI: 10.1073/pnas.0806118105. eprint: https://www.pnas.org/doi/pdf/10.1073/pnas.0806118105. URL: https://www.pnas.org/doi/abs/10.1073/pnas.0806118105.

[99] J. A. Knapp et al. "Finite-element modeling of nanoindentation." In: *Journal of Applied Physics* 85.3 (Feb. 1999), pp. 1460–1474. ISSN: 0021-8979. DOI: 10.1063/1.369178.

[100] K. Frydrych et al. "Multiscale nanoindentation modelling of concentrated solid solutions: A continuum plasticity model." In: *Mechanics of Materials* 181 (2023), p. 104644. ISSN: 0167-6636. DOI: https://doi.org/10.1016/j.mechmat.2023.104644.

[101] Lianping Wu and Teng Li. "A machine learning interatomic potential for high entropy alloys." In: *Journal of the Mechanics and Physics of Solids* 187 (2024), p. 105639. ISSN: 0022-5096. DOI: https://doi.org/10.1016/j.jmps.2024.105639. URL: https://www.sciencedirect.com/science/article/pii/S0022509624001054.

[102] Lei Zhang et al. "Efficiency, accuracy, and transferability of machine learning potentials: Application to dislocations and cracks in iron." In: *Acta Materialia* 270 (2024), p. 119788. ISSN: 1359-6454. DOI: https://doi.org/10.1016/j.actamat.2024.119788. URL: https://www.sciencedirect.com/science/article/pii/S135964542400140X.

[103] T. Okita et al. “Construction of machine-learning Zr interatomic potentials for identifying the formation process of c-type dislocation loops.” In: *Computational Materials Science* 202 (2022), p. 110865. ISSN: 0927-0256. DOI: https://doi.org/10.1016/j.commatsci.2021.110865.

[104] Hideki Mori et al. “Dynamic interaction between dislocations and obstacles in bcc iron based on atomic potentials derived using neural networks.” In: *Phys. Rev. Mater.* 7 (6 June 2023), p. 063605. DOI: 10.1103/PhysRevMaterials.7.063605. URL: https://link.aps.org/doi/10.1103/PhysRevMaterials.7.063605.

[105] Albert P. Bartók et al. “Gaussian Approximation Potentials: The Accuracy of Quantum Mechanics, without the Electrons.” In: *Phys. Rev. Lett.* 104 (13 Apr. 2010), p. 136403. DOI: 10.1103/PhysRevLett.104.136403. URL: https://link.aps.org/doi/10.1103/PhysRevLett.104.136403.

[106] Siddarth K. Achar, Leonardo Bernasconi, and J. Karl Johnson. “Machine Learning Electron Density Prediction Using Weighted Smooth Overlap of Atomic Positions.” In: *Nanomaterials* 13.12 (2023). ISSN: 2079-4991. DOI: 10.3390/nano13121853. URL: https://www.mdpi.com/2079-4991/13/12/1853.

[107] Volker L. Deringer and Gábor Csányi. “Machine learning based interatomic potential for amorphous carbon.” In: *Phys. Rev. B* 95 (9 Mar. 2017), p. 094203. DOI: 10.1103/PhysRevB.95.094203. URL: https://link.aps.org/doi/10.1103/PhysRevB.95.094203.

[108] Andrea Grisafi et al. “Symmetry-Adapted Machine Learning for Tensorial Properties of Atomistic Systems.” In: *Phys. Rev. Lett.* 120 (3 Jan. 2018), p. 036002. DOI: 10.1103/PhysRevLett.120.036002.

[109] Ryosuke Jinnouchi, Ferenc Karsai, and Georg Kresse. “On-the-fly machine learning force field generation: Application to melting points.” In: *Phys. Rev. B* 100 (1 July 2019), p. 014105. DOI: 10.1103/PhysRevB.100.014105. URL: https://link.aps.org/doi/10.1103/PhysRevB.100.014105.

[110] Wojciech J. Szlachta, Albert P. Bartók, and Gábor Csányi. “Accuracy and transferability of Gaussian approximation potential models for tungsten.” In: *Phys. Rev. B* 90 (10 Sept. 2014), p. 104108. DOI: 10.1103/PhysRevB.90.104108.

[111] Albert P. Bartók, Risi Kondor, and Gábor Csányi. “On representing chemical environments.” In: *Phys. Rev. B* 87 (18 May 2013), p. 184115. DOI: 10.1103/PhysRevB.87.184115. URL: https://link.aps.org/doi/10.1103/PhysRevB.87.184115.

[112] Alexander V. Shapeev. “Moment Tensor Potentials: A Class of Systematically Improvable Interatomic Potentials.” In: *Multiscale Modeling & Simulation* 14.3 (2016), pp. 1153–1173. DOI: 10.1137/15M1054183.

[113] Ivan S Novikov et al. "The MLIP package: moment tensor potentials with MPI and active learning." In: *Machine Learning: Science and Technology* 2.2 (Dec. 2020), p. 025002. DOI: 10.1088/2632-2153/abc9fe. URL: https://dx.doi.org/10.1088/2632-2153/abc9fe.

[114] Konstantin Gubaev et al. "Accelerating high-throughput searches for new alloys with active learning of interatomic potentials." In: *Computational Materials Science* 156 (2019), pp. 148–156. ISSN: 0927-0256. DOI: https://doi.org/10.1016/j.commatsci.2018.09.031.

[115] Konstantin Gubaev, Evgeny V. Podryabinkin, and Alexander V. Shapeev. "Machine learning of molecular properties: Locality and active learning." In: *The Journal of Chemical Physics* 148.24 (Apr. 2018), p. 241727. ISSN: 0021-9606. DOI: 10.1063/1.5005095.

[116] Andre Lomaka and Toomas Tamm. "Linearization of moment tensor potentials for multicomponent systems with a preliminary assessment for short-range interaction energy in water dimer and trimer." In: *The Journal of Chemical Physics* 152.16 (Apr. 2020), p. 164115. ISSN: 0021-9606. DOI: 10.1063/5.0007473.

[117] Geneviève Dusson et al. "Atomic cluster expansion: Completeness, efficiency and stability." In: *Journal of Computational Physics* 454 (2022), p. 110946. ISSN: 0021-9991. DOI: https://doi.org/10.1016/j.jcp.2022.110946.

[118] Ralf Drautz. "Atomic cluster expansion for accurate and transferable interatomic potentials." In: *Phys. Rev. B* 99 (1 Jan. 2019), p. 014104. DOI: 10.1103/PhysRevB.99.014104. URL: https://link.aps.org/doi/10.1103/PhysRevB.99.014104.

[119] William C. Witt et al. "ACEpotentials.jl: A Julia implementation of the atomic cluster expansion." In: *The Journal of Chemical Physics* 159.16 (Oct. 2023), p. 164101. ISSN: 0021-9606. DOI: 10.1063/5.0158783.

[120] Yury Lysogorskiy et al. "Performant implementation of the atomic cluster expansion (PACE) and application to copper and silicon." In: *npj Computational Materials* 7.1 (June 2021), p. 97. ISSN: 2057-3960. DOI: 10.1038/s41524-021-00559-9. URL: https://doi.org/10.1038/s41524-021-00559-9.

[121] Ilyes Batatia et al. "MACE: Higher Order Equivariant Message Passing Neural Networks for Fast and Accurate Force Fields." In: *Advances in Neural Information Processing Systems*. Ed. by S. Koyejo et al. Vol. 35. Curran Associates, Inc., 2022, pp. 11423–11436. URL: https://proceedings.neurips.cc/paper_files/paper/2022/file/4a36c3c51af11ed9f34615b81edb5bbc-Paper-Conference.pdf.

[122] Dávid Péter Kovács et al. "Evaluation of the MACE force field architecture: From medicinal chemistry to materials science." In: *The Journal of Chemical Physics* 159.4 (July 2023), p. 044118. ISSN: 0021-9606. DOI: 10.1063/5.0155322.

[123] Simon Batzner et al. “E(3)-equivariant graph neural networks for data-efficient and accurate interatomic potentials.” In: *Nature Communications* 13.1 (May 2022), p. 2453. ISSN: 2041-1723. DOI: 10.1038/s41467-022-29939-5. URL: https://doi.org/10.1038/s41467-022-29939-5.

[124] Anton Bochkarev, Yury Lysogorskiy, and Ralf Drautz. “Graph Atomic Cluster Expansion for Semilocal Interactions beyond Equivariant Message Passing.” In: *Phys. Rev. X* 14 (2 June 2024), p. 021036. DOI: 10.1103/PhysRevX.14.021036. URL: https://link.aps.org/doi/10.1103/PhysRevX.14.021036.

[125] Cas van der Oord et al. “Hyperactive learning for data-driven interatomic potentials.” In: *npj Computational Materials* 9.1 (Sept. 2023), p. 168. ISSN: 2057-3960. DOI: 10.1038/s41524-023-01104-6. URL: https://doi.org/10.1038/s41524-023-01104-6.

[126] Jonathan Vandermause et al. “On-the-fly active learning of interpretable Bayesian force fields for atomistic rare events.” In: *npj Computational Materials* 6.1 (Mar. 2020), p. 20. ISSN: 2057-3960. DOI: 10.1038/s41524-020-0283-z. URL: https://doi.org/10.1038/s41524-020-0283-z.

[127] Cameron J. Owen et al. *Unbiased Atomistic Predictions of Crystal Dislocation Dynamics using Bayesian Force Fields*. 2024. arXiv: 2401.04359 [cond-mat.mtrl-sci]. URL: https://arxiv.org/abs/2401.04359.

[128] Cameron J. Owen et al. “Complexity of many-body interactions in transition metals via machine-learned force fields from the TM23 data set.” In: *npj Computational Materials* 10.1 (May 2024), p. 92. ISSN: 2057-3960. DOI: 10.1038/s41524-024-01264-z. URL: https://doi.org/10.1038/s41524-024-01264-z.

[129] Yunxing Zuo et al. “Performance and Cost Assessment of Machine Learning Interatomic Potentials.” In: *The Journal of Physical Chemistry A* 124.4 (Jan. 2020), pp. 731–745. ISSN: 1089-5639. DOI: 10.1021/acs.jpca.9b08723. URL: https://doi.org/10.1021/acs.jpca.9b08723.

[130] G. P. Purja Pun et al. “Development of a general-purpose machine-learning interatomic potential for aluminum by the physically informed neural network method.” In: *Phys. Rev. Mater.* 4 (11 Nov. 2020), p. 113807. DOI: 10.1103/PhysRevMaterials.4.113807.

[131] Takayuki Nishiyama, Atsuto Seko, and Isao Tanaka. “Application of machine learning potentials to predict grain boundary properties in fcc elemental metals.” In: *Phys. Rev. Mater.* 4 (12 Dec. 2020), p. 123607. DOI: 10.1103/PhysRevMaterials.4.123607. URL: https://link.aps.org/doi/10.1103/PhysRevMaterials.4.123607.

[132] Hao Gao, Junjie Wang, and Jian Sun. “Improve the performance of machine-learning potentials by optimizing descriptors.” In: *The Journal of Chemical Physics* 150.24 (June 2019), p. 244110. ISSN: 0021-9606. DOI: 10.1063/1.5097293. URL: https://doi.org/10.1063/1.5097293.

[133] Susumu Fujii and Atsuto Seko. "Structure and lattice thermal conductivity of grain boundaries in silicon by using machine learning potential and molecular dynamics." In: *Computational Materials Science* 204 (2022), p. 111137. ISSN: 0927-0256. DOI: https://doi.org/10.1016/j.commatsci.2021.111137.

[134] T. Yokoi et al. "Neural-network interatomic potential for grain boundary structures and their energetics in silicon." In: *Phys. Rev. Mater.* 4 (1 Jan. 2020), p. 014605. DOI: 10.1103/PhysRevMaterials.4.014605.

[135] Yoshinori Shiihara et al. "Artificial neural network molecular mechanics of iron grain boundaries." In: *Scripta Materialia* 207 (2022), p. 114268. ISSN: 1359-6462. DOI: https://doi.org/10.1016/j.scriptamat.2021.114268.

[136] Chao Jiang et al. "Machine learning potential assisted exploration of complex defect potential energy surfaces." In: *npj Computational Materials* 10.1 (Jan. 2024), p. 21. ISSN: 2057-3960. DOI: 10.1038/s41524-024-01207-8.

[137] Rodrigo Freitas and Yifan Cao. "Machine-learning potentials for crystal defects." In: *MRS Communications* 12.5 (Oct. 2022), pp. 510–520. ISSN: 2159-6867. DOI: 10.1557/s43579-022-00221-5. URL: https://doi.org/10.1557/s43579-022-00221-5.

[138] V. Vítek. "Intrinsic stacking faults in body-centred cubic crystals." In: *The Philosophical Magazine: A Journal of Theoretical Experimental and Applied Physics* 18.154 (1968), pp. 773–786. DOI: 10.1080/14786436808227500.

[139] Daniele Dragoni et al. "Achieving DFT accuracy with a machine-learning interatomic potential: Thermomechanics and defects in bcc ferromagnetic iron." In: *Phys. Rev. Mater.* 2 (1 Jan. 2018), p. 013808. DOI: 10.1103/PhysRevMaterials.2.013808. URL: https://link.aps.org/doi/10.1103/PhysRevMaterials.2.013808.

[140] M.S. Duesbery and V. Vitek. "Plastic anisotropy in b.c.c. transition metals." In: *Acta Materialia* 46.5 (1998), pp. 1481–1492. ISSN: 1359-6454. DOI: https://doi.org/10.1016/S1359-6454(97)00367-4.

[141] A. P. Thompson et al. "LAMMPS - a flexible simulation tool for particle-based materials modeling at the atomic, meso, and continuum scales." In: *Comp. Phys. Comm.* 271 (2022), p. 108171.

[142] Qing-Jie Li, Howard Sheng, and Evan Ma. "Strengthening in multi-principal element alloys with local-chemical-order roughened dislocation pathways." In: *Nature Communications* 10.1 (2019), p. 3563.

[143] Fu-Hua Cao, Yun-Jiang Wang, and Lan-Hong Dai. "Novel atomic-scale mechanism of incipient plasticity in a chemically complex CrCoNi medium-entropy alloy associated with inhomogeneity in local chemical environment." In: *Acta Materialia* 194 (2020), pp. 283–294.

[144] Wu-Rong Jian et al. “Effects of lattice distortion and chemical short-range order on the mechanisms of deformation in medium entropy alloy CoCrNi.” In: *Acta Materialia* 199 (2020), pp. 352–369.

[145] Xiaofeng Yang et al. “Chemical short-range order strengthening mechanism in CoCrNi medium-entropy alloy under nanoindentation.” In: *Scripta Materialia* 209 (2022), p. 114364.

[146] Diana Farkas and Alfredo Caro. “Model interatomic potentials and lattice strain in a high-entropy alloy.” In: *Journal of Materials Research* 33.19 (2018), pp. 3218–3225.

[147] Yu N Osetsky and David J Bacon. “An atomic-level model for studying the dynamics of edge dislocations in metals.” In: *Modelling and Simulation in Materials Science and Engineering* 11.4 (2003), p. 427.

[148] Babak Sadigh et al. “Scalable parallel Monte Carlo algorithm for atomistic simulations of precipitation in alloys.” In: *Phys. Rev. B* 85 (18 May 2012), p. 184203.

[149] F. J. Domínguez-Gutiérrez et al. “Nanoindentation of tungsten: From interatomic potentials to dislocation plasticity mechanisms.” In: *Phys. Rev. Mater.* 7 (4 Apr. 2023), p. 043603. DOI: 10.1103/PhysRevMaterials.7.043603. URL: https://link.aps.org/doi/10.1103/PhysRevMaterials.7.043603.

[150] F.J. Dominguez-Gutierrez et al. “Nanoindentation of single crystalline Mo: Atomistic defect nucleation and thermomechanical stability.” In: *Materials Science and Engineering: A* 826 (2021), p. 141912. ISSN: 0921-5093. DOI: https://doi.org/10.1016/j.msea.2021.141912.

[151] Warren C Oliver and George M Pharr. “An improved technique for determining hardness and elastic modulus using load and displacement sensing indentation experiments.” In: *Journal of Materials Research* 7 (1992), pp. 1564–1583. DOI: 10.1557/JMR.1992.1564.

[152] Javier Varillas et al. “Unraveling deformation mechanisms around FCC and BCC nanocontacts through slip trace and pileup topography analyses.” In: *Acta Materialia* 125 (2017), pp. 431–441. DOI: https://doi.org/10.1016/j.actamat.2016.11.067.

[153] T.P. Remington et al. “Plastic deformation in nanoindentation of tantalum: A new mechanism for prismatic loop formation.” In: *Acta Materialia* 78 (2014), pp. 378–393. ISSN: 1359-6454. DOI: https://doi.org/10.1016/j.actamat.2014.06.058. URL: https://www.sciencedirect.com/science/article/pii/S1359645414004881.

[154] Johannes J Möller and Erik Bitzek. “BDA: A novel method for identifying defects in body-centered cubic crystals.” In: *MethodsX* 3 (2016), pp. 279–288. DOI: 10.1016/j.mex.2016.03.013.

[155] Franco Pellegrini et al. *PANNA 2.0: Efficient neural network interatomic potentials and new architectures*. 2023. arXiv: 2305.11805 [physics.comp-ph].

[156] Ruggero Lot et al. "PANNA: Properties from Artificial Neural Network Architectures." In: *Computer Physics Communications* 256 (2020), p. 107402. ISSN: 0010-4655. DOI: https://doi.org/10.1016/j.cpc.2020.107402. URL: https://www.sciencedirect.com/science/article/pii/S0010465520301843.

[157] Martín Abadi et al. *TensorFlow: Large-Scale Machine Learning on Heterogeneous Systems*. Software available from tensorflow.org. 2015. URL: https://www.tensorflow.org/.

[158] J. S. Smith, O. Isayev, and A. E. Roitberg. "ANI-1: an extensible neural network potential with DFT accuracy at force field computational cost." In: *Chem. Sci.* 8 (4 2017), pp. 3192–3203. DOI: 10.1039/C6SC05720A. URL: http://dx.doi.org/10.1039/C6SC05720A.

[159] Zhenwei Li, James R. Kermode, and Alessandro De Vita. "Molecular Dynamics with On-the-Fly Machine Learning of Quantum-Mechanical Forces." In: *Phys. Rev. Lett.* 114 (9 Mar. 2015), p. 096405. DOI: 10.1103/PhysRevLett.114.096405. URL: https://link.aps.org/doi/10.1103/PhysRevLett.114.096405.

[160] Diederik P. Kingma and Jimmy Ba. *Adam: A Method for Stochastic Optimization*. 2017. arXiv: 1412.6980 [cs.LG].

[161] Paolo Giannozzi et al. "QUANTUM ESPRESSO: a modular and open-source software project for quantum simulations of materials." In: *Journal of Physics: Condensed Matter* 21.39 (Sept. 2009), p. 395502. DOI: 10.1088/0953-8984/21/39/395502. URL: https://doi.org/10.1088/0953-8984/21/39/395502.

[162] P Giannozzi et al. "Advanced capabilities for materials modelling with Quantum ESPRESSO." In: *Journal of Physics: Condensed Matter* 29.46 (Oct. 2017), p. 465901. DOI: 10.1088/1361-648x/aa8f79. URL: https://doi.org/10.1088/1361-648x/aa8f79.

[163] Gianluca Prandini et al. "Precision and efficiency in solid-state pseudopotential calculations." In: *npj Computational Materials* 4.1 (Dec. 2018), p. 72. ISSN: 2057-3960. DOI: 10.1038/s41524-018-0127-2. URL: https://doi.org/10.1038/s41524-018-0127-2.

[164] Kurt Lejaeghere et al. "Reproducibility in density functional theory calculations of solids." In: *Science* 351.6280 (2016), aad3000. DOI: 10.1126/science.aad3000. eprint: https://www.science.org/doi/pdf/10.1126/science.aad3000. URL: https://www.science.org/doi/abs/10.1126/science.aad3000.

[165] D. R. Hamann. "Optimized norm-conserving Vanderbilt pseudopotentials." In: *Phys. Rev. B* 88 (8 Aug. 2013), p. 085117. DOI: 10.1103/PhysRevB.88.085117. URL: https://link.aps.org/doi/10.1103/PhysRevB.88.085117.

[166] Hendrik J. Monkhorst and James D. Pack. "Special points for Brillouin-zone integrations." In: *Phys. Rev. B* 13 (12 June 1976), pp. 5188–5192. DOI: 10.1103/PhysRevB.13.5188. URL: https://link.aps.org/doi/10.1103/PhysRevB.13.5188.

[167] M. Methfessel and A. T. Paxton. "High-precision sampling for Brillouin-zone integration in metals." In: *Phys. Rev. B* 40 (6 Aug. 1989), pp. 3616–3621. DOI: 10.1103/PhysRevB.40.3616. URL: https://link.aps.org/doi/10.1103/PhysRevB.40.3616.

[168] M-C Marinica et al. "Interatomic potentials for modelling radiation defects and dislocations in tungsten." In: *Journal of Physics: Condensed Matter* 25.39 (Sept. 2013), p. 395502. DOI: 10.1088/0953-8984/25/39/395502. URL: https://dx.doi.org/10.1088/0953-8984/25/39/395502.

[169] D R Mason, D Nguyen-Manh, and C S Becquart. "An empirical potential for simulating vacancy clusters in tungsten." In: *Journal of Physics: Condensed Matter* 29.50 (Nov. 2017), p. 505501. DOI: 10.1088/1361-648X/aa9776. URL: https://dx.doi.org/10.1088/1361-648X/aa9776.

[170] Praveenkumar Hiremath et al. "Effects of interatomic potential on fracture behaviour in single- and bicrystalline tungsten." In: *Computational Materials Science* 207 (2022), p. 111283. ISSN: 0927-0256. DOI: https://doi.org/10.1016/j.commatsci.2022.111283. URL: https://www.sciencedirect.com/science/article/pii/S0927025622000805.

[171] N. Juslin et al. "Analytical interatomic potential for modeling nonequilibrium processes in the WCH system." In: *Journal of Applied Physics* 98.12 (Dec. 2005), p. 123520. ISSN: 0021-8979. DOI: 10.1063/1.2149492.

[172] J. Byggmästar, K. Nordlund, and F. Djurabekova. "Simple machine-learned interatomic potentials for complex alloys." In: *Phys. Rev. Mater.* 6 (8 Aug. 2022), p. 083801. DOI: 10.1103/PhysRevMaterials.6.083801.

[173] Ben D. Beake and Saurav Goel. "Incipient plasticity in tungsten during nanoindentation: Dependence on surface roughness, probe radius and crystal orientation." In: *International Journal of Refractory Metals and Hard Materials* 75 (2018), pp. 63–69. ISSN: 0263-4368. DOI: https://doi.org/10.1016/j.ijrmhm.2018.03.020.

[174] Kensuke MIYAHARA, Saburo MATSUOKA, and Nobuo NAGASHIMA. "Nanoindentation Measurement for a Tungsten(001)Single Crystal." In: *JSME International Journal Series A* 41.4 (1998), pp. 562–568. DOI: 10.1299/jsmea.41.562.

[175] E Salonen et al. "Effects of the surface structure and cluster bombardment on the self-sputtering of molybdenum." In: *Journal of Physics: Condensed Matter* 15.34 (Aug. 2003), p. 5845. DOI: 10.1088/0953-8984/15/34/314. URL: https://dx.doi.org/10.1088/0953-8984/15/34/314.

[176] J. Byggmästar, K. Nordlund, and F. Djurabekova. "Gaussian approximation potentials for body-centered-cubic transition metals." In: *Phys. Rev. Mater.* 4 (9 Sept. 2020), p. 093802. DOI: 10.1103/PhysRevMaterials.4.093802. URL: https://link.aps.org/doi/10.1103/PhysRevMaterials.4.093802.

[177] S. Jakob et al. "Influence of crystal orientation and Berkovich tip rotation on the mechanical characterization of grain boundaries in molybdenum." In: *Materials & Design* 182 (2019), p. 107998. ISSN: 0264-1275. DOI: https://doi.org/10.1016/j.matdes.2019.107998.

[178] Flynn Walsh, Mark Asta, and Robert O Ritchie. "Magnetically driven short-range order can explain anomalous measurements in CrCoNi." In: *Proceedings of the National Academy of Sciences* 118.13 (2021), e2020540118.

[179] Jun Ding et al. "Tunable stacking fault energies by tailoring local chemical order in CrCoNi medium-entropy alloys." In: *Proceedings of the National Academy of Sciences* 115.36 (2018), pp. 8919–8924.

[180] C Wolverton, V Ozolins, and Alex Zunger. "Short-range-order types in binary alloys: a reflection of coherent phase stability." In: *Journal of Physics: Condensed Matter* 12.12 (Mar. 2000), p. 2749. DOI: 10.1088/0953-8984/12/12/314. URL: https://dx.doi.org/10.1088/0953-8984/12/12/314.

[181] Xiaofeng Yang et al. "Chemical short-range order strengthening mechanism in CoCrNi medium-entropy alloy under nanoindentation." In: *Scripta Materialia* 209 (2022), p. 114364. ISSN: 1359-6462. DOI: https://doi.org/10.1016/j.scriptamat.2021.114364. URL: https://www.sciencedirect.com/science/article/pii/S1359646221006448.

[182] Wu-Rong Jian et al. "Effects of lattice distortion and chemical short-range order on the mechanisms of deformation in medium entropy alloy CoCrNi." In: *Acta Materialia* 199 (2020), pp. 352–369. ISSN: 1359-6454. DOI: https://doi.org/10.1016/j.actamat.2020.08.044.

[183] Amir H. Naghdi et al. "Dislocation plasticity in equiatomic NiCoCr alloys: Effect of short-range order." In: *Phys. Rev. B* 107 (9 Mar. 2023), p. 094109. DOI: 10.1103/PhysRevB.107.094109. URL: https://link.aps.org/doi/10.1103/PhysRevB.107.094109.

[184] Jae Bok Seol et al. "Mechanically derived short-range order and its impact on the multi-principal-element alloys." In: *Nature Communications* 13.1 (Nov. 2022), p. 6766. ISSN: 2041-1723. DOI: 10.1038/s41467-022-34470-8.

Nanoindentation of tungsten: From interatomic potentials to dislocation plasticity mechanisms

F. J. Domínguez-Gutiérrez,[1] P. Grigorev,[2] A. Naghdi,[1] J. Byggmästar,[3] G. Y. Wei,[3,4] T. D. Swinburne,[2] S. Papanikolaou,[1] and M. J. Alava[1,5]

[1]*NOMATEN Centre of Excellence, National Center for Nuclear Research, 05-400 Swierk/Otwock, Poland*
[2]*Aix-Marseille Universite, CNRS, CINaM UMR 7325, Campus de Luminy, 13288 Marseille, France*
[3]*Department of Physics, University of Helsinki, P.O. Box 43, FI-00014, Finland*
[4]*Henan Academy of Big Data, Zhengzhou University, Zhengzhou 450052, China*
[5]*Department of Applied Physics, Aalto University, P.O. Box 11000, 00076 Aalto, Espoo, Finland*

(Received 25 January 2023; accepted 17 March 2023; published 24 April 2023)

In this study, we employed molecular dynamics simulations, both traditional and machine learned, to emulate spherical nanoindentation experiments of crystalline W matrices at different temperatures and loading rates using different approaches, such as EAM, EAM with Ziegler, Biersack, and Littmark corrections, modified EAM, analytic bond-order approach, and a recently developed machine-learned tabulated Gaussian approximation potential (tabGAP) framework for describing the W-W interaction and plastic deformation mechanisms. Results showed similarities between the recorded load-displacement curves and dislocation densities, for different interatomic potentials and crystal orientations at low and room temperature. However, we observe concrete differences in the early stages of elastic-to-plastic deformation transition, revealing different mechanisms for dislocation nucleation and dynamics during loading, especially at higher temperatures. This is attributed to the particular features of orientation dependence in crystal plasticity mechanisms and, characteristically, the stacking fault and dislocation glide energies information in the interatomic potentials, with tabGAP being the one with the most well-trained results compared to density functional theory calculations and experimental data.

DOI: 10.1103/PhysRevMaterials.7.043603

I. INTRODUCTION

Nanoindentation is a technique used to measure the mechanical properties of a potential candidate material at the nanoscale for applications at extreme operating conditions. It entails using a small, sharp tip into the sample surface to measure the force required to do so and the resulting displacement into the material [1–4]. A pop-in event that defines the elastic to plastic deformation transition is produced as the indenter tip starts to penetrate the surface; it is often used as a reference point for analyzing the mechanical behavior of a material, as it can provide insight into the internal structure of the sample, which gives the opportunity to explore the mechanisms of plastic deformation initiation responsible for modification of mechanical properties of the material [5]. In addition, nanoindentation-induced plastic patterning is a process that involves the creation of patterns or structures in a material at the nanoscale with a wide range of applications, including the fabrication of nanostructured surfaces with enhanced functionalities and the development of new materials with tailored mechanical properties [6]. Plastic patterning due to nanoindentation is highly affected by the applied load, surface orientation, temperature, and the properties of the material itself, which needs a fundamental understanding of the materials deformation at the plastic zone beneath the indented surface region [2].

Tungsten is a refractory BCC material that can mechanically sustain extreme operating conditions due to its high melting point, low sputtering yield, and low tritium inventory [7–11]. W is often used in the production of high-strength steel alloys, as well as in the manufacturing of tungsten carbide, which is a very hard and durable material used in cutting tools and wear-resistant products, besides being the main candidate to design a plasma facing component (PFM) for the next generation of fusion reactors [12–15] experiencing a harsh environment due to the hydrogen/deuterium ions irradiation from the fusion plasma that causes indentation size effects at a scale of 100 nm. Moreover, ISO:14577 provides guidelines for the use of spherical indentation techniques and defines W to have a high elastic modulus which makes it a reference material for indirectly calibrating nanomechanical test instruments [16]. Therefore, it is necessary to study the relationship between indentation load-displacement curves and the evolution of the surface plastic patterning formation in order to better understand the plastic deformation mechanism of W matrices and its alloys. Atomistic simulations based on molecular dynamics (MD) can provide information about plastic deformation mechanisms, although there are limitations in some cases. These simulations are now capable of saving financial and technological resources [1–3,16–22].

The goal of our work is to explore the advantages and limitations of several EAM-based interatomic potentials reported in the literature for describing plastic deformation of tungsten at the early stages of the nanoindentation test, where experimental observation is currently inaccessible. Our objective is to investigate the role of the most used interatomic potentials in nanoindentation test modeling, where the mechanisms of dislocation nucleation and evolution are modeled differently. Despite similarities in the stress-strain curves and dislocation densities that are commonly utilized to characterize the

mechanical properties of a material, this work aims to provide an atomistic insight into the nanoindentation-induced plasticity of crystalline tungsten matrices using different approaches to model defect nucleation, as well as dislocation loop formation. Finally, we present an analysis of screw and junction dislocations using a nudged elastic band method (NEB) to clarify the differences in dislocation dynamics and surface plastic patterning in the MD simulation due to the chosen interatomic potential.

II. COMPUTATIONAL METHODS

In general, the EAM approach is used as a first attempt to computationally model the physical processes of the nanomechanical response of crystalline metals under external load. In this approach, the energy of the ith atom is defined as

$$E_i = \frac{1}{2}\sum_{j\in\mathcal{N}_i} V(r_{ij}) + F[\rho_i]. \tag{1}$$

Here $\mathcal{N}_i$ represents the atoms within the cutoff range, $V(r)$ is a pairwise potential, repulsive at short range, and $F[\cdot]$ is the embedding function for an atom in a region of electron density, given by $\rho_i = \sum_{j\neq i}\phi(r_{ij})$.

According to the OpenKIM project [23], there are more than 15 interatomic potentials for tungsten based on EAM. The one developed by Marinica *et al.* [24] (referred to as EAM2 by the authors in this work and labeled as **EAM**) has been reported to provide relatively good approximations to experimental values such as lattice constant measurements, cohesive energies of tungsten in the BCC phase, and elastic constants. This EAM potential has been evaluated by comparing it with DFT results for surface energy, dislocation core energy, and Peierls energy barrier calculations. The results show that, in general, this potential is a good choice for dislocation-involved simulations of tungsten, being commonly used to investigate dislocation nucleation in tungsten [25]. In addition, this potential has been used to develop potentials for tungsten with other metals, hydrogen, and carbides. For example, Wang *et al.* [26] used **EAM** potentials to develop W-H potentials.

The defect nucleation during nanoindentation load is important to model due to the inclusion of open boundaries in the MD simulations. Thus we consider an EAM potential developed by Mason *et al.* [27] that introduces smoothly varying, physically motivated modifications to the Ackland-Thetford potential [28] and adding $V_{\mathrm{ZBL}}(r)$ the Ziegler, Biersack, and Littmark (ZBL) universal screening potential contribution to improve vacancy- and surface-related properties. This potential, labeled as **EAM/ZBL**, was parametrized to improve the description of vacancy-type defects formation at different temperatures with vast surface properties aiming to model surface plastic patterning in a better way than EAM.

The correct description of the interaction of W-W and the intrinsic BCC crystal geometry of W is needed during the nanoindentation-induced dislocation nucleation. Thus we include in our work simulations with the modified-EAM that consider angular dependent interactions, which enter via the electron density term. These potentials were developed by Hiremath *et al.* [29] (labeled as **MEAM**) to investigate mechanisms of fracture in W samples providing an atomic insight, which also yields surface and unstable twinning energies that are in slightly better agreement with DFT than EAM results. This can help to describe the formation of twins during early stages of nanoindenation load simulations. Here, the total potential energy of the system is given as

$$E = \sum_i F_i(\overline{\rho}_i) + \sum_i \sum_{j\neq i} S_{ij}\phi_{ij}(r_{ij}), \tag{2}$$

where $F_i(\overline{\rho}_i)$ represents the embedding energy associated with placing the i atom into the background electron density $\overline{\rho}_i$. The function $\phi_{ij}(r_{ij})$ is defined as the pair interaction contribution between i and j atoms, separated by the distance r_{ij}, while S_{ij} is a screening function. The fitting process was done by using the open-source M-EAM parameter calibration (MPC) tool [30] to reproduce DFT data that serves as input data.

Another attempt to describe the W-W interaction in a material is the analytic bond-order potential (labeled as **ABOP** in this paper), which is a type of interatomic potential based on the concept of bond order measuring the strength of the chemical bond between atoms. It is constructed by fitting the potential energy of a system to a functional form that depends on the bond orders between atoms. In an analytic bond-order potential for W developed by Juslin *et al.* [31], the total energy is expressed as a sum over individual bond energies:

$$E = \sum_{i>j} V_{ij}^{\mathrm{R}}(r_{ij}) + b_{ij}V_{ij}^{\mathrm{A}}(r_{ij}), \tag{3}$$

where the pairlike repulsive, V^{R}, and attractive, V^{A}, terms are defined by Morse-type pair potentials and the bond-order parameter b_{ij} contains information of three-body contributions and angularity [32]. ABOP has several advantages over other EAM-based interatomic potentials capturing the effects of changes in bond order on the behavior of materials. Moreover, this bond-order potential includes second-neighbor interactions for pure tungsten samples and accurately captures the contributions of metallic W-W bonds. As discussed by the authors, the W potential provides a good description of the coordination dependence of structural parameters, cohesive energies, and surface properties, which are all important for nanoindentation modeling.

Nanoindentation simulations require detailed information of the material's surface due to open boundaries involved in the modeling. For this reason, we include the tabulated Gaussian approximation potential (**tabGAP**) in this work, which is a GAP machine-learning potential with enough surface information in the training data set being developed by Byggmästar *et al.* [33]. It has been trained with only simple low-dimensional descriptors (two-body, three-body, and an EAM-like density). The low dimensionality of the descriptors allows for creating faster tabulated versions, where the machine-learning energy contributions are mapped onto grids [34–36]. The total energy is then evaluated efficiently using

TABLE I. Value of elastic constants, shear modulus G, Poisson ratio ν, elastic modulus E (GPa), cohesive energy E_{coh} (eV/atom), and Burgers vector magnitude $|\vec{b}| = a_0\sqrt{3}/2$ (a_0 is the lattice constant) of tungsten. The last column is experimental values of C_{ij} [40] and G, ν, and E values [41].

Variable	EAM	EAM/ZBL	MEAM	ABOP	tabGAP	Expt.
C_{11}	523	511	527	541	524	501
C_{12}	203	201	194	191	200	198
C_{44}	160	161	177	162	148	151
G	160	161	177	162	135	130–160
ν	0.28	0.27	0.27	0.26	0.28	0.27–0.29
E	409	431	423	442	449	340–405
E_{coh}	−8.899	−8.9	−8.65	−8.89	−8.39	−8.9
$\|b\|$	2.72	2.75	2.74	2.74	2.75	2.74

cubic splines as

$$E_{\text{tot}} = \sum_{i<j}^{N} S_{ij}^{1\text{D}}(r_{ij}) + \sum_{i,j<k}^{N} S_{ijk}^{3\text{D}}(r_{ij}, r_{ik}, \cos\theta_{ijk}) + \sum_{i}^{N} S_{\text{emb}}^{1\text{D}}\left(\sum_{j}^{N} S_{\varphi}^{1\text{D}}(r_{ij})\right). \quad (4)$$

Here, $S_{ij}^{1\text{D}}(r_{ij})$ represents a one-dimensional cubic spline for the two-body contribution, $S_{ijk}^{3\text{D}}$ is the three-dimensional spline for the three-body contribution, and the final term is the embedding energy contribution similar to the EAM potentials. Despite the simplicity compared to other machine-learning potentials, the tabGAP achieves meV/atom accuracy for tungsten-based high-entropy alloys and compares well with DFT for various elastic, defect, and melting properties [33,36] that can be applied to model defect production at high temperatures [37].

To perform our simulations, we use the large-scale atomic/molecular massively parallel simulator (LAMMPS) software [38], which allows us to study the behavior of materials under a wide range of conditions. One of our goals is to accurately model plastic deformation, which is a crucial aspect of how materials respond to external loads. Thus we start by calculating the elastic constants C_{ij} and other properties of tungsten using different interatomic potentials that are presented in Table I noticing similar results in most respects and a good agreement with DFT calculations with $C_{11} = 520.35$ GPa, $C_{12} = 199.88$ GPa, and $C_{44} = 142.42$ GPa [39]. This information will help us understand how the interatomic potentials affect the mechanical behavior of the material and how they can be used to predict the response of tungsten to external loads. By studying these properties in detail, we hope to gain a deeper understanding of the underlying mechanisms of plasticity in tungsten.

Nanoindentation modeling

We first defined the initial W sample based on its crystal orientation, as shown in Table II. The FIRE (fast inertial relaxation engine) 2.0 protocol [42] is then used to optimize the energy of the sample and find the lowest energy structure.

TABLE II. Size of the numerical samples used to perform MD simulations. Sample size (d_x, d_y, d_z) in units of nm.

Orientation	[001]	[011]	[111]
d_x	37.92	34.76	33.52
d_y	41.08	37.99	33.52
d_z	31.60	36.65	46.52
Atoms	3 120 000	3 066 800	3 442 500
x axis	(100)	(100)	$(\bar{1}01)$
y axis	(010)	$(01\bar{1})$	$(1\bar{2}1)$
z axis	(001)	(011)	(111)

After that, we conducted an equilibration process for 100 ps using a Langevin thermostat at 77 and 300 K with a time constant of 100 fs [21]. This process continued until the system reached a homogeneous temperature and pressure profile with a density of 19.35 g/cm^3, which is in good agreement with the experimental value of 19.35 g/cm^3 [41]. In the first stage, the W samples are divided into three sections in the z direction to set up boundary conditions along its depth, d_z: (1) a frozen section with a width of approximately $0.02 \times d_z$, which was used for stability of the numerical cell, (2) a thermostatic section at approximately $0.08 \times d_z$ above the frozen section, which was used to dissipate the heat generated during nanoindentation, and (3) a dynamical atoms section, where the interaction with the indenter tip modifies the surface structure of the samples. In addition, a 5 nm vacuum section was included at the top of the sample as an open boundary [3].

The indenter tip is considered as a nonatomic repulsive imaginary (RI) rigid sphere with a force potential defined as $F(t) = K[\vec{r}(t) - R]^2$, where $K = 236$ eV/Å^3 (37.8 GPa) is the force constant and $\vec{r}(t)$ is the position of the center of the tip as a function of time, with radius $R = 6$ nm. We apply MD simulations using an NVE statistical thermodynamic ensemble and the velocity Verlet algorithm to emulate an experimental nanoindentation test. Periodic boundary conditions are set on the x and y axes to simulate an infinite surface, while the z orientation contains a fixed bottom boundary and a free top boundary in all MD simulations [21]. Here, $\vec{r}(t) = x_0\hat{x} + y_0\hat{y} + (z_0 \pm vt)\hat{z}$, with x_0 and y_0 as the center of the surface sample on the xy plane. The initial gap between the surface and the indenter tip, $z_0 = 0.5$ nm, moves with a speed of $v = 20$ m/s. The center of the indenter tip was randomly changed to 10 different positions to consider statistics in our results, resulting in a total of 150 MD simulations. Each process is performed for 125 ps with a time step of $\Delta t = 1$ fs. The maximum indentation depth is chosen to be 3.0 nm to avoid the influence of boundary layers in the dynamical atoms region. The load-displacement curve is then obtained by plotting the force on the indenter tip as a function of its displacement relative to the surface, as the indenter is driven into the material over time.

III. RESULTS

Figure 1 shows the recorded average load-displacement curves for nanoindentation loading of (001) W using the tabGAP framework at 77 and 300 K. Our results are in good

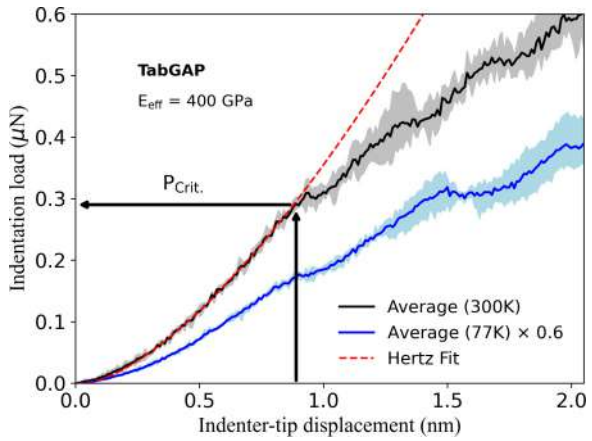

FIG. 1. Average nanoindentation load as a function of the displacement at 77 and 300 K as determined by the tabGAP framework. The color region represents the range of minimum and maximum load obtained from all MD simulations. Temperature has a significant impact on the plastic deformation mechanisms modeled by different approaches, as indicated by the Hertz fit curve that defines the critical load, P_{crit}. The results at 77 K are scaled by a factor of 0.6 for visualization.

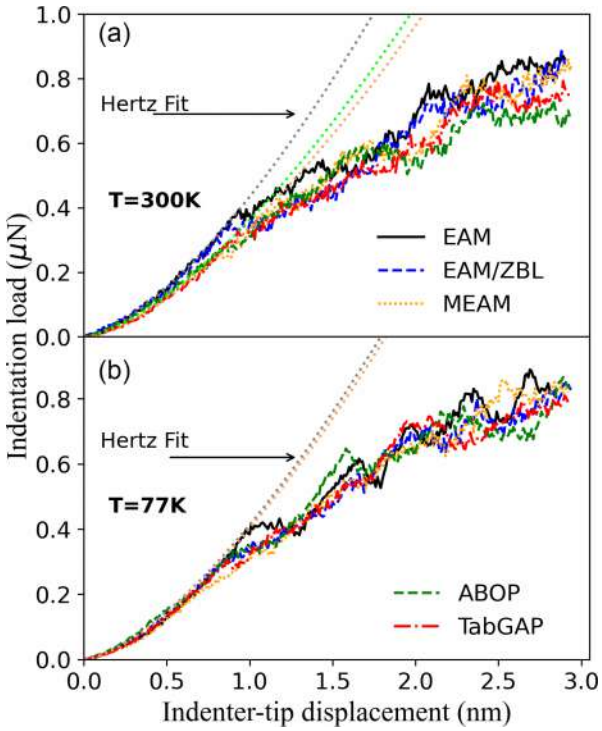

FIG. 2. Average load displacement curves from nanoindentation test by using different approaches at sample temperature of 300 in (a) and 77 K in (b). Hertz fitting curve is added to show the pop-in event. Temperature effects on surface morphology are shown by the elastic part where the surface information is required in the interatomic potentials.

qualitative agreement with the experimental data reported by Beake *et al.* [16,17]. These findings demonstrate the potential of the tabGAP framework in accurately reproducing results in the field of nanoindentation research. The average load is computed as $P_{\rm av} = 1/N \sum_i^N P_i$ with P_i as the load obtained from each MD simulation with random positions for the center of the indenter tip on the W surface. In our results, we include the maximum and minimum load as a function of indentation displacement from all MD simulations, represented by a colored region to show the statistical analysis in our work. The elastic nanocontact during loading process is characterized by a Hertz fitting curve based on the sphere-flat surface contact and expressed as

$$P_{\rm H} = \tfrac{4}{3} E_{\rm eff} R^{1/2} h^{3/2}, \tag{5}$$

where R is the indenter radius, h is the indenter displacement, and $E_{\rm eff}$ is the effective elastic modulus, where the tabGAP result of 400 GPa agrees well with experimental data [16]. The elastic to plastic deformation transition can be identified during the loading process by the pop-in event with a critical load, $P_{\rm crit}$, which is well modeled by all the approaches and can be correlated to experimental results to study stress distributions under the tip. As shown in Fig. 1, the elastic part of the loading process is sensitive to the surface morphology and sample temperature. Results at 300 K show considerable fluctuations around the pop-in point, while these fluctuations disappear when the temperature decreases to 77 K, resulting in more stable data.

In Fig. 2, we report results for the average load of [001] W as a function of the indenter displacement by using different interatomic potentials.

As the indenter tip makes contact with the surface, the force on the indenter increases until the material begins to deform plastically. All approaches report a similar value for the indentation displacement point at 0.9 ± 0.1 showing the elastic to plastic transition, while the critical pop-in load is maximum for EAM and minimum for MEAM, noting the importance of surface information in the approach due to contact responses of the W matrix, regardless of the surface temperature. The effective Young's modulus at 300 K is 420 GPa for EAM and EAM/ZBL, 400 GPa for ABOP and tabGAP, and 355 GPa for MEAM, which is in the experimental range of 350–405 GPa [41]. At 77 K temperature, all the MD simulations resulted in an elastic modulus of 395 ± 5 GPa. This can be attributed to the interaction between the nonatomic RI sphere of the indenter tip, which has a hard sphere, and the W atoms in the top layers of the material, which exhibit only small thermal vibrations. As a result, the elastic behavior modeled by all the methods is similar.

Temperature effects are observed during the elastic part where the interatomic potentials are required to have surface information like surface energy due to the open boundary and plastic deformation initiation by the penetration of the indenter tip in the material. The effect of the crystal orientation is presented in the Supplemental Material (SM) [43], where a sequence is found by every approach used following the characteristic maximum pop-in load for [001] orientation and the minimum one for [111] orientation for BCC metals [2,21,44].

Figure 3 reports the mean contact pressure p, of [001] W to Young's modulus $E_{\rm klm}$, ratio calculated as a linear elastic

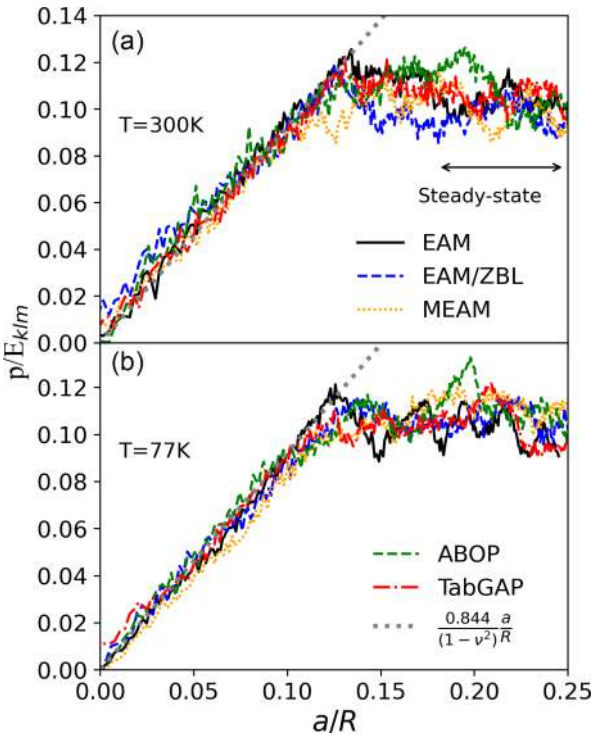

FIG. 3. Evolution of average contact pressure, p, normalized to Young's modulus with normalized contact radius for (011) W by using different approaches at 300 K in (a) and 77 K in (b). Results follow the universal linear relationship as [20] $0.844/(1-\nu^2)a/R_i$, regardless of the employed interatomic potential.

contact mechanics formulation [5,20]:

$$\frac{p}{E_{\rm klm}} = \frac{2\pi}{3E_{\rm klm}}\left[24P\left(\frac{E_{\rm klm}R}{1-\nu^2}\right)^2\right]^{1/3} \tag{6}$$

as a function of the normalized contact radius, a/R, between the sample and the tip with the geometrical relationship $a(h) = [3PR(1-\nu^2)/8E_{\rm klm}]^{1/3}$, which is related to the inner radius of the plastic region where the defects nucleate. The results seem to follow the universal linear relationship as [20] $0.844/(1-\nu^2)a/R_i$, with R_i as the indenter radius for all the approaches with tabGAP results reaching the best agreement, which indicates that the atomic ensembles fulfill coarse-grained, linear elastic contact mechanics and boundary conditions do not affect the simulation dynamics. As observed in Fig. 3, the recorded load curves can be affected by both the spatial arrangement of the surface atoms and the thermally induced atomic vibrations [2]. Thus temperature effects are observed in the elastic part by fluctuations of the mean contact as a response of the interaction of the indenter tip with the W atom at the top layer of the surface sample. Due to the size of the indenter tip, the transitional regime is defined between 0.12 and 0.15 a/R, while the steady state of the loading process is reached at bigger values at both temperatures. The value $p/E_{001} = 0.09 \pm 0.012$ at the steady state is similar to the one reported for (001) Ta and other BCC metals by Varilla *et al.* [20], showing a good agreement between the approaches for calculations of material's hardness.

It is well established that plastic deformation in a material does not initiate at the surface, but rather at some atomic layers' depth below it. This depth is known as the yield point or yield depth at which the material begins to nucleate defects and further dislocations under the applied load or stress [5], within the closest plastic region along the vertical z axis underneath the spherical indenter tip expressed as

$$\sigma_{zz} = -\left(\frac{3F}{2\pi\,\mathrm{a}(h)^2}\right)\left[\left(1-\left|\frac{z}{\mathrm{a}(h)}\right|\arctan\left|\frac{\mathrm{a}(h)}{z}\right|\right)(1+\nu) - \frac{1}{2[1+z^2/\mathrm{a}(h)^2]}\right] \tag{7}$$

as an attempt to determine the strength and stability of the W matrix under load. The stress applied in the direction parallel to the indenter surface is then expressed as

$$\sigma_{xx} = \sigma_{yy} = -\left(\frac{3F}{2\pi\,\mathrm{a}(h)^2}\right)\frac{1}{1+z^2/\mathrm{a}(h)^2}, \tag{8}$$

where x, y, and z are the coordinates in the Cartesian system, ν is the Poisson's ratio, and F is the nanoindentation load. This defines the maximum shear stress as $\tau_{\rm Max} = (\sigma_{zz} - \sigma_{xx})/2$ that the material can withstand before it begins to undergo plastic deformation as reported in Fig. 4, being normalized by the applied pressure (equal to the force F divided by the contact area). The normalized depth is the distance from the surface of the material to the point at which the

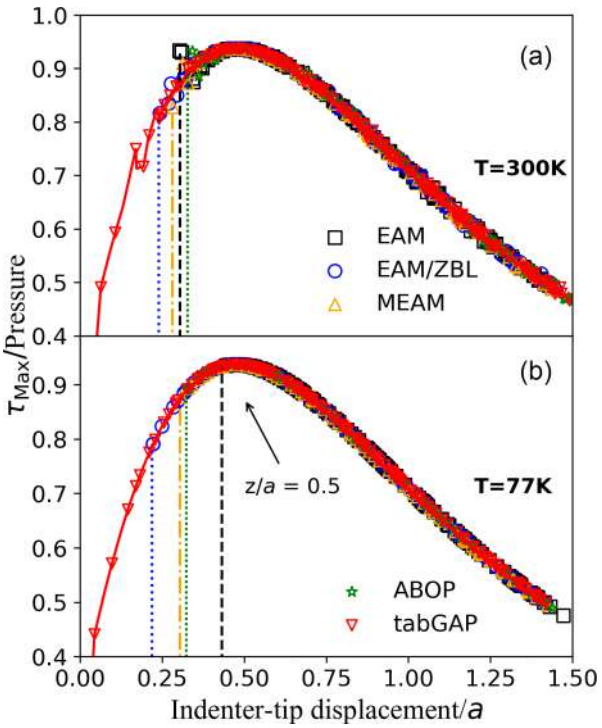

FIG. 4. Hertzian calculation of normalized maximum shear stress by the applied pressure, $\tau_{\rm Max}/P$, as a function of normalized depth at a temperature of 300 K in (a) and 77 K in (b). Surface information is needed in the interatomic potentials to model nanoindentation as observed in the range of 0.2 to 0.49 z/a. The vertical lines indicate the points where $\tau_{\rm Max}$ is not zero, which provides valuable surface information as demonstrated by the tabGAP simulations.

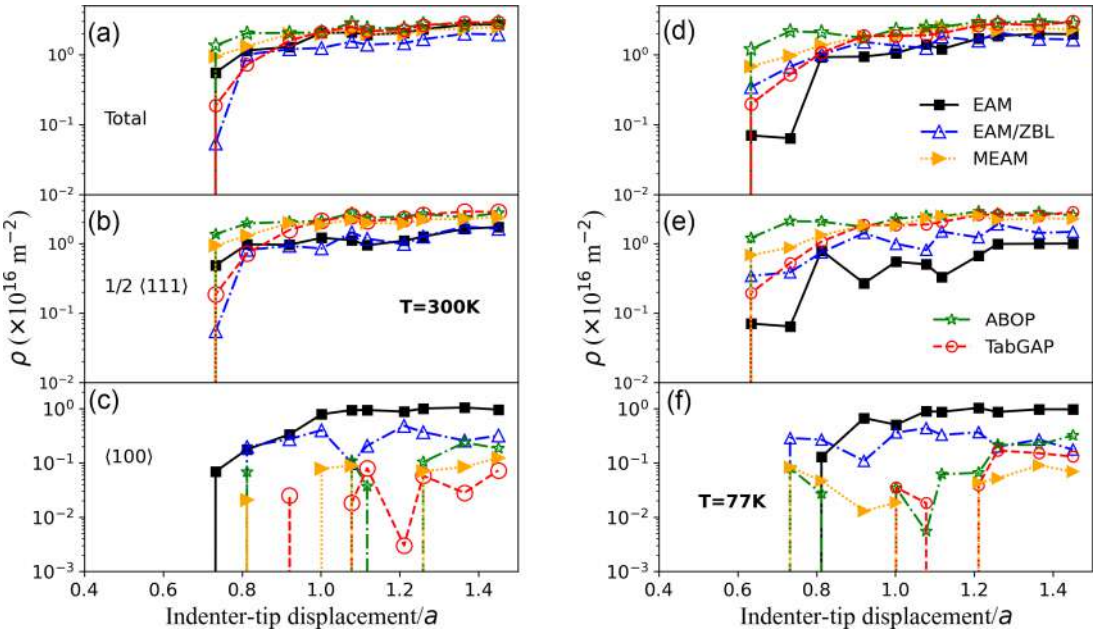

FIG. 5. Average total, $1/2\langle 111\rangle$, and $\langle 100\rangle$ type dislocation density as a function of the normalized indentation depth during loading process at a temperature of 300 K in (a)–(c) and 77 K in (d)–(f), showing the differences of the description of W-W interaction by the MD potentials.

maximum shear stress occurs, normalized by the radius of the indenter that is used to apply the shear forces. Our MD results showed that the point at which plastic deformation begins is at a normalized depth of $z/a = 0.5$ for both temperatures considered. We also observed that the choice of interatomic potential can have an impact on the modeling of the contact between the indenter tip and the surface of the material. Specifically, our findings indicate that the tabGAP method offers a more precise depiction of the interaction between the indenter tip and the surface, exhibiting a smooth increase of the shear stress within the range of 0–0.2 z/a. In contrast, other methods are not able to capture this information.

A. Dislocation nucleation

In general, dislocation glide occurs in the closest-packed $\langle 111\rangle$ directions for BCC metals with Burgers vector $b = 1/2\langle 111\rangle$ and slip planes belong to the $\{110\}$ and $\{112\}$. To analyze the atomic structure during the nanoindentation test which provides information about the mechanisms of dislocation nucleation and evolution [45], we use OVITO [46] with the DXA package [47] to identify dislocations into several dislocation types according to their Burgers vectors as $1/2\langle 111\rangle$, $\langle 100\rangle$, and $\langle 110\rangle$ dislocation types with their corresponding dislocation density, ρ, defined as

$$\rho = \frac{l_{\mathrm{klm}}}{V_D}, \tag{9}$$

where l_{klm} is the dislocation length of each type, by using a hemispherical radius of the plastic zone of $r_{\mathrm{pz}} = a_{\mathrm{pz}}[r^2 - (r-h)^2]^{1/2}$ with $a_{\mathrm{pz}} = 1.9$ and the total volume equal to the hemispherical volume excluding the volume displaced by the indenter tip as $V_D = (2\pi r_{\mathrm{pz}}^3/3) - [\pi h^2(r-h)/3]$, with r as the indenter radius and h the indentation depth, excluding pileup or sink in effects in this model [48].

Figure 5 shows dislocation densities as a function of normalized indentation depth for 300 and 77 K of (001) W samples. Oscillations are observed in the loading process for the densities of both $\langle 111\rangle$ and total dislocations at both temperatures, with minima occurring at 0.9 and 1.1 z/a points, where prismatic loops were observed to nucleate. It is worth noting that the different potentials we used yielded different results for the nucleation and evolution of dislocation junctions at the $\langle 100\rangle$ plane, where a good representation of dislocation glide is important. This mechanism is poorly represented by the EAM and EAM/ZBL methods. We also observed that the formation of this type of defect is common under the indenter tip, where the interaction or dissociation of $1/2\langle 111\rangle$ dislocations can lead to the nucleation of dislocation junctions as $1/2\langle 111\rangle + 1/2\langle \bar{1}\bar{1}1\rangle = \langle 001\rangle$ and other symmetrically geometrical combinations. We observed temperature effects at the point where dislocations begin to nucleate; this difference is likely due to the increased thermal motion of the atoms in the top layer at the higher temperature, which affects the dislocations' mechanisms to nucleate and propagate through the material. In the SM, we report results for the (011) and (111) W matrices with results for those of (001) W.

We visualize the dislocation network nucleated at a depth of $z = 0.9a$ in Fig. 6, where initial half loops are noted, and $z = 1.22a$ in Fig, 7, where prismatic loops evolve through the sample at 77 and 300 K sample temperature. For BCC materials with a (001) orientation, it is well known that the nucleation of prismatic loops is initiated by the formation of shear loops after the yield point [5,20], which then propagate along the expected $\langle 111\rangle$ slip directions. This mechanism was observed in our MD simulations using MEAM, ABOP, and particularly tabGAP [Figs. 6(c) and 6(d)]. Temperature effects on this mechanism are associated with the faster propagation of shear loops at lower temperatures; this is due to the more

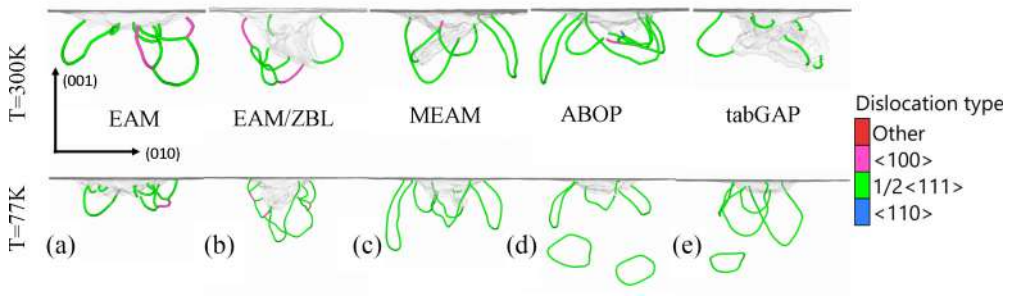

FIG. 6. Visualization of the dislocation nucleation and evolution at depth $z = 0.9a$.

stable lattice positions of the W atoms during the loading process, which leads to the more efficient nucleation of prismatic loops [see Figs. 7(c) and 7(d)]. As the indenter tip goes deeper into the sample, the shear loops expand through the advancement of edge dislocations, while the screw dislocations can undergo limited cross slip, as seen in the simulations using MEAM, ABOP, and tabGAP. This cross slip of the screw dislocations eventually leads to a pinch-off action, resulting in the formation of prismatic loops. It is worth noting that the edge dislocations cannot undergo cross slip. As plastic deformation proceeds during the loading process, the formed prismatic loop advances and the process of shear loop formation and cross slip repeats itself underneath the indenter tip. We noticed that, among the different potentials we used, tabGAP simulations provided the most accurate modeling of this mechanism, showing good qualitative agreement with the results that are expected to be observed in experiments [16,17].

It is well known that dislocation glide in BCC metals is mainly governed by the Peierls barrier, which measures the stress that needs to be applied in order to move a dislocation core to the next atomic valley in the glide plane. Moreover, the Peierls barrier is smaller for edge dislocations than for screw dislocations, where the BCC metal plasticity is dominated by the sluggish glide of screw dislocation segments, as shown by our MD simulations [49,50]. Thus the "lasso" mechanism is observed by all methods for (111) W, suggesting that the main dislocation nucleation mechanism remains analogous to other BCC metals [20,21], with a difference on the number loops nucleated by each approach. In Table III we present the number of prismatic loops nucleated at the maximum indentation depth, quantified for all the potentials we tested at different temperatures. We noticed that ABOP and tabGAP are capable to model the nucleation of dislocation loops on the expected ⟨111⟩ and ⟨112⟩ slip directions. The visualization of the dislocation dynamics during the nanoindentation test for both the (011) and (111) orientations can be found in the Supplemental Material [43].

B. Nanoindentation-induced plastic patterning

The formation of slip traces at the surface is an important aspect of the crystal plasticity process that occurs during a nanoindentation test, as these traces provide evidence of the underlying dislocation glide processes occurring in the subsurface. As shown in Fig. 8, the four ⟨111⟩ slip directions that occur at 300 K temperature lead to the formation of surface pileups with fourfold symmetry. This figure provides a visualization of this process at the maximum indentation depth by using different approaches. The figure includes a color palette that indicates the magnitude of the displacement, revealing that the pileups form around the indenter mark in the shape of a fourfolded rosette due to the (001) orientation of the W matrix, as expected for BCC metals on a (001) orientation. This has been reported experimentally for tungsten by Argus images reported by Yu *et al.* [51], where the surface morphology shows fourfold slip traces on the $(1\bar{1}0)$ and (110) planes. Moreover, large-scale MD simulations for α-Fe [2] have also demonstrated similar pileups resulting from the slip directions.

In Fig. 9, we present the results of von Mises strain atomic mapping at the maximum indentation depth, as obtained from OVITO and reported in our previous work [21]. The sample

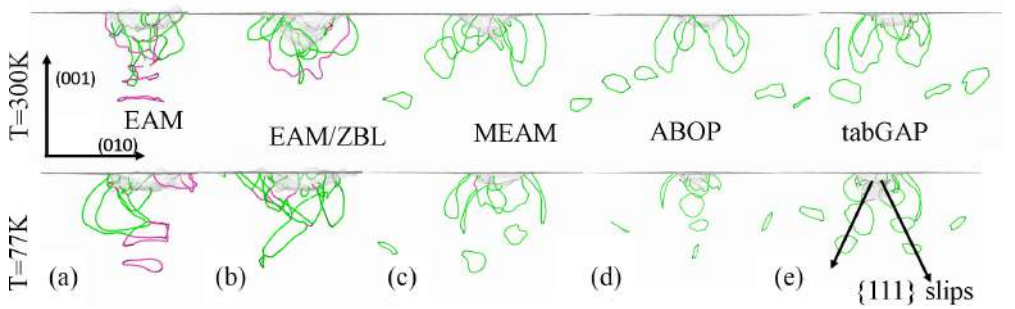

FIG. 7. Visualization of the dislocation nucleation and evolution at depth $z = 1.22a$, using all approaches. Shear dislocation loops are nucleated at the maximum indentation depth in the case of all potentials.

TABLE III. Average number of dislocation loops nucleated at the maximum indentation depth for W by different potentials. Results for temperatures of 300 K and 77 K.

	(001)		(011)		(111)	
Potentials	300 K	77 K	300 K	77 K	300 K	77 K
EAM	1	2	3	4	1	2
EAM/ZBL			2	3	1	2
MEAM	3	4	6	9	4	5
ABOP	4	6	5	6	6	7
tabGAP	4	6	5	7	6	8

was slid on the (011) plane, revealing that the maximum strain follows the ⟨111⟩ slip directions, due to the BCC crystal geometry of the W samples. This highlights the importance of accurate modeling for simulations involving open boundaries. From our MD simulations, the formation of indentation plastic imprints is a process associated to the onset of plastic bursts during mechanical loading that is modeled in a similar manner by tabGAP, ABOP, and the modified EAM potential, where our results are in good agreement with experimental electron microscopy images [17,19,51]. Results for both (011) and (111) orientations can be found in the Supplemental Material [43]. In addition, the dynamics of twin nucleation and twin annihilation during the loading process is a key aspect of the plastic deformation of the W material that needs to be observed in the experimental nanoindentation test. Twin nucleation refers to the process by which a twinned region forms within the W lattice, while twin annihilation refers to the process by which twinned regions transform into dislocations or a dislocation network beneath the indenter tip, as reported experimentally by Wang *et al.* [52] in compression experiments. These processes are generally influenced by the surface energy of the sample, which is a measure of the energy required to create or modify the surface of the material by external load. In our simulations, we utilized the BDA method [53] to identify material defects as twin planes {112} as described in the Appendix A. Although some W atoms were identified as twins in all the simulations, consistent with the literature [44], they can be likely misidentified as screw dislocations. Only in the tabGAP simulations were several W atoms observed in the near vicinity of the indenter tip, which exhibited twin-like defects upon structural analysis and visual examination [see Fig. 8(f)].

There are several machine-learning-based interatomic potentials for W reported in the literature, such as GAP [54] and spectral neighbor analysis potential (SNAP) [55]. However, nanoindentation simulations require simulation cells with

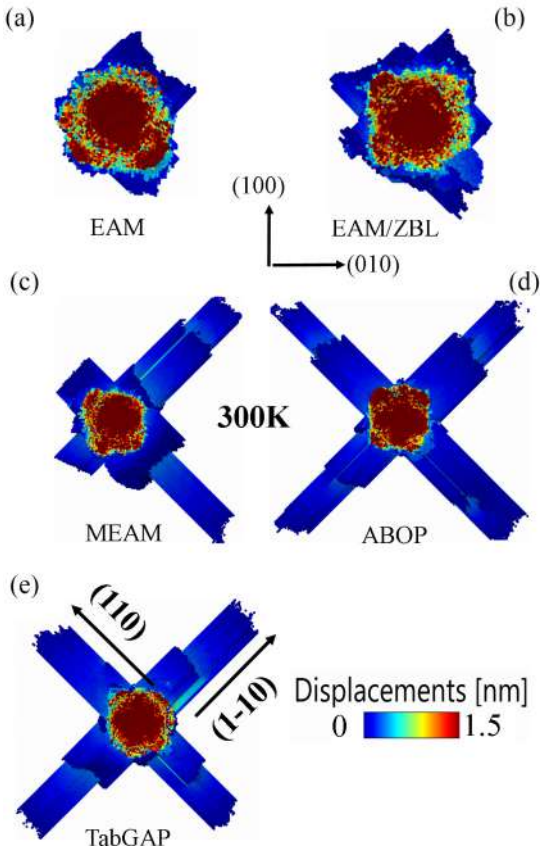

FIG. 8. Visualization of the formation of pileups and slip traces for the indented [001] W sample at the maximum depth (3 nm). The surface morphology for ABOP and tabGAP show fourfold slip traces on the $(1\bar{1}0)$ and (110) planes in good agreement with experimental findings [51].

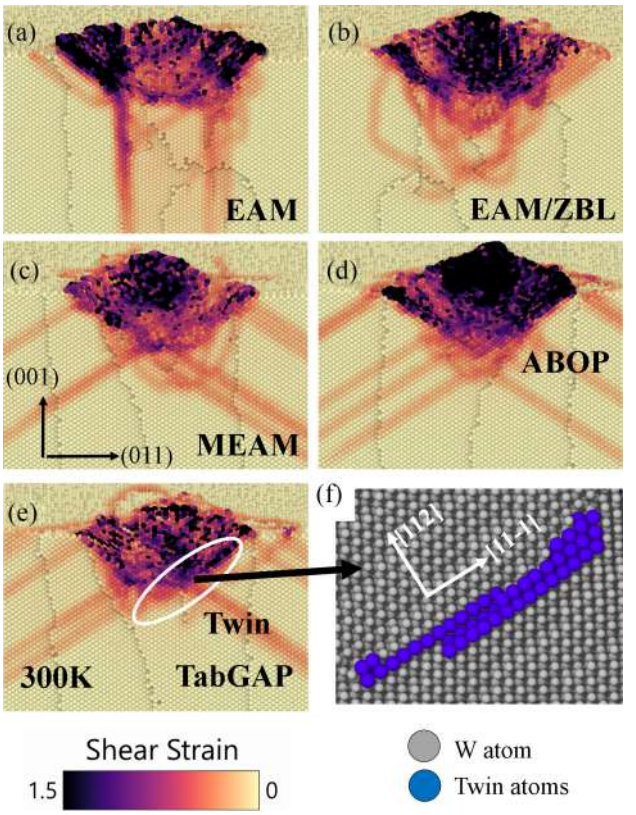

FIG. 9. Visualization of the von Mises strain mapping for the indented [001] W sample at the maximum depth, at room temperature. The W matrix is slid on the (011) plane for better visualization. BCC {112} twin boundaries are identified in our simulations as depicted in (f) by BDA method and are marked by white circles for the tabGAP simulations.

millions of atoms and open boundaries. A single MD simulation using GAP and SNAP potentials would require a wall time of 10–20 days with high computational resource demands, as we tested for our simulation cells. In our work, we are focused on modeling nanoindentation with interatomic potentials that offer the possibility of a good description of the plastic deformation of W matrices with modest computer resources and wall times on the scale of hours. Therefore, we used a Linux cluster with 120 Intel(R) Xeon(R) CPU E5-2680 v2 processors at 2.80 GHz, with wall time of 82 min for the EAM potential, 63 min for the EAM/ZBL potential, 780 min for the MEAM potential, 960 min for the ABOP potential, and 1658 min for the tabGAP potential that seems to model several defect nucleation and evolution mechanisms.

C. Nanoindentation load rate

We have shown that tabGAP simulations provide a reliable description of the mechanism of plastic deformation of W during the loading process. Thus we decided to decrease the load rate to 10 m/s and 5 m/s to give W samples more time to dissipate the energy and yield more ductile behavior. This will give us the opportunity to better understand the nanocontact between the indenter tip and the surface and, consequently, the initiation of plastic deformation, which is of importance in experiments [56]. In Fig. 10, we present the results of the evolution of the average contact pressure, p, normalized to the Young's modulus, at different load rates. Sample temperature is 300 K in (a) and 77 K in (b). It is observed that when indentation goes beyond linear elasticity, the W matrix responds with sudden, first pop-in events characterized by different magnitudes of the load drop, Δp. The load drops mark the early inception of defects and are more pronounced as the load rate decreases, regardless of the sample temperature. We argue that the ratio of the contact pressure, p_c, defined as the point where the drop is identified, to the Young's modulus, E_{klm}, can be used as an intrinsic measure of the surface resistance to dislocation nucleation mechanisms.

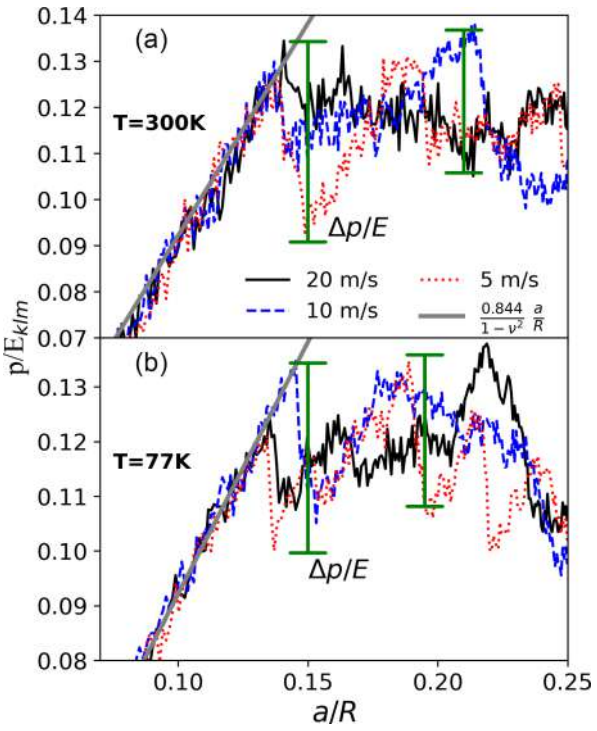

FIG. 10. Evolution of p/E with normalized contact radius at room temperature (a) and 77 K (b) showing the effect of load rate on the nanomechanical response of (001) W. The critical normalized pressure is identified as a deviation from the Hertz fitting and is marked in the figures. This deviation triggers early defect nucleation and is accompanied by the first hardness drop, $\Delta p/E$, and a subsequent second one.

Furthermore, the contact pressure results obtained from our study can be compared qualitatively with the compression experimental stress-strain curves reported by Wang *et al.* [52] (see Fig. 3 in the main text and Fig. S3 in the Supplemental Material for a qualitative comparison to our results). Wang *et al.* demonstrated the antitwinning phenomenon in BCC W nanowires with diameters less than approximately 20 nm during compression, where a transition from dislocation slip to antitwinning shear was observed with decreasing nanowire diameter. This transition was attributed to the limited plastic deformation carriers in nanosized BCC crystals. Our nanoindentation simulations conducted with tabGAP revealed that, at a load rate of 20 m/s and particularly at 5 m/s, a load drop of $\Delta p/E = 0.035$ in a range of 0.13 to 0.15 a/R resulted in ultrahigh stresses that triggered the formation and growth of twins, as shown in Fig. 9.

D. Stacking fault and dislocation glide energies

Generalized stacking fault energy (GSFE) is a measure of the energy required to create a specific defect or deformation in the W lattice, such as a twin or stacking fault. To understand the mechanisms of twin nucleation during loading process, we compute the GSFE for W using different interatomic potentials. The GSFE is computed by cutting a perfect crystal along a specific direction, known as the γ line, and calculating the energy required to move one part of the cut crystal relative to the other. The γ line is parallel to the cut plane and the movement of the two parts of the cut crystal results in the creation of a specific defect or deformation. In our computations, we applied periodic boundary conditions along the cut plane with unit cells from dislocation objects with 2×2 lattice units (l.u.) surface area and 30 l.u. perpendicular to the cut plane. For relaxation, we used a force tolerance of 0.01 eV/Å. Figure 11 shows the results for the GSFE for each displacement vector, where the atomic positions are relaxed only in the direction perpendicular to the cut plane [57]. These results confirmed the different shapes of the slip traces showing that EAM/ZBL potentials subestimate the SFEs, which may explain why this method does not predict the formation of twinned regions. However, MEAM and tabGAP agree well with reported DFT calculations [39] for $\langle 111 \rangle \{110\}$ with a value of $\sim$0.1 eV/Å^2 at the stable point.

In order to evaluate the ability of the applied potentials to model the nucleation and motion of dislocations during loading, we compute the screw and junction dislocation glide energies. These energies measure the resistance of the material to plastic deformation in a specific direction and

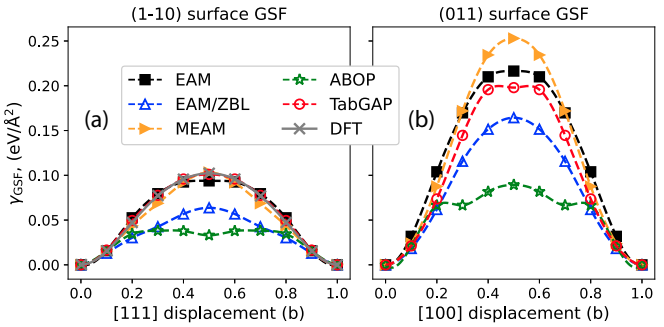

FIG. 11. Generalized stacking fault energies for ⟨111⟩{110} in (a) and ⟨100⟩{011} in (b) computed for all approaches. Data for ⟨111⟩{110} is compared with DFT results from [24].

are calculated by considering the motion of dislocations between two easy cores using the nudged elastic band (NEB) method. A force tolerance of 0.025 eV/Å is used during the minimization process and the initial path of the dislocation is determined using linear interpolation of the atomic positions between the initial and final relaxed configurations with force tolerance of 0.001 eV/Å, which are obtained using anisotropic elasticity within the Stroh formalism [58] using the elastic constants reported in Table I. As presented in Fig. 12, the tabGAP seems to have the overall best compromise with comparable barriers for two-junction dislocation glide planes and reasonable screw dislocation barriers as compared to recent QM/ML results [59]. The other potentials have some inaccuracies: (i) MEAM and EAM/ZBL potentials poorly represent screw dislocation core stability; (ii) EAM and MEAM significantly overestimate the glide barrier for a junction dislocation in the {001} glide plane; (iii) MEAM, ABOP, and EAM/ZBL predict almost zero glide for the junction dislocation in the {011} glide plane. The results obtained can guide experiments in understanding the fundamental mechanisms for nanoindentation induced dislocation nucleation through *in situ* transmission electron microscopy (TEM) images [60].

IV. CONCLUDING REMARKS

This work investigates the nanomechanical response of crystalline W during nanoindentation tests by performing MD simulations with different interatomic potentials: traditional EAM, EAM with ZBL corrections, modified EAM (MEAM), analytic bond-order potential (ABOP), and a recently developed tabulated Gaussian approximation potential (tabGAP). The study analyzes the dislocation nucleation and evolution mechanisms for each approach at different temperatures and loading rates. The nanoindentation loading process is characterized by recording load-displacement curves, dislocation densities, and atom displacement mapping. The comparison of the potentials shows similarities in stress-strain curves, but differences are observed while describing the nanocontact mechanisms between the indenter tip and the surface. Dislocation nucleation mechanisms are differently modeled by the approaches, where prismatic loop nucleation is highly affected by the surface, stacking faults, and dislocation glide energies information for each method. It is also worth noting that the computational time and resources required for performing MD simulations can vary significantly depending on the chosen interatomic potential. The tabGAP simulations were found to be slower than EAM-based simulations, but provided a better modeling for mechanical testing.

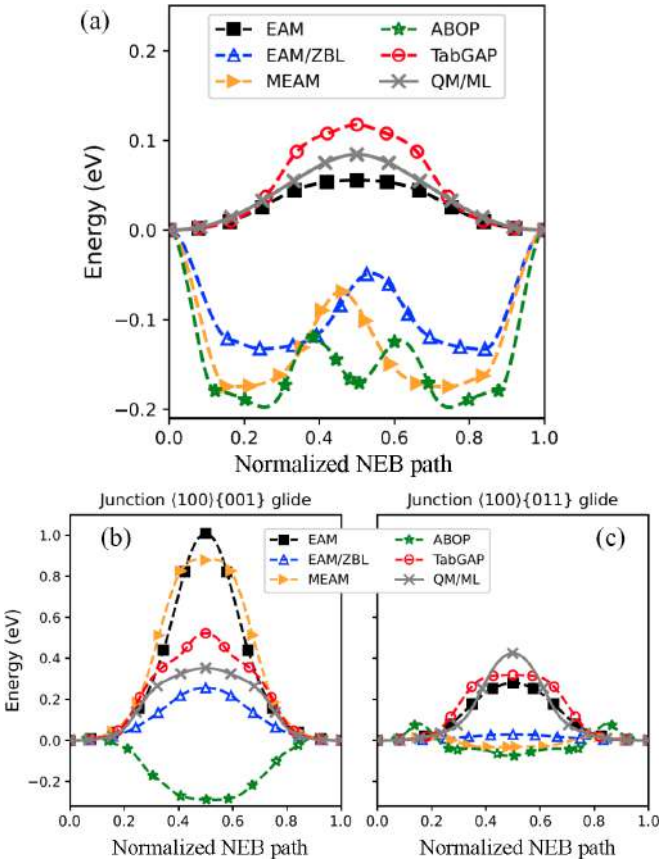

FIG. 12. Screw in (a) and junction in (b) dislocation glide 1/2⟨111⟩{110} energy of crystalline W by NEB method for different MD potentials. We compare to reported results by QM/ML calculations [59].

A general conclusion is that nanomechanical tests can be modeled by several interatomic potentials, with similar load-displacement and stress-strain curves, but dislocation dynamics depends on the approach used being exhibited by NEB calculations of screw and edge dislocation glide of 1/2⟨111⟩{110} and junction ⟨100⟩{001} and ⟨100⟩{110} energies, and stacking fault energies showing that tabGAP simulations can emulate the nanoindentation test as close as possible to experiments. In our future work, we will investigate the nanomechanical response of chemically complex BCC metals under external load by using recently developed tabGAP potentials that can be compared to experimental SEM and TEM images.

ACKNOWLEDGMENTS

We would like to thank M.-C. Marinica and J. Alcalá for inspiring conversations. We acknowledge support from the European Union Horizon 2020 research and innovation program under Grant Agreement No. 857470 and from the European Regional Development Fund via the Foundation for

Polish Science International Research Agenda PLUS program Grant No. MAB PLUS/2018/8. We acknowledge the computational resources provided by the Interdisciplinary Centre for Mathematical and Computational Modelling (ICM) University of Warsaw under computational allocation No. g91–1427. P.G. gratefully recognizes support from the Agence Nationale de Recherche, via the MeMoPAS Project No. ANR-19-CE46-0006-1 as well as access to the HPC resources of IDRIS under the allocations No. A0090910965 and No. A0120913455 attributed by GENCI.

APPENDIX: DEFECTS IDENTIFICATION

In order to identify the defects in nanoindentation simulations, we apply the BCC Defect Analysis (BDA) developed by Möller and Biztek [53], which utilizes coordination number (CN), centrosymmetry parameter (CSP), and common neighbor analysis (CNA) techniques to detect typical defects found in bcc crystals. Then, BDA compares the CN and CSP values of each atom that is not in a BCC perfect lattice point according to CNA or has a CN of 14 with empirically determined values for common defects such as surfaces, vacancies, twin boundaries, screw dislocations, {110} planar faults, and edge dislocations.

The results of the BDA technique used to identify defects in the plastic region beneath the indenter tip of the (001) W sample at 300 K with MD simulation performed by tabGAP are presented in Fig. 13. The developers of BDA have reported that the line direction of screw dislocations corresponds to the shearing direction for producing a deformation twin, making it impossible to differentiate their characteristics from those of twin boundaries. However, since dislocations are line defects, they can easily be distinguished from planar twin structures by comparing their dimensionalities. Although this comparison is not yet implemented in the BDA algorithm, precise defect identification is performed by visual inspection of the analysis output mainly observed beneath the indenter tip. Additionally, CNA can detect twinning dislocations as bcc and characterize them by a relatively high CSP (>8) but less than nine perfect bcc neighbors. Atoms near twin boundaries that lack one neighbor atom have either a low CSP (<1) but four 14-coordinated neighbors with CSP > 8 or a relatively high CSP (>4.5) and a fixed number of perfect, 13-, and 14-coordinated neighbors. This methodology was utilized to identify twin boundaries in our simulation, and it may be the reason why twinning was challenging to model using traditional EAM-based methods.

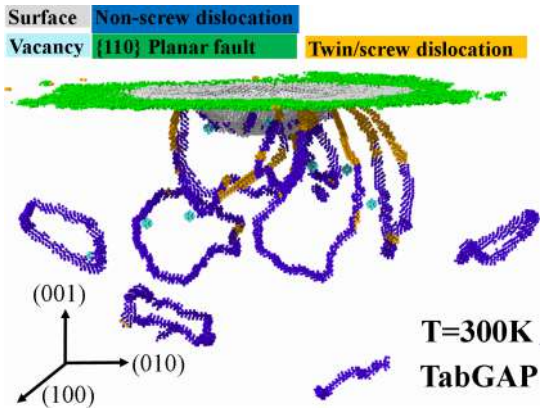

FIG. 13. Defects in the plastic region beneath the indenter tip at the maximum depth of the (001) W sample were identified using the BCC defect analysis (BDA) technique.

[1] C. A. Schuh, Mater. Today **9**, 32 (2006).
[2] J. Varillas, J. Ocenasek, J. Torner, and J. Alcala, Acta Mater. **125**, 431 (2017).
[3] L. Kurpaska, F. J. Dominguez-Gutierrez, Y. Zhang, K. Mulewska, H. Bei, W. J. Weber, A. Kosińska, W. Chrominski, I. Jozwik, R. Alvarez-Donado, S. Papanikolaou, J. Jagielski, and M. Alava, Mater. Des. **217**, 110639 (2022).
[4] S. Pathak and S. R. Kalidindi, Mater. Sci. Eng.: R: Rep. **91**, 1 (2015).
[5] T. Remington, C. Ruestes, E. Bringa, B. Remington, C. Lu, B. Kad, and M. Meyers, Acta Mater. **78**, 378 (2014).
[6] Z. Li, S. Gao, U. Brand, K. Hiller, and H. Wolff, Nanotechnology **31**, 305502 (2020).
[7] M. Mayer, M. Andrzejczuk, R. Dux, E. Fortuna-Zalesna, A. Hakola, S. Koivuranta, K. Krieger, K. J. Kurzydlowski, J. Likonen, and G. Matern, Phys. Scr. **2009**, 014039 (2009).
[8] P. Piaggi, E. Bringa, R. Pasianot, N. Gordillo, M. Panizo-Laiz, J. del RÃo, C. G. de Castro, and R. Gonzalez-Arrabal, J. Nucl. Mater. **458**, 233 (2015).
[9] B. Lipschultz, J. Roth, J. W. Davis, R. P. Doerner, A. A. Haasz, A. Kalenbach, A. Kirschner, R. D. Kolasinski, A. Loarte, V. Philipps, K. Schmid, W. R. Wampler, G. M. Wright and, D. G. Whyte, Tech. Rep. MIT **PSFC/RR**, 10 (2010).
[10] M. Kaufmann and R. Neu, Fusion Eng. Des. **82**, 521 (2007).
[11] T. Schwarz-Selinger, J. Bauer, S. Elgeti, and S. Markelj, Nucl. Mater. Energy **17**, 228 (2018).
[12] R. Pitts, S. Carpentier, F. Escourbiac, T. Hirai, V. Komarov, S. Lisgo, A. Kukushkin, A. Loarte, M. Merola, A. Sashala Naik, R. Mitteau, M. Sugihara, B. Bazylev, and P. Stangeby, J. Nucl. Mater. **438**, S48 (2013), proceedings of the 20th International Conference on Plasma-Surface Interactions in Controlled Fusion Devices.
[13] M. Rieth, J. Boutard, S. Dudarev, T. Ahlgren, S. Antusch, N. Baluc, M.-F. Barthe, C. Becquart, L. Ciupinski, J. Correia, C. Domain, J. Fikar, E. Fortuna, C.-C. Fu, E. Gaganidze, T. Galán, C. García-Rosales, B. Gludovatz, H. Greuner, K. Heinola *et al.*, J. Nucl. Mater. **417**, 463 (2011), proceedings of ICFRM-14.
[14] J. Pamela, A. Bécoulet, D. Borba, J.-L. Boutard, L. Horton, and D. Maisonnier, Fusion Eng. Des. **84**, 194 (2009), proceeding of the 25th Symposium on Fusion Technology.
[15] N. Holtkamp, Fusion Eng. Des. **84**, 98 (2009), proceeding of the 25th Symposium on Fusion Technology.
[16] B. D. Beake and S. Goel, Int. J. Refract. Met. Hard Mater. **75**, 63 (2018).
[17] K. Miyahara, S. Matsuoka, and N. Nagashima, JSME Int. J. Ser. A **41**, 562 (1998).

[18] Z. Wen, G. Xuanqiao, Z. Pingxiang, H. Zhongwu, L. Laiping, and C. Jun, Rare Met. Mater. Eng. **46**, 3626 (2017).

[19] J. Wang, T. Volz, S. Weygand, and R. Schwaiger, J. Mater. Res. **36**, 2166 (2021).

[20] J. Varillas-Delgado and J. Alcala Cabrelles, A molecular dynamics study of nanocontact plasticity and dislocation avalanches in FCC and BCC crystals, Ph.D. dissertation, Universitat Politècnica de Catalunya, Departament de Ciència dels Materials i Enginyeria Metallúrgica, 2019.

[21] F. Domínguez-Gutiérrez, S. Papanikolaou, A. Esfandiarpour, P. Sobkowicza, and M. Alava, Mater. Sci. Eng.: A **826**, 141912 (2021).

[22] G. Po, Y. Cui, D. Rivera, D. Cereceda, T. D. Swinburne, J. Marian, and N. Ghoniem, Acta Mater. **119**, 123 (2016).

[23] E. Tadmor, R. Elliott, J. Sethna, R. E. Miller, and C. A. Becker, JOM **63**, 17 (2011).

[24] M.-C. Marinica, L. Ventelon, M. R. Gilbert, L. Proville, S. L. Dudarev, J. Marian, G. Bencteux, and F. Willaime, J. Phys.: Condens. Matter **25**, 395502 (2013).

[25] U. Bhardwaj, A. E. Sand, and M. Warrier, J. Nucl. Mater. **569**, 153938 (2022).

[26] L.-F. Wang, X. Shu, G.-H. Lu, and F. Gao, J. Phys.: Condens. Matter **29**, 435401 (2017).

[27] D. R. Mason, D. Nguyen-Manh, and C. S. Becquart, J. Phys.: Condens. Matter **29**, 505501 (2017).

[28] G. J. Ackland and R. Thetford, Philos. Mag. A **56**, 15 (1987).

[29] P. Hiremath, S. Melin, E. Bitzek, and P. A. Olsson, Comput. Mater. Sci. **207**, 111283 (2022).

[30] C. Barrett and R. Carino, Integr. Mater. Manuf. Innov. **5**, 177 (2016).

[31] N. Juslin, P. Erhart, P. Träskelin, J. Nord, K. O. E. Henriksson, K. Nordlund, E. Salonen, and K. Albe, J. Appl. Phys. **98**, 123520 (2005).

[32] G. C. Abell, Phys. Rev. B **31**, 6184 (1985).

[33] J. Byggmästar, K. Nordlund, and F. Djurabekova, Phys. Rev. Mater. **6**, 083801 (2022).

[34] A. Glielmo, C. Zeni, and A. De Vita, Phys. Rev. B **97**, 184307 (2018).

[35] J. Vandermause, S. B. Torrisi, S. Batzner, Y. Xie, L. Sun, A. M. Kolpak, and B. Kozinsky, npj Comput. Mater. **6**, 20 (2020).

[36] J. Byggmästar, K. Nordlund, and F. Djurabekova, Phys. Rev. B **104**, 104101 (2021).

[37] F. Dominguez-Gutierrez, Nucl. Instrum. Methods Phys. Res., B **512**, 38 (2022).

[38] A. P. Thompson, H. M. Aktulga, R. Berger, D. S. Bolintineanu, W. M. Brown, P. S. Crozier, P. J. in 't Veld, A. Kohlmeyer, S. G. Moore, T. D. Nguyen, R. Shan, M. J. Stevens, J. Tranchida, C. Trott, and S. J. Plimpton, Comput. Phys. Commun. **271**, 108171 (2022).

[39] X. Wang, S. Xu, W.-R. Jian, X.-G. Li, Y. Su, and I. J. Beyerlein, Comput. Mater. Sci. **192**, 110364 (2021).

[40] R. W. Hertzberg, *Deformation and Fracture Mechanics of Engineering Materials* (Wiley, New York, 1996).

[41] CiDRA Precision Services—Machining of Materials, Tungsten, https://www.azom.com/article.aspx?ArticleID=614.

[42] J. Guénolé, W. G. Nöhring, A. Vaid, F. Houllé, Z. Xie, A. Prakash, and E. Bitzek, Comput. Mater. Sci. **175**, 109584 (2020).

[43] See Supplemental Material at http://link.aps.org/supplemental/10.1103/PhysRevMaterials.7.043603 for (i) lD curves and pile-ups formation of (011) and (111) crystal orientations, (ii) structural analysis of W sample with tab gap, and (iii) principal shear stress calculations.

[44] S. Goel, G. Cross, A. Stukowski, E. Gamsjäger, B. Beake, and A. Agrawal, Comput. Mater. Sci. **152**, 196 (2018).

[45] A. D. Backer, D. Mason, C. Domain, D. Nguyen-Manh, M.-C. Marinica, L. Ventelon, C. Becquart, and S. Dudarev, Nucl. Fusion **58**, 016006 (2018).

[46] A. Stukowski, Modell. Simul. Mater. Sci. Eng. **18**, 015012 (2010).

[47] A. Stukowski, V. V. Bulatov, and A. Arsenlis, Modell. Simul. Mater. Sci. Eng. **20**, 085007 (2012).

[48] C. Begau, J. Hua, and A. Hartmaier, J. Mech. Phys. Solids **60**, 711 (2012).

[49] P. Grigorev, T. D. Swinburne, and J. R. Kermode, Phys. Rev. Mater. **4**, 023601 (2020).

[50] T. D. Swinburne and S. L. Dudarev, Phys. Rev. Mater. **2**, 073608 (2018).

[51] H. Yu, S. Das, H. Yu, P. Karamched, E. Tarleton, and F. Hofmann, Scr. Mater. **189**, 135 (2020).

[52] J. Wang, Z. Zeng, M. Wen, Q. Wang, D. Chen, Y. Zhang, P. Wang, H. Wang, Z. Zhang, S. X. Mao, and T. Zhu, Sci. Adv. **6**, eaay2792 (2020).

[53] J. J. Möller and E. Bitzek, MethodsX **3**, 279 (2016).

[54] W. J. Szlachta, A. P. Bartók, and G. Csányi, Accuracy and transferability of gap models for tungsten, arXiv:1405.4370.

[55] M. A. Wood and A. P. Thompson, Quantum-accurate molecular dynamics potential for tungsten, arXiv:1702.07042.

[56] V. Maier, K. Durst, J. Mueller, B. Backes, H. W. Happel, and M. Gaken, J. Mater. Res. **26**, 1421 (2011).

[57] L. Ventelon and F. Willaime, Philos. Mag. **90**, 1063 (2010).

[58] A. N. Stroh, Philos. Mag. **3**, 625 (1958).

[59] P. Grigorev, A. M. Goryaeva, M. C. Marinica, J. R. Kermode, and T. D. Swinburne, Acta Mater. **247**, 118734 (2023).

[60] B. Wang, Z. Zhang, J. Cui, N. Jiang, J. Lyu, G. Chen, J. Wang, Z. Liu, J. Yu, C. Lin, F. Ye, and D. Guo, ACS Appl. Mater. Interfaces **9**, 29451 (2017).

Nanoindentation of Tungsten: From interatomic potentials to dislocation plasticity mechanisms

F. J. Domínguez-Gutiérrez[a*], P. Grigorev[b], A. Naghdi[a], J. Byggmästar[b], G. Y. Wei[b,c], T. Swinburne[b], S. Papanikolaou[a], M. J. Alava[a,d]

[a]*NOMATEN Centre of Excellence, National Centre for Nuclear Research, ul. A. Sołtana 7, 05-400 Swierk/Otwock, Poland*
[b]*Aix-Marseille Universite, CNRS,CINam UMR 7325, Campus de Luminy, 13288 Marseille, France.*
[c]*Department of Physics, P.O. Box 43, FI-00014 University of Helsinki, Finland*
[d]*Henan Academy of Big Data, Zhengzhou University, Zhengzhou 450052, China*
[e]*Department of Applied Physics, Aalto University, P.O. Box 11000, 00076 Aalto, Espoo, Finland.*

We report the analysis of the dislocation nucleation and slip traces for different crystal orientations and methods.

011 crystal orientation

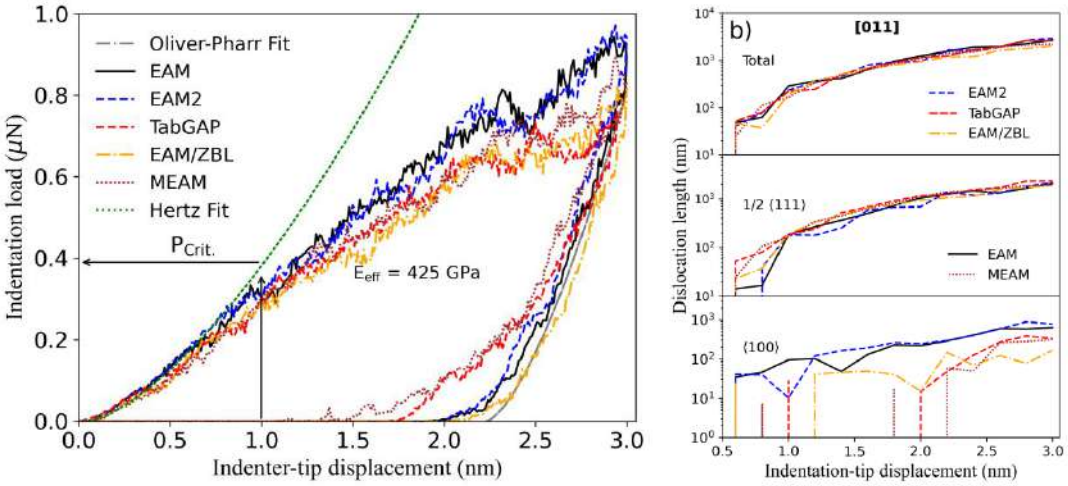

Figure 1 LD curves and dislocation density for the 011 crystal orientation by different methods

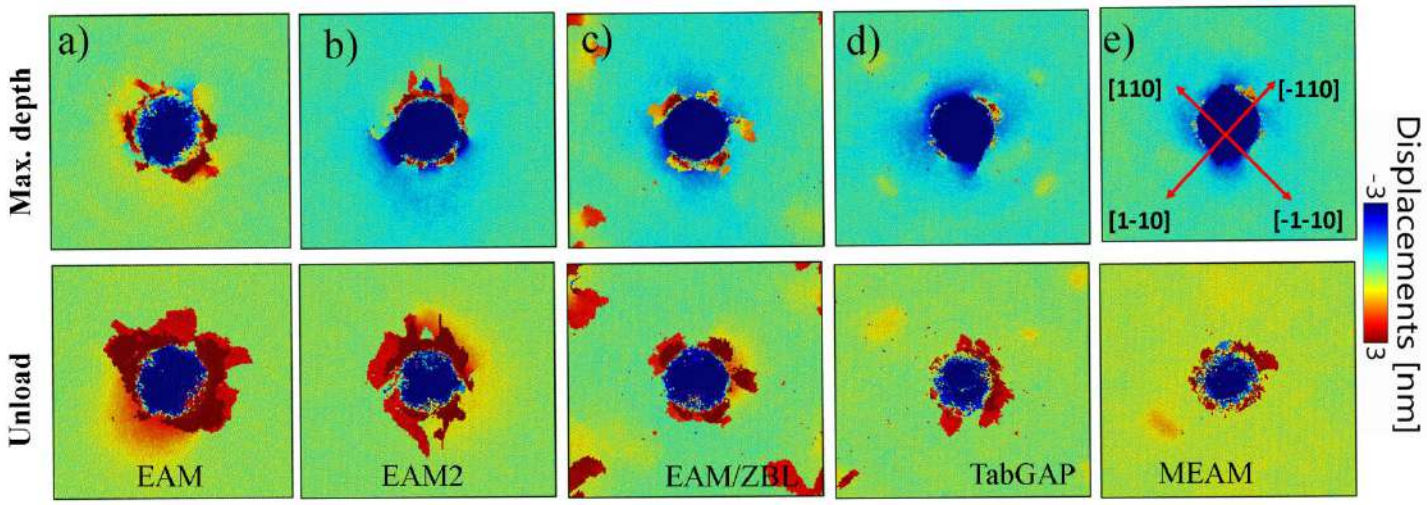

Figure 2. Pile ups and slip traces formed at maximum indentation depth and after unloading process

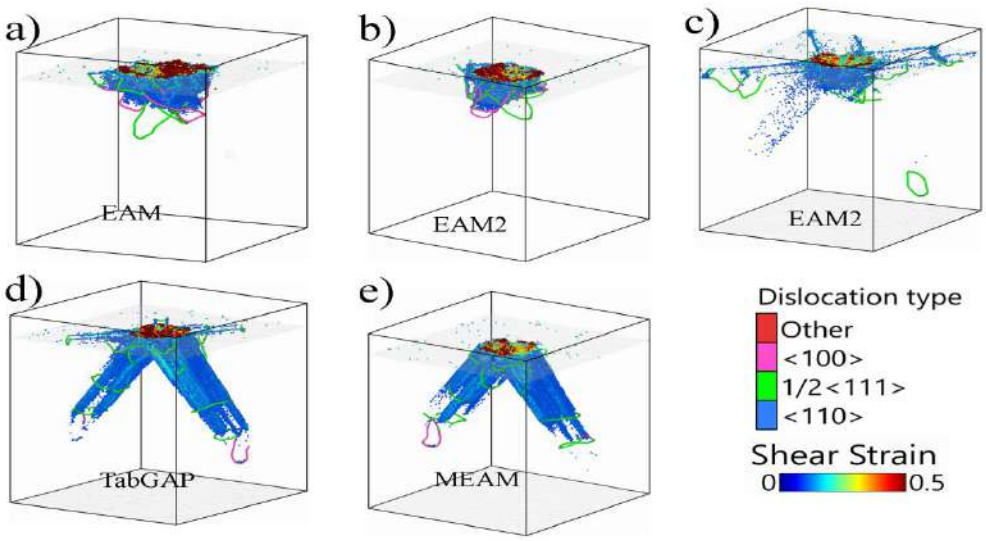

Figure 3. Dislocation loops and atomic shear strain mapping at maximum indentation depth for the [011] crystal orientation.

Structural analysis

BDA method applied to tabGAP simulations for the (001) orientation at 300K.

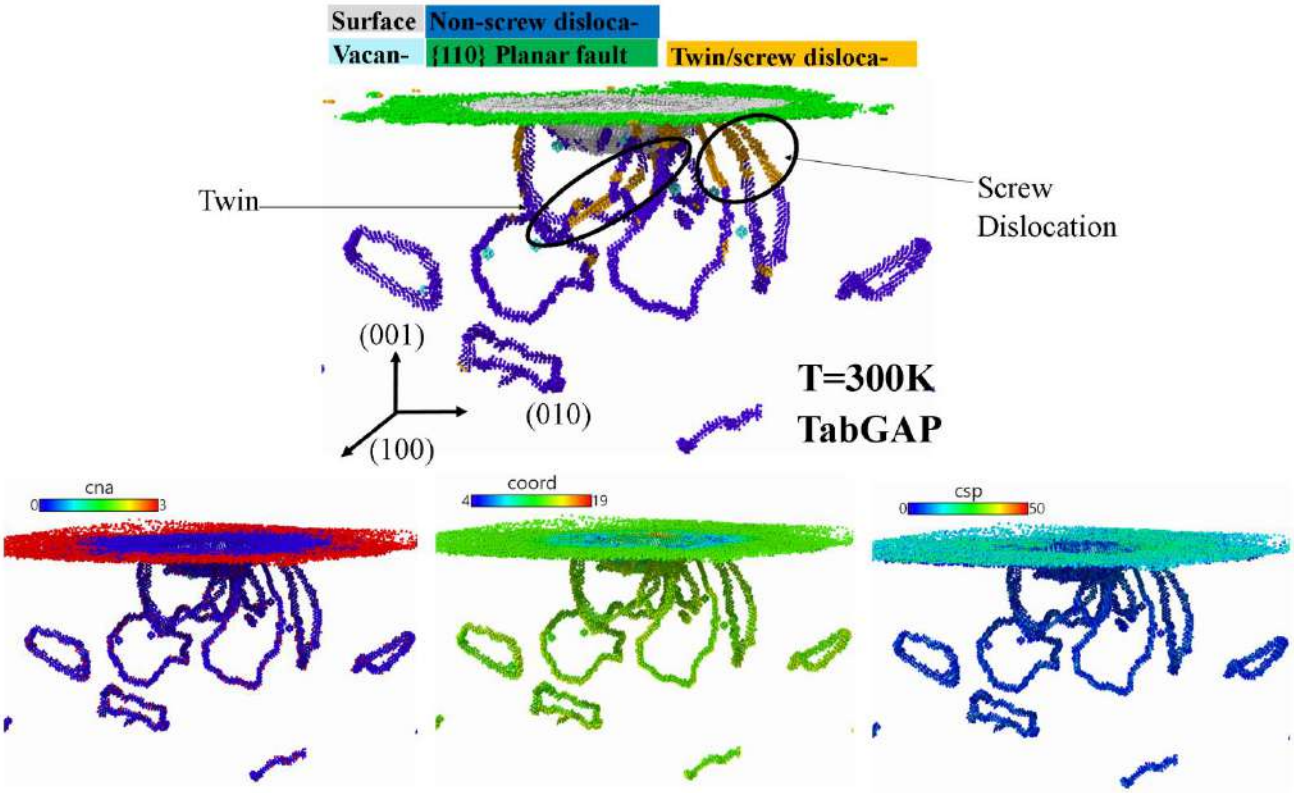

Figure 4. (Color on-line) Defects in the plastic region beneath the indenter tip at the maximum depth of the (001) W sample were identified using the BCC Defect Analysis (BDA) technique

111 crystal orientation

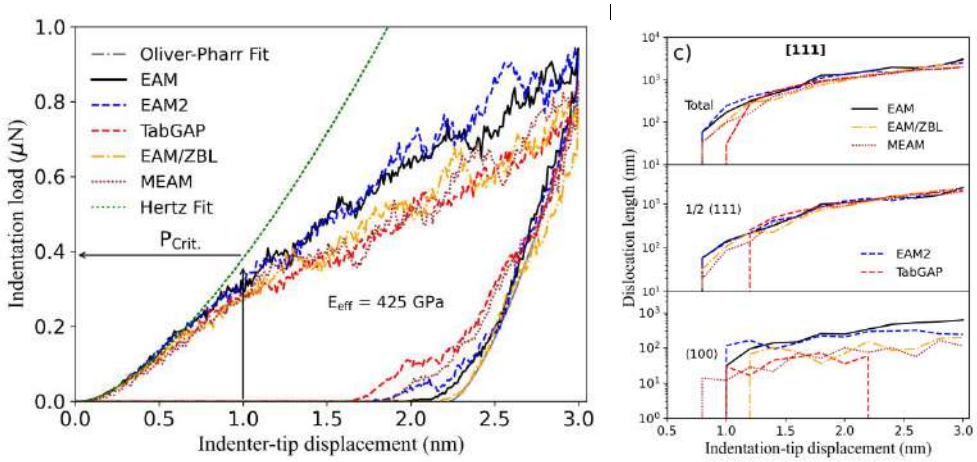

Figure 5 LD curves for the 011 crystal orientation by different methods

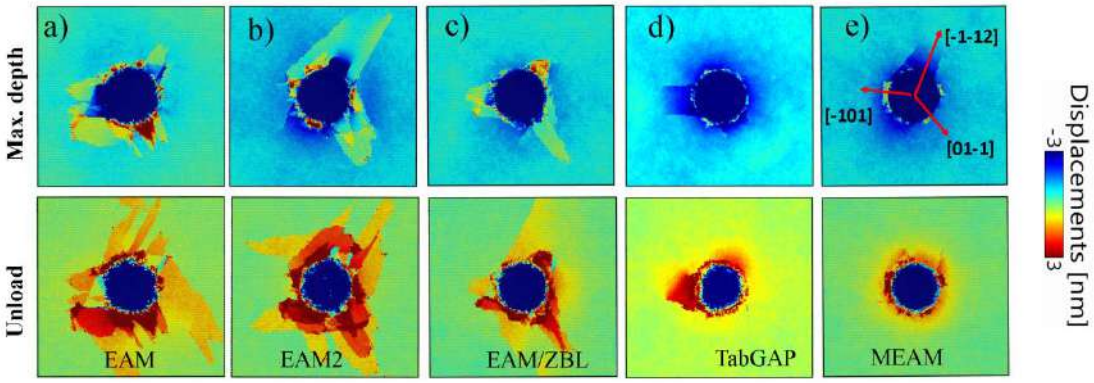

Figure 6. Pile ups and slip traces formed at maximum indentation depth and after unloading process

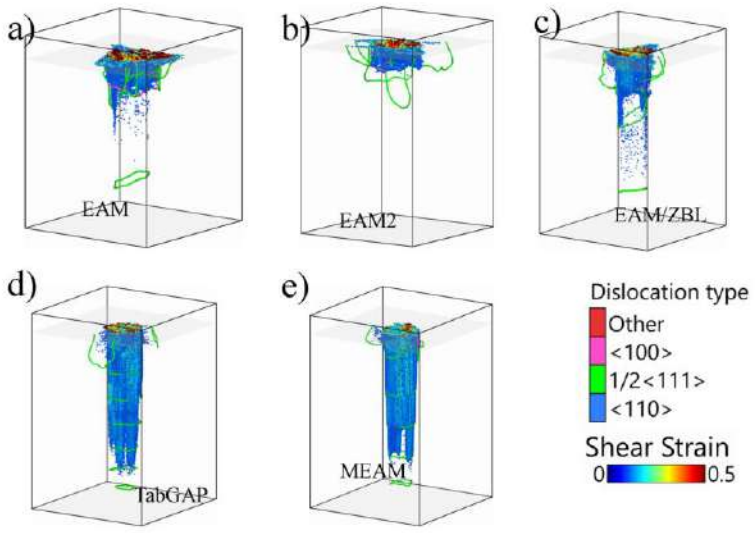

Figure 7. Dislocation loops and atomic shear strain mapping at maximum indentation depth for the [111] crystal orientation

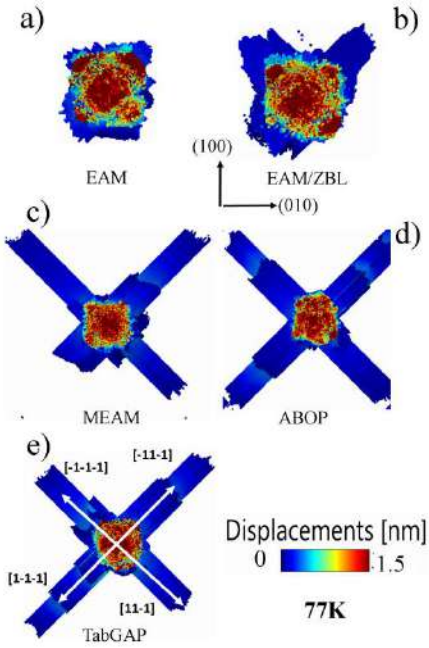

Figure 8 Displacement of (001) W at 77K

Principal shear stress

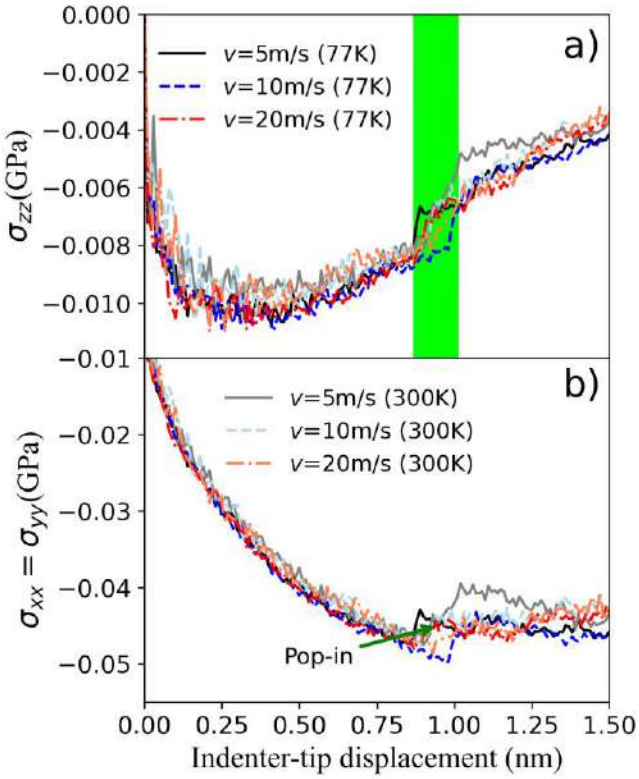

Figure 9 Principal shear stress for tabGAP simulations used to calculate maximum shear stress

Acta Materialia 277 (2024) 120200

Contents lists available at ScienceDirect

Acta Materialia

journal homepage: www.elsevier.com/locate/actamat

Full length article

Neural network interatomic potentials for open surface nano-mechanics applications

Amirhossein D. Naghdi [a,b,*], Franco Pellegrini [c], Emine Küçükbenli [d,e], Dario Massa [a,b], F. Javier Dominguez–Gutierrez [a], Efthimios Kaxiras [e,f], Stefanos Papanikolaou [a]

[a] NOMATEN Centre of Excellence, National Center for Nuclear Research, ul. A. Sołtana 7, 05-400 Swierk/Otwock, Poland
[b] IDEAS NCBR, ul. Chmielna 69, 00-801, Warsaw, Poland
[c] International School for Advanced Studies (SISSA), Via Bonomea, 265, I-34136 Trieste, Italy
[d] Nvidia Corporation, Santa Clara, CA, USA
[e] John A. Paulson School of Engineering and Applied Sciences, Harvard University, Cambridge, MA 02138, USA
[f] Department of Physics, Harvard University, Cambridge, MA 02138, USA

ARTICLE INFO

Keywords:
Neural network interatomic potentials
Nano-indentation
Nano-mechanics

ABSTRACT

Material characterization in nano-mechanical tests may provide information on the potential heterogeneity of mechanical properties. Here, we develop a robust neural-network interatomic potential (NNIP), and we provide a test for the example of molecular dynamics (MD) nanoindentation, and the case of body-centered cubic crystalline molybdenum (Mo). We employ a similarity measurement protocol, using standard local environment descriptors, to select ab initio configurations for the training dataset that capture the behavior of the indented sample. We find that it is critical to include generalized stacking fault (GSF) configurations, featuring a dumbbell self-interstitial on the surface, to capture dislocation cores, and also high-temperature configurations with frozen atom layers for the indenter tip contact. We develop a NNIP with distinct dislocation nucleation mechanisms, realistic generalized stacking fault energy (GSFE) curves, and an informative energy landscape for the atoms on the sample surface during nanoindentation. We compare our NNIP results with nanoindentation simulations, performed with three existing potentials – an embedded atom method (EAM) potential, a gaussian approximation potential (GAP), and a tabulated GAP (tabGAP) potential – that predict different dislocation nucleation mechanisms, and display the absence of essential information on the shear stress at the sample surface in the elastic region. Finally, we compared our NNIP nanoindentation results with experiments, showing reliable predictions for reduced Young's modulus and observable slip traces.

1. Introduction

Nano-mechanical tests serve as essential tools for probing the mechanical properties of materials at the nanoscale. Techniques such as nano-tensile/compression [1–3], nanoindentation [4–11], and creep testing [12] play a pivotal role in revealing the intrinsic properties of materials. This understanding, in turn, facilitates the design and production of innovative materials capable of functioning in extreme environments. These tests involve subjecting the material to controlled strain/stress at the nanoscale, enabling researchers to gain valuable insights into its mechanical response. This knowledge is crucial in the field of defect physics, as nano-mechanical tests provide a means to investigate the mechanisms of defects nucleation and their impact on the mechanical performance of materials under extreme conditions. In this study, we aim to present a comprehensive method for simulating nano-mechanical tests, taking nanoindentation as an example, on crystalline materials using neural-network interatomic potentials (NNIPs).

Nano-mechanical test techniques find application in several areas of materials science. Specifically, in situ techniques [13,14] contribute significantly to the understanding of material deformation under controlled applied stress or strain, while the specimen is simultaneously observed/measured by electron microscopic devices. These methodologies play a pivotal role in exploring materials properties at the nano scale, offering insights into the intrinsic properties of materials, such as the strength of each crystalline grain. Furthermore, these techniques prove invaluable in investigating temperature-related deformation mechanisms inherent in crystalline materials. The focus of this paper is on nanoindentation testing, a widely utilized method for

* Corresponding author at: NOMATEN Centre of Excellence, National Center for Nuclear Research, ul. A. Sołtana 7, 05-400 Swierk/Otwock, Poland.
E-mail address: Amirhossein.Naghdi@ncbj.gov.pl (A.D. Naghdi).

https://doi.org/10.1016/j.actamat.2024.120200
Received 23 April 2024; Received in revised form 14 July 2024; Accepted 14 July 2024
Available online 24 July 2024

assessing material properties on open surfaces. This technique yields results for various properties, encompassing hardness, strength, dislocation nucleation mechanisms, dislocation density, grain boundary effects, and dislocation junction formations [15–24]. However, it is essential to note that nanoindentation testing involves intricate defect nucleation mechanisms and plastic deformations, rendering accurate modeling a formidable challenge within the realm of computational materials science.

Various computational methods, such as finite element methods (FEM) [25–27], discrete dislocation dynamics (DDD) [28–32], and molecular dynamics (MD) [33–37], are employed for modeling nano-mechanical testing. In FEM, numerical solutions to differential equations in mathematical models are used to approximate and analyze the complex behavior of materials. While FEM and DDD methods prove useful in specific scenarios, they lack atomic-level precision, thereby falling short of achieving the desired level of accuracy. On the other hand, MD simulations can provide atomic-level insights into the dislocation dynamics of materials, given the use of interatomic potentials finely tuned for nano-mechanics in the simulations.

Machine-learned force fields (MLFFs) [38–47] offer a reliable method for modeling nano-mechanical tests with high precision. Various MLFF types, such as Gaussian Approximation Potentials (GAP) [39] and its tabulated version (tabGAP) [48], as well as active learning methods [49,50], are available in the literature. In addition, NNIPs exhibit exceptional accuracy in predicting atomic energies and forces [42,51–56], overcoming the time and system size limitations inherent in traditional ab initio molecular dynamics (AIMD) simulations. Given the ability of NNIPs to learn complex functions, such as the energy landscape of an extended dislocation in a metallic crystal, they prove to be excellent tools for modeling nano-mechanical testing simulations. MLFFs have been successfully applied to various problems, including catalysis [57,58], point defects modeling [59,60], multi-component materials modeling [61,62], and multi-phase systems [45], demonstrating their versatility. However, the exploration of nano-mechanical testing simulations using MLFFs is an area that remains to be fully explored.

In this paper, we present a study focused on the development of a robust NNIP by enhancing a starting dataset sourced from the literature [63] within the PANNA (Properties from Artificial Neural Network Architectures) framework [64]. While more complex models, such as MACE [55], offer improved accuracy, we chose PANNA to strike a balance between accuracy and simulation performance. We compare the Behler–Parrinello (BP) descriptor vectors [38] of the training dataset with those of a single crystal BCC Molybdenum configuration, indented with an embedded atom model (EAM) potential [65], to determine how closely the training dataset resembles the indentation process. This method is inspired by studies, such as those referenced in [66,67] , which utilize similarity measurements in the development of MLFFs. To improve the accuracy of the potential, we introduce high temperature configurations with a frozen layer and generalized stacking fault (GSF) configurations with a self-interstitial on the gamma surface. These configurations are designed to closely mimic atoms in the dislocation cores, on the surface, and under the indenter tip. Our results show that including these configurations in the training dataset reduces the distance between the atoms the potential is trained on and the indented sample. Finally, we present the results of an MD nanoindentation simulation using the potential trained with the modified dataset.

2. Methods

2.1. Descriptor parameters

In this work, PANNA: Properties from Artificial Neural Network Architectures [64], which utilizes Tensorflow [68] to train/evaluate fully-connected feed-forward NNIPs, is used to develop the interatomic potential, with the modified version of Behler–Parrinello (mBP) descriptors [38,69]. The mBP representation generates a fixed-size vector (the G-vector) for each atom in each configuration of the dataset. Each G-vector describes the environment of the corresponding atom of the configuration to which it belongs, up to a cutoff radius R_c. Although higher dimensional G-vectors lead to a more accurate representation of the target potential energy surface, oversized ones increase the MD simulation computational cost. In terms of the distances R_{ij} and R_{ik} of the atom i from its neighbors j and k and the angle subtended by those distances θ_{ijk}, the radial and angular G-vectors are given by:

$$G_i^{rad}[s] = \sum_{i \neq j} e^{-\eta(R_{ij}-R_s)^2} f_c(R_{ij}) \tag{1}$$

$$G_i^{ang}[s] = 2^{1-\zeta} \sum_{j,k \neq i} [1 + cos(\theta_{ijk} - \theta_s)]^{\zeta} \times e^{-\eta[\frac{1}{2}(R_{ij}+R_{ik})-R_s]^2} f_c(R_{ij}) f_c(R_{ik}) \tag{2}$$

where the smooth cutoff function (which includes the cutoff radius R_c) is given by:

$$f_c(R_{ij}) = \begin{cases} \frac{1}{2}\left[\cos\left(\frac{\pi R_{ij}}{R_c}\right) + 1\right], & R_{ij} \leq R_c \\ 0, & R_{ij} > R_c \end{cases} \tag{3}$$

and η, ζ, θ_s and R_s are parameters, different for the radial and angular parts. Table 1 shows all values selected for the descriptor parameters in this study. The choice of the cutoff value is made so that it covers up to three nearest neighbors of the center atom in the BCC Mo, which has a lattice constant of $a = 3.17$ Å, and thus the third nearest neighbor's distance is $a \times \sqrt{2} = 4.48$ Å. The length of the G-vector for a single element system is

$$|G_i[s]| = (R_s^{ang} \times \theta_s) + R_s^{rad}, \tag{4}$$

which leads to a G-vector of length 152, given the parameters reported in Table 1.

Table 1
Values of the parameters that appear in the definition of the radial and angular G-vectors, Eqs. (1), (2), (3). Where a number of components is given, the values are equispaced.

Descriptor parameter	Symbol	Value
Radial component:		
Radial exponent (Å^{-2})	η^{rad}	32
cutoff (Å)	R_c^{rad}	5
Number of R_s radial	R_s^{rad}	24
Angular component:		
Radial exponent (Å^{-2})	η^{ang}	16
cutoff (Å)	R_c^{ang}	5
Number of R_s angular	R_s^{ang}	8
Angular exponent	ζ	128
Number of θ_s	θ_s	16

2.2. Similarity measurements

In this study, a distance-based criterion, inspired by [66,67], is utilized to quantify the similarity between two distinct configurations. This criterion is subsequently extended to evaluate the closeness of two disparate datasets to one another. Consider two configurations, labeled as α and β, with n and m atoms per supercell, respectively. The distance matrix for the two configurations, $\boldsymbol{D}^{\alpha\beta}$, has a $n \times m$ dimension and each element of the matrix is the euclidean distance of atom i in α to atom j in β:

$$D_{i,j}^{\alpha\beta} = \left\| G_i^{\alpha}[s] - G_j^{\beta}[s] \right\|_2 \tag{5}$$

Where $i \in \{1, 2, \ldots, n\}$ and $j \in \{1, 2, \ldots, m\}$, and each $G[s]$ is a 152 dimensional vector, as explained in the previous section. Given this matrix, we can compute the minimum distance of each atom i in

Table 2
The original dataset from [63], showing N_s as the number of structures, N_{at} as the number of atoms per configuration, and N_{sel} as the number of selected configurations in the final dataset. The structure types in bold have been added to the original dataset.

Structure type	N_s	N_{at}	N_{sel}
Isolated atom	1	1	None
Dimer	19	2	None
Slice sample	1996	1	All
Distorted BCC	547	2	All
A15	100	8	None
C15	100	6	None
HCP	100	2	All
FCC	100	1	None
Diamond	100	2	None
Phonon	50	54	All
Self-interstitials (SIA)	32	121	14
di-Self-interstitials	14	122–252	All
Simple Cubic	100	1	None
Vacancy	210	53	All
di-Vacancy	10	118	All
tri-Vacancy	14	117	All
Liquid	45	128	None
Short range	90	53–55	None
Surface (100)	45	12	All
Surface (110)	45	12	All
Surface (111)	41	12	All
Surface (112)	45	12	All
Liquid Surface	24	128	All
γ-surface	178	12	All
GSFCs	100	18	All
GSFCs + SIA	100	55	All
Pileup	1000	32	All
HT + substrate	600	54–72	All

configuration α from any atom j in configuration β, and we define the similarity measure from α to β as the maximum among these minima, i.e.:

$$D^{\alpha\beta} = \max_i \min_j D^{\alpha\beta}_{i,j}. \tag{6}$$

It must be noted that this final quantity is not a proper distance, but a non-symmetric quantity giving us the "similarity measure" method, explained in this section, is subsequently employed to gain insights from the initial dataset. This also includes exploring ways to enhance the dataset through innovative configurations, specifically in relation to an indented supercell. For instance, one can compute the average of all $D^{\alpha\beta}$ values between atoms from two distinct datasets or configuration types within a dataset. This calculation provides an indication of the degree of (dis)similarity between considered datasets/configuration types. The same goes for measuring the similarity of a dataset to a targeted simulation, which in our case is an indented sample.

2.3. Dataset evaluation and improvement

As a starting point, we used a dataset [63] originally developed to train a MLFF within the GAP framework [39,70]. The objective was to determine whether this dataset accurately represents the atomic configurations occurring during nanoindentation simulations, for which we employed an EAM potential [65]. We then analyzed the obtained data to determine the degree of similarity between the atomic configurations in the dataset and those observed during the nanoindentation simulations.

This level of similarity is evaluated by identifying which atom j in the dataset has the minimum distance to each atom i in the indented sample. The obtained value corresponds to the *largest minimum* distance for each atom in the indented sample from all the atoms in the dataset. The concept of "distance" for two atoms i and j, refers to the l^2-norm of $G_i[s] - G_j[s]$, where $G[s]$ are the fixed-size mBP descriptor vectors [38,69], as discussed in the previous sections. To further analyze the similarity measurement method, we calculated the distances of sheared BCC configurations from a perfect BCC crystal (Fig. S10 in the supplementary material (SM)). It is shown that as the applied strain increases, the distance values also increase. This aligns with intuitive expectations, validating our similarity measurement method. To this end, we compared the configuration types present in the dataset to those of all atoms identified in the indented sample and drew conclusions based on the level of correspondence between the two sets. Through this analysis, we aimed to gain insights into the suitability of the selected dataset for studying nanoindentation behavior and identifying the underlying mechanisms governing it.

To generate a suitable dataset for training a NNIP targeted at nanoindentation simulations, it is crucial to ensure that the configurations included accurately represent the three essential regions of a sample under indentation. These regions include the atoms on the surface of the sample, which correspond to the pileup patterns, the atoms situated beneath the indenter tip that undergo significant plastic deformation, and the atoms located on the nucleated dislocation cores. The evaluation of these three critical regions and development of configurations that closely resemble them can serve as a benchmark for ML potentials for other BCC materials.

Before comparing the original dataset with the indented sample, we calculated the average minimum distance between each pair of configuration types and generated a correlation figure to visualize their proximity (Fig. 1(a)). It is evident from this figure that although the isolated atom and dimer configurations are quite distant from almost all other configurations, they are relatively close to the indented samples. However, these configurations were not included in the final dataset due to their low numbers (1 and 19, respectively), which were deemed insufficient for training a NNIP. Moreover, the A15, simple cubic (sc), diamond (dia), liquid and C15 configurations were removed from the final dataset as they were located at a distance beyond the set threshold from the indented configurations, with simple cubic, diamond, and C15 configurations having the largest distance. Furthermore, we excluded short-range configurations from the final dataset because their energies varied significantly (Fig. S1(a) in the SM), leading to training difficulties. Finally, to reduce computational cost, we kept only half of the self-interstitial configurations in the final dataset. Table 2 summarizes all modifications made to the original dataset.

Several methods can be employed to determine a "good" threshold for deciding whether to keep or remove a particular configuration from the dataset, based on its similarity to the indented configuration. In this study, we have chosen to use the start of the tail of the distribution of the minimum values in the dataset distance matrix as the threshold, which is approximately 6 based on Fig. 1(b). Fig. 1(b) also demonstrates that this value is consistent with the minimum distances between the dataset configurations and all three orientations of the indented samples. All decisions regarding whether to keep or remove a configuration from the final dataset in this study are based on this threshold.

To ensure the accuracy of the modifications made to the dataset, we removed one type of configuration from the dataset at a time and quantified the number of atoms in the indented samples that had minimum distances greater than 6 from the dataset (Fig. 1(c)). As our analysis show, the number of atoms with a minimum distance greater than 6 to the dataset does not increase when A15, diamond, Face-Centered Cubic (FCC), simple cubic, short range, isolated atom, and dimer configurations are removed, indicating the dataset's stability against the indented samples, whether these configurations are present in the dataset or not. However, upon removing Hexagonal Close-Packed (HCP) configurations, the number of atoms with a large distance from the dataset increases, which is consistent with the fact that the average minimum distance of HCP configurations to the indented samples is 5. The greatest increase in the number of atoms with a distance greater than 6 from the dataset occurs when surface configurations are removed, which underscores their importance since they represent the surface in the nanoindentation simulations.

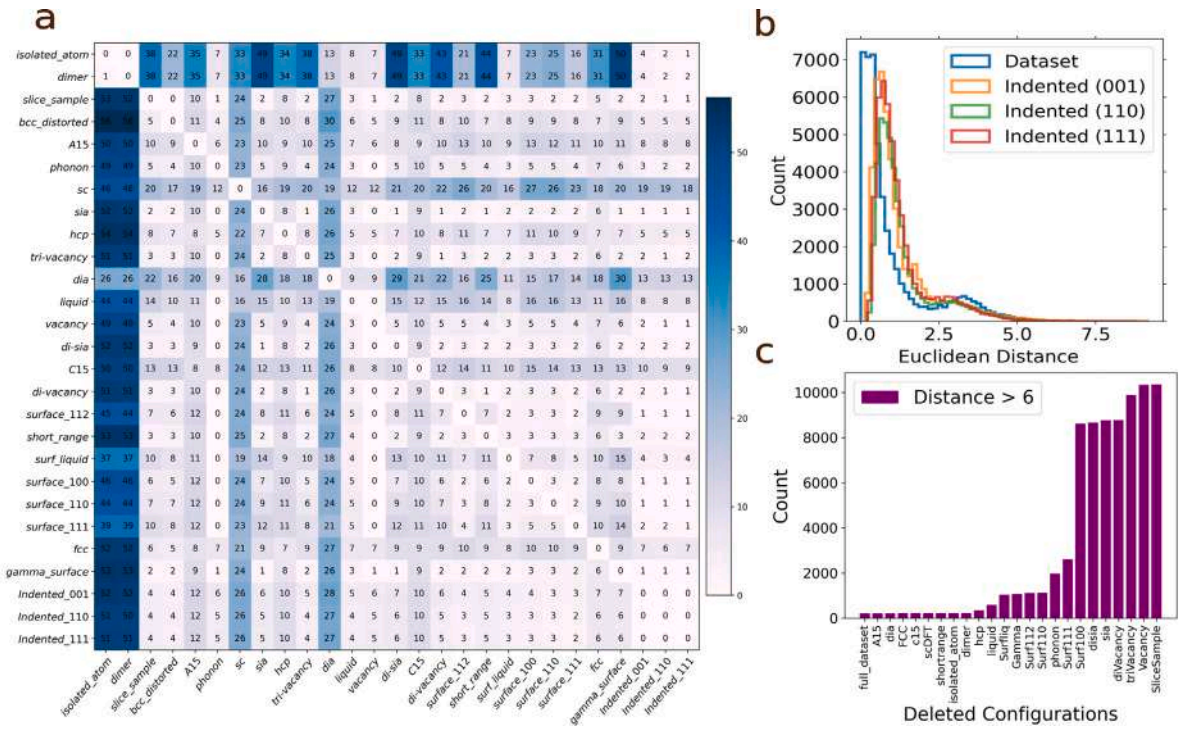

Fig. 1. Dataset evaluation and stability. (a) Average of minimum distances between different configuration types as well as with the indented samples. (b) Distribution of the minimum distances of different configurations to the rest of the data points in the dataset and the minimum distances of the dataset with the indented configurations. (c) Effect of configuration removal from the dataset on the minimum distances of the dataset to the indented sample.

Following the modifications made to the dataset obtained from [63], attempts were made to enhance its quality by incorporating various types of configurations and reevaluating the distances of the indented configuration from the dataset. Among the crucial local environments that should be included in the dataset are the atoms belonging to the dislocation cores. Furthermore, it was discovered that the distances of the atoms beneath the indenter tip and those on the surface exceeded the selected 6 threshold (Fig. 2(a)). These environments in the indented samples are critical to be covered in the dataset since dislocation cores play a vital role in the dislocation dynamics properties, and the atoms beneath the indenter tip trigger these line defects. Additionally, the plastic region beneath the surface is responsible for the pile-up patterns that appear on the surface of the indented configuration. It is also imperative to incorporate configurations in the dataset representing atoms on the surface to capture this phenomenon.

In order to model the aforementioned regions of an indented sample, we explored the use of high-temperature configurations to effectively reduce the distance between the atoms in these areas and the dataset, as depicted in Fig. 2(b). Nevertheless, accounting for the atoms beneath the indenter tip and on the surface requires the inclusion of a layer of frozen atoms in the high-temperature configurations that emulate the contact of the sample with the indenter tip. The addition of 1000 isothermal–isobaric ensemble (NPT) high-temperature configurations with 16 atoms in the $2 \times 2 \times 2$ supercells appeared to decrease the distances between the atoms on the dislocation cores and the dataset. We utilized the same approach for the atoms beneath the indenter tip. In this regard, we introduced 600 configurations, denoted as "high temperature (HT) + substrate", where a layer of atoms was frozen while other atoms were heated to high temperatures (under the melting point). While there are various unique layers of atoms that can be taken into account as the contact to the substrate, we verified that 300 configurations ($3 \times 3 \times 3$) with 54 atoms per supercell – displayed in the middle figure of Fig. 2-(b) – were adequate and most relevant after trying different layers of atoms. Additionally, we included 300 configurations ($4 \times 3 \times 3$) with 72 atoms per supercell, which featured a layer of atoms frozen on top. Moreover, it is crucial for a NNIP's dataset to incorporate configurations resembling the atoms located on the surface of the indented sample. To achieve this, we introduced 1000 BCC surface configurations ($3 \times 3 \times 2$) with 32 atoms per supercell, where a layer of atoms was frozen on top while the remaining atoms were subjected to high temperature. These configurations were named "pileup" in our study and enabled the dataset to account for the atoms in this region.

Another effective approach to cover the dislocation cores is through the use of GSFCs that incorporate a self-interstitial atom (SIA) atom on the surface (as illustrated in Fig. 3(a)). These configurations have been found to be particularly effective in reducing the distances of atoms on the dislocation cores from the dataset. While the use of GSFCs without an SIA on the surface can also reduce distances of atoms beneath the dislocation cores and on the slipping plane (as shown in Fig. 3(b)), it may not entirely cover all the atoms on the dislocation core.

Incorporating a SIA on the surface of the GSFCs leads to a significant decrease in the distances of almost all atoms on the dislocation cores from the dataset (as demonstrated in Fig. 3(c)). Notably, the use of GSFCs with a SIA instead of high-temperature configurations solely for the dislocation cores presents several advantages. For instance, the distribution of energies of these configurations is narrower, facilitating the learning process for the network (as depicted in Fig. S1((b) in the SM). Furthermore, only 100 GSFCs with SIA configurations, as opposed to the 1000 mentioned for high-temperature configurations, can ease the process of training the network. Additionally, using GSFCs with SIA configurations guarantees that no atoms on the dislocation core will have a distance greater than 6, thus ensuring the closeness of the distances of these configurations to the dislocation cores.

The visualization of the distances between the atoms in all three regions of interest and the dataset reveals a significant reduction in distances after incorporating the high-temperature configurations (see Fig. 2(c)). The distribution of distances for each region before and after adding the high-temperature configurations is depicted in Fig. 2(d). Although a few atoms still have distances greater than 6 under the

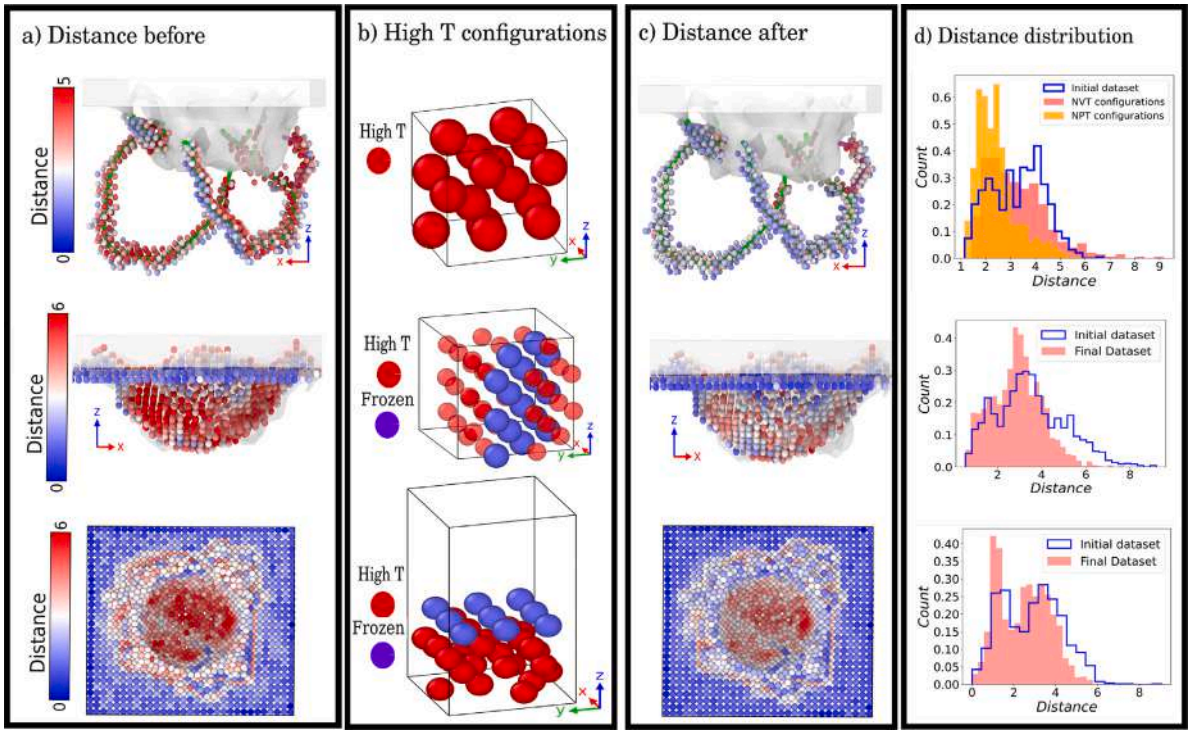

Fig. 2. Illustration of the novel configurations discovered in this study, which correspond to distinct regions of an indented sample. The figures are arranged horizontally to demonstrate the correlation between them. (a) The distances of the dislocation cores, atoms beneath the indenter tip, and pileup atoms on the surface from the original dataset. (b) The newly detected high-temperature configurations, which are associated with diverse regions of the indented sample, in terms of their distance. (c) The distance of the aforementioned regions shown in panel (a) after incorporating the newly found configurations to the dataset. (d) The distribution of distances of the aforementioned atoms from the dataset before and after incorporating the newly introduced configurations.

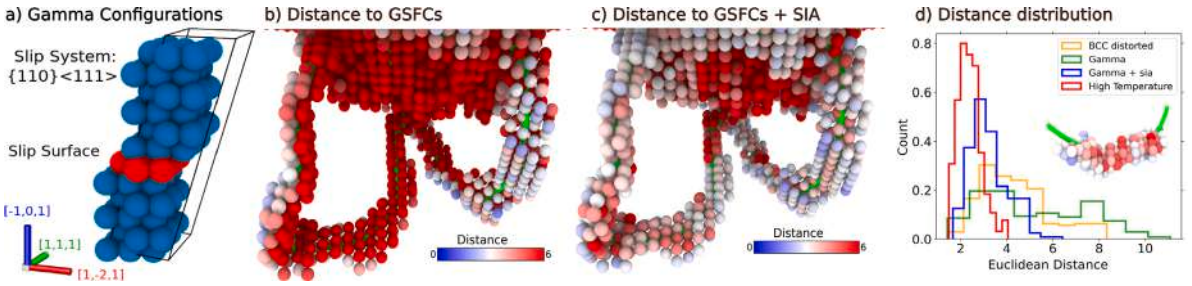

Fig. 3. The impact of incorporating GSFCs on the distances of atoms on dislocation cores from the dataset. (a) A schematic representation of the GSFCs integrated into the dataset. (b) Addition of GSFCs reduces the distances of atoms on the slip plane of dislocation cores from the dataset. (c) By including a SIA on the surface of GSFCs, all atoms on the dislocation cores can be covered. (d) The distribution of atom distances on dislocation cores reveals that GSFCs with SIA can effectively cover dislocation cores.

indenter tip, the number of such atoms has notably decreased after adding the appropriate configurations. Finally, because we are trying to develop a NNIP for the case of nanoindentation simulation during which atoms are compressed under the indenter tip, we added 300 compressed $3 \times 3 \times 4$ configurations with each of them including 72 atoms.

To further investigate the generalization of this distance-based approach, we calculated the distances of the indented samples acquired from the final trained NNIP from the final training dataset. The results are shown in Fig. S8 of the SM. The tail of the distance distributions is still lower than the threshold distance of 6 for all three regions of the indented sample. This demonstrates that the distance-based method used in this work could be expanded to mechanical simulations of at least other BCC materials.

2.4. DFT calculations

The DFT calculations were performed with the `Quantum Espresso` [71,72] (QE) package, using a norm-conserving PBEsol exchange–correlation functional [73–75] and 14 valence electrons. The Brillouin zone was sampled using Monkhorst–Pack method [76], and, from the convergence analysis of Fig. S2 in the SM, the k-point mesh and plane-wave cutoff energy in a Mo unit-cell were set to $8 \times 8 \times 8$ and 60 Ry, respectively. The selected k-point grid was rescaled for supercells calculations according to their dimension, implying the use of a $2 \times 2 \times 2$ grid for $4 \times 4 \times 4$ conventional super-cells, and was set to $1 \times 1 \times 1$ for any bigger configuration. Smearing was introduced within the Methfessel–Paxton method [77] to help convergence, with a spreading of 0.00735 Ry (0.1 eV). The structural properties, involving

elastic constants C_{ij}, Bulk modulus B (in the Voigt–Reuss–Hill approximation [78]) and Poisson ratio ν, have been computed running the QE driver `THERMO_PW` [79] on a Mo unit-cell.

The total energies of the configurations obtained from [63] were compared with the values calculated in our work to make sure of their consistency, which is shown in Fig. S4 of the SM.

2.5. Neural network training

In the PANNA framework, the environmental descriptors of each atom are provided as input to a fully connected network with two hidden layers, consisting of 256 and 128 nodes for the first and second layers, respectively, both with Gaussian activation function, and a single-node output layer with linear activation. The atomic environment is represented by a descriptor with 152 components, resulting in a network with 71808 weights and 385 biases. A batch size of 10 is utilized for training, while the model is trained using initial random weights and a constant learning rate of 10^{-4} throughout the training process. In this methodology, the energy of a configuration consisting of N atoms is defined as the sum of atomic energy contributions:

$$E = \sum_{i=1}^{N} E_i(G_i), \tag{7}$$

where E_i is the energy of atom i with a G-vector of G_i. The force on atom i which is situated at position $\vec{R}_i$ is given by:

$$\vec{F}_i = -\sum_j \sum_\mu \frac{\partial E_j}{\partial G_{j\mu}} \frac{\partial G_{j\mu}}{\partial \vec{R}_i} \tag{8}$$

with j labeling the atoms located within the cutoff distance of atom i and μ labeling the descriptor components.

To optimize the weights and bias parameters of the network, we use the Adam algorithm [80] to compute gradients of randomly selected batches of the training dataset. The loss function for optimizing the network weights, denoted collectively as W, consists of two terms, one for the energy $\mathcal{L}_E(W)$, and one for the forces, $\mathcal{L}_F(W)$:

$$\mathcal{L}(W) = \mathcal{L}_E(W) + \mathcal{L}_F(W). \tag{9}$$

The energy contribution is given by:

$$\mathcal{L}_E(W) = \sum_{s\in\text{batch}} \left[E_s^{\text{DFT}} - E_s(W)\right]^2 \tag{10}$$

where s refers to the atomic configuration, E_s^{DFT} is the total energy calculated from DFT (the target value) and $E_s(W)$ is the total energy predicted by the NNIP. The force contribution is given by:

$$\mathcal{L}_F(W) = \lambda_F \sum_{s\in\text{batch}} \sum_{i=1}^{N_s} \left|\vec{F}_{i;s}^{\text{DFT}} - \vec{F}_{i;s}(W)\right|^2 \tag{11}$$

with $\vec{F}_{i;s}^{\text{DFT}}$ the force obtained from DFT and $\vec{F}_{i;s}$ the force obtained from the NNIP, for atom i in configuration s; N_s is the total number of atoms in configuration s. The parameter λ_F adjusts the relative contribution of the force component and was set to $\lambda_F = 0.5$.

2.6. Nanoindentation simulations

2.6.1. Simulation method and parameters

To establish boundary conditions along the depth (dz) of the Mo samples, we divided them into three sections in the z direction during the initial stage: a frozen section with a width of approximately $0.02\times dz$, which ensured numerical cell stability; a thermostatic section about $0.08\times dz$ above the frozen section, which dissipated heat generated during nanoindentation; and a dynamical atoms section, where the interaction with the indenter tip modified the surface structure of the samples. Furthermore, we included a 5 nm vacuum section at the top of the sample as an open boundary [6]. We considered the indenter tip as a non-atomic repulsive imaginary (RI) rigid sphere and defined its force potential as

$$F(t) = K\left(\vec{r}(t) - R\right)^2, \tag{12}$$

where $K = 236$ eV/Å^3 (37.8 GPa) was the force constant, and $\vec{r}(t)$ was the position of the center of the tip as a function of time, with a radius $R = 3$ nm. In experiments, a Berkovich tip is used, which is spherical at the edge, matching our simulations and depth range studied [81]. We conducted molecular dynamics (MD) simulations using an NVE statistical thermodynamic ensemble and the velocity Verlet algorithm to emulate an experimental nanoindentation test. The x and y axes had periodic boundary conditions to simulate an infinite surface, while the z orientation had a fixed bottom boundary and a free top boundary in all MD simulations [20,34].

In our simulations, we chose $\vec{r}(t) = x_0\hat{x} + y_0\hat{y} + (z_0 \pm vt)\hat{z}$, where x_0 and y_0 were the center of the surface sample on the xy plane, and $z_0 = 0.5$ nm was the initial gap between the surface and the indenter tip. The tip moved with a speed of $v = 20$ m/s with a time step of $\Delta t = 1$ fs. We chose the maximum indentation depth to be 2.0 nm to avoid the influence of boundary layers in the dynamical atoms region.

2.6.2. Nanomechanical response of the material

The elastic nanocontact during loading process, P_{H}, is characterized by a Hertz fitting curve based on the sphere-flat surface contact and expressed [34,82] as:

$$P_{\text{H}} = \frac{4}{3} E_{\text{Hertz}} R^{1/2} h^{3/2}, \tag{13}$$

where R is the indenter radius, h is the indenter displacement, and E_{Hertz} is the reduced Young's modulus. Meanwhile, the contact pressure, P, is calculated by using a linear elastic contact mechanics formulation [5,34]:

$$P = 2\pi \left[24p \left(\frac{E_{\text{Y}} R}{1-\nu^2}\right)^2\right]^{1/3}, \tag{14}$$

with E_Y as the Young's modulus, p as the simulation load, R the indenter radius, and ν the Poisson's ratio; the radius of the contact area is obtained with the geometrical relationship:

$$\text{a}(h) = \left[3PR\left(1-\nu^2\right)/8E_{\text{Y}}\right]^{1/3} \tag{15}$$

which is related to the inner radius of the plastic region where the defects nucleate. These quantities provide an intrinsic measure of the surface resistance to a specific defect nucleation process [5,34], and yield to a universal linear relationship between P/E_Y and $a(h)/R_i$ given by

$$\frac{P}{E_Y} = \frac{0.844}{1-\nu^2} \frac{a(h)}{R_i}, \tag{16}$$

where $a(h)/R_i$ can be considered as the nanoindentation strain.

To determine the strength and stability of the Mo matrix under load, we compute the principal stress applied on the z direction as [9] :

$$\sigma_{zz} = -S\left[\left(1 - \frac{\arctan(\alpha)}{\alpha}\right)(1+\nu) - \frac{1}{2(1+1/\alpha^2)}\right], \tag{17}$$

where the quantities S and α are defined as:

$$S = \frac{3P_{\text{ave}}}{2\pi \text{a}(h)^2}, \quad \alpha = \frac{\text{a}(h)}{h}.$$

with h as the indentation depth and $a(h)$ the contact area between the indenter tip and the top atomic layers. The stress applied in the direction parallel to the indenter surface is then expressed as:

$$\sigma_{xx} = \sigma_{yy} = -\frac{S}{1+1/\alpha^2} \tag{18}$$

This gives the maximum shear stress:

$$\tau_{\max} = \frac{1}{2}\left(\sigma_{zz} - \sigma_{xx}\right), \tag{19}$$

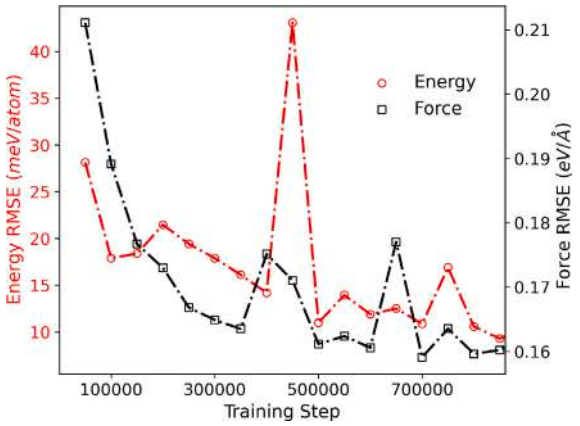

Fig. 4. Prediction of the Energies and forces for the validation set during the NNIP training.

that the material can withstand before it begins to undergo plastic deformation, being normalized by the applied pressure (equal to the applied force F divided by the contact area). The normalized depth is the distance from the surface of the material to the point at which the maximum shear stress occurs, normalized by the radius of the indenter that is used to apply the shear forces.

2.6.3. Defect analysis

In order to identify the defects in nanoindentation simulations, we apply the BCC Defect Analysis (BDA) developed by Möller and Biztek [83] which utilizes coordination number (CN), centrosymmetry parameter (CSP), and common neighbor analysis (CNA) techniques to detect typical defects found in bcc crystals. The characterization of the materials defects starts by calculating CN, CSP, and CNA values of all the atoms by considering a cutoff radius of $(1+\sqrt{2})/2a_0$ with a_0 as the lattice constant of Mo. Thus, the six next-nearest neighbors of perfect bcc atoms are into this cutoff and their CN value increases from 8 to 14. Consequently, BDA compares the CN and CSP values of each atom generating a list of non-bcc neighbors with CNA≠bcc and CN≠14 that classifies for the following typical defects: surfaces, vacancies, twin boundaries, screw dislocations, {110} planar faults, and edge dislocations.

2.6.4. Md simulation post-processing

All visualization of the simulations was performed using OVITO [84]. The surface areas for surface energy calculations were obtained using the “construct surface mesh" tool [85] in OVITO.

3. Results

3.1. NNIP validations

3.1.1. NNIP predictions for energies and forces

We assessed the accuracy of the trained NNIP by calculating the root mean square error (RMSE) for both energies per atom (E-RMSE) and forces components (F-RMSE) at each checkpoint saved during training. To ensure the reliability of the final model on unseen data, 10% of configurations of each structure type were reserved for validation prior to training. Fig. 4 shows that both the F-RMSE and E-RMSE decrease gradually as the network processes more data, reaching a plateau after 850 K training steps with minimum values of 9.2 meV/atom and 0.16 eV/Å, respectively.

The error distribution for both energies and forces are shown in the histogram plot of Fig. 5(a,b). The two islands in Fig. 5(a) are due to the energy difference between the pure and defected crystals. Also, the presence of three clusters in Fig. 5(b) is due to the large forces on the atoms in the defected configurations.

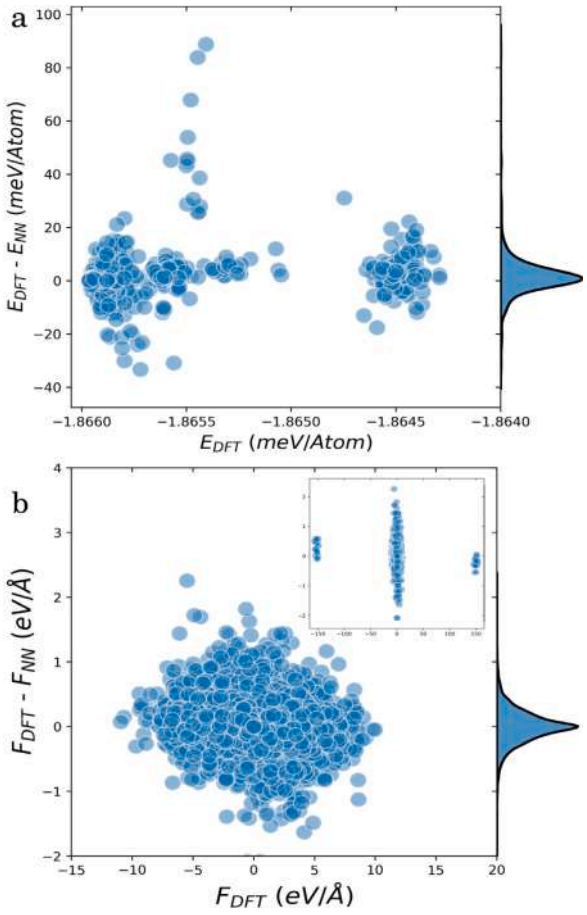

Fig. 5. NNIP error on **(a)** total energies and **(b)** forces of each atom.

3.1.2. Bulk validation

Next, we compare the elastic properties of the NNIP with both DFT and experimental results, as well as to those predicted by other interatomic potentials, such as GAP, tabGAP, and the EAM/FS potential, to evaluate the NNIP performance relative to other commonly used potentials. Table 3 summarizes the results of the comparison, explicitly reporting percentage errors with respect to the experimental values. The NNIP performs well for C_{11}, C_{44} and B, with percentage errors below 8% and in similar magnitude to GAP and EAM predictions. We here stress that the accurate prediction of the shear modulus, C_{44}, is crucial for simulating the stresses that are applied to the surface of the sample during nanoindentation, and, following the good results of EAM and GAP for this measure, the NNIP proves itself to be promising for such applications. While the largest error for the NNIP concerns the prediction of C_{12}, it can still be considered within a reasonable range as it does not exceedingly influence the prediction on B.[1]

3.1.3. NNIP accurately predicts generalized stacking fault energies (GSFE)

Finally, we compare the NNIP predictions for the GSFE against the DFT results, as well as other interatomic potentials mentioned in this work. The study focuses on the two most important slip systems of BCC crystals, namely the $\{110\}\langle\bar{1}11\rangle$ and $\{121\}\langle\bar{1}11\rangle$ families. The results were obtained for these directions in pure crystals. Additionally, since it was observed from Fig. 3 that $\{110\}\langle111\rangle$ GSF configurations with a $\langle111\rangle$ dumbbell interstitial on the surface are essential to cover the atomic environments of the dislocation core in terms of their distance

[1] We here remind that $B=\frac{1}{3}(C_{11}+2C_{12})$.

Table 3
Elastic constants C_{ij}, bulk modulus B, and Poisson ratio ν, as obtained with the GAP, tabGAP, EAM/FS and the NNIP potentials compared to DFT done in this work and experimental data. In parenthesis is reported the modulus of the percentage error with respect to the experimental value.

	GAP	tabGap	EAM	NNIP	DFT[a]	DFT[b]	Exp[c]
C_{11} (GPa)	478 (3.02%)	494 (6.47%)	465 (0.22%)	452 (2.59%)	459	468	464
C_{12} (GPa)	166 (4.40%)	146 (8.18%)	161 (1.26%)	121 (23.90%)	162	155	159
C_{44} (GPa)	108 (0.92%)	87 (20.18%)	109 (0%)	111 (1.83%)	97	100	109
B (GPa)	270 (8.00%)	262 (4.80%)	263 (5.20%)	231 (7.60%)	262	–	250
ν	0.26 (10.34%)	0.23 (20.69%)	0.26 (10.34%)	0.21 (27.59%)	0.30	–	0.29

[a] This work.
[b] Ref. [63].
[c] Ref. [86].

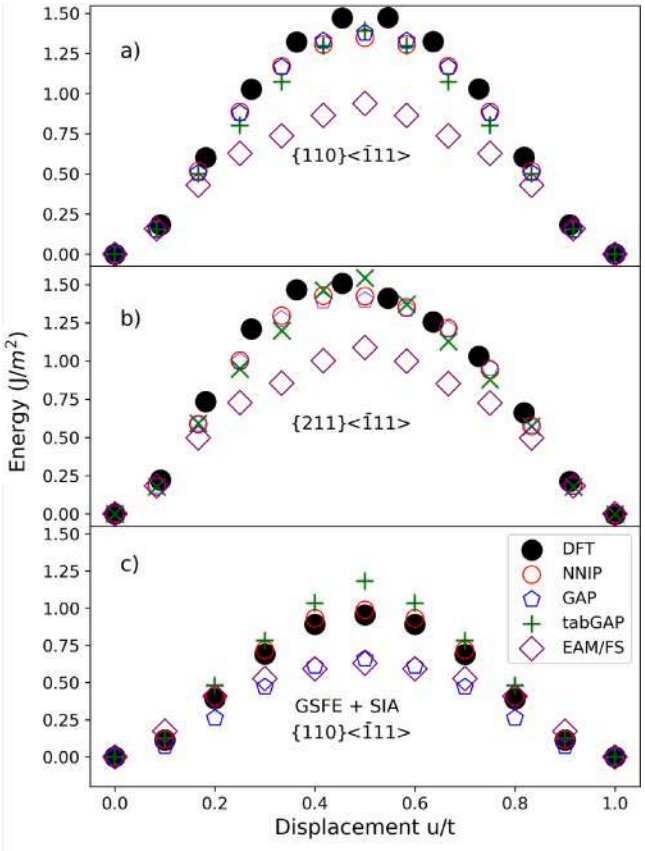

Fig. 6. Generalized Stacking Fault Energy (GSFE) for single crystalline Molybdenum for: (a) $\{110\}\langle\bar{1}11\rangle$ and (b) $\{211\}\langle\bar{1}11\rangle$. (c) The GSFE curve for the "GSFCs + SIA" configurations.

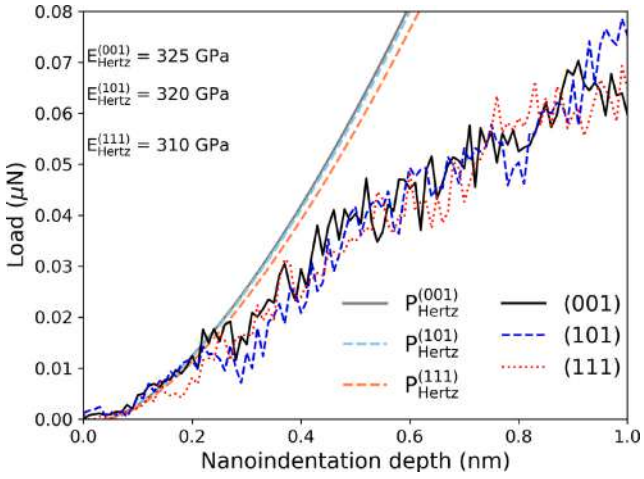

Fig. 7. Load–displacement curves for different crystal orientations, incorporating a Hertz fitting curve in the elastic region. The obtained values for the reduced Young's modulus are consistent with results from various computational approaches and experimental data [90]. Specifically, the (001), (011), and (111) crystal orientations show good agreement between experimental and simulated values, highlighting the accuracy of the developed interatomic potential, NNIP method, and ML-based atomistic approach in predicting mechanical properties.

to the indented samples, we also calculated and compared the GSFE for these configurations.

Fig. 6 shows that all potentials predict the GSFE very accurately for both slip system families and pure crystals. However, EAM/FS displays errors of about 50% and 32% for the peak of the curve for $\{110\}\langle\bar{1}11\rangle$ and $\{121\}\langle\bar{1}11\rangle$ slip families, respectively. The configurations associated with these curves are crucial, as they represent the atoms on the slip plane of an indented sample, as illustrated and discussed in Fig. 3. While it is important for an interatomic potential to accurately predict the GSFE curve for reliable dislocation modeling, it is equally crucial for the potential to correctly predict the energies and forces on the atoms for the dislocation cores. Therefore, in addition to the GSFE curves for pure crystals, we calculated the GSFE curve for configurations with a $\langle 111\rangle$ dumbbell interstitial on the surface. As depicted in Fig. 6(c), NNIP is the potential that best predicts these energies, indicating the accurate simulation of dislocation dynamics during nanoindentation. In contrast, GAP and EAM potentials showed errors of 40% and tabGAP showed an error of 20% against DFT results, indicating their inability to accurately predict these values. This is discussed further in the following section.

In Table S1 and Table S2 of the Supplementary Information, we report a comparison in the prediction of the Critical Resolved Shear (CRS) Peierls barrier and stress for the different potentials with respect to DFT level for two different Mo sample orientations. The results were obtained using the PNADIS [87] automated Peierls–Nabarro [88,89] analyzer for dislocation core structure and slip resistance. Among the inputs for the calculation are: the Poisson ratio and the Shear modulus (reportend in the Table), the burger vector and the GSFE for each potential. As it can be observed, for the $\{110\}\langle\bar{1}11\rangle$ Mo sample the NNIP provides the best energy barrier and stress predictions in comparison to DFT-accuracy. While the GAP and EAM potential underestimate in a similar way the result, tabGAP fails to capture a valuable estimate with substantial overestimates. For the $\{211\}\langle\bar{1}11\rangle$ Mo sample, similar observations can be made, with the exception of the NNIP result being close to the GAP and EAM overestimates.

3.2. Nanoindentation MD simulations

3.2.1. NNIP achieves experimentally accurate results in the hertzian regime

In Fig. 7, the load–displacement curves for the three main crystal orientations are presented, including a Hertz fitting curve in the elastic region [82]. The obtained values for the reduced Young's modulus align well with results from other computational methods and experimental data [20,90]. Specifically, for the (001) crystal orientation, the experimental value is 327 GPa, while our MD simulation with

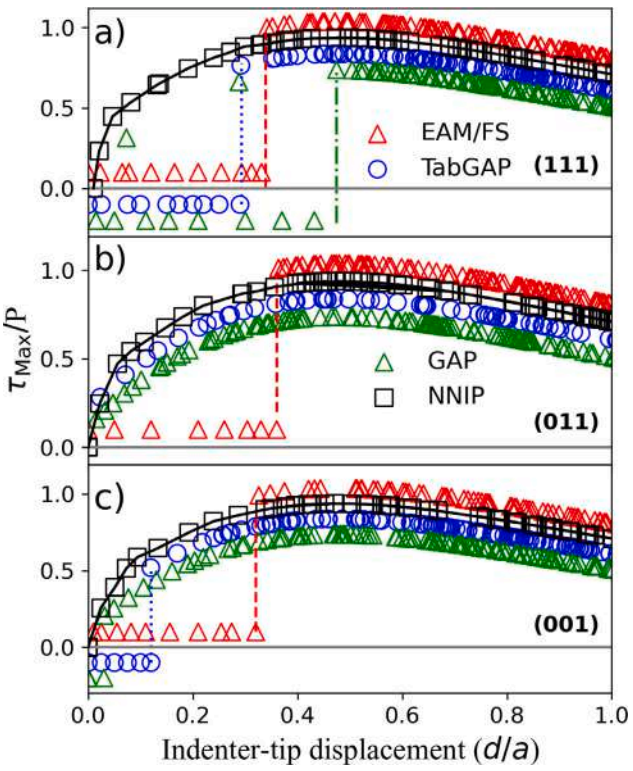

Fig. 8. Hertzian calculation of normalized maximum shear stress by the applied pressure, τ_{max}/P, as a function of normalized depth for main crystal orientations. Surface information is needed in the interatomic potentials to model nanoindentation induced plasticity in the range of 0.0 to 0.475 d/a. To aid the interpretation of the results, the values for EAM/FS were shifted by −0.1, the values for GAP were shifted by +0.2, and the values for tabGAP were shifted by +0.1 (all values in units of τ_{max}/P).

the developed NNIP yields 325 GPa. For the (011) orientation, the experimental value is 321 GPa, and NNIP method results in 320 GPa. Lastly, for the (111) orientation, the experimental value is 309 GPa, and our ML-based atomistic approach gives 310 GPa. Although these results are in excellent agreement with experimental data, the behavior of the loading curve can be obtained in a similar way by other interatomic potentials, as discussed in our previous work [34].

3.2.2. NNIP provides an informative surface energy landscape

In Fig. 8 we show results for the normalized maximum shear stress τ_{max}/P which is a dimensionless quantity, with P being the applied pressure (Eq. (14)) and τ_{max} the shear stress (Eq. (19)) calculated by using a linear elastic contact mechanics formulation [5,34], as a function of the displacement d for [001], [011], and [111] main crystal orientations [34]. A detailed explanation of the normalized shear stress calculation is provided in the Methods section. Our MD simulations report enough surface energy to model the nanoindentation induced plasticity as observed at distances close to the sample surface regardless of the crystal orientation, which is challenging for traditional and current ML interatomic potentials for BCC Mo. The modeling of the nanocontact of the indenter tip and the top atomic layers of the surface, from 0 to $\sim$ 0.3 d/a range with d the indentation depth and a the contact area, is important due to the nucleation of dislocation being dependent on this mechanisms.

The GAP simulations provide valuable insights into the interaction between the indenter tip and the top layer atoms for the (001) and (011) orientations. However, for the (111) orientation, this information is lacking, resulting in a limitation in accurately modeling the nanoindentation test before the yield point. This limitation arises due to the absence of the relevant atomic configurations in the training data for this specific potential. As a consequence, the tabGAP simulations follow a similar trend for the (111) orientation, reflecting the lack of detailed information on the interaction between the tip and the surface atoms.

In contrast, the NNIP simulations incorporate sufficient information on surface structures, allowing for a more accurate representation of the contact area. This is particularly important as the contact area depends on the applied load. The computed force between the tip and the atoms comprising the contact area is well-modeled in the NNIP simulations. The difference in spacing between data points in the elastic part of the graph is attributed to variations in the loading force, pressure, and maximum shear stress, which are considered in the contact area analysis. In addition, accurately describing the interaction between the indenter tip and the topmost atomic layers during the initial stages of nanoindentation loading is crucial for analyzing the effect of loading rate on the pop-in event. This is because the initial interaction can significantly influence the critical load required for pop-in to occur. Our NNIP simulations successfully captured the decrease in critical load with increasing loading rate (Fig. S7 in the SM), as observed experimentally [16] for different materials and in our previous work for BCC metals [34]. This suggests that NNIP effectively models the influence of the early-stage interaction on pop-in behavior. In contrast, the TabGAP simulations predicted a constant critical load regardless of loading rate, as shown in the supplementary material.

3.2.3. NNIP achieves experimentally accurate results for slip traces

In Fig. 9, we compare the results from NNIP simulations with experimental observations obtained via scanning electron microscopy (SEM) coupled with electron backscatter diffraction (EBSD) [90]. The experimental setup involved indenting a (001) Mo grain using a Berkovich tip. The computational modeling accounts for the Berkovich tip's roundness, which typically has a radius ranging from 50 to 100 nm, enabling a comparison with the early stages of nanoindentation. Upon comparing the MD simulation results obtained with different potentials to the experimental data, we find that the propagation of the slip trace along the [-110] direction closely resembles the four-folded rosette pattern observed in the MD simulation by NNIP potentials. However, notable discrepancies arise in the representation of surface information, particularly at this crystal orientation, where the NNIP simulations managed to capture the formation of pile-ups in good agreement with the experimental observations. While TabGAP and EAM potential exhibits limitations in representing the formation of pileups around the indenter tip.

From the results depicted in Fig. 8, it is evident that the interatomic potentials have limitations in representing the plastic deformation mechanisms across various crystal orientations. Specifically, for the [001] orientation, NNIP demonstrates excellent agreement with experimental data regarding surface morphology and mechanical properties. Motivated by these findings, we further investigate the surface behavior of the Mo sample at the [111] orientation, where NNIP has shown improved representation of the transition from elastic to plastic deformation compared to other potentials. In Fig. 10, we display the atomic displacement mapping of the [111] Mo sample obtained by NNIP in (a), EAM/FS in (b), GAP in (c), and tabGAP in (d) at the maximum indentation depth. The surface of the sample clearly shows displaced atoms aligned with the slip planes, forming the characteristic three-fold rosette pattern typical for BCC materials in the [111] orientation, as illustrated by the NNIP results in Fig. 10(a)). This pattern is created by $[11\bar{2}]$, $[\bar{1}01]$, and $[0\bar{1}1]$ planes [5,6]. To assist in identifying the shape of the rosette, we have added orange lines, reminiscent of what can be observed in SEM images of BCC materials [9]. Here NNIP simulations are in good agreement with typical observations of pile-up evolution. However, it is important to note that neither GAP, tabGAP, nor EAM can provide a comprehensive description due to their lack of information about open boundary simulation under external loading.

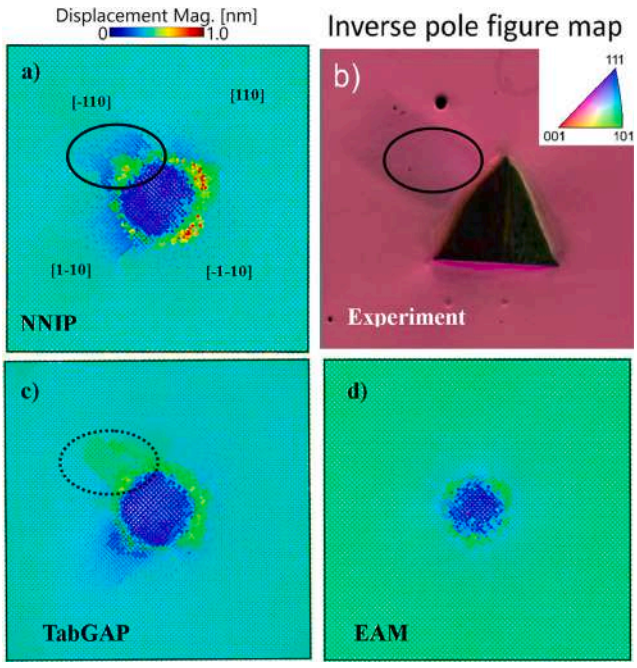

Fig. 9. Slip traces and pileup of [001] Mo at the maximum indentation depth for NNIP in (a), TabGAP in (c), and EAM in (d), compared to an experimental SEM observation reported in Ref. [90] (b). The four-fold rosette is well modeled by NNIP where the slip trace propagates on the [-110] and [1-10] planes in good qualitative agreement with the experimental result.

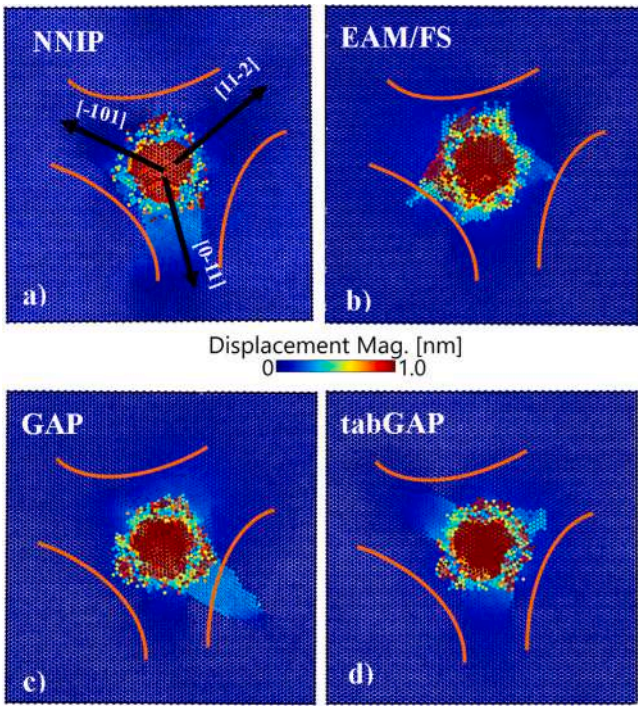

Fig. 10. Pileups and slip trace for the [111] Mo samples , at the maximum indentation depth, using different methods: NNIP in (a), EAM/FS in (b), GAP in (c), and tabGAP in (d). In this analysis, we have included an orange line to emphasize the 3-fold rosette characteristic commonly seen in the indentation of BCC samples where NNIP simulations are capable to model it [5,20,34]. (For interpretation of the references to color in this figure legend, the reader is referred to the web version of this article.)

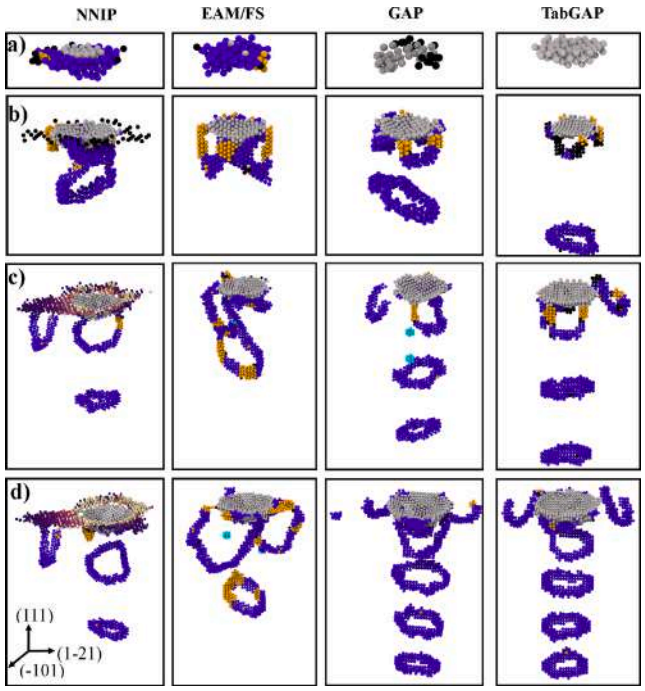

Fig. 11. Identified defects of indented (111) Mo sample by BDA method at different depths by NNIP, EAM, TabGAP, and GAP approaches. The various defect types are depicted using different colors: gray spheres represent surface atoms in direct contact with the indenter tip, blue spheres indicate edge dislocations, light-blue spheres represent atoms in the vicinity of vacancies, yellow spheres depict twin/screw dislocations, and black spheres highlight unidentified defect atoms. The nucleation and propagation of edge dislocations on the {111} slip family are observed, which then evolve into prismatic loops. In addition, identified slip traces and pile-ups are well modeled by NNIP simulations showing the well-known three-fold symmetric rosette depths below 1.45 nm that are formed by $[11\bar{2}]$, $[\bar{1}01]$ and $[0\bar{1}1]$ planes. (For interpretation of the references to color in this figure legend, the reader is referred to the web version of this article.)

3.2.4. NNIP demonstrates discernible dislocation nucleation stages

Fig. 11 illustrates the defects detected using the BCC Defect Analysis (BDA) method (see Methods) in a (111) Mo sample at different depths [83]. The NNIP nanoindentation simulations in the initial stages of loading process notably enhance the description of the interaction between the indenter tip and the atoms in the uppermost layers of the surface (see Fig. 11(a)). In this context, a few Mo atoms located at the very top surface layer are recognized as surface defects. Additionally, Mo atoms situated beneath these surface defects begin to coalesce, forming edge dislocations that have the potential to evolve into shear loops, contrary to the other simulations where the interatomic potentials are not aware of this mechanism. NNIP simulations are also anticipated to accurately capture the nucleation and propagation of shear loops on {112} planes (See Fig. 11(b)), as observed experimentally in BCC materials [5,9,91]. Furthermore, NNIP effectively models the nucleation of loops through a lasso mechanism, a behavior where GAP and tabGAP induced the formation of multiple loops, as observed in Fig. 11(c) at a depth of 1.45 nm. For NNIP, at the maximum indentation depth, it is evident on the sample's surface that displaced atoms align with the slip planes in a characteristic three-folded rosette pattern typical for BCC materials in the [111] orientation (Fig. 11(d)), formed by $[11\bar{2}]$, $[\bar{1}01]$, and $[0\bar{1}1]$ planes. In contrast, neither GAP nor tabGAP, nor EAM, can adequately incorporate this description due to the lack of information regarding pileup formations. Besides, the nucleation of more loops is noted, but the circumference of the second loop is larger than that of the first loop. The EAM and tabGAP simulations demonstrate a slower and faster process, respectively.

The variations in dislocation and loop nucleations across different potentials originate from two factors: (1) the prediction of the GSFE

+ SIA curve (Fig. 6(c)) varies across different potentials, and (2) the indentation surface energy as a function of depth differs among potentials, as demonstrated in Fig. S9 of the SM.

4. Discussion and conclusions

Interatomic potentials developed before the present work, although adequate for many applications, need to be improved for nanoindentation simulations. For example, J. Byggmästar et al. [63] developed a GAP potential for Mo, demonstrating accuracy and transferability for elastic, thermal, liquid, defect, and surface properties. However, this potential failed to produce reliable data for the shear stress in the elastic region in the early stages of the nanoindentation simulation. Furthermore, in contrast to the NNIP developed here, many prismatic loops were nucleated during the nanoindentation (see Fig. 11), potentially due to insufficient information in the energy landscape regarding the dislocation cores, a fact that was illustrated based on the similarity of the GSF configurations with the dislocation cores as depicted in Fig. 6.

The tabGAP potentials are designed for complex multi-element materials [48], employing simple low-dimensional descriptors. Although tabGAP potentials have notable accuracy for entropy alloys [62], the same issues as the GAP potential arise when it comes to single element BCC Mo. As mentioned earlier, the tabGAP potential leads to nucleation of too many prismatic dislocation loops in the nanoindentation simulations (see Fig. 11). Moreover, accurate predictions of shear stress in the initial phases of the nanoindentation simulations were not achieved.

The EAM/FS potential utilized in the present work [65], originally designed for radiation damage simulations, failed to accurately produce GSFE curve for Mo in both pristine crystalline and GSF configurations representing dislocation cores. Consequently, it is unclear whether or not this potential can reliably predict dislocation nucleation during indentation. In addition, similar to the other potentials, it does not correctly predict the nanoindentation shear stress.

Considering the challenges faced in nanoindentation simulations, the presence of a well-developed methodology to tackle these issues would be highly beneficial. In this work, we met this goal by introducing to the training dataset new configurations which resemble the local atomic environments of an indented sample. The similarity measurements presented here ensure the relevance of the newly introduced structures to a nanoindentation simulation. To the best of our knowledge, this study represents the first attempt to develop a MLFF specifically designed for nanoindentation simulations. The novel configurations introduced here could aid the development of MLFFs for other materials.

CRediT authorship contribution statement

Amirhossein D. Naghdi: Writing – review & editing, Writing – original draft, Visualization, Validation, Methodology, Formal analysis, Data curation, Conceptualization. **Franco Pellegrini:** Writing – review & editing, Methodology, Investigation, Formal analysis, Conceptualization. **Emine Küçükbenli:** Writing – review & editing, Methodology, Investigation, Conceptualization. **Dario Massa:** Writing – review & editing, Methodology, Data curation. **F. Javier Dominguez–Gutierrez:** Writing – review & editing, Visualization, Methodology, Data curation. **Efthimios Kaxiras:** Writing – review & editing, Supervision, Formal analysis, Conceptualization. **Stefanos Papanikolaou:** Writing – review & editing, Supervision, Methodology, Investigation, Formal analysis, Conceptualization.

Declaration of competing interest

The authors declare that they have no known competing financial interests or personal relationships that could have appeared to influence the work reported in this paper.

Acknowledgments

We acknowledge support from the European Union Horizon 2020 Research and Innovation Programme under grant agreement no. 857470 and from the European Regional Development Fund via the Foundation for Polish Science International Research Agenda PLUS program grant No. MAB PLUS/2018/8.

Appendix A. Supplementary data

Supplementary material related to this article can be found online at https://doi.org/10.1016/j.actamat.2024.120200.

References

[1] J.-Y. Kim, J.R. Greer, Tensile and compressive behavior of gold and molybdenum single crystals at the nano-scale, Acta Mater. 57 (17) (2009) 5245–5253, http://dx.doi.org/10.1016/j.actamat.2009.07.027, URL https://www.sciencedirect.com/science/article/pii/S1359645409004510.

[2] J.-Y. Kim, D. Jang, J.R. Greer, Crystallographic orientation and size dependence of tension–compression asymmetry in molybdenum nano-pillars, Int. J. Plast. 28 (1) (2012) 46–52, http://dx.doi.org/10.1016/j.ijplas.2011.05.015, URL https://www.sciencedirect.com/science/article/pii/S0749641911000994.

[3] M. Motamedi, A. Naghdi, S. Jalali, Effect of temperature on properties of aluminum/single-walled carbon nanotube nanocomposite by molecular dynamics simulation, Proc. Inst. Mech. Eng. C 234 (2) (2020) 635–642, http://dx.doi.org/10.1177/0954406219878760.

[4] C.A. Schuh, Nanoindentation studies of materials, Mater. Today 9 (5) (2006) 32–40, http://dx.doi.org/10.1016/S1369-7021(06)71495-X.

[5] J. Varillas, J. Ocenasek, J. Torner, J. Alcala, Unraveling deformation mechanisms around FCC and BCC nanocontacts through slip trace and pileup topography analyses, Acta Mater. 125 (2017) 431–441, http://dx.doi.org/10.1016/j.actamat.2016.11.067.

[6] L. Kurpaska, F. Dominguez-Gutierrez, Y. Zhang, K. Mulewska, H. Bei, W. Weber, A. Kosińska, W. Chrominski, I. Jozwik, R. Alvarez-Donado, S. Papanikolaou, J. Jagielski, M. Alava, Effects of Fe atoms on hardening of a nickel matrix: Nanoindentation experiments and atom-scale numerical modeling, Mater. Des. 217 (2022) 110639, http://dx.doi.org/10.1016/j.matdes.2022.110639, URL https://www.sciencedirect.com/science/article/pii/S026412752200260X.

[7] S. Pathak, S.R. Kalidindi, Spherical nanoindentation stress strain curves, Mater. Sci. Eng. R 91 (2015) 1–36.

[8] G.Z. Voyiadjis, M. Yaghoobi, Review of nanoindentation size effect: Experiments and atomistic simulation, Crystals 7 (10) (2017) 321.

[9] T. Remington, C. Ruestes, E. Bringa, B. Remington, C. Lu, B. Kad, M. Meyers, Plastic deformation in nanoindentation of tantalum: A new mechanism for prismatic loop formation, Acta Mater. 78 (2014) 378–393, http://dx.doi.org/10.1016/j.actamat.2014.06.058, URL https://www.sciencedirect.com/science/article/pii/S1359645414004881.

[10] J. Gagel, D. Weygand, P. Gumbsch, Formation of extended prismatic dislocation structures under indentation, Acta Mater. 111 (2016) 399.

[11] A. Naghdi, F.J. Dominguez-Gutierrez, W.Y. Huo, K. Karimi, S. Papanikolaou, Dynamic nanoindentation and short-range order in equiatomic nicocr medium entropy alloy lead to novel density wave ordering, 2022, arXiv:2211.05436.

[12] M. Taneike, F. Abe, K. Sawada, Creep-strengthening of steel at high temperatures using nano-sized carbonitride dispersions, Nature 424 (6946) (2003) 294–296, http://dx.doi.org/10.1038/nature01740.

[13] M.A. Haque, M.T.A. Saif, In-situ tensile testing of nano-scale specimens in SEM and TEM, Exp. Mech. 42 (1) (2002) 123–128, http://dx.doi.org/10.1007/BF02411059.

[14] J.T.M. De Hosson, W.A. Soer, A.M. Minor, Z. Shan, E.A. Stach, S.A. Syed Asif, O.L. Warren, In situ TEM nanoindentation and dislocation-grain boundary interactions: a tribute to david brandon, J. Mater. Sci. 41 (23) (2006) 7704–7719, http://dx.doi.org/10.1007/s10853-006-0472-2.

[15] K. Durst, B. Backes, M. Göken, Indentation size effect in metallic materials: Correcting for the size of the plastic zone, Scr. Mater. 52 (11) (2005) 1093–1097, http://dx.doi.org/10.1016/j.scriptamat.2005.02.009, URL https://www.sciencedirect.com/science/article/pii/S1359646205000941.

[16] Maier-Kiener, Verena, Durst, Karsten, Advanced nanoindentation testing for studying strain-rate sensitivity and activation volume, JOM 69 (11) (2017) 2246–2255, http://dx.doi.org/10.1007/s11837-017-2536-y.

[17] O. Casals, J. Očenašek, J. Alcala, Crystal plasticity finite element simulations of pyramidal indentation in copper single crystals, Acta Mater. 55 (1) (2007) 55–68, http://dx.doi.org/10.1016/j.actamat.2006.07.018, URL https://www.sciencedirect.com/science/article/pii/S1359645406005295.

[18] R. Smith, D. Christopher, S.D. Kenny, A. Richter, B. Wolf, Defect generation and pileup of atoms during nanoindentation of Fe single crystals, Phys. Rev. B 67 (2003) 245405, http://dx.doi.org/10.1103/PhysRevB.67.245405, URL https://link.aps.org/doi/10.1103/PhysRevB.67.245405.

[19] S. Swaddiwudhipong, K. Tho, J. Hua, Z. Liu, Mechanism-based strain gradient plasticity in C0 axisymmetric element, Int. J. Solids Struct. 43 (5) (2006) 1117–1130, http://dx.doi.org/10.1016/j.ijsolstr.2005.05.026, URL https://www.sciencedirect.com/science/article/pii/S0020768305002921.

[20] F. Dominguez-Gutierrez, S. Papanikolaou, A. Esfandiarpour, P. Sobkowicz, M. Alava, Nanoindentation of single crystalline Mo: Atomistic defect nucleation and thermomechanical stability, Mater. Sci. Eng. A 826 (2021) 141912, http://dx.doi.org/10.1016/j.msea.2021.141912, URL https://www.sciencedirect.com/science/article/pii/S0921509321011783.

[21] D. Kramer, K. Yoder, W. Gerberich, Surface constrained plasticity: Oxide rupture and the yield point process, Phil. Mag. A 81 (2001) 2033–2058, http://dx.doi.org/10.1080/01418610108216651.

[22] M.M. Biener, J. Biener, A.M. Hodge, A.V. Hamza, Dislocation nucleation in BCC Ta single crystals studied by nanoindentation, Phys. Rev. B 76 (2007) 165422, http://dx.doi.org/10.1103/PhysRevB.76.165422, URL https://link.aps.org/doi/10.1103/PhysRevB.76.165422.

[23] G.Z. Voyiadjis, D. Faghihi, Microstructure to macro-scale using gradient plasticity with temperature and rate dependent length scale, Procedia IUTAM 3 (2012) 205–227, http://dx.doi.org/10.1016/j.piutam.2012.03.014, IUTAM Symposium on Linking Scales in Computations: From Microstructure to Macro-scale Properties, URL https://www.sciencedirect.com/science/article/pii/S2210983812000156.

[24] K.P.E. Plummer, The Temperature Dependence of Plasticity in Molybdenum (Ph.D. thesis), University of Oxford, 2019.

[25] K. Frydrych, F. Dominguez-Gutierrez, M. Alava, S. Papanikolaou, Multiscale nanoindentation modelling of concentrated solid solutions: A continuum plasticity model, Mech. Mater. 181 (2023) 104644, http://dx.doi.org/10.1016/j.mechmat.2023.104644, URL https://www.sciencedirect.com/science/article/pii/S016766362300090X.

[26] J.A. Knapp, D.M. Follstaedt, S.M. Myers, J.C. Barbour, T.A. Friedmann, Finite-element modeling of nanoindentation, J. Appl. Phys. 85 (3) (1999) 1460–1474, http://dx.doi.org/10.1063/1.369178, arXiv:https://pubs.aip.org/aip/jap/article-pdf/85/3/1460/10597542/1460_1_online.pdf.

[27] M. Lichinchi, C. Lenardi, J. Haupt, R. Vitali, Simulation of berkovich nanoindentation experiments on thin films using finite element method, Thin Solid Films 312 (1) (1998) 240–248, http://dx.doi.org/10.1016/S0040-6090(97)00739-6, URL https://www.sciencedirect.com/science/article/pii/S0040609097007396.

[28] C. Zhou, S.B. Biner, R. LeSar, Discrete dislocation dynamics simulations of plasticity at small scales, Acta Mater. 58 (5) (2010) 1565–1577, http://dx.doi.org/10.1016/j.actamat.2009.11.001, URL https://www.sciencedirect.com/science/article/pii/S1359645409007678.

[29] C. Motz, D. Weygand, J. Senger, P. Gumbsch, Micro-bending tests: A comparison between three-dimensional discrete dislocation dynamics simulations and experiments, Acta Mater. 56 (9) (2008) 1942–1955, http://dx.doi.org/10.1016/j.actamat.2007.12.053, URL https://www.sciencedirect.com/science/article/pii/S1359645408000062.

[30] H. Song, H. Yavas, E.V. der Giessen, S. Papanikolaou, Discrete dislocation dynamics simulations of nanoindentation with pre-stress: Hardness and statistics of abrupt plastic events, J. Mech. Phys. Solids 123 (2019) 332–347, http://dx.doi.org/10.1016/j.jmps.2018.09.005, The N.A. Fleck 60th Anniversary Volume, URL https://www.sciencedirect.com/science/article/pii/S0022509618305027.

[31] G. Po, M.S. Mohamed, T. Crosby, C. Erel, A. El-Azab, N. Ghoniem, Recent progress in discrete dislocation dynamics and its applications to micro plasticity, JOM 66 (10) (2014) 2108–2120, http://dx.doi.org/10.1007/s11837-014-1153-2.

[32] R. Santos-Güemes, G. Esteban-Manzanares, I. Papadimitriou, J. Segurado, L. Capolungo, J. LLorca, Discrete dislocation dynamics simulations of dislocation-θ' precipitate interaction in Al-Cu alloys, J. Mech. Phys. Solids 118 (2018) 228–244, http://dx.doi.org/10.1016/j.jmps.2018.05.015, URL https://www.sciencedirect.com/science/article/pii/S0022509617310037.

[33] Q. Xu, A. Zaborowska, K. Mulewska, W. Huo, K. Karimi, F.J. Domínguez-Gutiérrez, Ł. Kurpaska, M.J. Alava, S. Papanikolaou, Atomistic insights into nanoindentation-induced deformation of alpha-Al2O3 single crystals, Vacuum 219 (2024) 112733, http://dx.doi.org/10.1016/j.vacuum.2023.112733, URL https://www.sciencedirect.com/science/article/pii/S0042207X23009302.

[34] F.J. Domínguez-Gutiérrez, P. Grigorev, A. Naghdi, J. Byggmästar, G.Y. Wei, T.D. Swinburne, S. Papanikolaou, M.J. Alava, Nanoindentation of tungsten: From interatomic potentials to dislocation plasticity mechanisms, Phys. Rev. Mater. 7 (2023) 043603, http://dx.doi.org/10.1103/PhysRevMaterials.7.043603, URL https://link.aps.org/doi/10.1103/PhysRevMaterials.7.043603.

[35] A.H. Naghdi, K. Karimi, A.E. Poisvert, A. Esfandiarpour, R. Alvarez, P. Sobkowicz, M. Alava, S. Papanikolaou, Dislocation plasticity in equiatomic NiCoCr alloys: Effect of short-range order, Phys. Rev. B 107 (2023) 094109, http://dx.doi.org/10.1103/PhysRevB.107.094109, URL https://link.aps.org/doi/10.1103/PhysRevB.107.094109.

[36] K. Karimi, A. Esfandiarpour, S. Papanikolaou, Serrated plastic flow in slowly-deforming complex concentrated alloys: universal signatures of dislocation avalanches, 2023, arXiv:2310.03828.

[37] K. Karimi, S. Papanikolaou, Tuning brittleness in multi-component metallic glasses through chemical disorder aging, 2023, arXiv:2309.11867.

[38] J. Behler, M. Parrinello, Generalized neural-network representation of high-dimensional potential-energy surfaces, Phys. Rev. Lett. 98 (2007) 146401, http://dx.doi.org/10.1103/PhysRevLett.98.146401, URL https://link.aps.org/doi/10.1103/PhysRevLett.98.146401.

[39] A.P. Bartók, M.C. Payne, R. Kondor, G. Csányi, Gaussian approximation potentials: The accuracy of quantum mechanics, without the electrons, Phys. Rev. Lett. 104 (2010) 136403, http://dx.doi.org/10.1103/PhysRevLett.104.136403, URL https://link.aps.org/doi/10.1103/PhysRevLett.104.136403.

[40] A. Thompson, L. Swiler, C. Trott, S. Foiles, G. Tucker, Spectral neighbor analysis method for automated generation of quantum-accurate interatomic potentials, J. Comput. Phys. 285 (2015) 316–330, http://dx.doi.org/10.1016/j.jcp.2014.12.018, URL https://www.sciencedirect.com/science/article/pii/S0021999114008353.

[41] A.V. Shapeev, Moment tensor potentials: A class of systematically improvable interatomic potentials, Multiscale Model. Simul. 14 (3) (2016) 1153–1173, http://dx.doi.org/10.1137/15M1054183.

[42] A. Glielmo, C. Zeni, A. De Vita, Efficient nonparametric n-body force fields from machine learning, Phys. Rev. B 97 (2018) 184307, http://dx.doi.org/10.1103/PhysRevB.97.184307, URL https://link.aps.org/doi/10.1103/PhysRevB.97.184307.

[43] L. Zhang, J. Han, H. Wang, R. Car, W. E, Deep potential molecular dynamics: A scalable model with the accuracy of quantum mechanics, Phys. Rev. Lett. 120 (2018) 143001, http://dx.doi.org/10.1103/PhysRevLett.120.143001, URL https://link.aps.org/doi/10.1103/PhysRevLett.120.143001.

[44] J. Behler, Perspective: Machine learning potentials for atomistic simulations, J. Chem. Phys. 145 (17) (2016) 170901, http://dx.doi.org/10.1063/1.4966192.

[45] Y. Shaidu, E. Küçükbenli, R. Lot, F. Pellegrini, E. Kaxiras, S. de Gironcoli, A systematic approach to generating accurate neural network potentials: the case of carbon, npj Comput. Mater. 7 (1) (2021) 52, http://dx.doi.org/10.1038/s41524-021-00508-6.

[46] Q.-J. Li, E. Küçükbenli, S. Lam, B. Khaykovich, E. Kaxiras, J. Li, Development of robust neural-network interatomic potential for molten salt, Cell Rep. Phys. Sci. 2 (3) (2021) 100359, http://dx.doi.org/10.1016/j.xcrp.2021.100359, URL https://www.sciencedirect.com/science/article/pii/S2666386421000448.

[47] Y. Shiihara, R. Kanazawa, D. Matsunaka, I. Lobzenko, T. Tsuru, M. Kohyama, H. Mori, Artificial neural network molecular mechanics of iron grain boundaries, Scr. Mater. 207 (2022) 114268, http://dx.doi.org/10.1016/j.scriptamat.2021.114268, URL https://www.sciencedirect.com/science/article/pii/S1359646221005480.

[48] J. Byggmästar, K. Nordlund, F. Djurabekova, Simple machine-learned interatomic potentials for complex alloys, Phys. Rev. Mater. 6 (2022) 083801, http://dx.doi.org/10.1103/PhysRevMaterials.6.083801, URL https://link.aps.org/doi/10.1103/PhysRevMaterials.6.083801.

[49] J. Vandermause, S.B. Torrisi, S. Batzner, Y. Xie, L. Sun, A.M. Kolpak, B. Kozinsky, On-the-fly active learning of interpretable Bayesian force fields for atomistic rare events, npj Comput. Mater. 6 (1) (2020) 20, http://dx.doi.org/10.1038/s41524-020-0283-z.

[50] E.V. Podryabinkin, A.V. Shapeev, Active learning of linearly parametrized interatomic potentials, Comput. Mater. Sci. 140 (2017) 171–180, http://dx.doi.org/10.1016/j.commatsci.2017.08.031, URL https://www.sciencedirect.com/science/article/pii/S0927025617304536.

[51] F. Pellegrini, R. Lot, Y. Shaidu, E. Küçükbenli, PANNA 2.0: Efficient neural network interatomic potentials and new architectures, 2023, arXiv:2305.11805.

[52] A. Musaelian, S. Batzner, A. Johansson, L. Sun, C.J. Owen, M. Kornbluth, B. Kozinsky, Learning local equivariant representations for large-scale atomistic dynamics, Nature Commun. 14 (1) (2023) 579, http://dx.doi.org/10.1038/s41467-023-36329-y.

[53] I. Batatia, S. Batzner, D.P. Kovács, A. Musaelian, G.N.C. Simm, R. Drautz, C. Ortner, B. Kozinsky, G. Csányi, The design space of e(3)-equivariant atom-centered interatomic potentials, (arXiv:2205.06643) 2022, http://dx.doi.org/10.48550/arXiv.2205.06643, arXiv:2205.06643.

[54] C. Zeni, A. Anelli, A. Glielmo, K. Rossi, Exploring the robust extrapolation of high-dimensional machine learning potentials, Phys. Rev. B 105 (2022) 165141, http://dx.doi.org/10.1103/PhysRevB.105.165141, URL https://link.aps.org/doi/10.1103/PhysRevB.105.165141.

[55] I. Batatia, D.P. Kovacs, G. Simm, C. Ortner, G. Csanyi, MACE: Higher order equivariant message passing neural networks for fast and accurate force fields, in: S. Koyejo, S. Mohamed, A. Agarwal, D. Belgrave, K. Cho, A. Oh (Eds.), in: Advances in Neural Information Processing Systems, vol. 35, Curran Associates, Inc., 2022, pp. 11423–11436, URL https://proceedings.neurips.cc/paper_files/paper/2022/file/4a36c3c51af11ed9f34615b81edb5bbc-Paper-Conference.pdf.

[56] T. Miyagawa, K. Mori, N. Kato, A. Yonezu, Development of neural network potential for MD simulation and its application to TiN, Comput. Mater. Sci. 206 (2022) 111303, http://dx.doi.org/10.1016/j.commatsci.2022.111303, URL https://www.sciencedirect.com/science/article/pii/S0927025622000970.

[57] C.J. Owen, Y. Xie, A. Johansson, L. Sun, B. Kozinsky, Stability, mechanisms and kinetics of emergence of au surface reconstructions using Bayesian force fields, 2023, arXiv:2308.07311.

[58] C.J. Owen, N. Marcella, Y. Xie, J. Vandermause, A.I. Frenkel, R.G. Nuzzo, B. Kozinsky, Unraveling the catalytic effect of hydrogen adsorption on pt nanoparticle shape-change, 2023, arXiv:2306.00901.

[59] A.M. Goryaeva, J. Dérès, C. Lapointe, P. Grigorev, T.D. Swinburne, J.R. Kermode, L. Ventelon, J. Baima, M.-C. Marinica, Efficient and transferable machine learning potentials for the simulation of crystal defects in BCC Fe and W, Phys. Rev. Mater. 5 (2021) 103803, http://dx.doi.org/10.1103/PhysRevMaterials.5.103803, URL https://link.aps.org/doi/10.1103/PhysRevMaterials.5.103803.

[60] J. Byggmästar, A. Hamedani, K. Nordlund, F. Djurabekova, Machine-learning interatomic potential for radiation damage and defects in tungsten, Phys. Rev. B 100 (2019) 144105, http://dx.doi.org/10.1103/PhysRevB.100.144105, URL https://link.aps.org/doi/10.1103/PhysRevB.100.144105.

[61] G. Nikoulis, J. Byggmästar, J. Kioseoglou, K. Nordlund, F. Djurabekova, Machine-learning interatomic potential for W–Mo alloys, J. Phys.: Condens. Matter. 33 (31) (2021) 315403, http://dx.doi.org/10.1088/1361-648X/ac03d1.

[62] J. Byggmästar, K. Nordlund, F. Djurabekova, Modeling refractory high-entropy alloys with efficient machine-learned interatomic potentials: Defects and segregation, Phys. Rev. B 104 (2021) 104101, http://dx.doi.org/10.1103/PhysRevB.104.104101, URL https://link.aps.org/doi/10.1103/PhysRevB.104.104101.

[63] J. Byggmästar, K. Nordlund, F. Djurabekova, Gaussian approximation potentials for body-centered-cubic transition metals, Phys. Rev. Mater. 4 (2020) 093802, http://dx.doi.org/10.1103/PhysRevMaterials.4.093802, URL https://link.aps.org/doi/10.1103/PhysRevMaterials.4.093802.

[64] R. Lot, F. Pellegrini, Y. Shaidu, E. Küçükbenli, PANNA: Properties from artificial neural network architectures, Comput. Phys. Comm. 256 (2020) 107402, http://dx.doi.org/10.1016/j.cpc.2020.107402, URL https://www.sciencedirect.com/science/article/pii/S0010465520301843.

[65] E. Salonen, T. Järvi, K. Nordlund, J. Keinonen, Effects of the surface structure and cluster bombardment on the self-sputtering of molybdenum, J. Phys.: Condens. Matter. 15 (34) (2003) 5845, http://dx.doi.org/10.1088/0953-8984/15/34/314.

[66] Z. Li, J.R. Kermode, A. De Vita, Molecular dynamics with on-the-fly machine learning of quantum-mechanical forces, Phys. Rev. Lett. 114 (2015) 096405, http://dx.doi.org/10.1103/PhysRevLett.114.096405, URL https://link.aps.org/doi/10.1103/PhysRevLett.114.096405.

[67] A.P. Bartók, R. Kondor, G. Csányi, On representing chemical environments, Phys. Rev. B 87 (2013) 184115, http://dx.doi.org/10.1103/PhysRevB.87.184115, URL https://link.aps.org/doi/10.1103/PhysRevB.87.184115.

[68] M. Abadi, et al., TensorFlow: Large-scale machine learning on heterogeneous systems, 2015, Software available from tensorflow.org, URL https://www.tensorflow.org/.

[69] J.S. Smith, O. Isayev, A.E. Roitberg, ANI-1: an extensible neural network potential with DFT accuracy at force field computational cost, Chem. Sci. 8 (2017) 3192–3203, http://dx.doi.org/10.1039/C6SC05720A.

[70] J. Byggmästar, K. Nordlund, F. Djurabekova, Gaussian approximation potentials for body-centered-cubic transition metals, Phys. Rev. Mater. 4 (2020) 093802, http://dx.doi.org/10.1103/PhysRevMaterials.4.093802, URL https://link.aps.org/doi/10.1103/PhysRevMaterials.4.093802.

[71] P. Giannozzi, et al., QUANTUM ESPRESSO: a modular and open-source software project for quantum simulations of materials, J. Phys.: Condens. Matter. 21 (39) (2009) 395502, http://dx.doi.org/10.1088/0953-8984/21/39/395502.

[72] P. Giannozzi, et al., Advanced capabilities for materials modelling with Quantum ESPRESSO, J. Phys.: Condens. Matter. 29 (46) (2017) 465901, http://dx.doi.org/10.1088/1361-648x/aa8f79.

[73] G. Prandini, A. Marrazzo, I.E. Castelli, N. Mounet, N. Marzari, Precision and efficiency in solid-state pseudopotential calculations, npj Comput. Mater. 4 (1) (2018) 72, http://dx.doi.org/10.1038/s41524-018-0127-2.

[74] K. Lejaeghere, et al., Reproducibility in density functional theory calculations of solids, Science 351 (6280) (2016) aad3000, http://dx.doi.org/10.1126/science.aad3000, arXiv:https://www.science.org/doi/pdf/10.1126/science.aad3000, URL https://www.science.org/doi/abs/10.1126/science.aad3000.

[75] D.R. Hamann, Optimized norm-conserving Vanderbilt pseudopotentials, Phys. Rev. B 88 (2013) 085117, http://dx.doi.org/10.1103/PhysRevB.88.085117, URL https://link.aps.org/doi/10.1103/PhysRevB.88.085117.

[76] H.J. Monkhorst, J.D. Pack, Special points for Brillouin-zone integrations, Phys. Rev. B 13 (1976) 5188–5192, http://dx.doi.org/10.1103/PhysRevB.13.5188, URL https://link.aps.org/doi/10.1103/PhysRevB.13.5188.

[77] M. Methfessel, A.T. Paxton, High-precision sampling for Brillouin-zone integration in metals, Phys. Rev. B 40 (1989) 3616–3621, http://dx.doi.org/10.1103/PhysRevB.40.3616, URL https://link.aps.org/doi/10.1103/PhysRevB.40.3616.

[78] D. Chung, W. Buessem, The voigt-reuss-hill approximation and elastic moduli of polycrystalline MgO, CaF2, β-ZnS, ZnSe, and CdTe, J. Appl. Phys. 38 (6) (1967) 2535–2540.

[79] THERMO_PW driver for QE (Github link). URL https://dalcorso.github.io/thermo_pw/.

[80] D.P. Kingma, J. Ba, Adam: A method for stochastic optimization, 2017, arXiv:1412.6980.

[81] E. Nunez, K. Bashandeh, A. Polycarpou, Thermal and mechanical properties of polymer coatings, 2020, pp. 157–175, http://dx.doi.org/10.1201/9780429199226-9.

[82] W.C. Oliver, G.M. Pharr, An improved technique for determining hardness and elastic modulus using load and displacement sensing indentation experiments, J. Mater. Res. 7 (1992) 1564–1583, http://dx.doi.org/10.1557/JMR.1992.1564.

[83] J.J. Möller, E. Bitzek, BDA: A novel method for identifying defects in body-centered cubic crystals, MethodsX 3 (2016) 279–288, http://dx.doi.org/10.1016/j.mex.2016.03.013.

[84] A. Stukowski, Visualization and analysis of atomistic simulation data with OVITO-the Open Visualization Tool, Modelling Simul. Mater. Sci. Eng. 18 (1) (2010) http://dx.doi.org/10.1088/0965-0393/18/1/015012.

[85] A. Stukowski, Computational analysis methods in atomistic modeling of crystals, JOM 66 (3) (2014) 399–407, http://dx.doi.org/10.1007/s11837-013-0827-5.

[86] J. Rumble, CRC Handbook of Chemistry and Physics, hundredth ed., CRC Press, Boca Raton, FL, 2019.

[87] S. Zhang, D. Legut, R. Zhang, PNADIS: An automated Peierls–Nabarro analyzer for dislocation core structure and slip resistance, Comput. Phys. Comm. 240 (2019) 60–73.

[88] R. Peierls, The size of a dislocation, Proc. Phys. Soc. 52 (1) (1940) 34–37.

[89] F. Nabarro, Dislocations in a simple cubic lattice, Proc. Phys. Soc. 59 (2) (1947) 256.

[90] S. Jakob, A. Leitner, A. Lorich, M. Eidenberger-Schober, W. Knabl, R. Pippan, H. Clemens, V. Maier-Kiener, Influence of crystal orientation and Berkovich tip rotation on the mechanical characterization of grain boundaries in molybdenum, Mater. Des. 182 (2019) 107998, http://dx.doi.org/10.1016/j.matdes.2019.107998, URL https://www.sciencedirect.com/science/article/pii/S0264127519304368.

[91] K. Mulewska, F. Dominguez-Gutierrez, D. Kalita, J. Byggmästar, G. Wei, W. Chromiński, S. Papanikolaou, M. Alava, Ł. Kurpaska, J. Jagielski, Selfâ€“ion irradiation of high purity iron: Unveiling plasticity mechanisms through nanoindentation experiments and large-scale atomistic simulations, J. Nucl. Mater. 586 (2023) 154690, http://dx.doi.org/10.1016/j.jnucmat.2023.154690, URL https://www.sciencedirect.com/science/article/pii/S0022311523004580.

Supplementary Information for: Neural Network Interatomic Potentials For Open Surface Nanomechanics Applications

Amirhossein D. Naghdi[1,2], Franco Pellegrini[3], Emine Kücükbenli[4,5], Dario Massa[1,2], F. Javier Dominguez–Gutierrez[1], Efthimios Kaxiras[5,6], and Stefanos Papanikolaou[1]

[1]NOMATEN Centre of Excellence, National Center for Nuclear Research, ul. A. Sołtana 7, 05-400 Swierk/Otwock
[2]IDEAS NCBR, ul. Chmielna 69, 00-801, Warsaw, Poland
[3]International School for Advanced Studies (SISSA), Via Bonomea, 265, I-34136 Trieste, Italy
[4] Nvidia Corporation, Santa Clara, CA, USA
[5] John A. Paulson School of Engineering and Applied Sciences, Harvard University, Cambridge, Massachusetts 02138, USA
[6]Department of Physics, Harvard University, Cambridge, Massachusetts 02138, USA

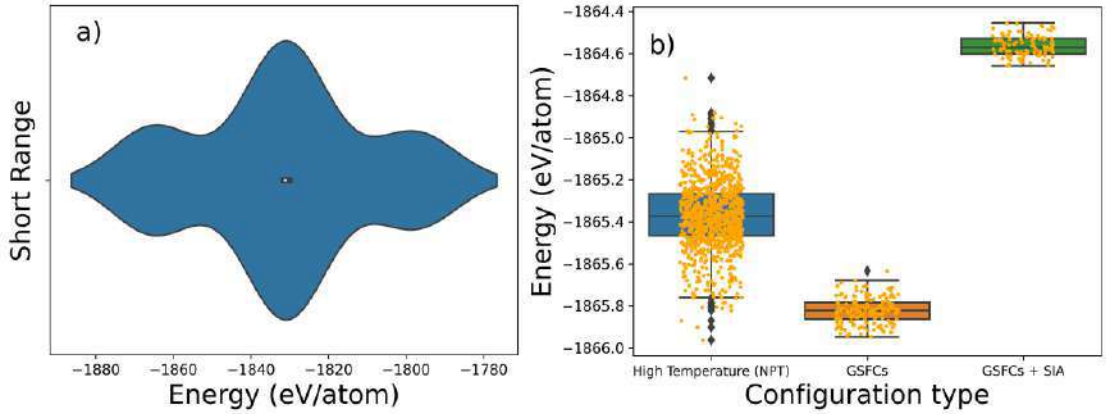

Figure S1: Energy distribution of **a)** Short range configurations and **b)** High temperature and GSFCs. The drastic variation of energies for short range configurations (100 meV/atom) suggest that these configurations would be problematic for training a NNIP. n addition, it is shown that although high temperature NPT configurations have a larger energy distribution than the GSFCs.

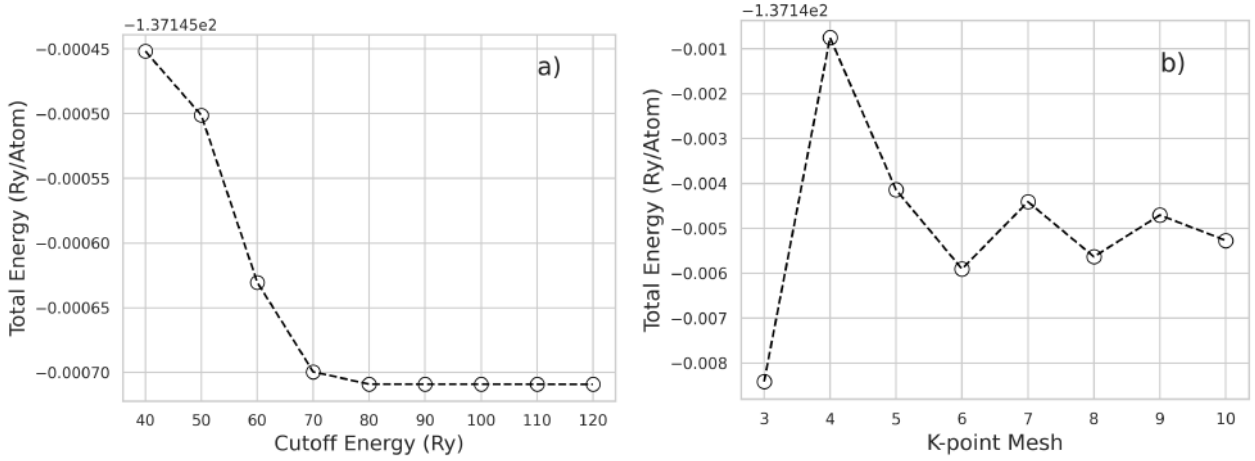

Figure S2: DFT convergence check for **a)** cutoff energy and **b** k-point mesh grid.

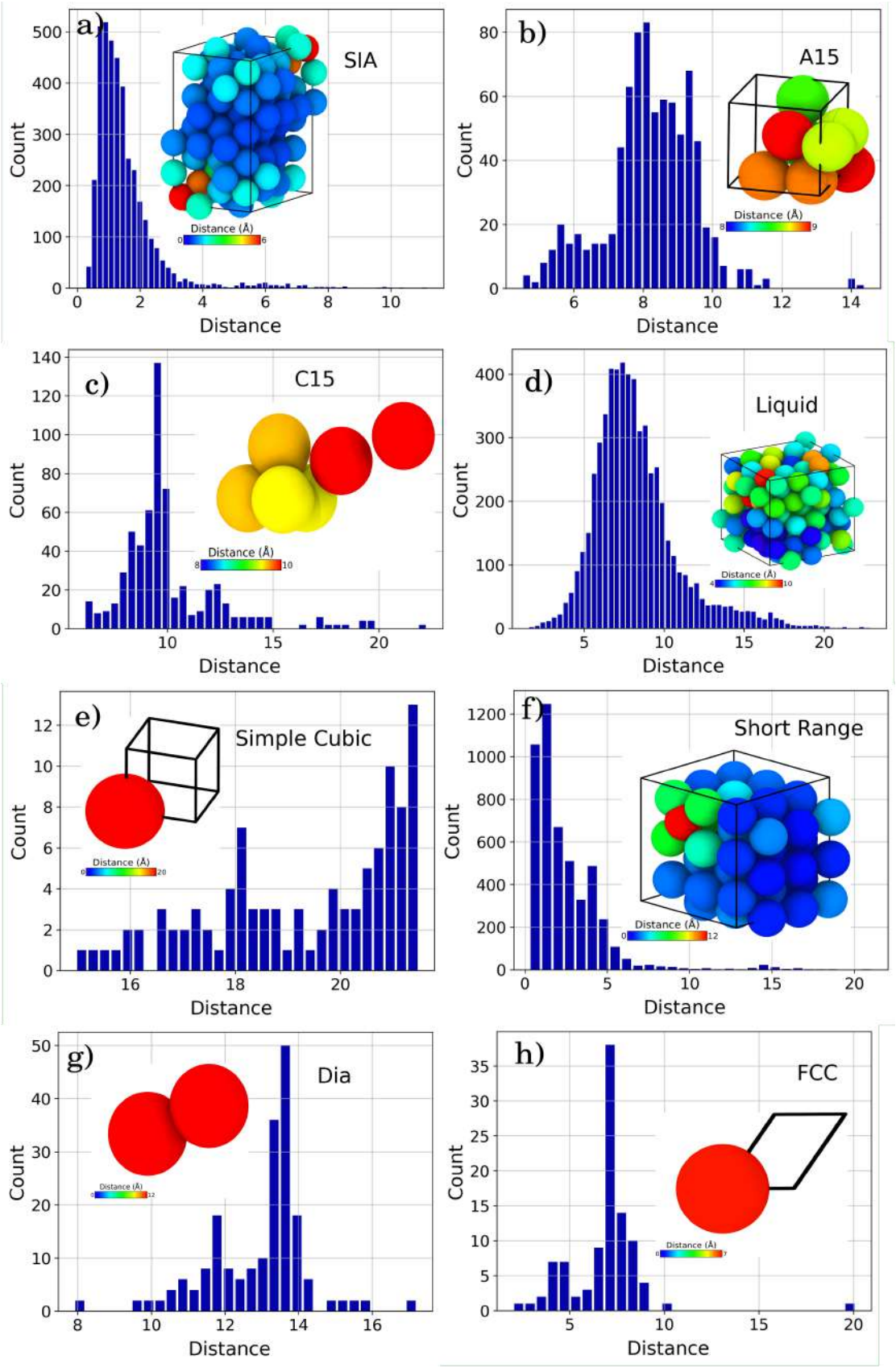

Figure S3: Distribution of minimum distances of each configuration to the indented sample for deleted configurations from the dataset. As it is shown in the insets, each configuration consists of number of atoms with large minimum distance.

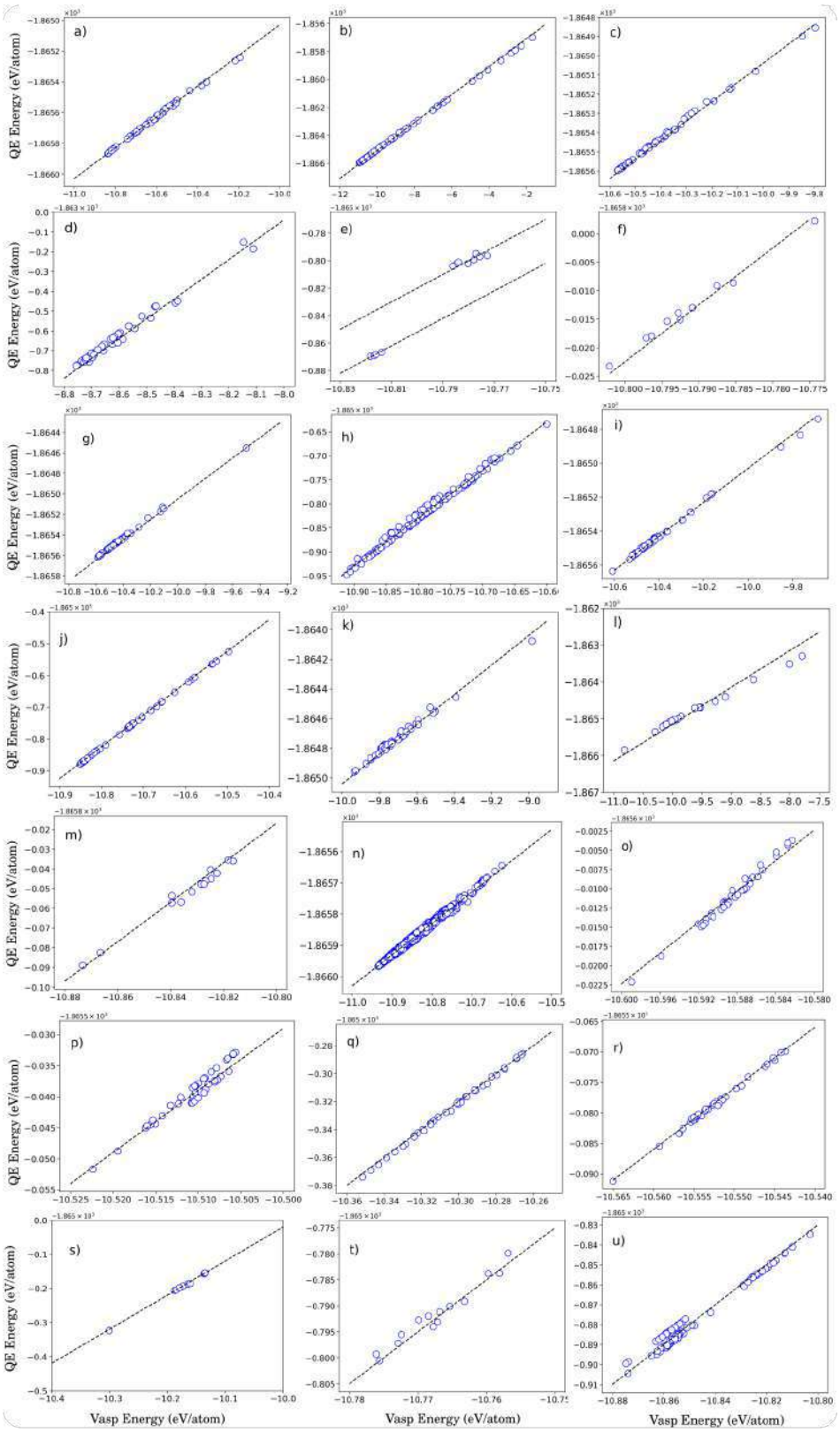

Figure S4: The total energies obtained in this work with Quantum Espresso (QE), compared to VASP (from the original GAP potential). The dashed lines represent a (y = x + b) function with y being the Quantum Espresso energy, x being the VASP energy and b is the y-intercept which is different for each panel and illustrates the correctness of the values we obtained from QE. Figures **a)** to **u)** are for the following configurations, respectively: A15, BCC, C15, diamond, di-sia, di-Vacancy, FCC, Gamma, HCP, phonon, sc, short range, sia, sliced sample, surface 100, surface 110, surface 111, surface 112, liquid surface, tri-Vacancy and vacancy.

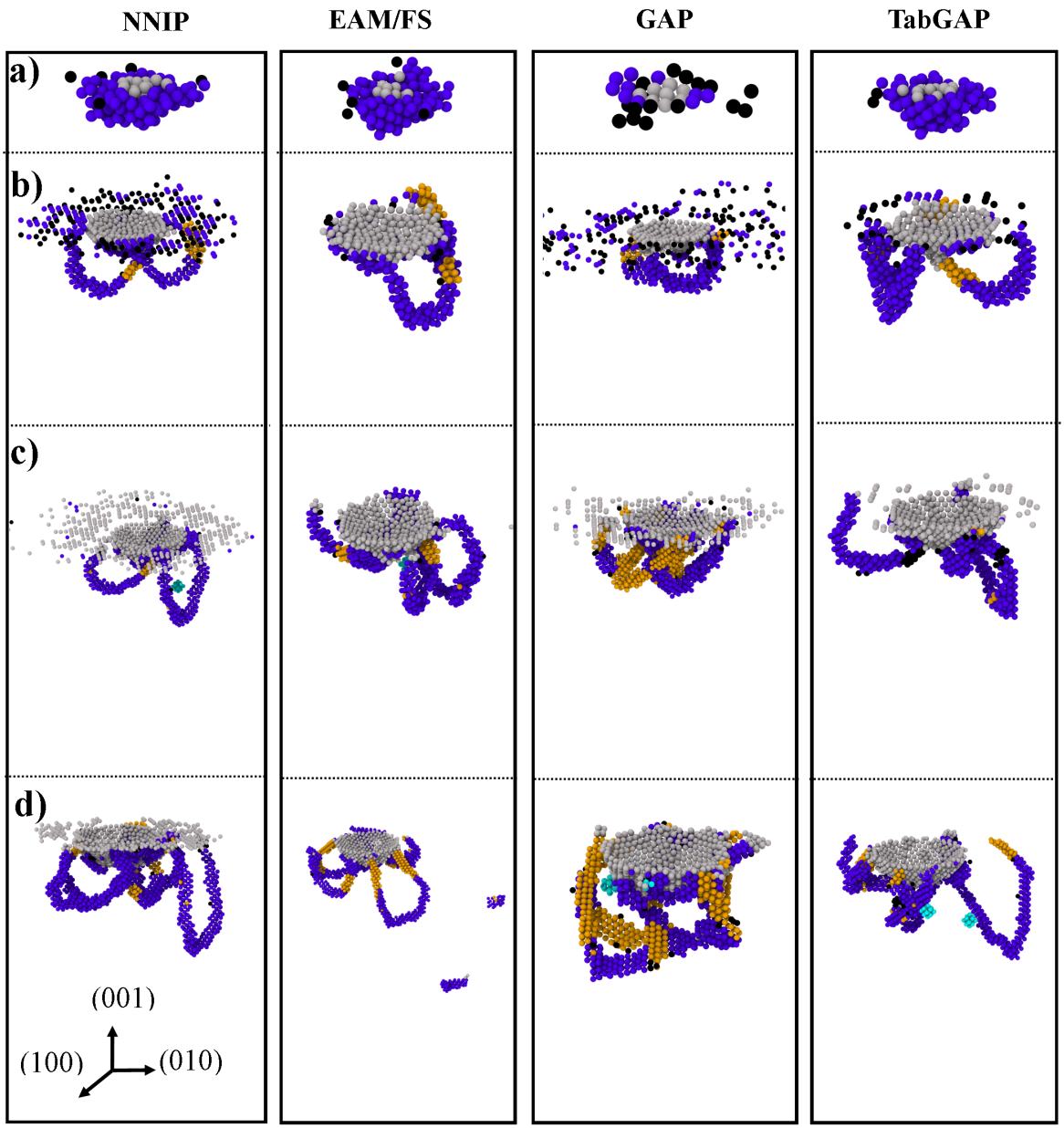

Figure S5: (Color online) Identified defects of indented (001) Mo sample by BDA method at different depths by NNIP, EAM, TabGAP, and GAP approaches. Material defects are depicted using different colors: gray spheres represent surface atoms in direct contact with the indenter tip, blue spheres indicate edge dislocations, light-blue spheres represent atoms in the vicinity of vacancies, yellow spheres depict twin/screw dislocations, and black spheres highlight unidentified defect atoms. The nucleation and propagation of edge dislocations on the {111} slip family are observed, which then evolve into prismatic loops. In addition, identified slip traces and pile-ups are well modeled by NNIP simulations showing the well–known three–fold symmetric rosette depths below 1.40 nm that are formed by $[11\bar{2}]$, $[\bar{1}01]$ and $[0\bar{1}1]$ planes.

$\{110\}\langle\bar{1}11\rangle$ (edge)	**NNIP**	**DFT**	**GAP**	**tabGAP**	**EAM**
Barrier (1E-10 J/m)	0.0134	0.0197	0.0085	0.0729	0.0074
Stress (MPa)	112.6496	165.9063	71.2785	615.0375	62.7665
Poisson Ratio	0.21	0.30	0.26	0.23	0.26
Shear Modulus (GPa)	111	97	108	87	109

Table S1: Comparison of CRS Peierls Barrier and Stress, computed using the relative Poisson Ratio and Shear Modulus values for the $\{110\}\langle\bar{1}11\rangle$ case.

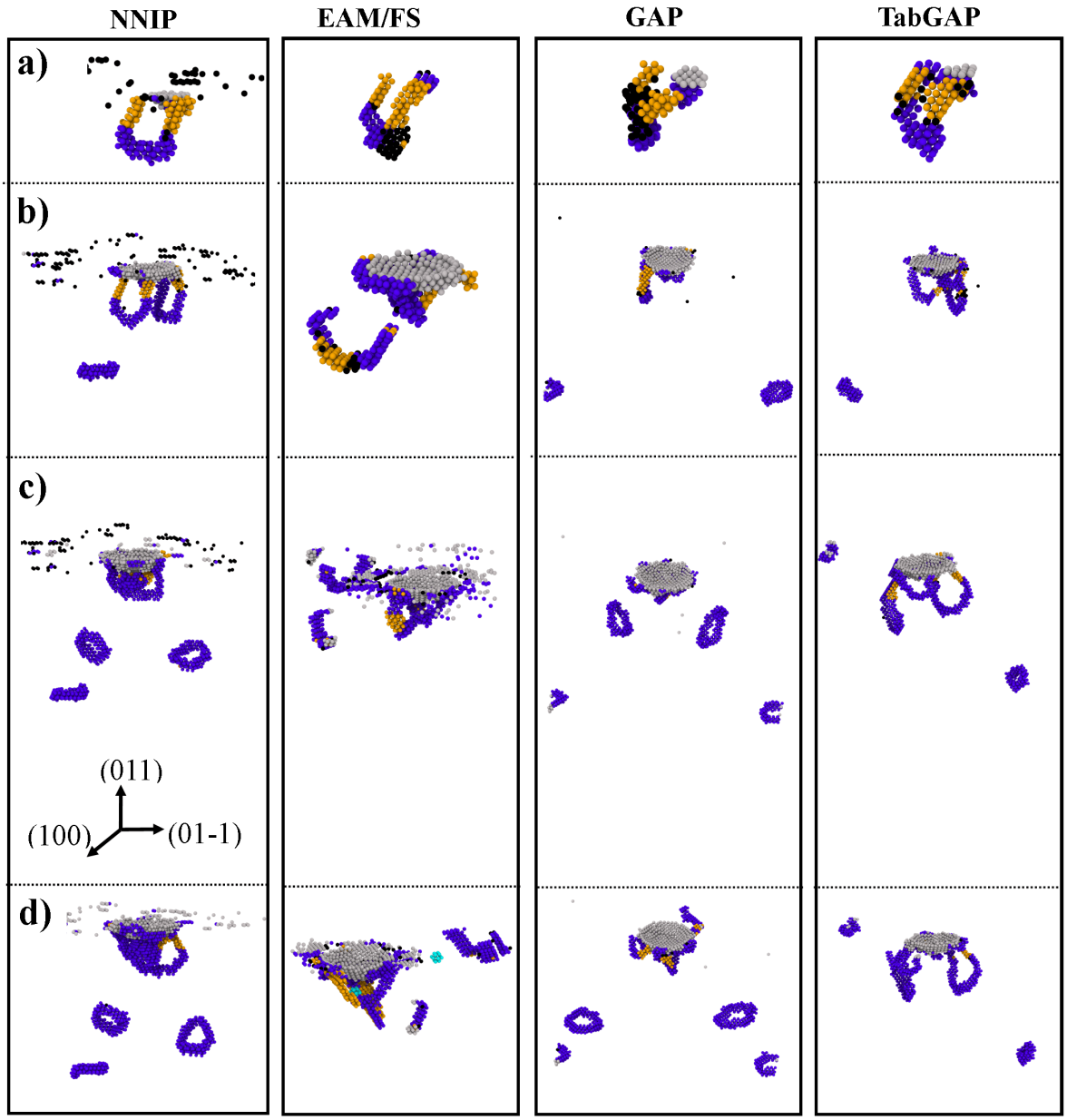

Figure S6: (Color online) Identified defects of indented (011) Mo sample by BDA method at different depths by NNIP, EAM, TabGAP, and GAP approaches. Material defects are depicted using different colors: gray spheres represent surface atoms in direct contact with the indenter tip, blue spheres indicate edge dislocations, light-blue spheres represent atoms in the vicinity of vacancies, yellow spheres depict twin/screw dislocations, and black spheres highlight unidentified defect atoms. The nucleation and propagation of edge dislocations on the {111} slip family are observed, which then evolve into prismatic loops. In addition, identified slip traces and pile-ups are well modeled by NNIP simulations showing the well–known three–fold symmetric rosette depths below 1.40 nm that are formed by $[11\bar{2}]$, $[\bar{1}01]$ and $[0\bar{1}1]$ planes.

$\{211\}\langle\bar{1}11\rangle$ (screw)	**NNIP**	**DFT**	**GAP**	**tabGAP**	**EAM**
Barrier (1E-10 J/m)	0.0556	0.013	0.0525	0.3658	0.0512
Stress (MPa)	469.2201	145.7044	444.4193	3231.6114	432.0303
Poisson Ratio	0.21	0.30	0.26	0.23	0.26
Shear Modulus (GPa)	111	97	108	87	109

Table S2: Comparison of CRS Peierls Barrier and Stress, computed using the relative Poisson Ratio and Shear Modulus values for the $\{211\}\langle\bar{1}11\rangle$ case.

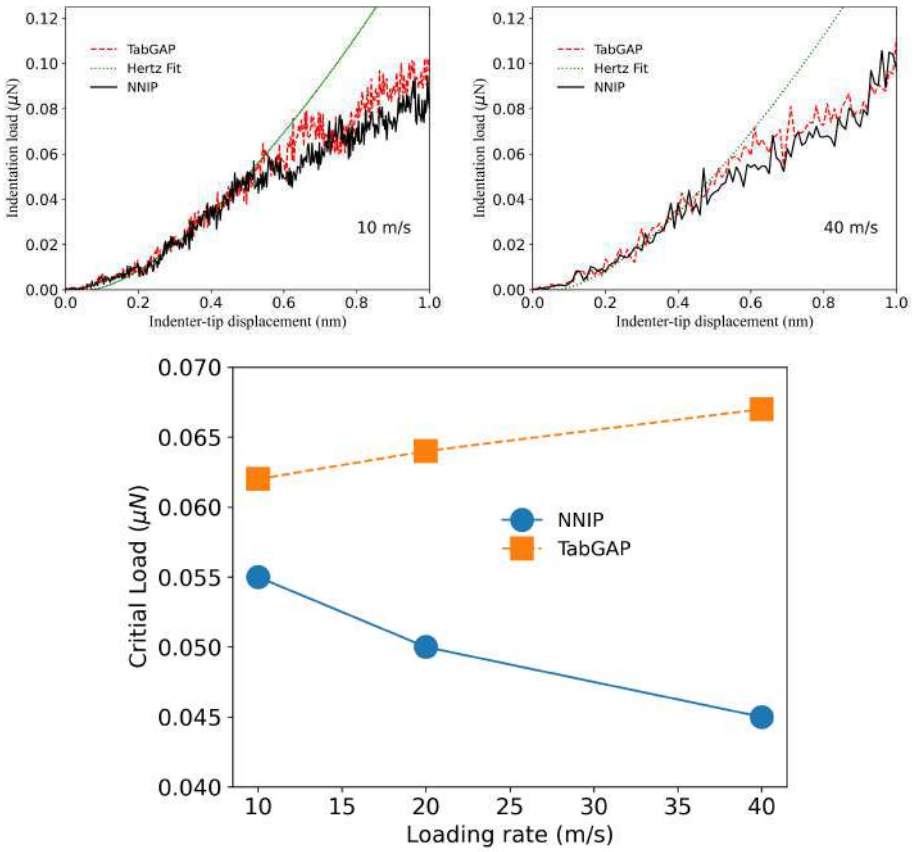

Figure S7: Comparison of the TabGAP and NNIP approaches in simulating the initiation of plastic deformation in a [111] Mo sample under varying loading rates. While both methods accurately capture the elastic regime, they diverge in predicting the critical load for the pop-in event (transition from elastic to plastic deformation).The critical load versus loading rate is plotted, highlighting the importance of surface information for accurate nanoindentation simulations. The NNIP approach demonstrates a good qualitative agreement with reported experimental data [16], showing a decrease in critical load with increasing loading rate. Conversely, the TabGAP approach predicts minimal changes in the pop-in event value.

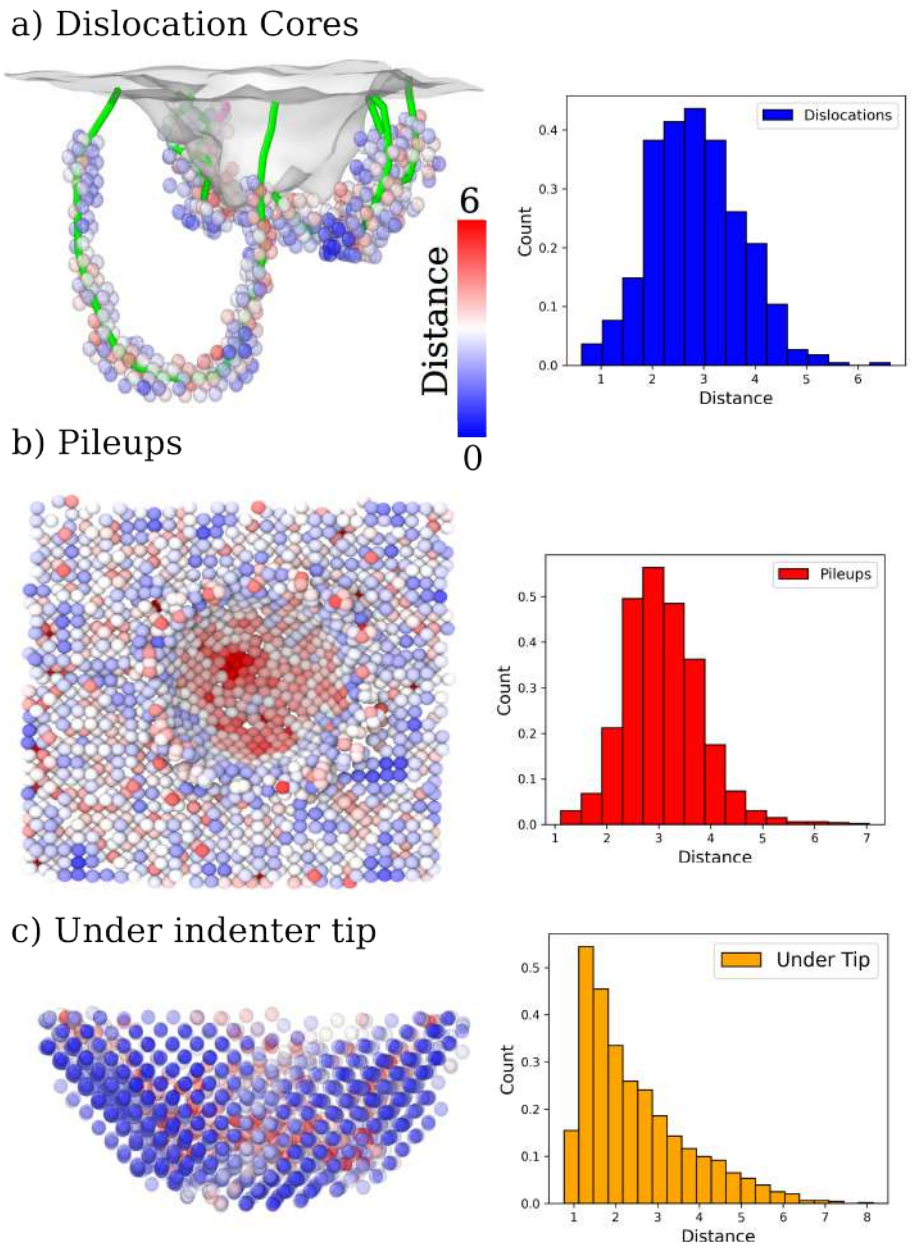

Figure S8: (Color online) Distances of NNIP indented (001) Mo sample from corresponding configurations in the dataset. Distances of atoms on the dislocation cores are calculated from the "GSFC + SIA" configurations, while the distances of atoms on the surface and under the indenter tip are calculated from the "Pileup" and "HT + substrate" configurations. The distance histograms depict that the tails of the distributions are still lower than the distance threshold of 6.

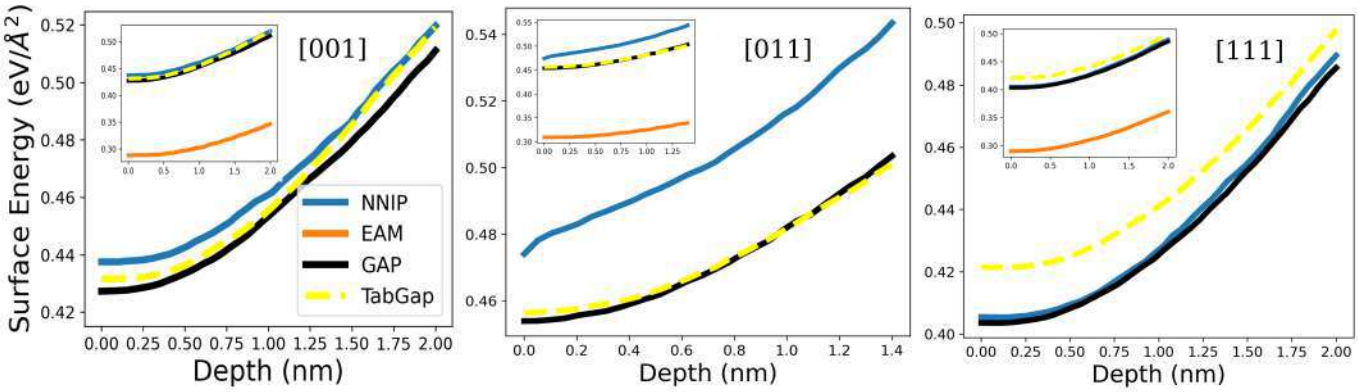

Figure S9: (Color online) Indentation surface energy as a function of indenter depth for **(Left)** [001], **(Middle)** [011] and **(Right)** [111] crystal orientations. The variation in results, specifically for [001] and [011] orientations, stems from the fact that the NNIP dataset is enriched with numerous surface configurations (pileup configurations), which capture the energetics of surface atoms. These differences in surface energies are connected to the nucleation and propagation of dislocations during nanoindentation. The surface area at each depth is calulated using the "construct surface mesh" tool [90] from OVITO package [91].

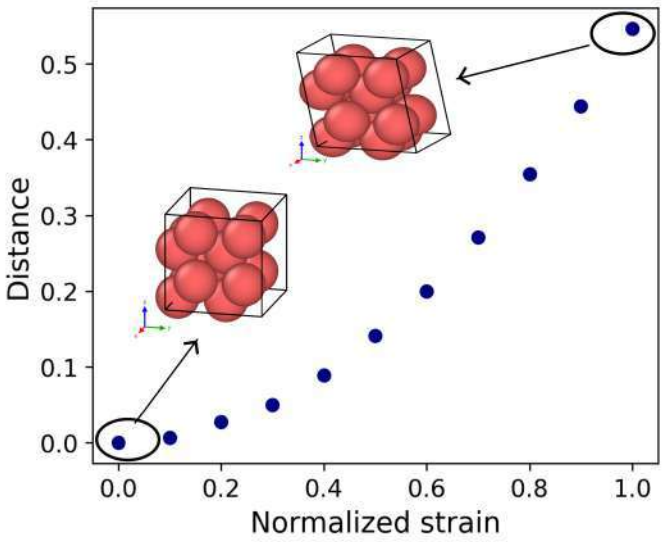

Figure S10: (Color online) Distance of sheared configurations from a perfect crystal as a function of applied strain. It is obvious that the increase in the strain value leads into higher distance values which makes intuitive sense.

Dislocation plasticity in equiatomic NiCoCr alloys: Effect of short-range order

Amir H. Naghdi,[1,*] Kamran Karimi,[1,*,†] Axel E. Poisvert,[1] Amin Esfandiarpour,[1] Rene Alvarez,[1] Pawel Sobkowicz,[1] Mikko Alava,[1,2] and Stefanos Papanikolaou[1,‡]

[1]*NOMATEN Centre of Excellence, National Center for Nuclear Research, 05-400 Swierk/Otwock, Poland*

[2]*Aalto University, Department of Applied Physics, P. O. Box 11000, 00076 Aalto, Espoo, Finland*

(Received 15 November 2022; revised 3 February 2023; accepted 9 February 2023; published 21 March 2023)

Equiatomic NiCoCr solid solutions have been shown by recent experiments and atomistic simulations to display exceptional mechanical properties that have been suggested to be linked to nanostructural short-range order (SRO) features that may arise from thermal treatments, such as annealing or/and aging. Here we use hybrid Monte Carlo–molecular dynamics simulations to gain further insights of thermal effects on the SRO formation as well as the edge dislocation plasticity mechanisms of equiatomic NiCoCr face-centered cubic solid solution. For that purpose, we utilize two well-known NiCoCr interatomic potentials, one of which displays well-documented SRO, believed to be linked to experimental evidence and labeled as the Li-Sheng-Ma potential, while the other (Farkas-Caro) does not. We use these two potentials to discern short-range ordering (from inherent randomness in random solid solutions) and understand how SROs influence dislocation depinning dynamics in various thermal annealing scenarios. In this context, we used robust, scale-dependent metrics to infer a characteristic SRO size in the Li-Sheng-Ma case by probing local concentration fluctuations which otherwise indicate uncorrelated patterns in the Farkas-Caro case in a close agreement with random alloys. Our Voronoi-based analysis shows meaningful variations of local misfit properties owing to the presence of SROs. Using relevant order parameters, we also report on the drastic increase of chemical ordering within the stacking fault region. More importantly, we find that the Li-Sheng-Ma potential leads to excellent edge dislocation depinning strength with low stacking fault width. Our findings indicate an enhanced roughening mechanism due to the SROs-misfit synergy that leads to significant improvements in dislocation glide resistance. We argue that the improvements in alloy strength have their atomistic origins in the interplay between nanoscopic SROs and atomic-level misfit properties.

DOI: 10.1103/PhysRevB.107.094109

I. INTRODUCTION

Metallurgy of alloys is at the core of technological progress. Concentrated solid solution alloys (CSAs) have recently emerged as major candidates for novel alloys for extreme conditions applications [1,2]. Of all, the equiatomic [3] NiCoCr CSA represents a simple-enough composition that has been consistently reported to show exceptional mechanical properties [1]. These include (among others) a relatively high (tensile) strength and ductility, fracture toughness, as well as (micro-)hardness that often exceed those of the "Cantor" alloy [4] yet with a fewer number of principal components. This is most likely rooted in the chemical composition and underlying substructure. However, the microstructural origin of the exceptional mechanical properties has been heavily debated, with a possible explanation being the presence of nanometer-level (chemical/structural) short-range order (SRO) [5–8] that arises from particular thermal processing and influences dislocation pinning and stacking fault widths. In addition, lattice distortions and local crystalline misfits, due to atomic size differences [9,10], have been shown to be correlated to the exceptional mechanical behavior of this alloy. Given the apparent importance of local misfit volumes [9], it remains a challenge to identify the role of SRO for exceptional mechanical properties. In this paper, we focus on extensive molecular simulations to understand how SRO influences dislocation plasticity and how it might depend on processing parameters (i.e., annealing temperature), the properties of the ordered phase, as well as the role of the MD atomic potentials in the ordering process. In this framework, we investigated two case studies involving commonly used NiCoCr interatomic potentials Li-Sheng-Ma (LSM) and Farkas-Caro (FC) potential. While LSM leads to the formation of short-range ordering on aging, FC displays chemical/structural features, under the exact same thermal treatment, that are almost indistinguishable from random solid solutions. Our multiscale characterization of local ordering was based on the use of novel descriptors that exhibit distinct structural/chemical signatures owing to the presence of nanoscopic SROs. We study the effects of the SRO on mechanical properties, showing that it significantly influences them via the interplay of dislocations and SRO structures. Such an interplay was quantified via a detailed analysis of the dislocation substructure indicating enhanced roughening properties due to combined SRO-misfit effects.

*These authors made equal contributions.

†kamran.karimi@ncbj.gov.pl

‡Stefanos.Papanikolaou@ncbj.gov.pl

Short-range order has been at the core of studies in CSAs across the board [11–13]. Thermodynamically speaking, SROs' ubiquity at low-temperature alloys has been mainly attributed to dominant enthalpic effects that, in the absence of entropy-driven mechanisms, do not favor idealistic perfect mixtures of equimolar elements [14]. In this context, SROs typically refer to coherent compositional deviations apart from (statistically) random distributions of atoms within the solution matrix as in random solid solution alloys (RSAs). More importantly, (thermal) processing parameters associated with annealing and homogenization procedures (i.e., temperature and time) or irradiation may have a drastic effect on the nucleation of SROs and associated substructural features [9,15,16]. Owing to their nanoscopic scales, laboratory-based observations of SROs are quite nontrivial involving intensive use of advanced characterization techniques such as high-resolution electron microscopy and atomic-resolution energy dispersive spectrometry mapping [8,17]. The latter are strongly tied to underlying physical mechanisms that govern fundamental alloy properties. For instance, the formation of Ni-rich nanoprecipitates and associated inhomogeneities within the annealed NiCoCr matrix has been recently suggested to tune the stacking fault width with evident consequences in terms of the alloy strengthening [14,18]. Similar conclusions were drawn experimentally by Ritchie *et al.* [5], who reported on the emergence of SROs in aged NiCoCr CSAs with significant impacts on the dislocation activation energy and hardness. In studies of NiCoCr-based alloys, stacking fault energy, hardness, and fracture toughness, as bulk properties, were recently shown to strongly correlate with the degree of Ni-rich SROs and corresponding structural features [19–22].

In contrast, local misfit properties have been conventionally viewed as a key solid solution strengthening mechanism [23]. In this framework, the inherent yield strength of alloys (or Peierls stress) associates to the stress threshold required for dislocation depinning, and in the context of multicomponent high-entropy alloys, their intrinsic hetrogeneity and randomness gives rise to somewhat uncorrelated perturbations to the local thresholds. This concept was theoretically put forward in the seminal work by Labusch [24], who hypothesized that the motion of dislocations within a random set of solute obstacles leads to significant hardening effects in dilute solutions. In a series of relevant papers, Varvenne and Curtin (VC) [25–27] further investigated the RSA context in terms of elastic-type long-range interactions between dislocation lines and residual strain fields resulting from atomic size misfits. Along these lines, a mean-field theoretical framework was proposed to make fairly accurate predictions of yield strengths solely based on the effective medium elastic properties and, more importantly, local misfit fluctuations. The proposed theory accounts for local compositional fluctuations described by spatial distributions of misfit volumes which are accessible through atomistic simulations and experimentation. The VC framework was further generalized to additionally account for thermal and strain-rate effects on the alloys' strength and checked in the context of random alloys [9,26]. In the case of high-entropy alloys (HEAs), however, there may often be a considerable degree of short-range ordering and, therefore, HEAs cannot be simply treated as fully random.

Short-range order and local misfits are not one-way streets but they combine and interplay in ways that are somewhat unpredictable in advance and inseparable [20]. Moreover, almost all crucial properties related to alloy strengths are strongly dependent on the underlying microstructure and processing methods used to synthesize CSAs. In an aged multicomponent alloy, the effective Peierls stress will be influenced by both randomness in the local composition distribution (giving rise to misfit fluctuations) and short-ranged (but still finite) spatial correlations introduced by SROs. Naturally, this combined effect leads to an effective yield stress that typically exceeds that of a random solid solution, lacking this finite-range ordering component. A naive picture in this context is that dislocations will move by locally bending between pinning sites to overcome locally fluctuating Peierls stresses leading to extra strengthening [28]. Nevertheless, a systematic study accounting for dislocations' glide resistance and their substructure discerning the separate roles of SROs and misfits seems necessary.

To this end, we use a versatile approach to investigate the microstructural/chemical origin of strengthening in NiCoCr including enthalpy-driven ordering effects and local distortions. We perform hybrid Monte Carlo–molecular dynamics (MC-MD) simulations at a range of annealing temperatures based on two commonly used NiCoCr interatomic potentials. We find that the emergence of SROs is not a robust feature of annealed model NiCoCr CSAs but, to a great extent, depends on the chosen potential energy. More specifically, the two models generate microstructurally different alloys (with/out SROs) with the exact same thermal processing. Following the numerical framework in Ref. [14], we probed effects of SROs in terms of local concentration fluctuations, stacking fault widths, dislocation glide resistance, and misfit volumes of NiCoCr as well as thermodynamic properties such as the specific heat and thermal expansion coefficient. Our analysis indicates meaningful correlations of the above observables with varying degrees of SROs in aged alloys, making them easily distinguishable from RSAs. We further observe a marked growth in the population of SROs inside the stacking fault region and remarkable strengthening behavior against dislocation glide with the latter rooted in the interplay between short-range ordering and local misfit properties.

The organization of this paper is the following. In Sec. II, we describe the numerical setup, sample preparation (including aging/annealing), loading protocols, and relevant simulation details including the hybrid MC-MD model, interatomic forces, and shear test description. Section III presents our simulation results relevant to the chemical/microstructural characterization of SROs and their potential effects on dynamics of dislocations. In this context, Sec. III A introduces robust structural/compositional metrics associated with local elemental fluctuations to characterize the temperature dependence of SROs and distribution of misfit volumes. Lattice distortions in the presence of short-range ordering will be discussed in Sec. III B. In Sec. III C, we provide an in-depth analysis of partial dislocations and their depinning mechanism in the presence of SROs. This includes autocorrelation

analyses associated with the dislocation line fluctuations as well as local variations of the dislocation velocity. Section IV presents relevant discussions and conclusions.

II. METHODS AND MATERIALS

Molecular dynamics simulations were carried out in LAMMPS [29] by implementing atomistic samples of size $N = 500\,000$ and $1\,700\,000$ within a three-dimensional periodic cell. In order to study SRO properties (in the absence of dislocations), we prepared cubic samples with length 10 nm along the $x[100]$, $y[010]$, and $z[001]$ directions. The NPT ensembles were implemented via a Nose-Hoover thermostat and barostat with relaxation timescales $\tau_d^{\text{therm}} = 10$ fs and $\tau_d^{\text{bar}} = 100$ fs. We also set the discretization time to $\Delta t \simeq 1.0$ fs. Samples were initially prepared via an energy minimization at $T = 0$ K (at a fixed volume) and subsequently thermalized at different temperatures and constant pressure $P = 0$ bar for 100 ps prior to annealing.

The interatomic forces are based on two commonly used embedded-atom method (EAM) potentials in the context of NiCoCr solid solution alloys: (i) the Li-Sheng-Ma potential proposed in Ref. [14], which has been utilized in recent SRO studies, modeling dislocation nucleation and glide dynamics [20,30], and nanoindentation tests [19] and (ii) the EAM Farkas–Caro potential [31], originally developed to model equimolar high-entropy FeNiCoCrCu alloys but used here to validate the SRO formation and its robustness against different potentials.

Annealed configurations were obtained performing hybrid MC-MD simulations based on the variance constrained semi-grand-canonical (VCSGC) ensemble [32] within the annealing temperature range $T_a = 400$–1300 K. To determine the values of $\Delta\mu_{X_1X_2} = \mu_{X_1} - \mu_{X_2}$ minimizing the composition errors, we perform a set of semi-grand-canonical simulations by varying the chemical composition at $T = 1500$ K and fit the MC data based on the equation: $\Delta\mu(X_1, P, T) = T\ln(X_1/[1 - X_1]) + \sum_{i=0}^{n} A_i X_1^i$ (see Fig. S1 in the Supplemental Material [33]). Here X_1 is the reference element (Ni in our work) and A_i's are the fitting parameters [34]. This allows us to perform hybrid MD/VCSGC-MC with a fixed target composition. During the annealing process, we perform 1 MC cycle consisting of $N/2$ attempts of transmutation every 20 MD steps. We carried out a total number of 800 000 MC cycles at all annealing temperatures T_a to ensure that the configurations reach thermal equilibrium and that the structure of SROs are statistically indifferent.

We also studied dynamics of a $\frac{1}{2}[\bar{1}10](111)$ edge dislocation which, under an external perturbation, dissociates into two separate partials with a stacking fault in face-centered cubic (fcc) crystals. To this end, we constructed a simulation cell with dimensions $L_x \simeq 80$, $L_y \simeq 20$, and $L_z \simeq 15$ nm (see Fig. S2) and performed annealing at a desired temperature T_a. We subsequently equilibrated the annealed alloy at a low temperature $T = 5$ K and pressure $P = 0$ for the duration of 100 ps. To create an edge dislocation within the aged sample, we used the periodic array of dislocation model proposed in Ref. [35] to ensure a periodic setup along the Burgers vector ($x[\bar{1}10]$) and dislocation line ($z[\bar{1}\bar{1}2]$). The dislocated sample was further relaxed using the NPT framework with $P_{xx} = P_{zz} = 0$ and $T = 5$ K (for 100 ps) leading to the dislocation dissociation into two Shockley partials. Shear tests were performed at $T = 5$ K in order to suppress thermal activation and isolate sole effects of local lattice distortion and SROs on yield properties. To this end, a stress-controlled framework was employed within the NVT ensemble by applying additional forces on the top plane (normal to y) with the bottom layer held fixed (with a thickness $\simeq 4$ Å) during the course of shear simulations. The applied stress was gradually increased from $\sigma = 50$ MPa (in a quasistatic fashion) above a critical (depinning) stress in order to move the partial dislocations.

III. RESULTS

The above methodology to prepare and anneal model CSAs indicates that aged NiCoCr alloys may exhibit varying degrees of chemical ordering under different annealing temperatures. Using robust composition-based metrics in Sec. III A, we further confirm the formation of SROs and their strong dependence on the thermal processing. Section III B presents the misfit volume analysis indicating meaningful correlations with the degree of short-range ordering. In Sec. III C, we analyze dynamics of partial dislocations in the presence of SROs and discuss potential implications in terms of the SRO-induced CSA strengthening.

A. Temperature dependence of SROs

Figure 1 illustrates that the formation of SROs within the solid solutions may strongly depend on the annealing temperature T_a. The color map of atoms, the inset of Fig. 1(a), indicates a clear segregation of Ni-rich phases (gray circles) in the NiCoCr CSA modeled via the Li-Sheng-Ma potential at $T_a = 800$ K. Overall, the observed clustering features tend to become less pronounced at higher annealing temperatures as shown in Fig. S3.

The presence of SROs appears to have a direct relevance on the (constant-pressure) heat capacity $C_p = \partial_T H$ in Fig. 1(a) featuring a maximum around $T_a \simeq 800$ K. Here H denotes the enthalpy [36]. The data presented in Fig. 1 correspond to a sample equilibrated at $T = 300$ K and subsequently aged at multiple annealing temperatures. The emerging peak in C_p may suggest a dominant role of enthalpic interactions over entropic effects that rule out the formation of an ideal random solid solution [14]. We note that the (ideal) heat capacity associated with the latter rises monotonically within the temperature range of interest. Such deviations seem to be less pronounced in terms of the thermal expansion coefficient $\alpha_p = \frac{1}{V}\partial_T V$, with V being the system volume, as shown in Fig. 1(b).

The notion of SROs typically refers to coherent compositional deviations from (statistically) random distributions of atoms within the solution matrix. Along these lines, we investigated the Warren–Cowley SRO parameters $p_{ab}(r)$ [13] probing the concentration variations of type-b atoms at a distance r from a center type-a element. For an equimolar random NiCoCr solid solution, one obtains $p_{ab}^{\text{rsa}} = 0.33$ (on average) at any r—more precisely, between the successive valleys of the pair correlation function $g(r)$ as in Fig. 2(g). The SRO parameters could be also determined locally for

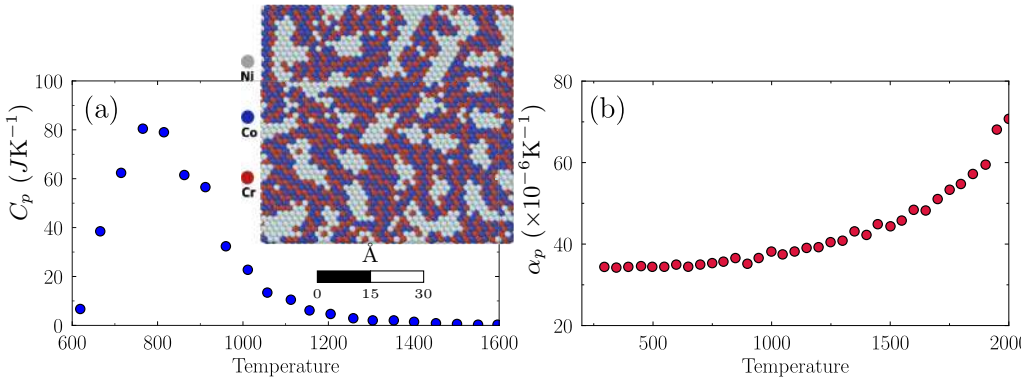

FIG. 1. Annealing temperature effects on NiCoCr based on the Li-Sheng-Ma potential. (a) Heat capacity C_p and (b) thermal expansion coefficient α_p versus anealing temperature T_a. The inset represents a (111) cross section of Ni (gray), Co (blue), and Cr (red) atoms at $T_a =$ 800 K.

individual atoms which will presumably show strong fluctuations in the presence of SROs. Nevertheless, the "averaged" Warren–Cowley parameters should be relevant as the system tends to be statistically homogeneous beyond the mean SRO size.

Figures 2(a)–2(f) illustrates deviations of p_{ab} associated with the annealed CSAs from p_{ab}^{rsa} including the six (distinct) elemental pairs at $T_a = 400$ K. The order parameters reveal several interesting features describing the SRO microstructure. The abundance of the Ni-Ni pairs beyond random concentrations is remarkable and appears to persist up to $r \simeq$ 5 Å in Fig. 2(a). It should be noted that twice this lengthscale is in a rough agreement with the visual impression one gets from the segregation map, the inset of Fig. 1(a), regarding the mean SRO size. Below the base line, the dip in p_{ab} corresponding to Ni-Ni pairs should indicate their scarcity above the mean size. The order parameter recrosses the horizontal line beyond which it features a fairly broad peak at $r \simeq 15$ Å before going asymptotically to p_{ab}^{rsa}. We remark that the inferred lengthscale could potentially relate to the average spacing between adjacent SROs. Figures 2(b) and 2(c) associated with p_{NiCo} and p_{NiCr} feature fairly identical properties but with opposite trends as seen in p_{NiNi} since they must all add up to unity.

As opposed to Ni-Ni ordering, we observe fewer coherent patterns associated with the identical (same-element) pairs Co-Co and Cr-Cr as in Figs. 2(d) and 2(f). In particular, p_{CoCo} and p_{CrCr} seem to indicate ordering as well as antiordering (potentially due to repulsion) at the first- and next-nearest-neighbor distances. The strong bonding between Co-Cr in

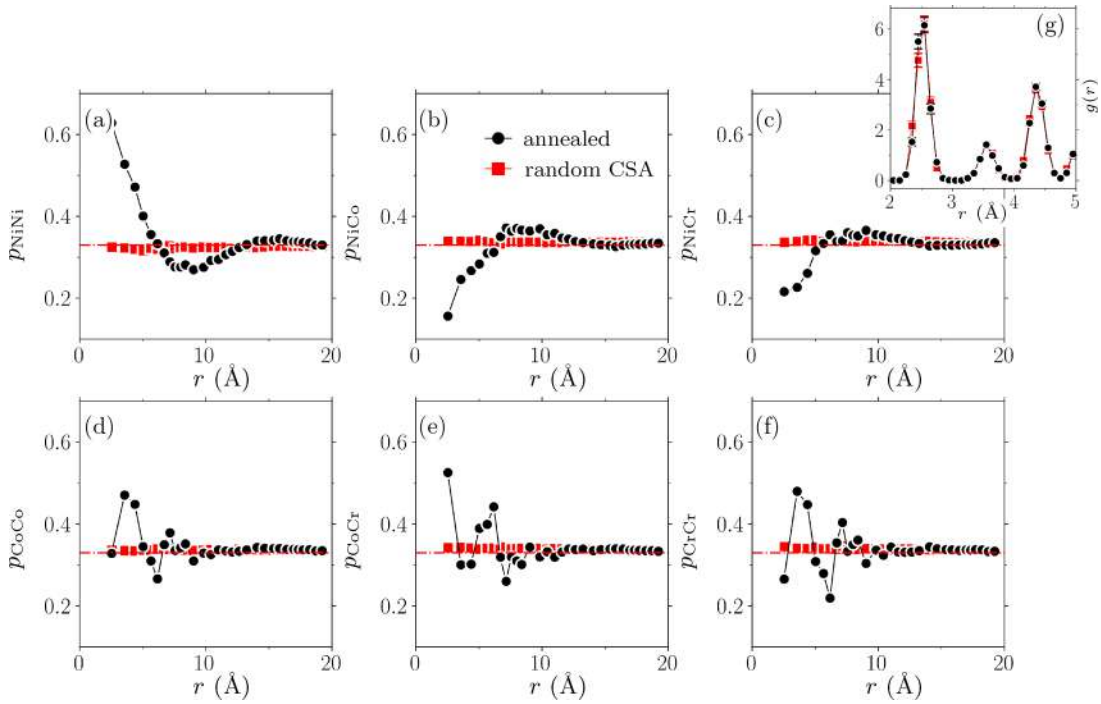

FIG. 2. Short-range ordering in annealed NiCoCr CSAs based on the Li-Sheng-Ma potential. Warren–Cowley SRO parameters including (a) p_{NiNi}, (b) p_{NiCo}, (c) p_{NiCr}, (d) p_{CoCo}, (e) p_{CoCr}, and (f) p_{CrCr} plotted against distance r at $T_a = 400$ K. (g) Pair correlation function $g(r)$ at $T_a = 400$ K. The base (red) dash-dotted line indicates the random concentration.

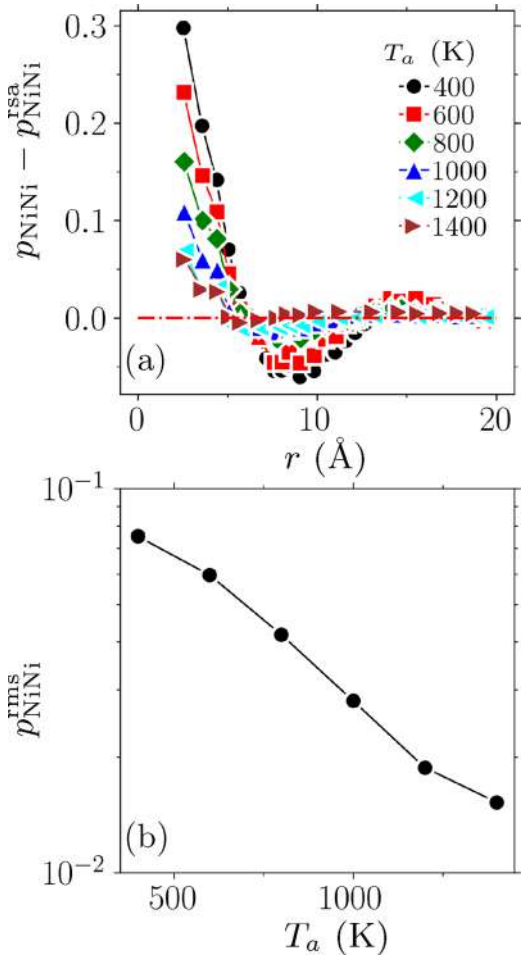

FIG. 3. SRO variations with annealing temperature T_a. (a) $p_{\rm NiNi}$-$p^{\rm rss}_{\rm NiNi}$ as a function of pair distance r and (b) root-mean-squared fluctuations $p^{\rm rms}_{\rm NiNi}$ plotted against T_a. The (red) base line indicates zero correlations associated with RSAs. The results are based on the Li-Sheng-Ma interatomic potential.

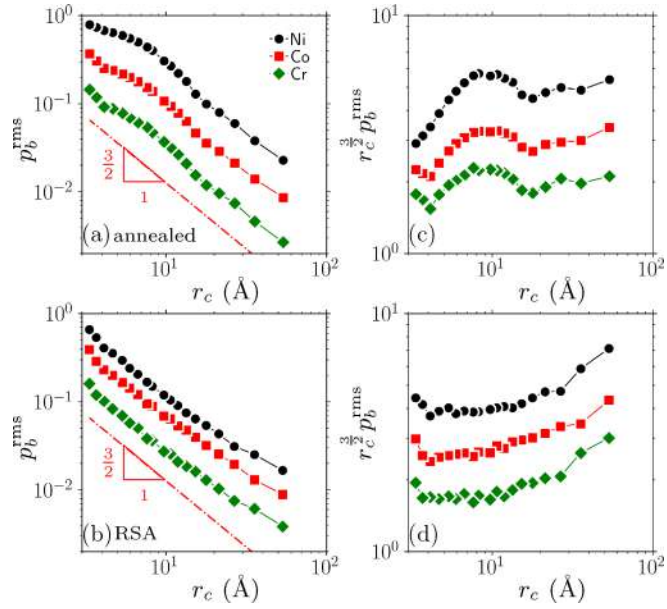

FIG. 4. Root-mean-squared (rms) fluctuations $p^{\rm rms}_b$ of local Ni, Co, and Cr concentrations as a function of window size r_c in (a) annealed NiCoCr CSAs at $T_a = 400$ K and (b) NiCoCr RSAs at $T = 400$ K based on the Li-Sheng-Ma potential. The panels in (c) and (d) are the same as in (a) and (b) but with the y axis rescaled by $r_c^{-\frac{3}{2}}$. The curves are shifted for the sake of clarity.

Fig. 2(e) at the first nearest neighbor is also remarkable (see also Refs. [14,19,20]). We further note that, unlike p_{ab}, the pair correlation function $g(r)$ does not suggest any *structural* differences between annealed and random solid solutions as shown in Fig. 2(g).

Figure 3 quantifies the abundance of Ni-Ni elemental pairs on annealing at multiple temperatures between $T_a =$ 400–1400 K. As shown in Fig. 3(a), the curves show quite complex nonmonotonic features with certain characteristic lengthscales that seem to scale nontrivially with temperature. Nevertheless, the SRO-related features in $p_{\rm NiNi}$-$p^{\rm rsa}_{\rm NiNi}$ become less and less pronounced with an increase in T_a continually approaching their asymptote at the zero-valued base line. This is mathematically quantified by the metric $p^{\rm rms}_{\rm NiNi} = \langle (p_{\rm NiNi} - p^{\rm rsa}_{\rm NiNi})^2 \rangle^{\frac{1}{2}}$ as a root-mean-squared (rms) measure of deviations from RSAs. Figure 3(b) features a monotonic growth of $p^{\rm rms}_{\rm NiNi}$ on decreasing T_a. We also note the tendency for the saturation of $p^{\rm rms}_{\rm NiNi}$ at $T_a \simeq 1400$ K or above potentially due to residual SRO distributions at atomistic levels that preclude an ideal RSA formation. The above analysis was repeated for NiCoCr alloys simulated based on the Farkas-Caro potential. Interestingly, we found no clear signature of clustering in these samples as opposed to those generated via the Li-Sheng-Ma potential (see Fig. S4).

We probed fluctuations in *local* concentrations of the constituent elements in annealed NiCoCr alloys that, in the presence of SROs, should deviate from those of random solid solution alloys. In this context, the entire space was partitioned using subvolumes of varying size r_c, and local molar compositions $p_{\rm Ni}$, $p_{\rm Co}$, and $p_{\rm Cr}$ were determined within each cube. As illustrated in the scatter plot of Fig. S5 associated with NiCoCr CSAs annealed at $T_a = 400$ K, the fluctuations tend to self-average at larger r_c which could be also understood in terms of counting statistics.

We also investigated *local* fluctuations in CSA elemental concentrations in space that, in the presence of SROs, show marked deviations from those of RSAs. Figure 4 shows rms fluctuations of local concentrations $p_{\rm Ni}$, $p_{\rm Co}$, and $p_{\rm Cr}$ and their decay with distance r_c. In Figs. 4(a) and 4(c), rms fluctuations in annealed NiCoCr CSAs seem to self-average but only above some certain lengthscale above which the decay is well predicted by the expected $r_c^{-3/2}$ power-law behavior. The latter is the relevant scaling in purely random atomic configurations as illustrated in Figs. 4(b) and 4(d). We take the characteristic peak in Fig. 4(c) as a signature of spatial correlations which may be interpreted as the average SRO size $\xi^{\rm sro} \simeq 10$ Å. Furthermore, the inferred lengthscale closely agrees with the one extracted from the SRO order parameters in the preceding paragraphs which is within the typical range of SRO size (0.5–1.5 nm) seen experimentally [5,17]. Figure 5 illustrates the probability distribution functions (PDFs) of the local Ni concentrations $p_{\rm Ni}$ at $r_c = 10$ Å for different annealing temperatures. We note the marked deviation of the

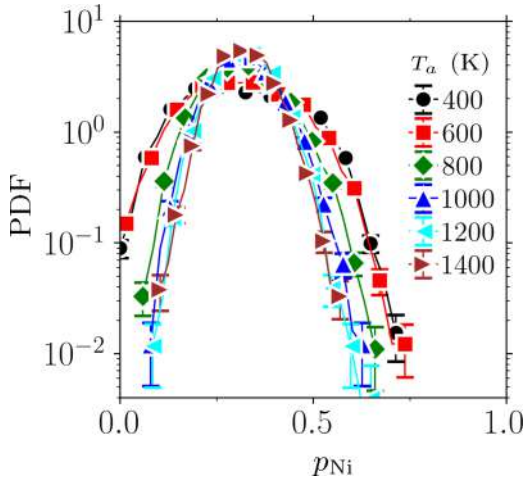

FIG. 5. Probability distribution functions of the local concentrations $p_{\rm Ni}$ in an annealed CSA based on the Li-Sheng-Ma potential at the window size $r_c = 10$ Å and various T_a.

low-T_a PDFs from a standard Gaussian distribution which, otherwise, seems to be the asymptotic limit for the $p_{\rm Ni}$ distributions at higher annealing temperatures. One could also observe a marked abundance of low and high (local) Ni concentrations away from the average at $p_{\rm Ni} = 0.33$ for $T_a = 400$ and 600 K which is indicative of the strong segregation of Ni phases.

B. Lattice distortions

To characterize local distortion properties, we analyzed fluctuations in atomic Voronoi cell volumes and associated temperature dependence in annealed alloys. The aged solid solutions were equilibrated at 5 K on annealing in order to suppress thermal fluctuations. Figures 6(a) and 6(b) shows alloy atomic volumes and associated PDFs for the Ni, Co, and Cr atoms in annealed and random solid solutions. Both alloys feature quite narrow distributions with well-defined mean values $\langle V_{\rm Ni}\rangle$, $\langle V_{\rm Co}\rangle$, and $\langle V_{\rm Cr}\rangle$ that show slight variations with T_a as in Fig. 7(a). The measured mean atomic volume in annealed NiCoCr samples is $\langle V\rangle \simeq 11.3$ Å^3—which is equivalent to the average lattice constant of $a = 3.56$ Å—in very close agreement with experimental observations reported in Ref. [9]. Figure 7(a) indicates features near a characteristic annealing temperature $T_a \simeq 800$ K below which the mean atomic volumes seem to accelerate, potentially a signature of remarkable enthalpy-driven ordering [14]. This observation is in accordance with the heat capacity C_p developing a characteristic peak in Fig. 1(a).

The misfit volumes $\Delta V_b = \langle V_b\rangle - \langle V\rangle$ of Ni, Co, and Cr are determined as $+0.04$, -0.03, and -0.01 Å^3, respectively. The estimated atomic misfits appear to be at least one order of magnitude off from precise experiments [9] but are otherwise reasonably close to *ab initio*–based estimates in Ref. [37]. We further explored the scaled fluctuation $\mathrm{var}^{\frac{1}{2}}(V_b)/\langle V_b\rangle$ as a relevant measure of atomic distortions in Fig. 7(b) with b denoting Ni, Co, and Cr. $\mathrm{var}^{\frac{1}{2}}(V_b)/\langle V_b\rangle$ shows a (fairly) monotonic increase for Ni as a function of T_a until it saturates at a limiting value that appears to be lower than the one

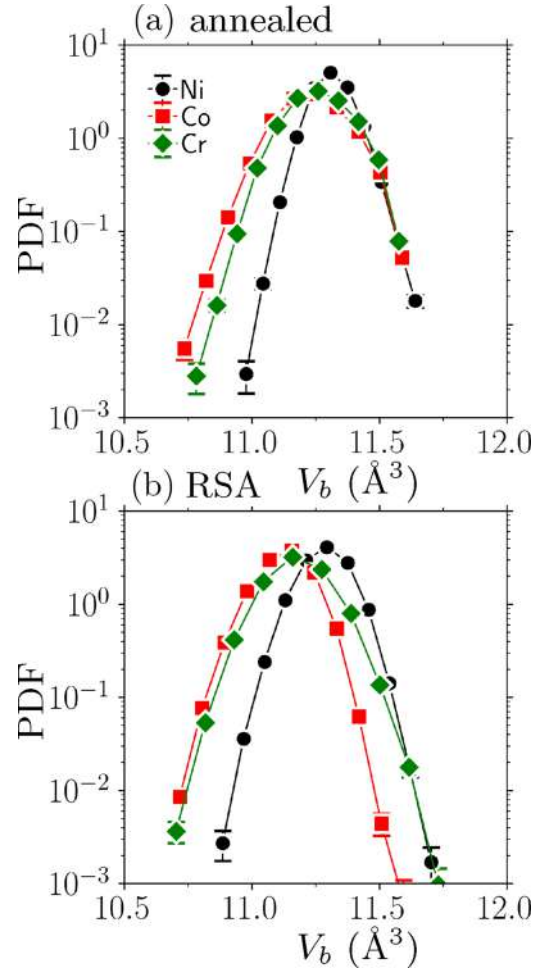

FIG. 6. Probability distributions of alloy atomic (Voronoi) volumes V_b with b denoting the Ni, Co, and Cr atoms in (a) the NiCoCr alloy aged at $T_a = 600$ K and (b) NiCoCr RSA. The volume measurements were carried out at 5 K.

set by the RSA. This is in line with our SRO analysis that the abundance of Ni-Ni pairs within the first-nearest-neighbor distance and, therefore, ordering tends to curtail local atomic misfits or randomness in aged systems. As for Co and Cr, we observe a nonmonotonic evolution with a pronounced peak at $T_a \simeq 600$ K that, in the case of the former, even exceeds the associated RSA limit. Apart from the observed peaks, the relative variance for aged Co/Cr seem to always fall short of those of RSAs with a more dramatic decrease associated with Cr (the green diamonds). This, we conjecture, might be attributed to the favored formation of Cr-Co regions and less tendency for Cr-Ni as well as Cr-Cr bonding as evidenced by the behavior of the first-nearest-neighbor order parameters in Fig. 2. We conclude this subsection by stating that short-range order will have strong bearings on misfit volumes of NiCoCr as our data suggest direct correlations between the latter and the order parameters presented in Sec. III A. One may infer a characteristic scale based on the rms fluctuations analysis presented in Fig. 7(b) which we interpret as the (mean) misfit size $\xi^{\rm misfit} \simeq 1$ Å. Together with nanoscopic SROs ($\xi^{\rm sro} \simeq 10$ Å), atomic-level misfit fluctuations will determine the dislocation glide resistance as discussed in Sec. III C.

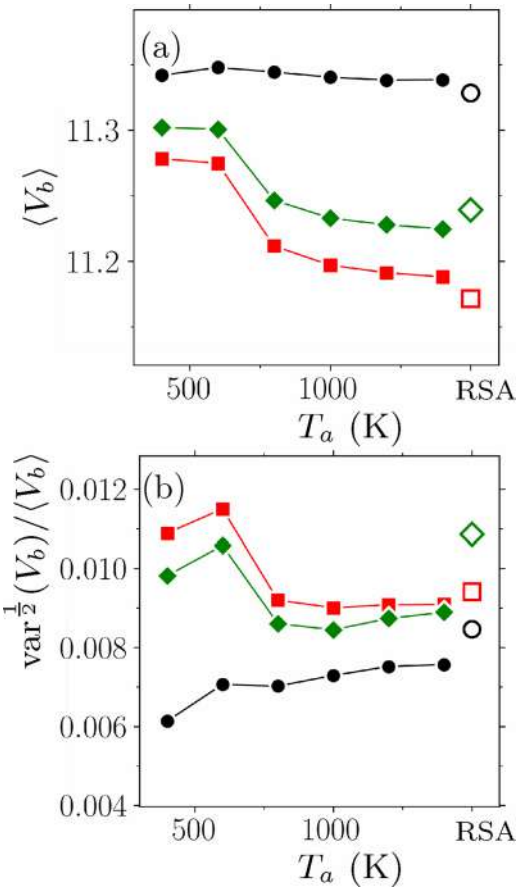

FIG. 7. Dependence of (a) average Voronoi volume $\langle V_b \rangle$ and (b) rms volume fluctuations scaled by the average value $\mathrm{var}^{\frac{1}{2}}(V_b)/\langle V_b \rangle$ on the annealing temperature T_a. The empty symbols correspond to a NiCoCr RSA.

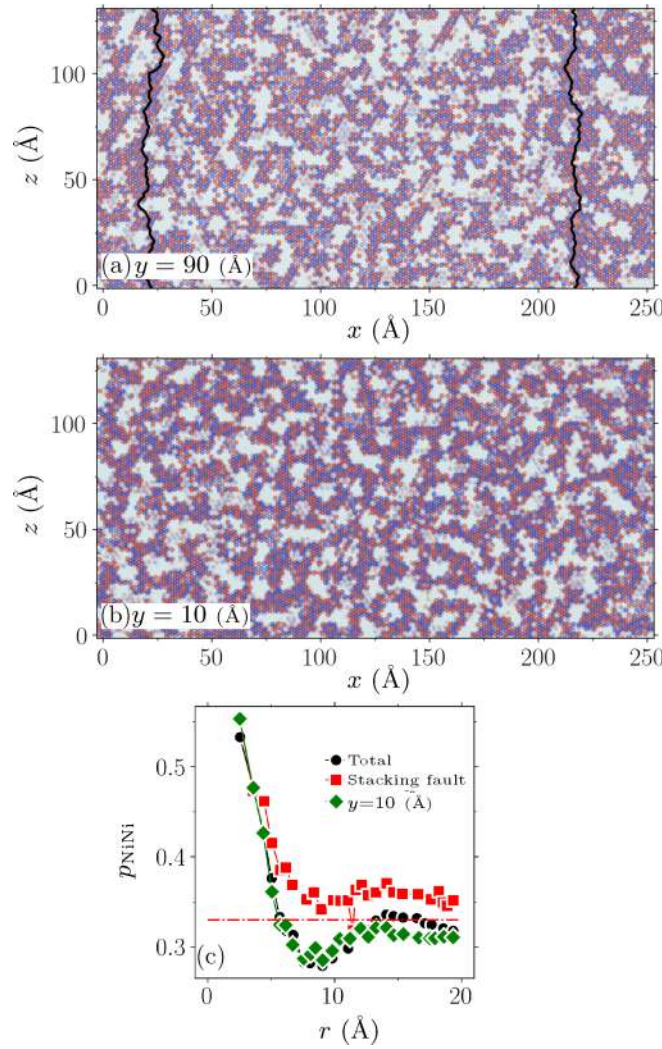

FIG. 8. SRO microstructure in the presence of (partial) dislocations in aging NiCoCr at $T_a = 600$ K. (a) Cross section containing the stacking fault, (b) cross section at $y = 10$ Å, and (c) the SRO parameter p_{NiNi} as a function of pairwise distance r. The different curves in (c) correspond to the entire configuration as well as the two-dimensional stacks depicted in (a) and (b). The black segments denote dislocation lines. The dash-dotted (red) line indicates RSAs. The stacking fault region in (a) lies between $x \simeq 25$ and 220 Å.

C. Interplay between SROs and dislocations

We follow two different approaches to address the dislocation-SRO interplay in NiCoCr CSAs: (i) study of dislocation effects on the nucleation of SROs in *aging* alloys and (ii) investigations of strengthening mechanisms at play in *as-aged* SRO-rich alloys driven out of equilibrium. In (i), we aged samples with a dislocation allowing for both the dislocation dissociation process and spatiotemporal evolution of SROs while annealing. In (ii), on the other hand, we embedded partial dislocations in as-annealed alloys and performed shear depining tests, with no appreciable change in the SRO microstructure.

In line with (i), Fig. 8 compares the structure of SROs within the dislocation dissociation bounds and outside in aging NiCoCr at $T_a = 600$ K. In Fig. 8(a), the denser population of SROs within the stacking fault is visually apparent in comparison with a dislocation-free two-dimensional stack at $y = 10$ Å illustrated in Fig. 8(b). We quantified the observed trend in Fig. 8(c) where the SRO parameter p_{NiNi} associated with the former reveals a shallower decay relative to that of atoms outside the fault plane. To our knowledge, the drastic increase in chemical ordering within the stacking fault region has not been previously reported in the literature. As one possible mechanism at play, we speculate that the long-range stress field and mutual interactions between the two partials [38] might favor the SRO nucleation and its growth within the dissociation zone. Figure S6(a) and S6(b) illustrates that such interactions at $T_a = 600$ K lead to a notable reduction in the stacking fault width which implies the enhanced fault energy due to SROs [14,18]. It is expected that the fault dimension, and therefore the associated formation energy, will be strongly controlled by the annealing temperature as well. We note that a detailed description of the SRO kinetics and dynamics of the dislocation dissociation as well as their (dynamical) interplay during the aging processs is outside the scope of our current study.

Following approach (ii), the notion of "plastic flow" in solute strengthening theories directly links to the existence of the intrinsic friction stress σ_c beyond which dislocations tend

to glide rather smoothly at a non-negligible (mean) velocity $\langle v \rangle$. Below this critical stress, by contrast, the migration of dislocations within CSAs (with a severely distorted energy landscape) typically occurs in a very intermittent manner with long periods of quiescent states (i.e., $\langle v \rangle \simeq 0$) interrupted by bursts of displacements [39]. In the absence of thermal activation, this depinning transition is phenomenologically described as [40]

$$\langle v \rangle \propto (\sigma - \sigma_c)^{1/\beta}, \tag{1}$$

at $\sigma \geqslant \sigma_c$ and $\langle v \rangle = 0$ otherwise, with $\beta \geqslant 1$ reflecting a marked discontinuity at σ_c [41]. Here σ is the applied shear stress resolved in the glide plane.

To estimate σ_c, we performed atomistic simulations of dislocation properties in fcc-based NiCoCr CSAs by studying dynamics of $\frac{1}{2}\langle 110 \rangle \{111\}$ edge dislocations which, under an external drive, dissociate into two mixed partials and a stacking fault in between [38]. To measure the dislocation velocity and its spatial-temporal evolution, we first identified all dislocation line defects in the atomistic crystal, along with their Burgers vectors, and output a line representation of the dislocations by using OVITO [42]. Due to inherent lattice distortions, dislocation lines are not straight but show local fluctuations with respect to the average line direction along z. We describe line fluctuations projected along the glide direction x by the function $h_x(z)$ discretized via a fine grid of size 2 Å across the glide plane parallel to the z direction. We obtain the dislocation velocity $v_x(z) = \delta h_x(z)/\delta t$ by considering successive dislocation snapshots that are apart by the time window $\delta t \simeq 4$ ps. The latter is chosen to be at least three orders of magnitude longer than the discretization time Δt yet short enough to resolve displacements down to atomistic scales. The subsequent correlation analysis was performed on CSAs initially annealed at $T = 600$ K and sheared, along with the RSAs, at 5 K.

Figures S7 and S8 illustrate configurations of (frozen) dislocations in an annealed NiCoCr as well as a NiCoCr RSA under different loads well below the depinning transition ($\sigma < \sigma_c$). The local curvatures associated with the dislocation segments in Fig. S7 indicate fairly coherent pinning effects that somewhat correlate with the spatial locations of SROs. Such features might be also present in RSAs, as in Fig. S8, but to a very limited extent in space. The local line curvature, and its positive sign with respect to the glide direction, should potentially indicate how effectively dislocations are pinned near SROs and/or due to local atomic misfits. In this context, line fluctuations associated with the aged alloy in Fig. 9(a) appear to be correlated over larger lengthscales than those of the random alloy in Fig. 10(a). Similar trends could be also inferred from the associated correlation functions

$$c_h(|z - z'|) = \langle\, \hat{h}_x(z).\hat{h}_x(z')\,\rangle, \tag{2}$$

with the z-scored fluctuations $\hat{h}_x = (h_x - \langle h_x \rangle)/\mathrm{var}^{\frac{1}{2}}(h_x)$. Here the angular brackets $\langle . \rangle$ denote averaging in space. Overall, the slower decay of correlations $c_h(|z - z'|)$ in Fig. 9(b), in comparison with Fig. 10(b), may indicate additional SRO-induced pinning effects in annealed alloys. We note that the absence of SROs does not necessarily rule out long-range fluctuation patterns in RSAs, as in Fig. 10(b), and, therefore, coherent pinning patterns due to atomic-scale distortions [43,44].

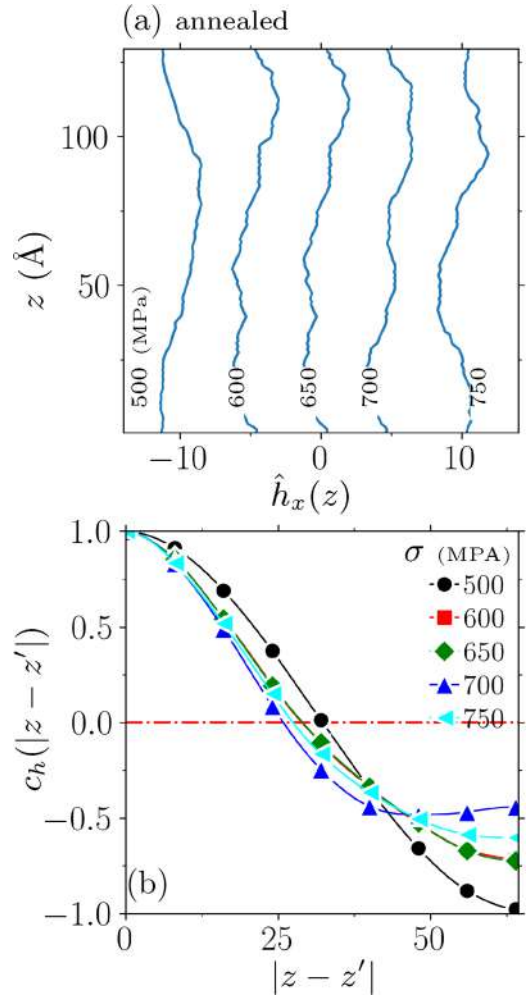

FIG. 9. (a) Configurations of (immobile) partial edge dislocations and (b) associated correlations $c_h(|z - z'|) = \langle\, \hat{h}_x(z).\hat{h}_x(z')\,\rangle$ as a function of distance $|z - z'|$ in an annealed NiCoCr under different applied stresses (below the depinning transition) at $T_a = 600$ K. This includes $\sigma = 500$, 600, 650, 700, and 750 MPa. The shear tests were carried out at 5 K. Here the two-dimensional x-z glide plane denotes a (111) cross section. The dislocation configurations are shifted vertically for the clarity.

We repeated the above analysis by probing velocity fluctuations $v_x(z)$ associated with the gliding dislocations (at $\sigma > \sigma_c$) in annealed as well as random alloys (see Fig. 11). Figure 12 illustrates the shear stress dependence of the mean dislocation velocity as well as (mean) velocity correlations (averaged over different configurations) for the aged and random alloys. As shown in Fig. 12(a), the observed behavior of $\langle v_x \rangle$ versus σ at σ_c marks the dislocation pinning-to-depinning transition which is in agreement with the expected generic dependence around the transition. This seems to be fairly insensitive to annealing except for a meaningful shift of σ_c to larger strengths. The estimated critical shear stresses are $\sigma_c \simeq 950$ and 650 MPa associated with aged and random samples, respectively. The (mean) velocity autocorrelations,

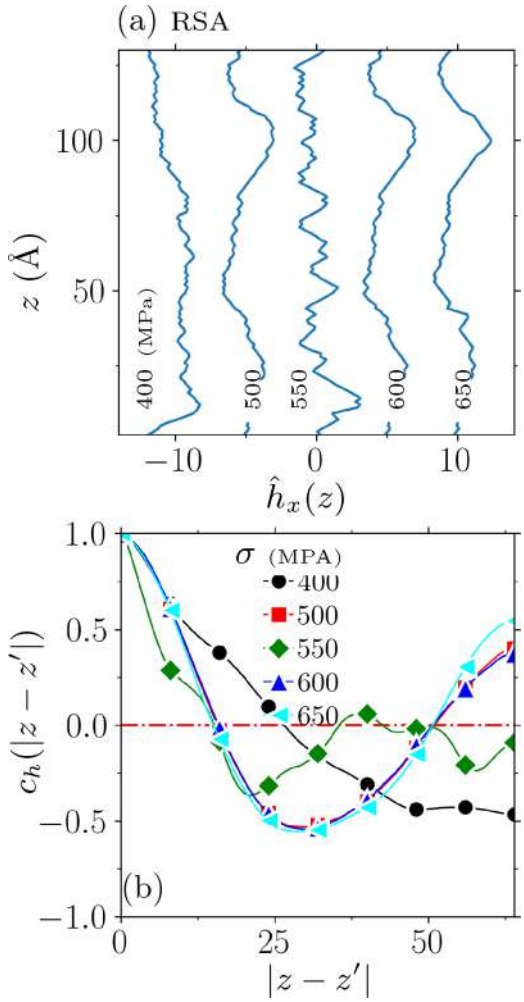

FIG. 10. (a) Configurations of (immobile) partial edge dislocations and (b) associated correlations $c_h(|z-z'|) = \langle\, \hat{h}_x(z).\hat{h}_x(z')\,\rangle$ as a function of distance $|z-z'|$ in a NiCoCr RSA under different applied stresses below the depinning transition. This includes $\sigma = 400$, 500, 550, 600, and 650 MPa.

averaged over different realizations, $\langle c_v(|z-z'|)\rangle_{\rm ens}$ [see the definition of $c_v(|z-z'|)$ below] are shown at different stress levels beyond σ_c in Figs. 12(b) and 12(c), both indicating a finite correlation length.

The marked increase of σ_c is despite (relatively) insignificant variations of elastic properties (Fig. S10) and, therefore, improving yielding properties against RSAs cannot be naively attributed to the enhancement in elasticity of aged alloys (see Sec. IV). The elastic constants we probed in this study include C_{11}, C_{12}, and C_{44} (based on the Voigt notation) as well as the bulk modulus B and Poisson's ratio that were determined by using the Li-Sheng-Ma interatomic potential. Here the x, y, and z dimensions are parallel to [100], [010], and [001] crystal directions, respectively. The overall trend we observe in Fig. S10 is consistent with the study of Li *et al.* [14] which reported the change of elastic properties with increasing SROs (on decreasing T_a). The elastic constants seem to develop features near $T_a \simeq 800$ where the dominant presence of chemical ordering is expected.

We further investigate individual dislocation configurations and associated fluctuations of local velocities in Fig. 13 and 14 where the dislocations move at an average speed $\langle v_x\rangle \simeq 1000\ \mathrm{ms}^{-1}$ in both systems subject to the applied shear stress of $\sigma = 1200$ MPa, well above the corresponding depinning thresholds. The (z-scored) velocity profiles $\hat{v}_x(z)$ in Figs. 13(a) and 14(a) correspond to five different snapshots of gliding dislocations that are shifted for a better view of variations across the (average) dislocation line direction z. We remark that the regions to the left of the dash-dotted lines indicate local velocities below the average speed $\langle v_x\rangle$, as depicted by the left-headed arrows in Fig. 11 . Statistically speaking, the segments with $v_x(z) < \langle v_x\rangle$ somewhat correlate with the positively bent segments of dislocation lines which are mostly influenced by the existence of SROs and/or atomic misfits. Nevertheless, velocity fluctuations quantified by the velocity auto correlations,

$$c_v(|z-z'|) = \langle\, \hat{v}_x(z).\hat{v}_x(z')\,\rangle, \tag{3}$$

does not appear to be statistically different in annealed and random alloys in Figs. 13(b) and 14(b).

IV. DISCUSSIONS AND CONCLUSIONS

Our atomistic simulations of NiCoCr CSAs under special thermal treatments have revealed the formation of nanostructural local chemical ordering and enhanced dislocation glide resistance in close agreement with recent SRO-based studies in simulated and *real* NiCoCr experiments [5,14]. On the ordering effects, we made use of the Li-Sheng-Ma potential function that has been validated in terms of detailed and accurate modeling of Ni, Co, and Cr interatomic interactions [14]. Our direct measurements of local lattice strains agree very closely with a recent *ab initio* study [37] but failed to fully reproduce experimental findings [9]. By using the Farkas-Caro potential, we find very limited relevance to real annealed NiCoCr alloys. The simulated alloys, in this context, exhibit no ordering (beyond statistical fluctuations) but also no notable improvement in yield strengths or elastic properties as reported in Table I in the Supplemental Material (see also Refs. [4,45]). We have interpreted the physical origin of such differences by using robust (experimentally relevant) SRO descriptors in various thermal annealing scenarios. We find that the Li-Sheng-Ma potential, under the proper aging process, leads to an exceptional dislocation depinning strength with low stacking fault width that falls short of that of RSAs. The latter is associated with the enhanced stacking fault energy which might, in part, relate to improved elasticity as a result of SROs but, compared to the yield strength, the ordering effects appear to be less pronounced. The intrinsic strengthening mechanism is mostly dominated by coherent SROs-induced pinning effects, but random spatial distributions of misfit volumes and the resulting roughening seem to be also at play.

Our correlation analyses of the dislocation structure and its spatial-temporal evolution allow for inferring a characteristic pinning length ξ_p and optimal displacement w_p [25]. We interpret the latter as being the rms fluctuations in the dislocation height (with respect to the mean), i.e., $w_p = \langle h_x^2 - \langle h_x\rangle^2\rangle^{\frac{1}{2}}$, whereas the former is determined as the shortest distance

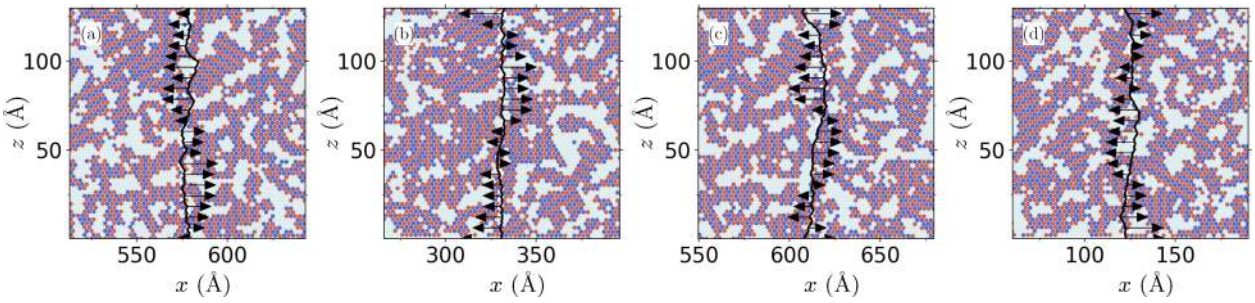

FIG. 11. (z-Scored) Velocity of partial edge dislocations $\hat{v}_x(z)$, illustrated by the black arrows, in annealed NiCoCr at $T_a = 600\,\mathrm{K}$ and under the applied stress $\sigma = 1200$ MPa (above σ_c). The shear tests were carried out at 5 K. Here the panels indicate different realizations associated with the gliding dislocations and the two-dimensional plane denotes a (111) cross section. The arrows denote the velocity field.

where the height correlations cross zero, e.g., $c_h(|z - z'|) = 0$ at $|z - z'| = \xi_p$. At $T_a = 600\,\mathrm{K}$ and $\sigma < \sigma_y$, it follows that $w_p = 5.6$–11.2 Å and $\xi_p = 25$–31 Å associated with the annealed alloy. We conjecture that these two quantities should both correlate with the observed increase in the depinning stress. Based on our present data, however, we are not able to quantify such (anti-)correlations numerically. Both observables w_p and ξ_p are also expected to show meaningful associations with the average SRO size ξ^{sro} as well as the amplitude of misfit fluctuations (characterized by ξ^{misfit}) and are relevant ingredients in *mean-field* solute models that make yield strength predictions based on dislocation line properties (e.g., line tension Γ, length L, and Burgers vector b). In this mean-field picture, SROs introduce the characteristic scale ξ^{sro} that *effectively* decreases the pinning length ξ_p leading to a reduction of the optimal displacement w_p and, therefore, an extra strengthening. Within these mean-field model frameworks, the depinning stress should scale with the line tension Γ, which itself is proportional to the shear modulus and, based on our findings, annealing is not expected to boost σ_y simply because of such elasticity-based contributions but instead variations in the disorder strength and the pinning field are the key factors. To validate such theories in simulations, one must be vigilant to use appropriate mesoscopic lengths (beyond atomistic scales) where continuum-like concepts such as line tension and local curvature are well defined [25]. To explore the full dislocation waviness in MD, it is also necessary that the dislocation length $L \gg \xi_p$ and associated deformation $w_p \ll \xi_p$ [46]. However, the above separation of scales is typically a limit beyond atomistic modeling assumptions including the present study.

Complications might also arise in the application of strengthening theories (e.g., the VC model) due to SRO-induced correlations. The latter are at odds with the "randomness" hypothesis taken as granted based on solutes' arrangements in RSAs. Given that the VC theory is constructed exclusively on misfit information, an *effective* treatment in the presence of spatial correlations is the assumption that SROs should alter dramatically local misfit distributions and, in that case, an alternative length $\xi_{\mathrm{eff}}^{\mathrm{misfit}}$ may be used to describe the strength of distortions. Alternatively, Zaiser and Wu (ZW) [44,47] formulated a more relevant approach based on the fact that pinning forces caused by obstacles are not fully random but rather correlated over some certain length a [48] that we tend to interpret as the effective SRO size ($a \simeq \xi^{\mathrm{sro}}$). In their formulation of dislocation dynamics, ZW introduced a order/disorder length that, along with the strength of misfit fluctuations, may describe the SRO- and misfit-induced noise field in a more accurate way than the VC methodology. Similar efforts were made by Zhang *et al.* [49] along these lines who developed a stochastic Peierls-Nabarro model to incorporate the role of both CSA randomness and short-range ordering effects on glide dynamics of roughened dislocations.

The existing literature reports the emergence of (varying degrees of) SROs as a rather generic feature across a broad

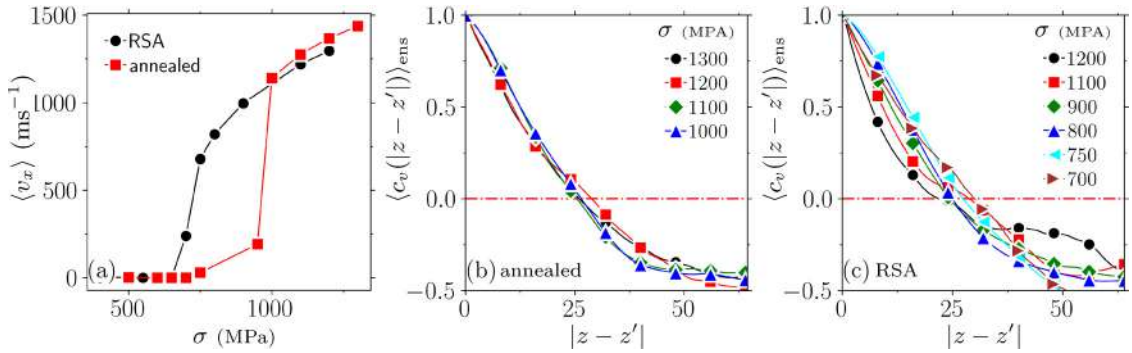

FIG. 12. Stress dependence of the mean dislocation velocity and associated fluctuations. (a) Mobility rule describing the mean dislocation velocity $\langle v_x \rangle$ as a function of applied stress σ. Mean velocity auto correlations $\langle c_v(|z - z'|)\rangle_{\mathrm{ens}}$ as a function of distance $|z - z'|$ in (b) annealed NiCoCr and (c) NiCoCr RSA subject to multiple applied stresses σ above σ_y.

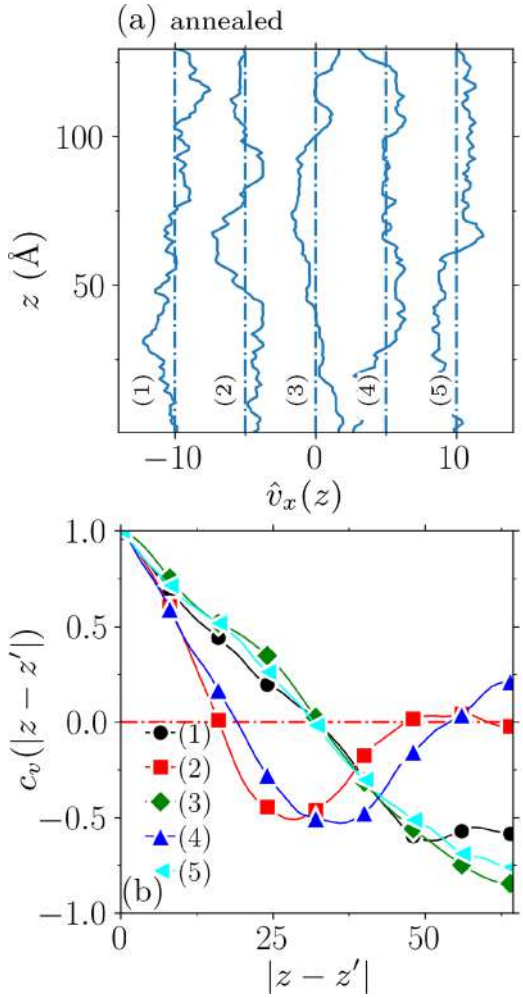

FIG. 13. (a) (Scaled) velocity of partial edge dislocations $\hat{v}_x(z)$ and (b) associated correlations $c_v(|z-z'|) = \langle\, \hat{v}_x(z).\hat{v}_x(z')\,\rangle$ as a function of distance $|z-z'|$ in an annealed NiCoCr at $T_a = 600$ K under the applied stress $\sigma = 1200$ MPa (above σ_c). The shear tests were carried out at 5 K. Here the numbers indicate different realizations associated with gliding dislocations and the two-dimensional plane denotes a (111) cross section. The velocity profiles are shifted vertically for the clarity.

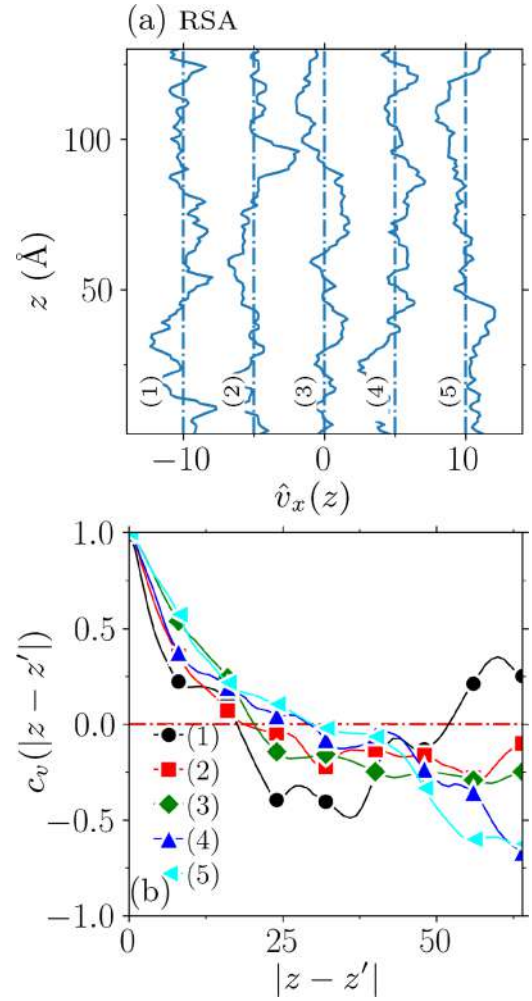

FIG. 14. (a) (Scaled) velocity of partial edge dislocations $\hat{v}_x(z)$ and (b) associated correlations $c_v(|z-z'|) = \langle\, \hat{v}_x(z).\hat{v}_x(z')\,\rangle$ as a function of distance $|z-z'|$ in a NiCoCr RSA under the applied stress $\sigma = 1200$ MPa (above σ_c).

range of high-entropy alloys (see Ref. [6] and references therein). Nevertheless, the focus has been placed on different variants of NiCoCr-based alloys (including the well-studied Cantor alloy) and, owing to similar atomic size and electron negativity, such compositions might tend to favor SRO nucleation [50]. In terms of mechanical properties, the SRO-induced enhancement in the dislocation glide resistance may also constitute fairly universal mechanisms associated with it, i.e., coherent pinning and enhanced roughening, not specific to particular chemical compositions but their robustness over a broader range of compositionally complex solid solutions has yet to be fully explored.

There is a large multitude of results in this work, some of which including the dislocation roughening and SRO emergence could be potentially validated experimentally through the *in/ex situ* electron microscopy analysis or other image-based characterization techniques. Similar efforts were made by Sandfeld *et al.* [43] based on the image processing of *in situ* electron microscopy micrographs to obtain dislocation velocity profiles in a deforming NiCoCrFeMn (Cantor) alloy. Based on their observations, kinematics of dislocation lines and associated pinning patterns suggest the direct relevance of lattice distortions as the dominant roughening mechanism. On the other hand, SROs and associated pinning effects are more subtle to be detected experimentally owing to their nanoscopic origins.

Our finding will have important implications for discrete dislocation dynamics (DDD) models and associated mobility rules that additionally consider spatial correlations within the rough potential energy landscape [51]. This is conceptually similar to intrinsic Peierls stresses that are locally distributed in space but also correlated over certain microstructural scales. Incorporating and tuning SROs' structural features as model ingredients will potentially lead to further improvements in DDD predictive capabilities and design-level hardening features in the context of NiCoCr-based CSAs with dense and complex networks of interacting dislocations.

ACKNOWLEDGMENTS

This research was funded by the European Union Horizon 2020 research and innovation program under Grant Agreement No. 857470 and from the European Regional Development Fund via Foundation for Polish Science International Research Agenda PLUS program Grant No. MAB PLUS/2018/8.

[1] Z. Li, S. Zhao, R. O. Ritchie, and M. A. Meyers, Mechanical properties of high-entropy alloys with emphasis on face-centered cubic alloys, Prog. Mater. Sci. **102**, 296 (2019).

[2] Y. Shang, J. Brechtl, C. Psitidda, and P. K. Liaw, *Mechanical Behavior of High-Entropy Alloys: A Review, High-Entropy Materials Theory, Experiments, and Applications* (Springer, Cham, 2021), pp. 435–522.

[3] Containing equal numbers of Ni, Co, and Cr atoms.

[4] B. Gludovatz, A. Hohenwarter, K. V. S. Thurston, H. Bei, Z. Wu, E. P. George, and R. O. Ritchie, Exceptional damage-tolerance of a medium-entropy alloy CrCoNi at cryogenic temperatures, Nat. Commun. **7**, 10602 (2016).

[5] R. Zhang, S. Zhao, J. Ding, Y. Chong, T. Jia, C. Ophus, M. Asta, R. O. Ritchie, and A. M. Minor, Short-range order and its impact on the CrCoNi medium-entropy alloy, Nature (London) **581**, 283 (2020).

[6] Y. Wu, F. Zhang, X. Yuan, H. Huang, X. Wen, Y. Wang, M. Zhang, H. Wu, X. Liu, H. Wang *et al.*, Short-range ordering and its effects on mechanical properties of high-entropy alloys, J. Mater. Sci. Technol. **62**, 214 (2021).

[7] L. Zhou, Q. Wang, J. Wang, X. Chen, P. Jiang, H. Zhou, F. Yuan, X. Wu, Z. Cheng, and E. Ma, Atomic-scale evidence of chemical short-range order in CrCoNi medium-entropy alloy, Acta Mater. **224**, 117490 (2022).

[8] X. Chen, Q. Wang, Z. Cheng, M. Zhu, H. Zhou, P. Jiang, L. Zhou, Q. Xue, F. Yuan, J. Zhu *et al.*, Direct observation of chemical short-range order in a medium-entropy alloy, Nature (London) **592**, 712 (2021).

[9] B. Yin, S. Yoshida, N. Tsuji, and W. Curtin, Yield strength and misfit volumes of NiCoCr and implications for short-range-order, Nat. Commun. **11**, 1 (2020).

[10] W. G. Noehring and W. Curtin, Correlation of microdistortions with misfit volumes in high entropy alloys, Scr. Mater. **168**, 119 (2019).

[11] L. Liu, Y. Zhang, J. Han, X. Wang, W. Jiang, C.-T. Liu, Z. Zhang, and P. K. Liaw, Nanoprecipitate-strengthened high-entropy alloys, Adv. Sci. **8**, 2100870 (2021).

[12] Q. He, P. Tang, H. Chen, S. Lan, J. Wang, J. Luan, M. Du, Y. Liu, C. Liu, C. Pao *et al.*, Understanding chemical short-range ordering/demixing coupled with lattice distortion in solid solution high entropy alloys, Acta Mater. **216**, 117140 (2021).

[13] C. Wolverton, V. Ozolins, and A. Zunger, Short-range-order types in binary alloys: A reflection of coherent phase stability, J. Phys.: Condens. Matter **12**, 2749 (2000).

[14] Q.-J. Li, H. Sheng, and E. Ma, Strengthening in multi-principal element alloys with local-chemical-order roughened dislocation pathways, Nat. Commun. **10**, 3563 (2019).

[15] F. Walsh, M. Asta, and R. O. Ritchie, Magnetically driven short-range order can explain anomalous measurements in crconi, Proc. Natl. Acad. Sci. USA **118**, e2020540118 (2021).

[16] F. Zhang, S. Zhao, K. Jin, H. Xue, G. Velisa, H. Bei, R. Huang, J. Ko, D. Pagan, J. Neuefeind *et al.*, Local Structure and Short-Range Order in a NiCoCr Solid Solution Alloy, Phys. Rev. Lett. **118**, 205501 (2017).

[17] J. Wang, P. Jiang, F. Yuan, and X. Wu, Chemical medium-range order in a medium-entropy alloy, Nat. Commun. **13**, 1021 (2022).

[18] J. Ding, Q. Yu, M. Asta, and R. O. Ritchie, Tunable stacking fault energies by tailoring local chemical order in CrCoNi medium-entropy alloys, Proc. Natl. Acad. Sci. USA **115**, 8919 (2018).

[19] X. Yang, Y. Xi, C. He, H. Chen, X. Zhang, and S. Tu, Chemical short-range order strengthening mechanism in CoCrNi medium-entropy alloy under nanoindentation, Scr. Mater. **209**, 114364 (2022).

[20] W.-R. Jian, Z. Xie, S. Xu, Y. Su, X. Yao, and I. J. Beyerlein, Effects of lattice distortion and chemical short-range order on the mechanisms of deformation in medium entropy alloy CoCrNi, Acta Mater. **199**, 352 (2020).

[21] D. Liu, Q. Yu, S. Kabra, M. Jiang, P. Forna-Kreutzer, R. Zhang, M. Payne, F. Walsh, B. Gludovatz, M. Asta *et al.*, Exceptional fracture toughness of crconi-based medium-and high-entropy alloys close to liquid helium temperatures, Science **378**, 978 (2022).

[22] J. Miao, C. Slone, S. Dasari, M. Ghazisaeidi, R. Banerjee, E. P. George, and M. J. Mills, Ordering effects on deformation substructures and strain hardening behavior of a crconi based medium entropy alloy, Acta Mater. **210**, 116829 (2021).

[23] S. S. Sohn, A. Kwiatkowski da Silva, Y. Ikeda, F. Körmann, W. Lu, W. S. Choi, B. Gault, D. Ponge, J. Neugebauer, and D. Raabe, Ultrastrong medium-entropy single-phase alloys designed via severe lattice distortion, Adv. Mater. **31**, 1807142 (2019).

[24] R. Labusch, A statistical theory of solid solution hardening, Phys. Status Solidi B **41**, 659 (1970).

[25] C. Varvenne, A. Luque, and W. A. Curtin, Theory of strengthening in fcc high entropy alloys, Acta Mater. **118**, 164 (2016).

[26] C. Varvenne, G. P. M. Leyson, M. Ghazisaeidi, and W. A. Curtin, Solute strengthening in random alloys, Acta Mater. **124**, 660 (2017).

[27] C. Varvenne and W. A. Curtin, Predicting yield strengths of noble metal high entropy alloys, Scr. Mater. **142**, 92 (2018).

[28] D. Utt, S. Lee, Y. Xing, H. Jeong, A. Stukowski, S. H. Oh, G. Dehm, and K. Albe, The origin of jerky dislocation motion in high-entropy alloys, Nat. Commun. **13**, 4777 (2022).

[29] A. P. Thompson, H. M. Aktulga, R. Berger, D. S. Bolintineanu, W. M. Brown, P. S. Crozier, P. J. in 't Veld, A. Kohlmeyer, S. G. Moore, T. D. Nguyen, R. Shan, M. J. Stevens, J. Tranchida, C. Trott, and S. J. Plimpton, LAMMPS—A flexible simulation tool for particle-based materials modeling at the atomic, meso, and continuum scales, Comput. Phys. Commun. **271**, 108171 (2022).

[30] F.-H. Cao, Y.-J. Wang, and L.-H. Dai, Novel atomic-scale mechanism of incipient plasticity in a chemically complex crconi

medium-entropy alloy associated with inhomogeneity in local chemical environment, Acta Mater. **194**, 283 (2020).

[31] D. Farkas and A. Caro, Model interatomic potentials and lattice strain in a high-entropy alloy, J. Mater. Res. **33**, 3218 (2018).

[32] B. Sadigh, P. Erhart, A. Stukowski, A. Caro, E. Martinez, and L. Zepeda-Ruiz, Scalable parallel Monte Carlo algorithm for atomistic simulations of precipitation in alloys, Phys. Rev. B **85**, 184203 (2012).

[33] See Supplemental Material at http://link.aps.org/supplemental/10.1103/PhysRevB.107.094109 for further discussions relevant to simulation details, characterization of local ordering, and yield properties corresponding to model NiCoCr alloys.

[34] C. A. Becker, M. Asta, J. J. Hoyt, and S. M. Foiles, Equilibrium adsorption at crystal-melt interfaces in lennard-jones alloys, J. Chem. Phys. **124**, 164708 (2006).

[35] Y. N. Osetsky and D. J. Bacon, An atomic-level model for studying the dynamics of edge dislocations in metals, Modell. Simul. Mater. Sci. Eng. **11**, 427 (2003).

[36] We only report the (excess) configurational heat capacity (and thermal expansion coefficient) neglecting (ideal) kinetic contributions.

[37] H. S. Oh, S. J. Kim, K. Odbadrakh, W. H. Ryu, K. N. Yoon, S. Mu, F. Körmann, Y. Ikeda, C. C. Tasan, D. Raabe *et al.*, Engineering atomic-level complexity in high-entropy and complex concentrated alloys, Nat. Commun. **10**, 1 (2019).

[38] D. Hull and D. J. Bacon, *Introduction to Dislocations* (Butterworth-Heinemann, Oxford, 2001).

[39] Y. N. Osetsky, G. M. Pharr, and J. R. Morris, Two modes of screw dislocation glide in fcc single-phase concentrated alloys, Acta Mater. **164**, 741 (2019).

[40] M. Zaiser, Scale invariance in plastic flow of crystalline solids, Adv. Phys. **55**, 185 (2006).

[41] A. Esfandiarpour, S. Papanikolaou, and M. Alava, Edge dislocations in multicomponent solid solution alloys: Beyond traditional elastic depinning, Phys. Rev. Res. **4**, L022043 (2022).

[42] A. Stukowski, V. V. Bulatov, and A. Arsenlis, Automated identification and indexing of dislocations in crystal interfaces, Modell. Simul. Mater. Sci. Eng. **20**, 085007 (2012).

[43] C. Zhang, H. Song, D. Oliveros, A. Fraczkiewicz, M. Legros, and S. Sandfeld, Data-mining of in-situ tem experiments: On the dynamics of dislocations in CoCrFeMnNi alloys, Acta Mater. **241**, 118394 (2022).

[44] M. Zaiser and R. Wu, Pinning of dislocations in disordered alloys: Effects of dislocation orientation, arXiv:2109.07796.

[45] G. Laplanche, M. Schneider, F. Scholz, J. Frenzel, G. Eggeler, and J. Schreuer, Processing of a single-crystalline crconi medium-entropy alloy and evolution of its thermal expansion and elastic stiffness coefficients with temperature, Scr. Mater. **177**, 44 (2020).

[46] W. A. Curtin (private communication, 2022).

[47] A. Vaid, D. Wei, E. Bitzek, S. Nasiri, and M. Zaiser, Pinning of extended dislocations in atomically disordered crystals, arXiv:2110.12507.

[48] P.-A. Geslin, A. Rida, and D. Rodney, Microelasticity model of random alloys. part ii: Displacement and stress correlations, J. Mech. Phys. Solids **153**, 104480 (2021).

[49] L. Zhang, Y. Xiang, J. Han, and D. J. Srolovitz, The effect of randomness on the strength of high-entropy alloys, Acta Mater. **166**, 424 (2019).

[50] Q. Ding, Y. Zhang, X. Chen, X. Fu, D. Chen, S. Chen, L. Gu, F. Wei, H. Bei, Y. Gao *et al.*, Tuning element distribution, structure and properties by composition in high-entropy alloys, Nature (London) **574**, 223 (2019).

[51] H. Salmenjoki, A. Lehtinen, L. Laurson, and M. J. Alava, Plastic yielding and deformation bursts in the presence of disorder from coherent precipitates, Phys. Rev. Mater. **4**, 083602 (2020).

Dislocation plasticity in equiatomic NiCoCr alloys: The effect of short-range order

Amir H. Naghdi[1], Kamran Karimi[1], Axel E. Poisvert[1], Amin Esfandiarpour[1],
Rene Alvarez[1], Pawel Sobkowicz[1], Mikko Alava[1,2], and Stefanos Papanikolaou[1]
[1] *NOMATEN Centre of Excellence, National Center for Nuclear Research, ul. A. Sołtana 7, 05-400 Swierk/Otwock, Poland*
[2] *Aalto University, Department of Applied Physics, PO Box 11000, 00076 Aalto, Espoo, Finland*

SUPPLEMENTARY MATERIALS

In this Supplementary Materials, we will present further information relevant to simulation details, characterization of local ordering, and yield properties corresponding to model NiCoCr alloys.

Figure S1 shows $\Delta\mu_{\text{Ni-Cr}}$ and $\Delta\mu_{\text{Ni-Co}}$ as the difference of the chemical potentials of Co and Cr with respect to Ni using the semi-grand canonical (SGC) ensemble. In Figure S2, we illustrate our shear simulation setup with dimensions $L_x \simeq 80$ nm, $L_y \simeq 20$ nm, and $L_z \simeq 15$ nm. Figure S3 displays snapshots of NiCoCr realizations associated with random solid solutions and annealed samples at various temperatures. Figure S4(a-f) illustrates that the the Warren–Cowley SRO parameters p_{ab} associated with the annealed CSAs obtained from the Farkas-Caro potential function are statistically indistinguishable from p_{ab}^{rsa} at $T_a = 400$ K. The scatter plot of Fig. S5 displays local concentration fluctuations p_b (with b being Ni, Co, and Cr in an annealed CSA (based on the Li-Sheng-Ma potential) at $T_a = 400$ K and multiple lengthscales ($r_c = 5, 10, 18$ Å). Figure S6(a) and (b) illustrate realizations of partial dislocations in a RSA as well as a NiCoCr annealed at $T_a = 600$ K. Figure S7 and S8 display realizations of (immobile) partial edge dislocations in an annealed NiCoCr and a RSA at different stress levels. Figure S9 illustrates the structure of local (von Mises) stresses in an annealed NiCoCr at $T_a = 600$ K and under the applied stress $\sigma = 1200$ MPa (above σ_c). Elastic constants and their dependence on the annealing temperature T_a are shown in Fig. S10. Table I compares elastic constants and depinning stress σ_c measured at $T = 5$ K for NiCoCr with and without annealing using the Farkas-Caro potential.

TABLE I. Cubic elastic constants and depinning stress σ_c at 5 K for NiCoCr with and without annealing using the Farkas-Caro potential.

	$T_a = 1100$ (K)	$T_a = 600$ (K)	RSA	Experiment
C_{11} (GPa)	269.3	251.4	270.1	255.3 [1]
C_{12} (GPa)	146.8	149.1	147.9	159.4 [1]
C_{44} (GPa)	126.7	126.8	126.7	146.7 [1]
σ_c (GPa)	0.075	0.070	0.080	1.3 [2]

[1] G. Laplanche, M. Schneider, F. Scholz, J. Frenzel, G. Eggeler, and J. Schreuer, Processing of a single-crystalline crconi medium-entropy alloy and evolution of its thermal expansion and elastic stiffness coefficients with temperature, Scripta Materialia **177**, 44 (2020).
[2] B. Gludovatz, A. Hohenwarter, K. V. S. Thurston, H. Bei, Z. Wu, E. P. George, and R. O. Ritchie, Exceptional damage-tolerance of a medium-entropy alloy CrCoNi at cryogenic temperatures, Nature Communications **7**, 10602 (2016).

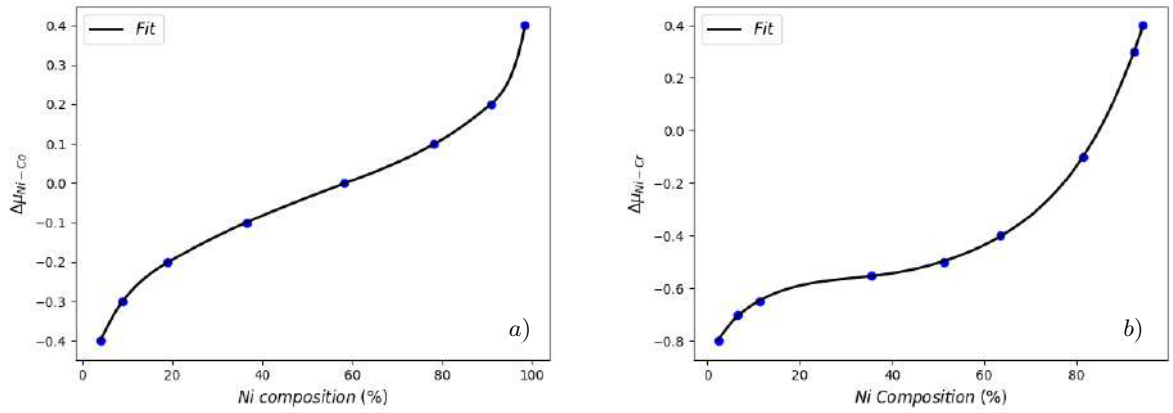

FIG. S1. Chemical potential differences for **a)** Ni-Co and **b)** Ni-Cr pairs used for variance constrained semi-grand canonical (VCSGC) ensemble.

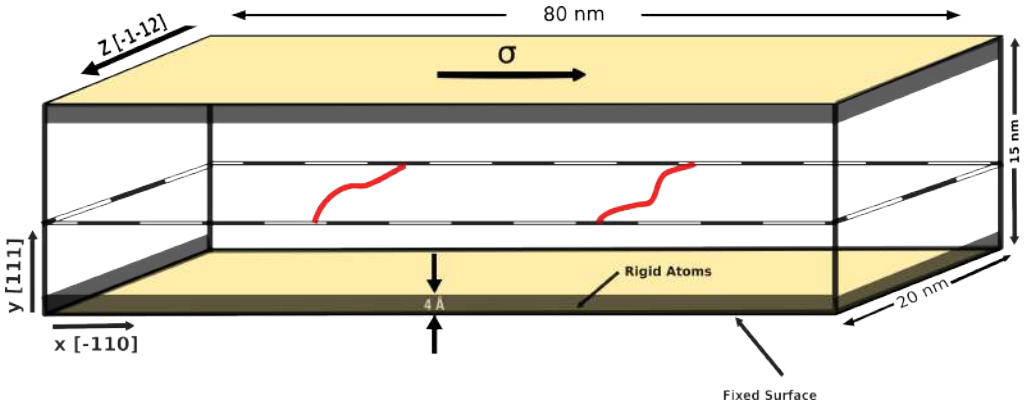

FIG. S2. A sketch of the shear setup including the partial dislocations. Periodic boundary conditions are applied parallel to the dislocation lines and the glide direction (x and z dimensions, respectively) and fixed boundaries are implemented along the y direction (rigid slabs in gray). To shear, rigid atoms within the bottom surface are held fixed (i.e. zero displacements) while the shear stress σ is applied on the rigid top plane.

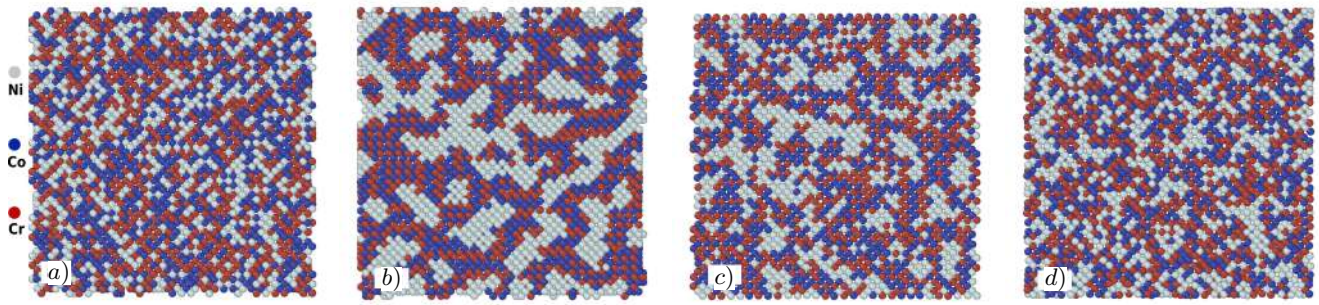

FIG. S3. Snapshots of NiCoCr samples **a)** RSA equilibrated at $T = 400$ K, **b)** annealed at $T_a = 400$ K, **c)** annealed at $T_a = 800$ K and **d)** annealed at $T_a = 1400$ K.

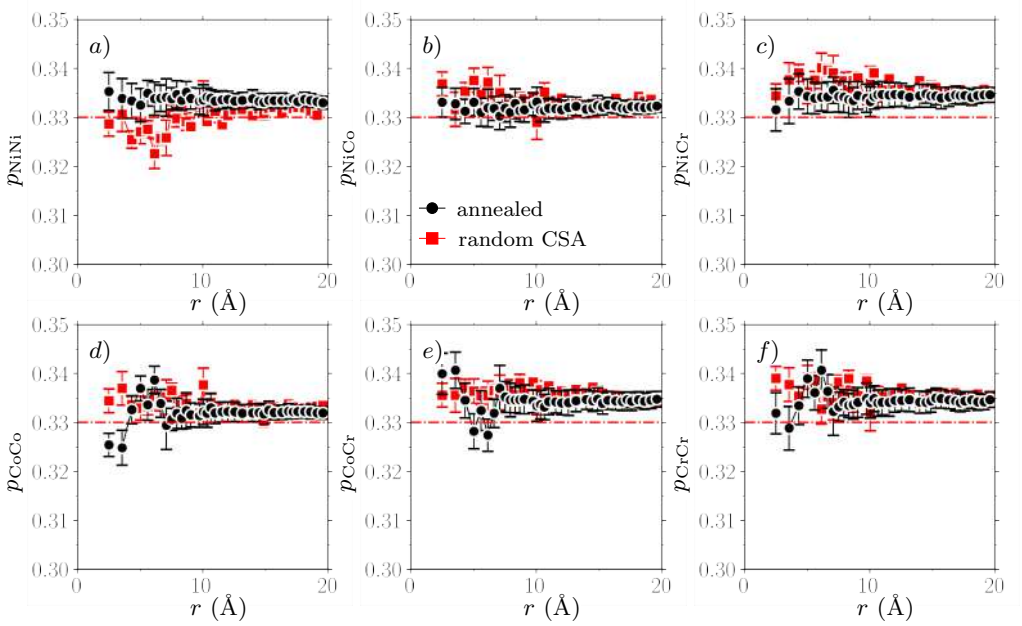

FIG. S4. Short range ordering in annealed NiCoCr CSAs based on the Farkas-Caro potential. Warren–Cowley SRO parameters including **a)** p_{NiNi} **b)** p_{NiCo} **c)** p_{NiCr} **d)** p_{CoCo} **e)** p_{CoCr} **f)** p_{CrCr} plotted against distance r at $T_a = 400$ K. The base (red) dashdotted line indicates the random concentration.

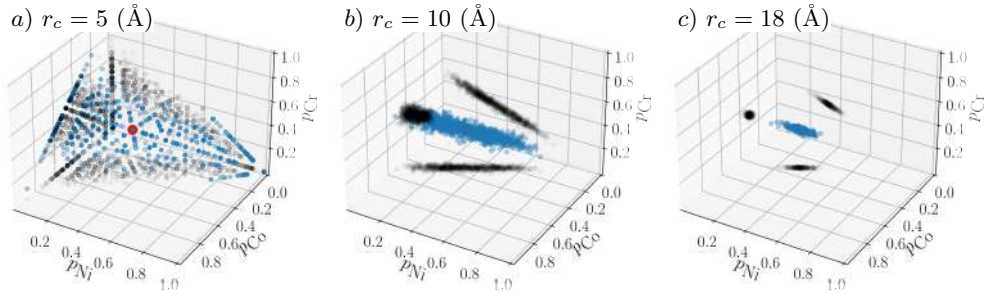

FIG. S5. Local concentration fluctuations p_b with b being Ni, Co, and Cr in an annealed CSA (based on the Li-Sheng-Ma potential) at $T_a = 400$ K and multiple lengthscales **a)** $r_c = 5$ Å **b)** $r_c = 10$ Å **c)** $r_c = 18$ Å. We note that at low distance scales $r_c = 5$ and 10 Å, the segregation of Ni and Co/Cr domains is very strong. The black scatter points represent the two dimensional projections. The red dot denotes the equimolar concentration.

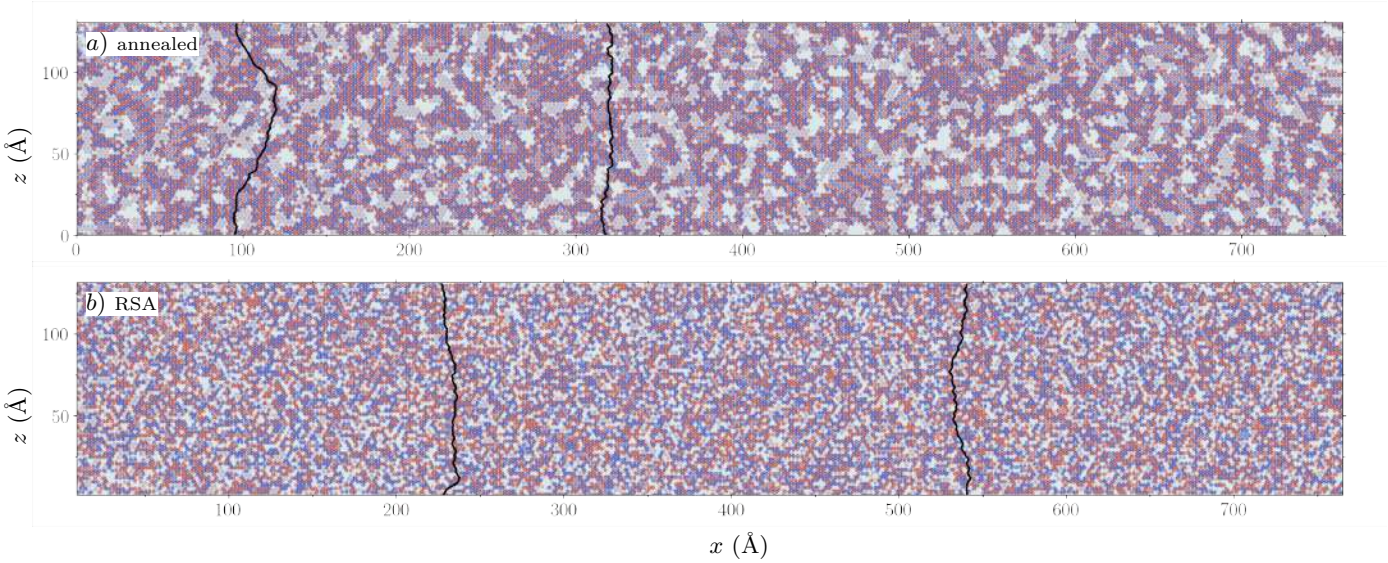

FIG. S6. Realizations of partial dislocations in **a)** NiCoCr annealed at $T_a = 600$ K **b)** RSA.

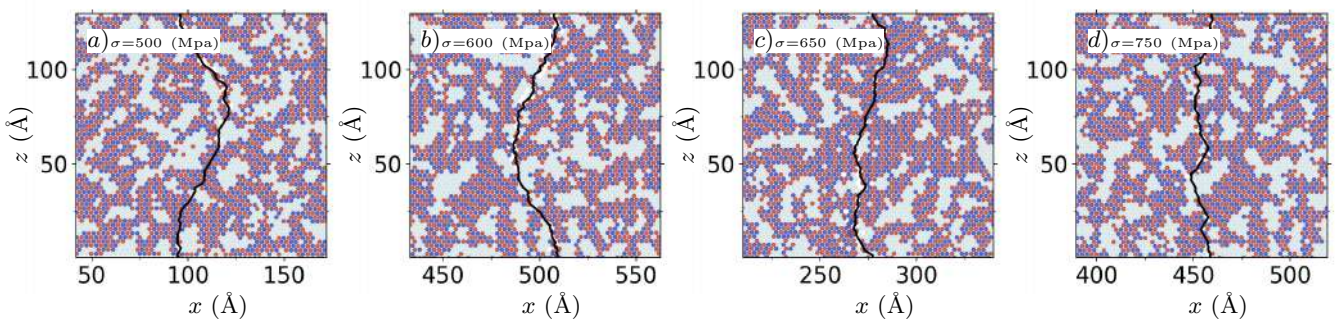

FIG. S7. Realizations of (immobile) partial edge dislocations in an annealed NiCoCr subject to the shear stress **a)** $\sigma = 500$, **b)** 600, **c)** 650, and **d)** 750 MPa. Here the two-dimensional stack denotes the (111) glide plane.

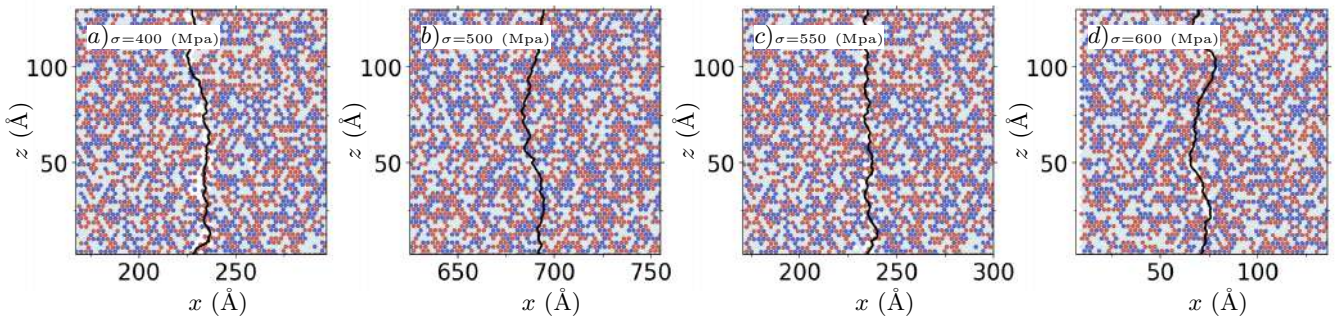

FIG. S8. Realizations of (immobile) partial dislocations in a NiCoCr RSA subject to the shear stress **a)** $\sigma = 400$, **b)** 500, **c)** 550, and **d)** 600 MPa.

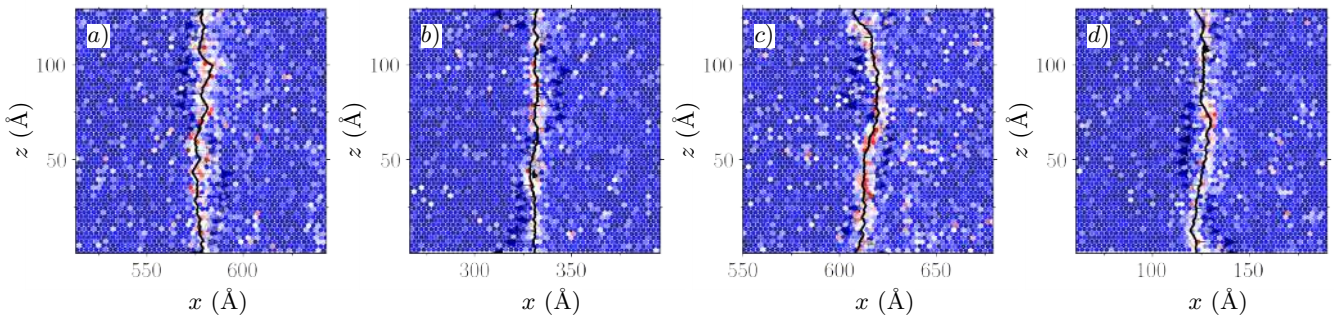

FIG. S9. Structure of residual (von Mises) stresses in annealed NiCoCr at $T_a = 600$ K and under the applied stress $\sigma = 1200$ MPa (above σ_c). The shear tests were carried out at 5 K. Here, the panels indicate different realizations associated with the gliding dislocations and the two-dimensional plane denotes a (111) cross section. The red, white, and blue colors indicate high, medium, and low stresses.

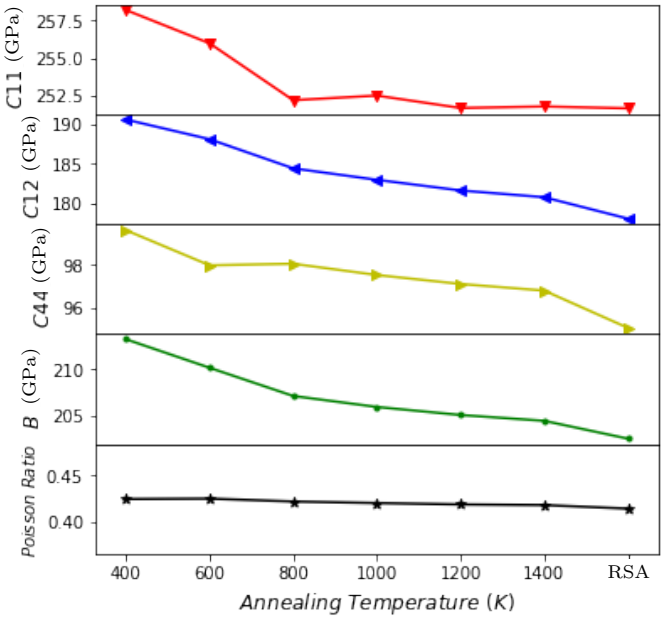

FIG. S10. Elastic constants and their dependence on the annealing temperature T_a. Measurements were carried out at $T = 5$ K. The rightmost data point represents elastic properties of a random solid solution. Samples were generated based on the Li-Sheng-Ma potential.

Dynamic Nanoindentation and Short-Range Order in Equiatomic NiCoCr Medium-Entropy Alloy Lead to Novel Density Wave Ordering

A. Naghdi,[1,2] F. J. Domínguez-Gutiérrez,[1] W. Y. Huo,[1,3] K. Karimi,[1] and S. Papanikolaou[1,*]
[1]NOMATEN Centre of Excellence, National Center for Nuclear Research, ulica A. Sołtana 7, 05-400 Swierk/Otwock, Poland
[2]IDEAS NCBR, ulica Chmielna 69, 00-801 Warsaw, Poland
[3]College of Mechanical and Electrical Engineering, Nanjing Forestry University, Nanjing 210037, China

(Received 10 November 2022; revised 27 December 2023; accepted 9 February 2024; published 12 March 2024)

Chemical short-range order is believed to be a key contributor to the exceptional properties of multicomponent alloys. However, its direct validation and confirmation has been highly elusive in most compounds. Recent studies for equiatomic NiCoCr alloys have shown that thermal treatments (i.e., annealing and aging) may facilitate and manipulate such ordering. In this work, by using molecular simulations, we show that nanomechanical probes, such as nanoindentation, may be utilized toward further manipulation of chemical short-range order, providing explicit validation pathways. By using well established interatomic potentials, we perform hybrid molecular-dynamics–Monte Carlo at room temperature to demonstrate that particular dwell nanoindentation protocols can lead, through thermal Monte Carlo equilibration, to local reorganization under the indenter tip, toward a density-wave stripe pattern. We characterize the novel density-wave structures, which are highly anisotropic and dependent on local, nanoindentation-induced stress concentrations, and we show how they deeply originate from intrinsic features of interelemental interactions. Furthermore, we show that these novel patterns consistently scale with the incipient plastic zone, under the indenter tip, justifying their observation at experimentally feasible nanoindentation depths.

DOI: 10.1103/PhysRevLett.132.116101

Concentrated multicomponent alloys, and in particular, the celebrated Cantor alloys [1–3], such as equiatomic single-phase CoCrFeMnNi, have been instrumental into guiding the exploration for the discovery of affordable, durable alloys, suitable for applications under extreme conditions [4,5]. It has been conjectured that a major contributor to the exceptional properties of these alloys is the formation of chemical short-range (1 nm) order (CSRO) that may pin or/and obstruct moving lattice defects, such as dislocations. While the observation of CSRO is quite common in such complex alloys, its causal connection to *exceptional* mechanical properties has been a subject of intense debate. Extensive investigations have culminated toward the focus shining on the curious case of single-phase equiatomic NiCoCr. This alloy has outstanding mechanical properties, namely hardness, strength, and ductility [6], and there is plausible formation of CSROs in the alloys, especially after sample aging at high temperatures [7–11]. Numerous studies have explored the nanoindentation creep behavior of materials such as high-entropy alloys, nanoglass films, and medium-entropy alloys demonstrating that factors such as internal structure, external loading sequence, and strain rate sensitivity significantly influence creep behavior, where thermomechanical processing can improve performance under shock loads [12–16]. On one hand, it has been observed that dislocation stacking fault widths are sensitive to the formation of such short-range order [14,17], which is commonly (in metallurgy) associated with large(r) mechanical strength.

Moreover, such improvements in NiCoCr strength have been also greatly attributed to solid solution strengthening, due to lattice distortion effects, with no or very little contributions from short-range ordering [18]. Therefore, a deeper understanding of CSRO is required to identify how to control and possibly, augment CSRO features, and check its causal effects on mechanical properties. For this purpose, in this work, we theoretically consider dwell nanoindentation as a possible way to locally manipulate CSRO in equiatomic NiCoCr, and lead to causal connections between hardness and microscopy-resolvable nanostructural features. We utilize molecular simulation, as well as Monte Carlo methods, and we show that CSRO (if it exists) will be unstable to the formation of unconventional density-wave ordered (DWO) stripe patterns, that are highly anisotropic and originate due to interatomic potential features.

CSRO is commonly observable at the nanoscale, ranging between 0.5–2 nm in linear size [8]. Starting from a random

solid solution (RSS), it is natural to expect that constituent element enthalpic interactions may cause CSRO formation at the atomic scale [7,11,14,18–29]. CSROs have a notable effect on defects (dislocations, interstitials, and vacancies, etc.) and their dynamical behavior, as well as macroscopic alloy mechanical properties [7,14,18,19,27–30]. CSRO is commonly inferred through implicit experimental measurements, through their relation to macroscopic properties, such as stacking-fault energy, hardness, irradiation effects, etc. [24–26,31]. CSRO is also investigated in theoretical and computational works [10,27,32], with the most intense focus being on the case of equiatomic NiCoCr [17,27]. Molecular dynamics (MD), spin polarized density functional theory [10], but also Monte Carlo (MC) simulations have been utilized to characterize CSRO structural features [32].

Creep deformation studies in multicomponent alloys are abundant [33–39]. Here, we aim at utilizing creep deformation to comprehend in a deeper sense the character of CSRO by promoting nontrivial predictions for elemental density wave ordering at the nanoscale. While uniaxial testing [39–43] and nanoindentation, alongside microscopy, have been used for the elucidation of lattice defect deformation mechanisms [44], the constant-load dwell nanoindentation tests, between 1 min to 10 h of dwell time, have been solely popular for investigating the relation between hardness and indentation strain rate over a, possibly wide, temperature range [45–48]. We use this concept to generate predictions for CSRO nanopatterning at room temperature that may be directly observable using electron microscopy techniques. While this work is fully focused on modeling aspects and predictions for CSRO saturation regimes that may emerge at each loading depth, prior alloy studies [45–48] shall allow us to conclude that the proposed scenario is attainable at room conditions.

In this Letter, we utilize hybrid MC-MD simulations, using LAMMPS [49], to demonstrate the plausible thermomechanical effects of a dwell nanoindentation scenario in single-phase equiatomic RSS NiCoCr. RSS samples were generated using random elemental sampling on appropriate face-centered cubic (FCC) lattices, with crystal orientations of $x = [100]$, $y = [010]$, and $z = [001]$ or $x = [100]$, $y = [01\bar{1}]$, and $z = [011]$, and dimensions $25.85 \times 23.59 \times 15.14$ nm^3. Samples then undergo energy minimization at $T = 0$ K and then relaxation for 100 ps at $T = 300$ K with time discretization $\Delta t \simeq 1.0$ fs, in an isothermal–isobaric (NPT) ensemble at temperature T, pressure P and particle number N, with a Nose-Hoover thermostat and barostat with relaxation time scales of $\tau_d^{\text{therm}} = 10$ fs and $\tau_d^{\text{bar}} = 100$ fs, using an embedded-atom method-based potential, first proposed by Li *et al.* [27], who also showed that annealing of the samples (even at room temperature) leads to the formation of characteristic Ni-rich SRO patterning, which we will generally refer to as short-range order (SRO) samples in this Letter. The nanoindentation process was performed through an canonical ensemble NVE (with system of particle number N, volume V, energy E). Furthermore, nanoindentation was performed along z, using a tip at radii of 3.5, 5, and 7 nm. To set up boundary conditions along the depth (d_z), the samples are divided into three sections in the z direction: a frozen section for numerical cell stability ($0.02 \times d_z$), a thermostatic section to dissipate heat from nanoindentation ($0.08 \times d_z$) and a dynamical atoms section where the surface structure is modified by the indenter tip. A 5 nm vacuum section was also included as an open boundary at the top of the sample. The indenter tip is assumed to be a rigid sphere with force: $F(t) = K[\vec{r}(t) - R]^2$, where $K = 1000$ eV/Å^3 and R is the tip radius, moving along the z direction with a speed of $v = 20$ m/s, a value which is independent of the final result of our study. Also, the tip velocity is below the speed of sound in solids [50]. This allows us to capture the elastic Hertzian regime and model early dislocation nucleation [51–53]. The methods are elaborated further in Supplemental Material [54]. In addition, we randomly changed the position of the indenter tip center to ten different locations to account for statistical variability in our results, across three different samples (RSS, SRO, DWO) with all the samples considered with the same box size of $25.85 \times 23.59 \times 15.14$ nm^3. Additionally, to ensure that results are not affected by the underlying atomic structure,

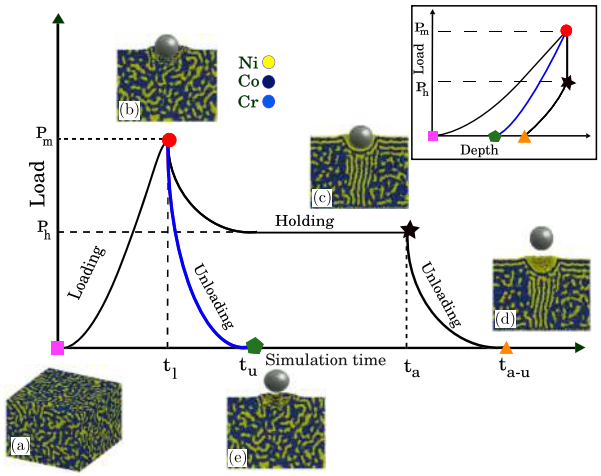

FIG. 1. Nanoindentation protocol for SRO reorganization in equiatomic NiCoCr alloys. The process starts when the aged NiCoCr sample (a) is indented up to a certain depth (b). Afterward, the indenter's velocity is set to zero, this is the moment when the hybrid MD-MC process starts again and leads to a configuration in which Ni and Co-Cr segregate or are no longer randomly distributed but are reorganized and form stripe patterns under the indenter tip (c). The resulting pattern retains its shape even after the indenter is removed from the sample (d). This pattern is not observed during normal loading-unloading nanoindentation simulation like the process shown by the blue line (e). The inset figure displays the corresponding processes in the load-depth coordinates, where symbol types define the loading path.

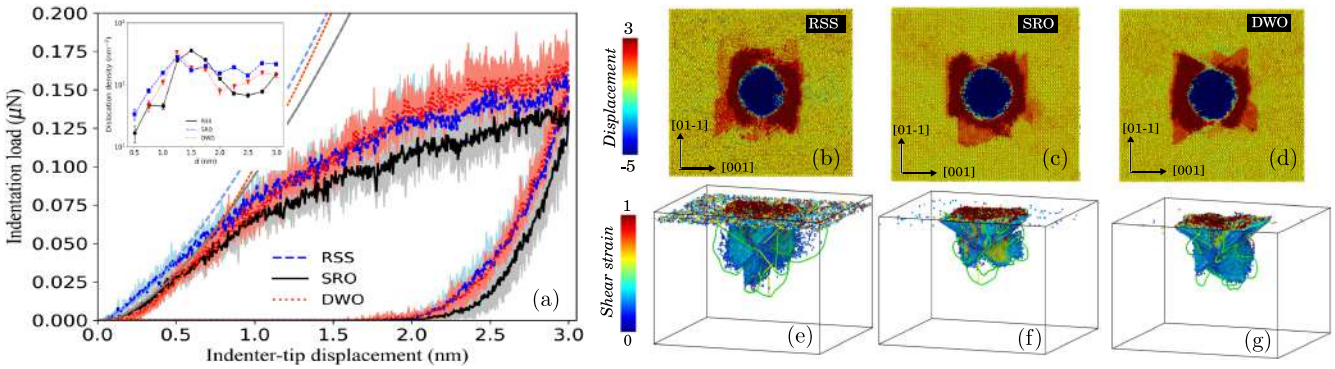

FIG. 2. Nanoindentation-induced reorganization of short-range ordering in metallic alloys. (a) Load-displacement (LD) curves, along with the Hertz fitting, for a random solid solution (RSS), an annealed sample, and a DWO sample created out of the dwell nanoindentation protocol with an indenter of radius 20 nm and in the elastic regime. The annealed and striped samples exhibit higher strength compared to the RSS. The inset shows the effect of sample preparation on dislocation density evolution during the loading process. (b)–(d) Pileup patterns for RSS, annealed (SRO), and striped (DWO) FCC samples preserving the characteristic fourfold symmetry rosette. (e)–(g) Stacking planes identified by a shear-strain mapping and dislocation network underneath the indenter tip, illustrating the smaller plastic region for the annealed and striped samples.

we studied five equiatomic samples for each crystal orientation, differing in their initial RSS atomic positions. As shown in Fig. 1, when the indenter reached the target depth (1, 2, or 3 nm), v was set to zero and then MC thermal relaxation ("holding") process was performed using the variance-constrained semigrand canonical (VCSGC) ensemble [27,61] at $T = 300$ K. The chemical potential differences $\Delta\mu_{\text{Ni-Cr}} = -0.31$ and $\Delta\mu_{\text{Ni-Co}} = 0.021$ and the variance constraint $\kappa = 1000$ are set as in Ref. [27]. The holding part (cf. Fig. 1) includes 1 MC cycle for every 20 MD steps within the VCSGC ensemble for a total number of 150000 MC cycles, ensuring that the thermalized configuration contains stable SRO patterning.

In the studied protocol (cf. Fig. 1), equiatomic NiCoCr, which has been shown to display Ni-rich SRO patterns [27], is indented to a specified indentation depth in the "loading" step. The CSRO changes only during the holding step, where the indenter is held fixed and thermomechanical MC-MD relaxation is performed at room temperature (cf. Fig. 1). Because of holding, a load drop is commonly observed from maximum P_m at time t_l to P_h at time t_a. The "unloading" step consists of removing the load altogether at a velocity of $v = -20$ nm/s, using MD, and then perform further MC-MD relaxation at the sample. We find that a characteristic DWO pattern emerges after unloading at $t_{\text{a-u}}$ (cf. Fig. 1), that would not appear without the holding stage. The whole protocol is also illustrated in the load-depth plot in the inset of Fig. 1.

The characterization of the resulting nanoindentation-driven DWO pattern observed in our simulations, is shown and compared to a RSS and a Ni-rich SRO sample in Fig. 2. The DWO and SRO rich samples happen to have a larger mechanical strength and hardness than a RSS, as their load-depth (P-d) curves illustrate in Fig. 2(a). This could be due to the already observed Ni-dominated solute segregation, that is pinning and obstructing dislocation motion [17,62]. This phenomenon may also be implied by a drastic dislocation density increase for DWO and SRO samples at smaller depths, compared to RSS ones, as shown in the inset of Fig. 2(a). Although the fourfold rosette pileup pattern is preserved for all the samples due to FCC crystal structure [Figs. 2(b)–2(d)], the RSS plastic zone is typically larger than those of the DWO and SRO samples, as shown in Figs. 2(e)–2(g), concluding that SRO and DWO have analogous dislocation pinning effects.

The character and origin of the emergent DWO onset was further investigated, by considering the effect of crystal orientation. We find that the behavior for crystals along $x = [100]$, $y = [010]$, and $z = [001]$ [cf. Fig. 3(b)] is drastically different from the original orientation behavior [cf. Fig. 3(a)] with the DWO orientation being tilted. However, further inspection shows that DWO forms along $z = [011]$ universally in the same direction relative to the crystal [cf. Fig. 3(b)]. The same protocol yields asymmetric outcomes in tension and compression tests, with reorganization evident in tension but not in compression (see Supplemental Material [54]). The DWO pattern also aligns with the maximum von Mises and principal stress, accumulated in the [011] planes [cf. Figs. 3(c) and 3(d)], a fact that implies material anisotropy. To further elucidate this issue, we estimate the pairwise potential energy for the Ni-Ni, Ni-Cr, and Ni-Co pairs in a RSS crystal oriented in $x = [100]$, $y = [01\bar{1}]$, and $z = [011]$, as shown in Fig. 3 [cf. 3(f)], is calculated for each atom [cf. Fig. 3(e)], considering only the first nearest neighbors defined by the first pick of the pair correlation function $g(r)$ (3 Å). With this input, we compare the total energy of a DWO ansatz (see Supplemental Material for details [54]) order that compares well with Fig. 3(a) and contains the interstripe distance as a free parameter. By comparing this

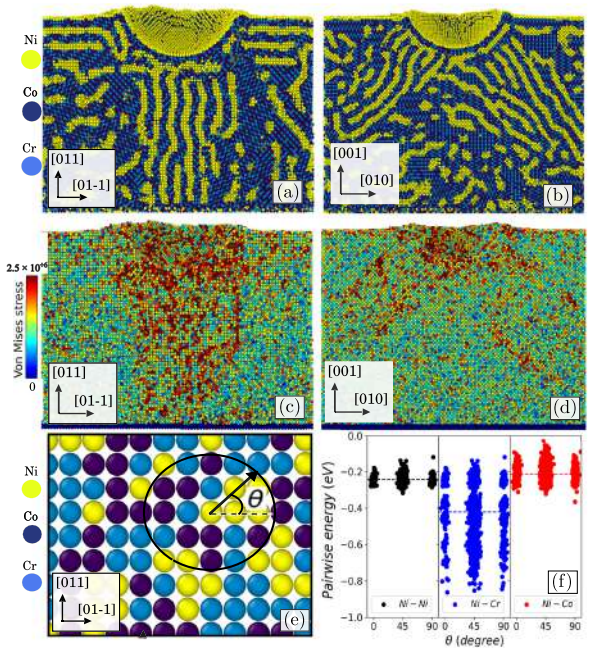

FIG. 3. Origin of nanoindentation-driven reorganization of short-range ordering. (a),(b) are the SRO patterns found along the $z[011]$ and $z[001]$ orientations, respectively. (c),(d) illustrate the correlation between the stripe patterns' orientation shown in (a),(b) and the von Mises stress. The pairwise energy between Ni-Ni, Ni-Cr, and Ni-Co atoms within each atom's neighbor list (e) is plotted in the same plane in (a) (but for separate Ni, Ni-Cr, and Ni-Co crystals) with respect to the in-plane angle of the pair atoms (f). As shown in (f), the Ni-Cr pairs have an average energy lower by 3 orders of magnitude compared to Ni-Ni and Ni-Co pairs.

DWO ansatz energy to the energy of RSS samples, we find that the optimal interstripe distance is very close to the one realized in MD simulations. In this way, we conclude that the DWO emergence is deeply linked to the energetic features of the interatomic potential, which is also the key cause of SRO emergence in equiatomic NiCoCr simulations. These peculiarities are also sufficient to closely resemble the nanometer-scale observations of SRO made possible by advanced experimental tools [9]. In order to verify our results, a comparison with an alternative interatomic potential, developed by Farkas *et al.* [59], is made. In that case, SRO is not observed, neither during aging [17], nor after the nanoindentation protocol implemented in the current work.

The emergent DWO displays strong size effects [63], which are dependent on the indentation depth and indenter tip radius as a function of temperature (cf. Fig. 4). In our displacement-controlled tests, we find that load-time (P-t) curves [cf. Figs. 4(a)–4(c)] display a larger load drop [63] during holding as depth or tip radius increases, leading to spatially extended DWO (cf. Fig. 4), resembling the plastic zone size. While not studied here, we also expect that size-dependent strain bursts should be observed in load-controlled tests. More specifically, the protocol discussed in Fig. 1 is implemented for two different indenter depths (1 and 3 nm) while the temperature (300 K) and the indenter tip radii (3.5 nm) are kept fixed [cf. Figs. 4(d) and 4(e)]. Furthermore, increasing the indenter radii from 2 to 7 nm gives rise to a larger plastic zone and as a result, a larger DWO pattern [cf. Figs. 4(h) and 4(i)]. This effect can also be observed from the larger load drop observed in the P-t curves for the larger radii [cf. Fig. 4(c)]. However, increasing the temperature (from 300 to 400 K), while the indenter depth and radii are the same, also results in a more organized DWO pattern shown in Fig. 4 [cf. 4(f) and 4(g)], but there is no pronounced size effect, as shown by the absence of a load-drop decrease [cf. Fig. 4(b)].

Given the elusive character of SRO formation in advanced alloys [31], the described dynamic nanoindentation protocol appears to be a plausible candidate for nanoscale manipulation and control of CSRO patterns in equiatomic NiCoCr and possibly, other multicomponent alloys. By the investigation of thermomechanical features

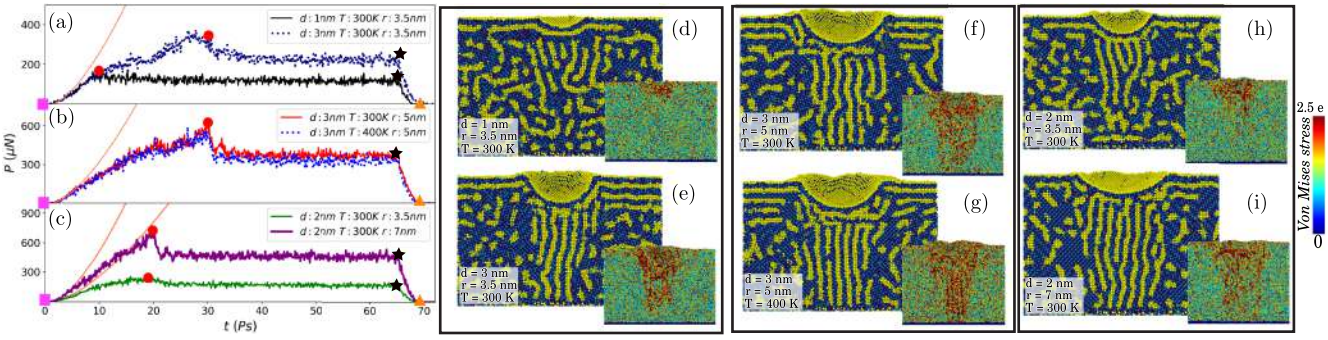

FIG. 4. Effect of size and temperature on nanoindentation-driven reorganization of short-range ordering. Load-redtime (P-t) curves for nanoindentation at different holding depths are shown in (a), where a larger holding depth results in more pronounced stripe patterns as depicted in (d),(e). The corresponding von Mises stress values, in units of gigapascals, are shown in inset snapshots of (d)–(i) and exhibit a similar correlation with the stripe patterns. Increasing the temperature by 100 K in (b) results in a more organized stripe pattern (f),(g) due to higher von Mises stress values (more red spots in the inset). The increase of indenter radius leads into a larger load drop (c) and affects the pattern size, as shown in (h),(i).

and size effects, we conclude that atomic scale Ni-rich segregation strongly influences the mechanical properties of equiatomic NiCoCr, in a way that can be quantified in dynamic nanoindentation. CSRO reorganization mechanisms in NiCoCr are shown to be energetic in character (as opposed to entropic) leading to highly complex and anisotropic patterns in space. Such morphological complexities may not be fully captured by the classical Guinier-Preston (GP) zone model describing early-stage kinetics of precipitation hardening as a transition from RSS states to clustered configurations. More recent approaches aim to incorporate local chemical complexities by considering the dominant role of enthalpic interactions over configurational entropic effects and their influence in short-range ordering [27]. In our study, the origin of DWO emergence is tracked back at the potential energy surface of a RSS crystal. Finally, the pronounced observed size effects of the emergent DWO suggest that, for experimentally relevant nanoindentation depths and tip radii, the emergent DWO shall be visible under common electron microscopy tools at the nanoscale.

As a concluding remark, the emergence of Ni-rich SROs under thermal annealing and their further enhancement due to the stress concentration could be a rather generic feature, not specific to particular chemical compositions and/or simulation details employed in this study. By utilizing a different interatomic potential in binary $Ni_{90}Al_{10}$, $Ni_{76}Al_{24}$, and $Ni_{60}Al_{40}$ alloys [57], we present evidence that the emerging stripelike patterns associated with Ni-based clusters may indeed constitute fairly universal mechanisms that could be understood from basic energetic arguments (see Supplemental Material [54] for further details). Nevertheless, it is necessary to explore the robustness of these findings across a broader range of chemically complex alloys by experimental means.

We would like to thank Mikko Alava, Pawel Sobkowicz, and Lukasz Kurpaska for fruitful discussions on features of short-range order. We acknowledge support from the European Union Horizon 2020 research and innovation program under Grant Agreement No. 857470 and from the European Regional Development Fund via the Foundation for Polish Science International Research Agenda PLUS program Grant No. MAB PLUS/2018/8.

*stefanos.papanikolaou@ncbj.gov.pl

[1] B. Cantor, I. Chang, P. Knight, and A. Vincent, Mater. Sci. Eng. **375–377**, 213 (2004).
[2] J.-W. Yeh, S.-K. Chen, S.-J. Lin, J.-Y. Gan, T.-S. Chin, T.-T. Shun, C.-H. Tsau, and S.-Y. Chang, Adv. Eng. Mater. **6**, 299 (2004).
[3] D. B. Miracle, J. D. Miller, O. N. Senkov, C. Woodward, M. D. Uchic, and J. Tiley, Entropy **16**, 494 (2014).
[4] Z. Li, S. Zhao, R. O. Ritchie, and M. A. Meyers, Prog. Mater. Sci. **102**, 296 (2019).
[5] Y. Shang, J. Brechtl, C. Psitidda, and P. K. Liaw, arXiv: 2102.09055.
[6] B. Gludovatz, A. Hohenwarter, K. V. S. Thurston, H. Bei, Z. Wu, E. P. George, and R. O. Ritchie, Nat. Commun. **7**, 10602 (2016).
[7] Y. Wu, F. Zhang, X. Yuan, H. Huang, X. Wen, Y. Wang, M. Zhang, H. Wu, X. Liu, H. Wang *et al.*, J. Mater. Sci. Technol. **62**, 214 (2021).
[8] L. Zhou, Q. Wang, J. Wang, X. Chen, P. Jiang, H. Zhou, F. Yuan, X. Wu, Z. Cheng, and E. Ma, Acta Mater. **224**, 117490 (2022).
[9] X. Chen, Q. Wang, Z. Cheng, M. Zhu, H. Zhou, P. Jiang, L. Zhou, Q. Xue, F. Yuan, J. Zhu *et al.*, Nature (London) **592**, 712 (2021).
[10] F. Walsh, M. Asta, and R. O. Ritchie, Proc. Natl. Acad. Sci. U.S.A. **118**, e2020540118 (2021).
[11] F. X. Zhang, S. Zhao, K. Jin, H. Xue, G. Velisa, H. Bei, R. Huang, J. Y. P. Ko, D. C. Pagan, J. C. Neuefeind, W. J. Weber, and Y. Zhang, Phys. Rev. Lett. **118**, 205501 (2017).
[12] Y. Ma, G. Peng, D. Wen, and T. Zhang, Mater. Sci. Eng. **621**, 111 (2015).
[13] C. Guo, Y. Fang, F. Chen, and T. Feng, Intermetallics **110**, 106480 (2019).
[14] R. Zhang, S. Zhao, J. Ding, Y. Chong, T. Jia, C. Ophus, M. Asta, R. O. Ritchie, and A. M. Minor, Nature (London) **581**, 283 (2020).
[15] W. He, Q. Zeng, C. Yan, J. Zhu, D. Zhang, and J. Cao, J. Mater. Sci. Technol. **101**, 173 (2022).
[16] Y. Lai, J. Yu, L. Sun, F. Wang, Q. Zheng, and H. He, J. Non-Cryst. Solids **597**, 121906 (2022).
[17] A. H. Naghdi, K. Karimi, A. E. Poisvert, A. Esfandiarpour, R. Alvarez, P. Sobkowicz, M. Alava, and S. Papanikolaou, Phys. Rev. B **107**, 094109 (2023).
[18] B. Yin, S. Yoshida, N. Tsuji, and W. A. Curtin, Nat. Commun. **11**, 2507 (2020).
[19] Q. Ding, Y. Zhang, X. Chen, X. Fu, D. Chen, S. Chen, L. Gu, F. Wei, H. Bei, Y. Gao, M. Wen, J. Li, Z. Zhang, T. Zhu, R. O. Ritchie, and Q. Yu, Nature (London) **574**, 223 (2019).
[20] M. Widom, W. P. Huhn, S. Maiti, and W. Steurer, Metall. Mater. Trans. A **45**, 196 (2014).
[21] A. Tamm, A. Aabloo, M. Klintenberg, M. Stocks, and A. Caro, Acta Mater. **99**, 307 (2015).
[22] L. J. Santodonato, Y. Zhang, M. Feygenson, C. M. Parish, M. C. Gao, R. J. Weber, J. C. Neuefeind, Z. Tang, and P. K. Liaw, Nat. Commun. **6**, 5964 (2015).
[23] P. Singh, A. V. Smirnov, and D. D. Johnson, Phys. Rev. B **91**, 224204 (2015).
[24] L. Koch, F. Granberg, T. Brink, D. Utt, K. Albe, F. Djurabekova, and K. Nordlund, J. Appl. Phys. **122**, 105106 (2017).
[25] A. Fernández-Caballero, J. S. Wróbel, P. M. Mummery, and D. Nguyen-Manh, J. Phase Equilib. Diffus. **38**, 391 (2017).
[26] Y. Ma, Q. Wang, C. Li, L. J. Santodonato, M. Feygenson, C. Dong, and P. K. Liaw, Scr. Mater. **144**, 64 (2018).
[27] Q.-J. Li, H. Sheng, and E. Ma, Nat. Commun. **10**, 3563 (2019).
[28] H. S. Oh, S. J. Kim, K. Odbadrakh, W. H. Ryu, K. N. Yoon, S. Mu, F. Körmann, Y. Ikeda, C. C. Tasan, D. Raabe, T. Egami, and E. S. Park, Nat. Commun. **10**, 2090 (2019).

[29] W.-R. Jian, Z. Xie, S. Xu, Y. Su, X. Yao, and I. J. Beyerlein, Acta Mater. **199**, 352 (2020).
[30] J. B. Seol, W.-S. Ko, S. S. Sohn, M. Y. Na, H. J. Chang, Y.-U. Heo, J. G. Kim, H. Sung, Z. Li, E. Pereloma *et al.*, Nat. Commun. **13**, 6766 (2022).
[31] E. George, W. Curtin, and C. Tasan, Acta Mater. **188**, 435 (2020).
[32] J. Ding, Q. Yu, M. Asta, and R. O. Ritchie, Proc. Natl. Acad. Sci. U.S.A. **115**, 8919 (2018).
[33] M. Lenz, Y. M. Eggeler, J. G. Müller, C. H. Zenk, N. Volz, P. Wollgramm, G. Eggeler, S. Neumeier, M. Göken, and E. Spiecker, Acta Mater. **166**, 597 (2019).
[34] A. Bezold, N. Volz, F. Xue, C. H. Zenk, S. Neumeier, and M. Göken, Metall. Mater. Trans. A **51**, 1567 (2020).
[35] F. Xue, C. Zenk, L. Freund, M. Hoelzel, S. Neumeier, and M. Göken, Scr. Mater. **142**, 129 (2018).
[36] C. H. Zenk, N. Volz, C. Zenk, P. J. Felfer, and S. Neumeier, Crystals **10**, 1058 (2020).
[37] R. K. Rhein, P. G. Callahan, S. P. Murray, J.-C. Stinville, M. S. Titus, A. Van der Ven, and T. M. Pollock, Metall. Mater. Trans. A **49**, 4090 (2018).
[38] L. Feng, D. Lv, R. Rhein, J. Goiri, M. Titus, A. Van der Ven, T. Pollock, and Y. Wang, Acta Mater. **161**, 99 (2018).
[39] J. May, H. Höppel, and M. Göken, Scr. Mater. **53**, 189 (2005).
[40] N. Chinh, P. Szommer, Z. Horita, and T. Langdon, Adv. Mater. **18**, 34 (2006).
[41] Y. Li, J. Mueller, H. Höppel, M. Göken, and W. Blum, Acta Mater. **55**, 5708 (2007).
[42] Q. Wei, S. Cheng, K. Ramesh, and E. Ma, Mater. Sci. Eng. **381**, 71 (2004).
[43] H. Höppel, J. May, and M. Göken, Adv. Eng. Mater. **6**, 781 (2004).
[44] V. Maier, B. Merle, M. Göken, and K. Durst, J. Mater. Res. **28**, 1177 (2013).
[45] W. H. Poisl, W. C. Oliver, and B. D. Fabes, J. Mater. Res. **10**, 2024 (1995).
[46] B. N. Lucas and W. C. Oliver, Metall. Mater. Trans. A **30**, 601 (1999).
[47] D. S. Stone, J. E. Joseph, J. Puthoff, and A. A. Elmustafa, J. Mater. Res. **25**, 611 (2010).
[48] I.-C. Choi, B.-G. Yoo, Y.-J. Kim, and J.-i. Jang, J. Mater. Res. **27**, 3 (2012).
[49] A. P. Thompson, H. M. Aktulga, R. Berger, D. S. Bolintineanu, W. M. Brown, P. S. Crozier, P. J. in 't Veld, A. Kohlmeyer, S. G. Moore, T. D. Nguyen, R. Shan, M. J. Stevens, J. Tranchida, C. Trott, and S. J. Plimpton, Comput. Phys. Commun. **271**, 108171 (2022).
[50] J. Varillas, J. Očenášek, J. Torner, and J. Alcalá, Acta Mater. **217**, 117122 (2021).
[51] F. Domínguez-Gutiérrez, S. Papanikolaou, A. Esfandiarpour, P. Sobkowicz, and M. Alava, Mater. Sci. Eng. **826**, 141912 (2021).
[52] L. Kurpaska, F. Dominguez-Gutierrez, Y. Zhang, K. Mulewska, H. Bei, W. Weber, A. Kosinka, W. Chrominski, I. Jozwik, R. Alvarez-Donado, S. Papanikolaou, J. Jagielski, and M. Alava, Mater. Des. **217**, 110639 (2022).
[53] F. J. Domínguez-Gutiérrez, P. Grigorev, A. Naghdi, J. Byggmästar, G. Y. Wei, T. D. Swinburne, S. Papanikolaou, and M. J. Alava, Phys. Rev. Mater. **7**, 043603 (2023).
[54] See Supplemental Material at http://link.aps.org/supplemental/10.1103/PhysRevLett.132.116101 for more details on the methods, deeper analysis of the results, and more simulation examples, including Refs. [17,30,50–52,55–60].
[55] A. Stukowski, Model. Simul. Mater. Sci. Eng. **18**, 015012 (2010).
[56] S. Picak, J. Liu, C. Hayrettin, W. Nasim, D. Canadinc, K. Xie, Y. Chumlyakov, I. Kireeva, and I. Karaman, Acta Mater. **181**, 555 (2019).
[57] A. Abu-Odeh and M. Asta, Acta Mater. **226**, 117615 (2022).
[58] C. Wolverton, V. Ozolins, and A. Zunger, J. Phys. Condens. Matter **12**, 2749 (2000).
[59] D. Farkas and A. Caro, J. Mater. Res. **33**, 3218 (2018).
[60] W. Huang and Y. Chang, Intermetallics **6**, 487 (1998).
[61] B. Sadigh, P. Erhart, A. Stukowski, A. Caro, E. Martinez, and L. Zepeda-Ruiz, Phys. Rev. B **85**, 184203 (2012).
[62] A. Esfandiarpour, S. Papanikolaou, and M. Alava, Phys. Rev. Res. **4**, L022043 (2022).
[63] S. Papanikolaou, Y. Cui, and N. Ghoniem, Model. Simul. Mater. Sci. Eng. **26**, 013001 (2017).

Supplementary material

Dynamic nanoindentation and short-range order in equiatomic NiCoCr medium entropy alloy lead to novel density wave ordering

A. Naghdi,[1,2] F. J. Domínguez-Gutiérrez,[1] W. Y. Huo,[1,3] K. Karimi,[1] and S. Papanikolaou[1,*]

[1] *NOMATEN Centre of Excellence, National Center for Nuclear Research, ul. A. Sołtana 7, 05-400 Swierk/Otwock, Poland*

[2] *IDEAS NCBR, ul. Chmielna 69, 00-801 Warsaw, Poland*

[3] *College of Mechanical and Electrical Engineering, Nanjing Forestry University, Nanjing, 210037, China*

COMPUTATIONAL METHODS

We first defined the initial pure fcc Ni sample with a lattice constant of 0.35295 nm followed by randomly replacing Ni atoms by Co and Cr atoms at [100] and [110] crystal orientations with a dimensions $25.85 \times 23.59 \times 15.14$ nm^3. The samples then follow a process of energy optimization to find the lowest energy structure. After that, we conducted an equilibration process for 100 ps using a Nose-Hoover thermostat at 300 K with a time constant of 100 fs [1, 2]. This process continued until the system reached a homogeneous temperature and pressure profile.

The indenter tip is considered as a non-atomic repulsive imaginary (RI) rigid sphere with a force potential defined as: $F(t) = K\left(\vec{r}(t) - R\right)^2$, where $K = 1000$ eV/Å^3 (160 GPa) is the force constant, and $\vec{r}(t)$ is the position of the center of the tip as a function of time, with radii $R = 3.5, 5$, and 7 nm which defines a hard sphere indenter. We apply MD simulations using an NVE statistical thermodynamic ensemble and the velocity Verlet algorithm to emulate an experimental nanoindentation test. Periodic boundary conditions are set on the x and y axes to simulate an infinite surface, while the z orientation contains a fixed bottom boundary and a free top boundary in all MD simulations [1]. Here, $\vec{r}(t) = x_0\hat{x} + y_0\hat{y} + (z_0 \pm vt)\hat{z}$, with x_0 and y_0 as the center of the surface sample on the xy plane. The initial gap between the surface and the indenter tip, $z_0 = 0.5$ nm, moves with a speed of $v = 20$ m/s and is chosen as positive for loading, as negative for unloading processes, and set to zero for holding process.

The center of the indenter tip was randomly changed to 10 different positions to consider statistics in our results, resulting in a total of 30 MD simulations; across three different samples (RSS,

SRO, DWO), while the box size for all the samples remained unchanged. Each process is performed for 125 ps with a time step of $\Delta t = 1$ fs. The maximum indentation depth is chosen to be 3.0 nm to avoid the influence of boundary layers in the dynamical atoms region. The load-displacement curve is then obtained by plotting the force on the indenter tip as a function of its displacement relative to the surface, as the indenter tip is driven into the material over time.

We calculate the average load, $P_{\text{ave}} = 1/N \sum_i^N P_i$, where P_i represents the load obtained from each MD simulation with randomly varied positions for the center of the indenter tip on the NiCoCr surface. Additionally, we include the maximum and minimum loads as a function of indentation displacement from all MD simulations, shown as a colored region to display the statistical analysis in our study. We use a Hertz fitting curve based on the sphere–flat surface contact to characterize the elastic nanocontact during the loading process. The Hertz fitting curve is expressed as:

$$P_{\text{H}} = \frac{4}{3} E_{\text{eff}} R^{1/2} h^{3/2}, \tag{1}$$

where R is the indenter radius, h is the indenter displacement, and E_{eff} is the effective elastic modulus.

We use OVITO [3] with the DXA package to identify compute the total dislocation length, l, of each crystal orientation and their corresponding dislocation density, ρ, defined as

$$\rho = \frac{l}{V_D}, \tag{2}$$

by using a hemispherical radius of the plastic zone of $r_{\text{pz}} = a_{\text{pz}} \left[r^2 - (r-h)^2\right]^{1/2}$ with $a_{\text{pz}} = 1.9$ and the total volume equals to the hemispherical volume excluding the volume displaced by the indenter tip as $V_D = \left(2\pi r_{\text{pz}}^3/3\right) - \left(\pi h^2 (r-h)/3\right)$, with r as the indenter radius and h the indentation depth. Excluding pile up or sink in effects in this model. Our observations show that the RSS, SRO, and DWO have an effect on the initiation of dislocation nucleation.

DISCUSSION

Uniaxial compression and tension

To simulate the compression and tension (tensile) test, the MD model was set up with loading applied along the [001] and [011] axes of samples with dimensions $14.28 \times 14.28 \times 24.98$ nm^3 and with crystal orientations of $x = [100]$, $y = [010]$ and $z = [001]$ or $x = [100]$, $y = [01\bar{1}]$ and $z = [011]$. The initial structures of the NiCoCr were equilibrated first with MD and then with hybrid MC/MD at room temperature for 100 ps, in an NPT ensemble with a Nose–Hoover thermostat and barostat with

relaxation time scales of $\tau_d^{\text{therm}} = 10$ fs and $\tau_d^{\text{bar}} = 100$ fs, leading into stable SRO configurations of the samples. Next, a constant engineering strain rate of 0.001 was applied along the wire direction in a canonical NVT ensemble to study the nanomechanical response of the material under zero load and uniform stress, with a displacement of 5%L (where L is the length of the sample). Afterwards, the MD/MC relaxation was redone in a NVT ensemble, ensuring the presence of uniform tensile and compression stress during the relaxation, depicted in Fig. S1.

Figure S1 shows the simulation results for NiCoCr alloys with (001) and (011) crystal orientations subjected to compression (a-b) and tension (c-d). Our findings indicated that compression simulations did not exhibit an ordering effect, while tensile simulations showed ordering, which followed the close-packed planes. During a tensile test, as the stress increases, dislocations begin to move and interact with each other, leading to plastic deformation. This motion of dislocations can result in the formation of strain hardening, where the material becomes harder and stronger as

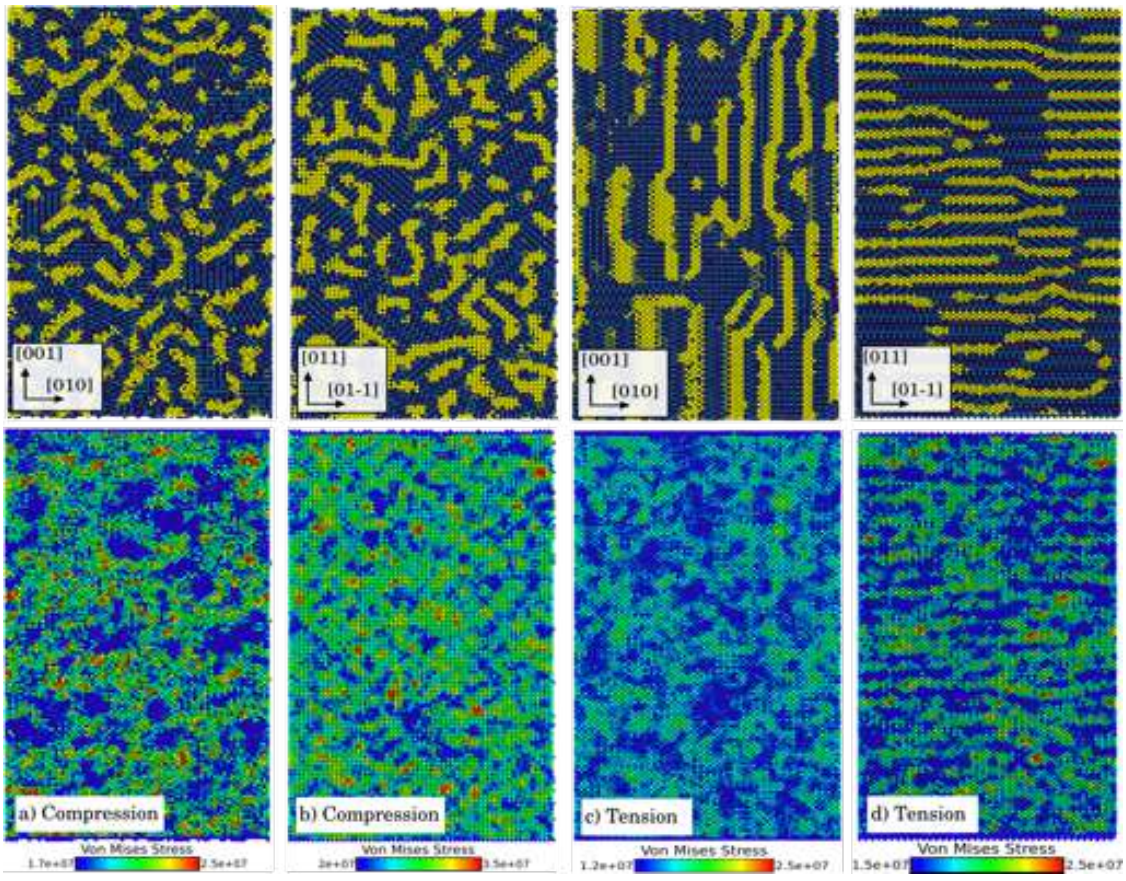

FIG. S1. Compression and tension induced ordering and von Mises stress mapping for NiCoCr sample at (001) in a-b) and (011) in c-d) crystal orientations, respectively. Noticing that the reorganization of Short-Range Ordering in metallic alloys is observed by tension test primarily.

it is deformed, as observed experimentally [4, 5]. The ordering effect observed in our simulations is linked to the close-packed planes, which have the highest number of atoms per area and are in close-packed directions. These results are consistent with our nanoindentation simulations, which involve both compression and tension during the loading process.

In addition, we carried out a calculation of the short-range ordering in SRO, RSS, and compression that is prepared by our novel protocol with MC+MD simulation for compression simulations. The Warren-Cowley SRO parameter is a widely used parameter to describe short-range order in alloys. It quantifies the degree of order in a binary alloy by measuring the probability of finding two atoms of the same type at a certain distance. Results for the Warren-Cowley SRO parameters (see the relevant definition below) are presented in Fig. S2, S3, and S4 [6].

Robustness analysis: interatomic potential function

As a robustness analysis, we further probed the simulated $Ni_{90}Al_{10}$ metal alloy based on the interatomic potential function employed by Abuodeh et al. [7] and sought for variations in the spatial re-organization of SROs due to nano-indentation, as depicted in Fig S5. Here, In this framework, we probed the Warren–Cowley SRO parameters $P_{ab}(r)$ [8] measuring the concentration

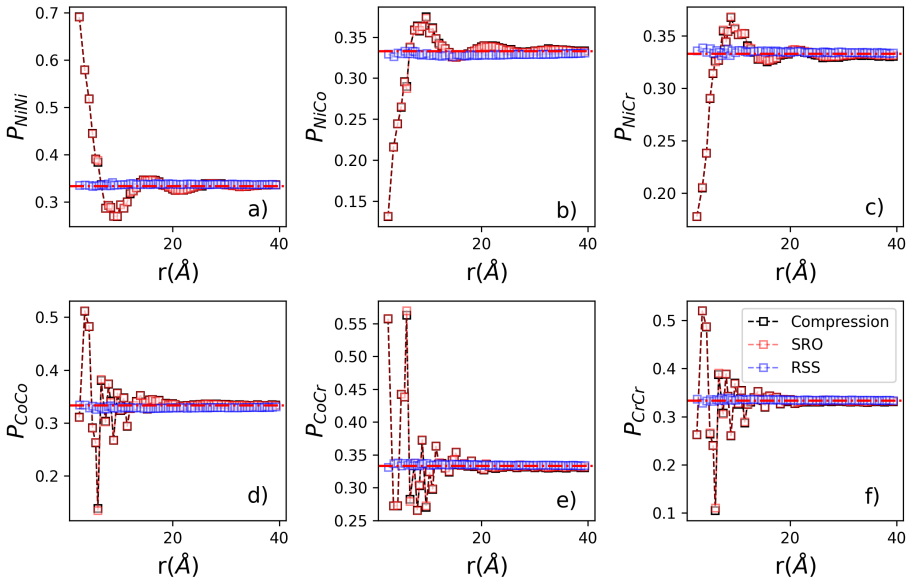

FIG. S2. Short-range ordering in SRO, RSS and samples preprared with our protocol under uniaxial compression. Warren–Cowley SRO parameters including (a) p_{NiNi}, (b) p_{NiCo}, (c) p_{NiCr}, (d) p_{CoCo}, (e) p_{CoCr}, and (f) p_{CrCr} plotted against distance r at Ta = 300 K.

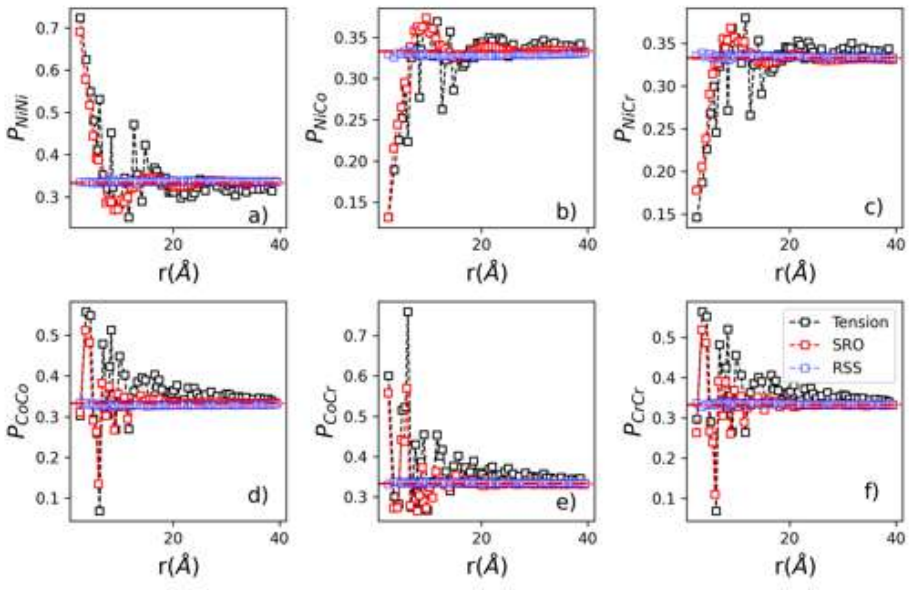

FIG. S3. Short-range ordering in SRO, RSS and samples preprared with our protocol under uniaxial tension. Warren–Cowley SRO parameters including (a) p_{NiNi}, (b) p_{NiCo}, (c) p_{NiCr}, (d) p_{CoCo}, (e) p_{CoCr}, and (f) p_{CrCr} plotted against distance r at Ta = 300 K.

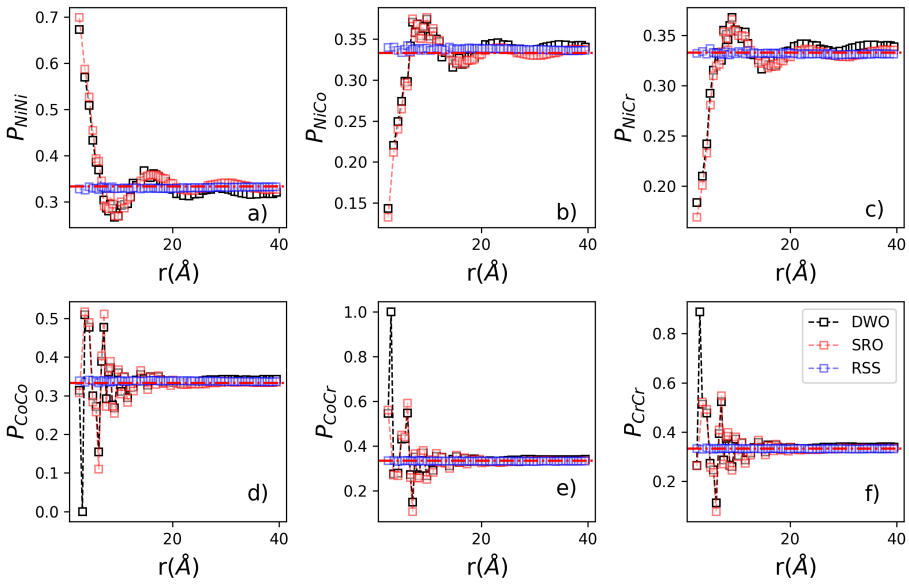

FIG. S4. Short-range ordering in SRO, RSS and DWO samples. Warren–Cowley SRO parameters including (a) p_{NiNi}, (b) p_{NiCo}, (c) p_{NiCr}, (d) p_{CoCo}, (e) p_{CoCr}, and (f) p_{CrCr} plotted against distance r at Ta = 300 K.

variations of type-b atoms at a distance r from a center type-a element. In the random solid solution limit, one obtains $P_{ab}^{\mathrm{RSS}} = \rho_b$ statistically at any r. Here ρ_b denotes the molar concentration of

type-b element.

Figure S5(a-d) illustrates P_{ab} as a function of distance r associated with the random solid solution (RSS), annealed sample (SRO), and pre-indented annealed alloy (DWO) including the NiNi, NiAl, AlNi, and AlAl elemental pairs at $T_a = 300$ K. In Fig. S5(a), the abundance of the Ni-Ni pairs in DWO beyond random concentrations is fairly pronounced and appears to persist up to $r \simeq 8$ Å. This is contrasted by a rather rapid decay of P_{NiNi} associated with SRO, reaching the noise floor above $r \simeq 4$ Å. We remark that the former exceeds the latter by at least 1% at almost every distance r. This observation is in very close agreement with our finding relevant to the indented NiCoCr that the stress concentration tends to enhance SRO features associated with NiNi bonding. As for the Al-Al pairs shown in Fig. S5(d), we observe an opposite trend implying that pre-indentation appears to slightly suppress AL ordering features in comparison with SRO. We further note that, by construction, $P_{\mathrm{NiAl}} = 1 - P_{\mathrm{NiNi}}$ and $P_{\mathrm{AlNi}} = 1 - P_{\mathrm{AlAl}}$ as in Fig. S5(b-c).

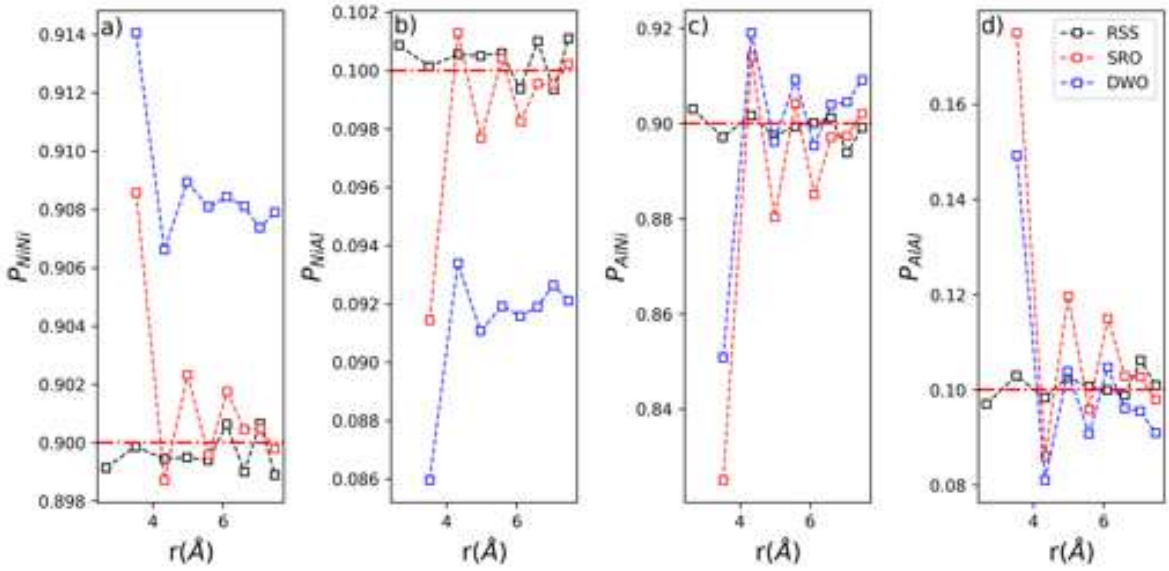

FIG. S5. Short-range ordering in SRO, RSS and DWO samples corresponding to $Ni_{90}Al_{10}$. Warren–Cowley SRO parameters including (a) P_{NiNi}, (b) P_{NiAl}, (c) P_{AlNi}, (d) P_{AlAl} plotted against distance r at $T_a = 300$ K.

Figure S6 compares the results obtained using the Farkas et al. [9] potential with those obtained by Li et al. [5]. The results clearly demonstrate the significance of short-range order (SRO) information in our nanoindentation protocol. In multi-principal element alloys, the behavior of dislocations is influenced by variable lattice constant offsets (LCOs), resulting in unique slip paths and nanoscale segment detrapping (NSD) processes that govern the alloy's strength. Through careful selection of processing parameters, such as the homogenization annealing temperature, we can optimize the

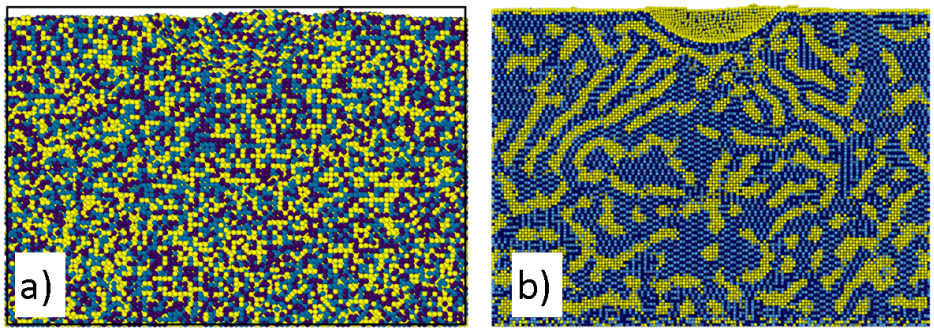

FIG. S6. Cross-section of indented (001) NiCoCr indented obtained by performing MD simulations based on the potential developed by Farkas et al. in a), stripes formation is not observed due to the lack of SRO information. We compare results to those obtained by using the Li-Sheng-Ma potential in b).

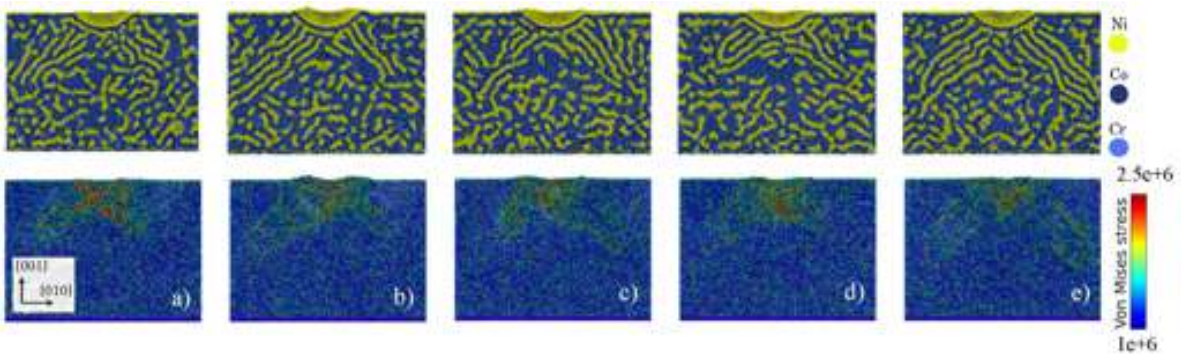

FIG. S7. Origin of nanoindentation–driven reorganization of Short-Range Ordering by considering different sample configurations. Figs (a-e)–upper panel depict the SRO patterns found along the $[001]_z$ orientations. Bottom panels illustrate the correlation between the stripe patterns' orientation and the von Mises stress.

material's properties. The Li et al. EAM potentials exhibit excellent features and capabilities, allowing us to effectively model the segregation and ordering induced by nanoindentation tests.

Stripes analysis

In our study, we investigated the effect of crystal orientation on the ordering of NiCoCr alloys using different configurations, as shown in Fig. S7 and S8. Our nanoindentation protocol resulted in the consistent observation of ordering in the NiCoCr samples. This ordering phenomenon can have significant implications for the material's mechanical properties, such as strength and ductility, as it can affect the formation and behavior of defects such as dislocations and voids.

We consider an approximate "mean-field" argument for explaining the separation distance between stripes in DWO samples (where the NiNi and CoCr stripes exist), by comparing an estimate

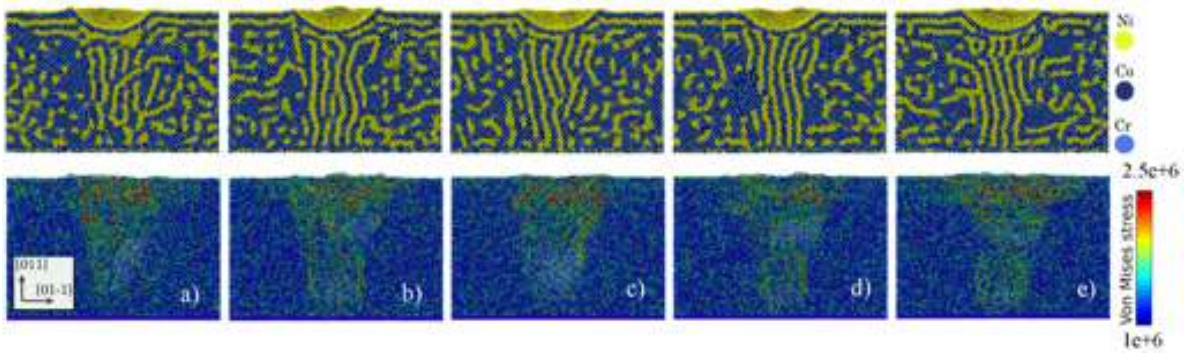

FIG. S8. Origin of nanoindentation–driven reorganization of Short-Range Ordering. Figs (a-e)–upper panel depict the SRO patterns found along the $[011]_z$ orientations. Bottom panels illustrate the correlation between the stripe patterns' orientation and the von Mises stress.

of the energy of a RSS sample of the same composition (Fig. S9) with a particular ansatz of two-dimensional stripes, of specific thickness, and separation distance equal to the stripe width (for simplicity purposes, given the simulation observations). These structures emerge in post-indent samples in MD simulations as reported in the main text of the manuscript, after room-temperature aging effects. By comparing the energy levels of the DWO ansatz with the RSS samples, we provide a theoretical estimate of the stripe's width value.

Configurations are shown in Fig. S9 and consist of 4412 atoms in which the Ni share is 43 percent while the Co and Cr share 28 and 29 percent, respectively.

A RSS sample's total energy, considering only the first nearest neighbours (a cutoff radius of 3 Åfrom any center atom, provided by the first peak of the pair correlation function $g(r)$), is equal to the sum of all pairwise energies, $\sum_{ij} E_{ij}$:

$$\begin{aligned} E_{RSS} = &\sum_{A_iB_j} E^{RSS}_{A_iB_j} + \sum_{A_iC_j} E^{RSS}_{A_iC_j} + \sum_{B_iC_j} E^{RSS}_{B_iC_j} \\ &+ \sum_{A_iA_j} E^{RSS}_{A_iA_j} + \sum_{B_iB_j} E^{RSS}_{B_iB_j} + \sum_{C_iC_j} E^{RSS}_{C_iC_j} \end{aligned} \tag{3}$$

Where A, B and C refer to Ni, Co and Cr elements, respectively. Formulation of the total energy of a DWO sample on the basis of stripe width 'd', configuration dimensions 'Λ' (width of box) and 'L' (height), considering a 2-dimensional system, and pairwise energies of NiNi and CoCr stripes results in:

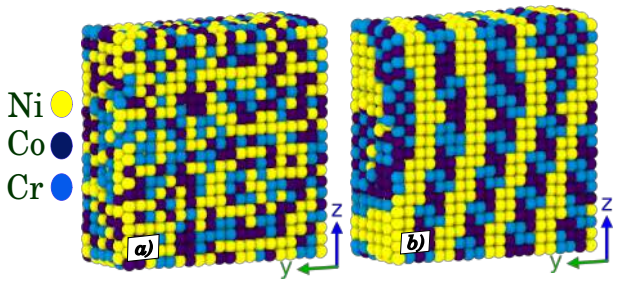

FIG. S9. DWO and RSS configurations considered for stripe width calculation. **a)** is a RSS configuration and **b)** is a DWO configuration with 4 NiNi stripe ribbons and other 4 CoCr stripes. Both configurations have the same elemental composition.

$$\begin{aligned} E_{DWO}[d] &= N_s \times d \times L \times \sum_{A_iA_j} E^{DWO}_{A_iA_j} \\ +N_s \times L \times &\frac{\sum_{A_iC_j} E^{DWO}_{A_iC_j} + \sum_{A_iB_j} E^{DWO}_{A_iB_j}}{2} \\ &+(\Lambda - d \times N_s) \times d \times L \times \sum_{B_iC_j} E^{DWO}_{B_iC_j} \end{aligned} \tag{4}$$

Table I is the extracted values of Eq. 3 and Eq. 4 from the configurations illustrated in Fig. S9. N_s refers to the number of NiNi and CoCr stripes here, which is 8 based on Fig. S9.(b) . Solving for $E_{RSS} = E_{DWO}[d]$ and inserting values reported in Table.I, generates a quadratic formula of the form $P \times d^2 + Q \times d + W = 0$:

$$1617759.26 \times d^2 - 10729446.41 \times d - 1406209.84 = 0 \tag{5}$$

solving for 'd' results in d = (6.761, −0.13). Since a negative stripe width is not allowed d = 6.761 Å, which is almost as wide as the two Ni atoms next to each other with an atomic radius of 1.63 Å.

TABLE I. Parameter Values

Parameter	E_{RSS}	N_s	L	Λ	$\sum E^{DWO}_{AA}$	$\sum E^{DWO}_{AB}$	$\sum E^{DWO}_{AC}$	$\sum E^{DWO}_{BC}$
Value	-1154.50 eV	8	47.66 Å	49.27 Å	-2009.22 eV	-2916.65 eV	-4461.02 eV	-4240.30 eV

Indenter tip velocity analysis

To investigate the impact of indenter tip velocity during the initial step of our protocol, we decreased the indenter velocity to 5 m/s, and compared with the results for a tip velocity of 20

m/s. Subsequently, we repeated the protocol using an equiatomic NiCoCr sample, with an indenter tip diameter of 5 nm and an indentation depth of 3 nm. Fig. S10 shows that very similar DWO patterns, with virtually identical correlation characteristics, emerge independent of the indenter tip velocity. The similar DWO patterns are expected, as the key aspect of the process is the "holding" step, where the strain rate is zero, a stage of the protocol that leads to the reorganization effects.

In addition, The speed is substantially lower than the speed of sound in solids [10]. This allows us to precisely capture the elastic Hertzian regime, allowing us insights that mimics real–world experiments [2].

Dwell Nanoindentation Analysis of NiAl40 Solid Solution

To further assess the applicability of the protocol introduced in this study, we examined NiAl40 as an additional case. According to the NiAl phase diagram [11], NiAl40 is identified as a solid solution. For this analysis, we explored two crystal orientations mirroring those selected for NiCoCr (($[001]_z$ and $[011]_z$)). Subsequently, the dwell nanoindentation protocol was employed on the samples.

As depicted in Fig. S11, the Short Range Order (SRO) patterns, comprising substantial Ni and Al clusters, undergo reorganization into smaller clusters beneath the indenter tip. Notably, the Von-Mises stress beneath the indenter tip reaches a significant magnitude. It is important to highlight the restructuring of the SRO patterns in response to the nanoindentation, indicating the protocol's effectiveness across different material compositions. Additionally, the substantial Von-Mises stress underscores the mechanical impact induced during the indentation process.

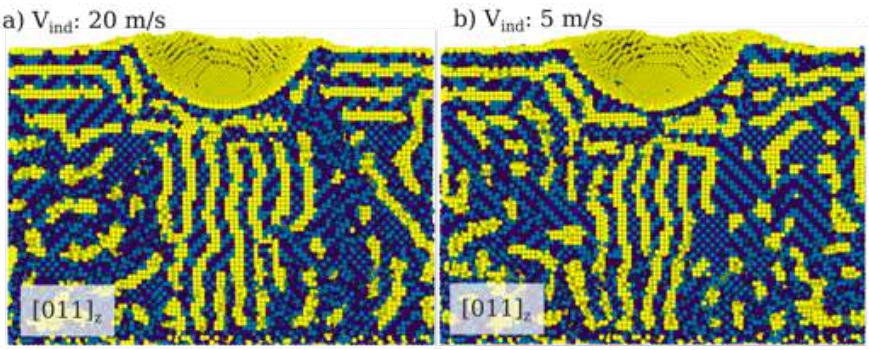

FIG. S10. Effect of indenter speed. Fig (a) is the studied protocol for equatomic NiCoCr with an indenter tip velocity of 20 m/s and Fig (b) 5 m/s. As shown, the final DWO pattern emerges independent of the indenter tip speed.

Dwell Nanoindentation Analysis of NiAl24 Solid Solution

As a final example, we focused on NiAl24 to investigate the reorganization effects facilitated by our dwell nanoindentation protocol. NiAl24, identified as a solid solution according to its phase diagram [11], underwent a hybrid MC-MD relaxation process when positioned along $[001]_z$ and $[011]_z$ orientations. Subsequently, we applied the nanoindentation protocol.

As depicted in Fig. S12, the NiAl L12 clusters beneath the indenter tip underwent a distinct transformation, evolving into small Al-dominated stripes within regions rich in Ni. It is noteworthy to highlight that the Von-Mises stress beneath the indenter tip reached its maximum, corresponding to the reorganized regions. This emphasizes the connection between the induced structural changes and the mechanical stress experienced during the nanoindentation process.

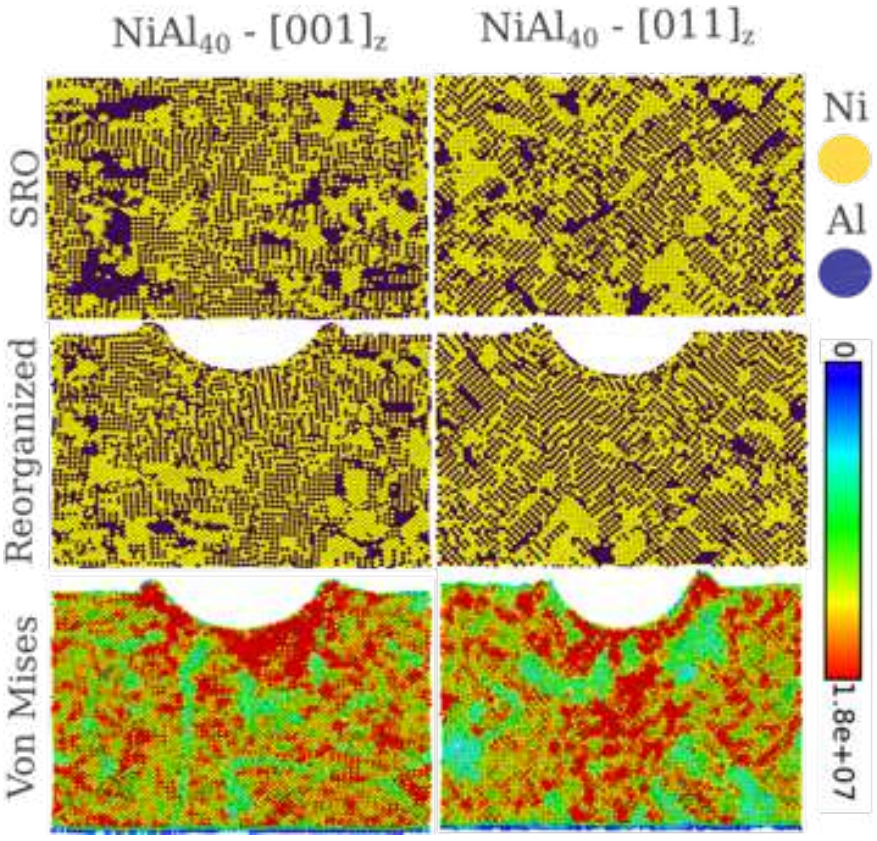

FIG. S11. Nanoindentation-induced reorganization of Short-Range Ordering in NiAl40 alloys. The nanoindentation protocol triggers the reorganization of SRO patterns (top row) in both [001] and [011] crystal orientations (middle row). The corresponding Von Mises stress, higher in the reorganized regions of the sample, is illustrated in the bottom row.

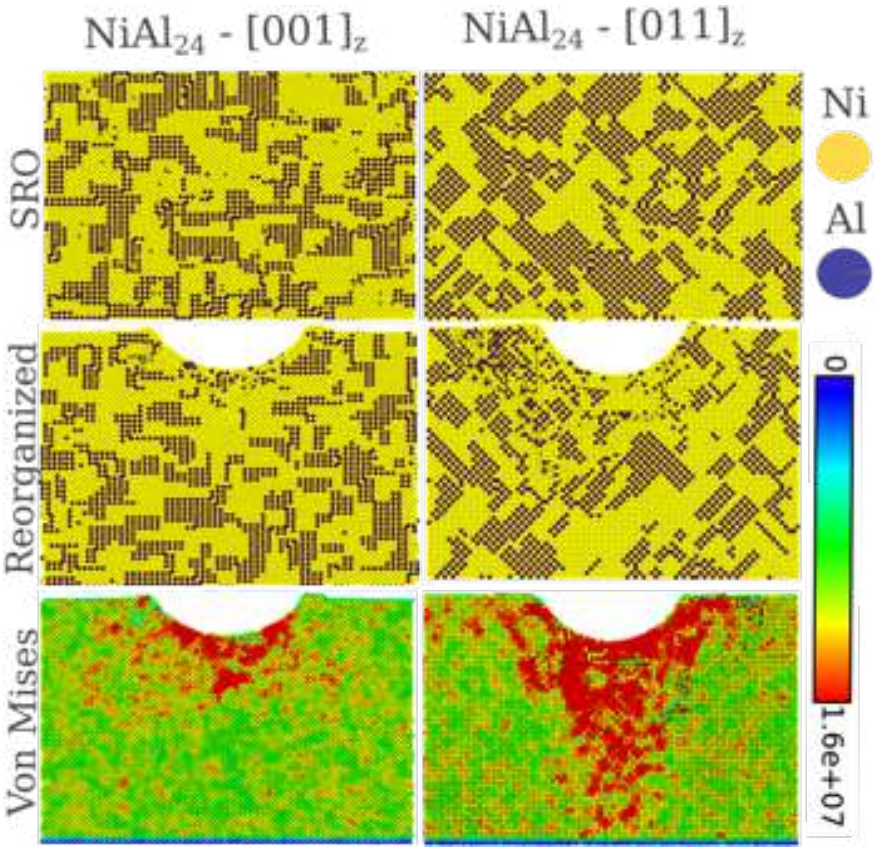

FIG. S12. Nanoindentation-induced reorganization of Short-Range Ordering in NiAl24 alloys. The nanoindentation protocol triggers the reorganization of SRO patterns (top row) in both [001] and [011] crystal orientations (middle row). The corresponding Von Mises stress, higher in the reorganized regions of the sample, is illustrated in the bottom row.

Principal Stress Analysis

To further investigate SRO patterns and their potential links with the stress state, we analyzed principal stresses $\sigma_1, \sigma_2, \sigma_3$ and corresponding planes n_1, n_2, n_3 per atom as in Fig. , illustrating these atom-wise quantities associated with the two loading planes (001) and (011). To facilitate meaningful comparisons between the variables of interest, we scale each eigenvalue by a norm $(\sigma_1^2 + \sigma_2^2 + \sigma_3^2)^{1/2}$ to account for stress variations with depth. We note that negative eigenvalues (i.e. $\sigma_1 < 0$) correspond to compressive normal stresses and our expectation is that, statistically speaking, principal stress values with a negative sign and large magnitudes ($|\sigma_1| \simeq 1$) will substantially contribute to the SRO formation. Overall, such correlations appear to be fairly pronounced in σ_1 maps illustrated in Fig. (c-d) but are also present (to a lesser extent) in Fig. (e-h) depicting σ_2 and σ_3.

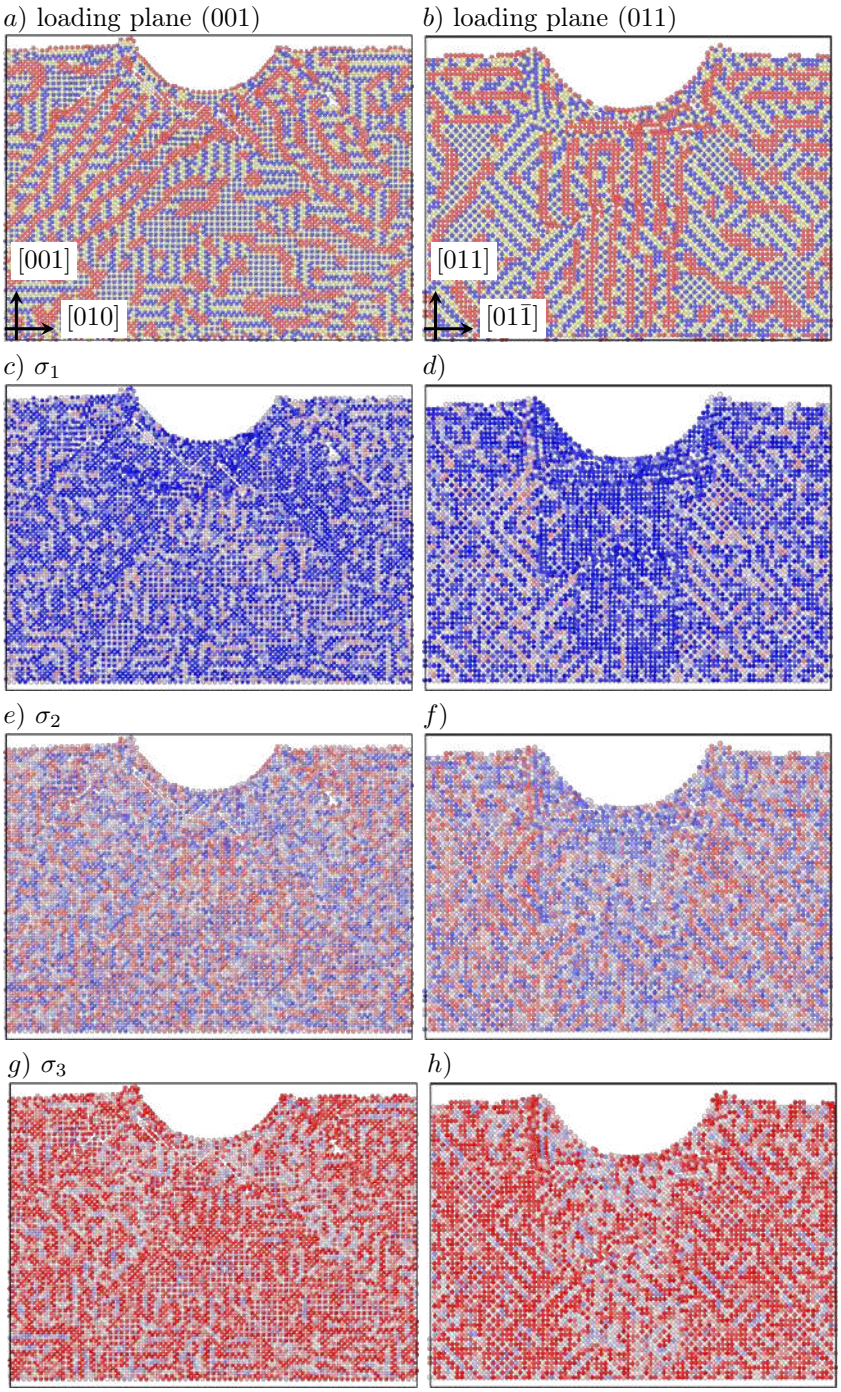

FIG. S13. Principal stress maps corresponding to (001) and (011) loading planes shown in the left and right panels, respectively. Here $\sigma_1 \leq \sigma_2 \leq \sigma_3$. The eigenvalues are normalized by $(\sigma_1^2 + \sigma_2^2 + \sigma_3^2)^{1/2}$ for a better clarity. The colors in a) and b) represent different chemical elements. The blue and red colors in $c - h$) denote (scaled) stress values of -1 and 1.

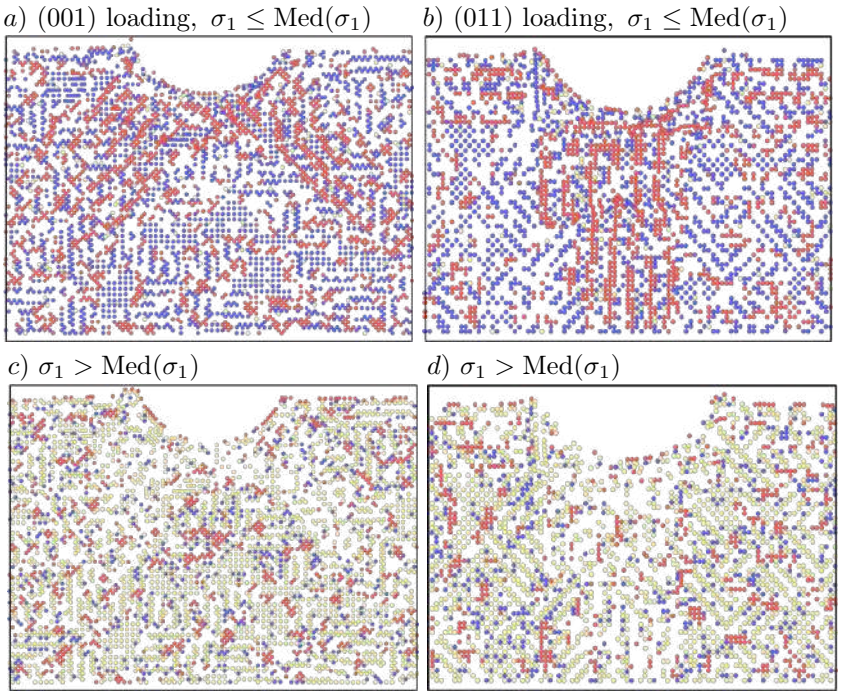

FIG. S14. Snapshots of atoms with σ_1 a, b) below c, d) above the median value. The colors represent different chemical elements.

The above observation is further validated in Fig. (a) and (b) displaying a fraction of atoms with the lowest principal stress below the corresponding median, $\sigma_1 \leq \text{Med}(\sigma_1)$. This conditioning can essentially capture a substantial amount of the Ni-rich stripes (red atoms) but also seems to incorporate individual Co atoms (in blue) which are typically one neighbor apart by Cr atoms (yellow spheres). These well-connected stripes almost disappear when applying the conditioning criterion of atoms with the lower-than-median σ_1 values, as in Fig. (c) and (d).

Fig. depicts the principal stress directions n_1 and n_3 associated with the lowest and highest eigenvalues. Here, we only include Ni atoms with $\sigma_1 \leq \text{Med}(\sigma_1)$ to enhance clarity. Despite the large amount of scatter in our data, the overall trend we discern is that the minor principal stress direction n_1 tends to be statistically aligned with the anisotropy features of the Ni-rich stripes. This alignment is influenced by the direction of loading as well as the crystal symmetry as evidenced in Fig. (a) and (b).

* stefanos.papanikolaou@ncbj.gov.pl

[1] F. Domínguez-Gutiérrez, S. Papanikolaou, A. Esfandiarpour, P. Sobkowicz, and M. Alava, Materials Science and Engineering: A **826**, 141912 (2021).

[2] L. Kurpaska, F. Dominguez-Gutierrez, Y. Zhang, K. Mulewska, H. Bei, W. Weber, A. KosiĹ„ska,

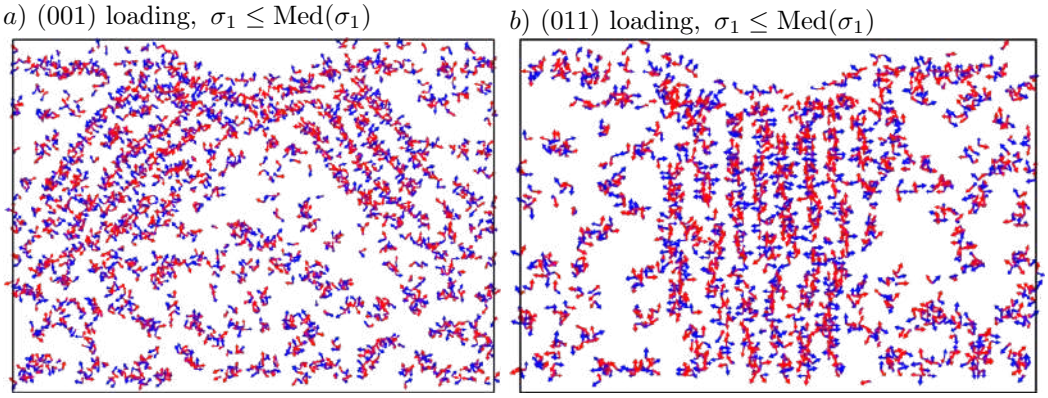

FIG. S15. Principal stress directions n_1 (red arrows) and n_3 (blue arrows). Here only eigenvectors associated with Ni atoms with $\sigma_1 \leq \text{Med}(\sigma_1)$ are shown.

W. Chrominski, I. Jozwik, R. Alvarez-Donado, S. Papanikolaou, J. Jagielski, and M. Alava, Materials and Design **217**, 110639 (2022).

[3] A. Stukowski, Modelling and simulation in materials science and engineering **18** (2010), 10.1088/0965-0393/18/1/015012.

[4] S. Picak, J. Liu, C. Hayrettin, W. Nasim, D. Canadinc, K. Xie, Y. Chumlyakov, I. Kireeva, and I. Karaman, Acta Materialia **181**, 555 (2019).

[5] J. B. Seol, W. S. Ko, S. S. Sohn, and et al., Nature Communications **13**, 6766 (2022).

[6] A. H. Naghdi, K. Karimi, A. E. Poisvert, A. Esfandiarpour, R. Alvarez, P. Sobkowicz, M. Alava, and S. Papanikolaou, Phys. Rev. B **107**, 094109 (2023).

[7] A. Abu-Odeh and M. Asta, Acta Materialia **226**, 117615 (2022).

[8] C. Wolverton, V. Ozolins, and A. Zunger, Journal of Physics: Condensed Matter **12**, 2749 (2000).

[9] D. Farkas and A. Caro, Journal of Materials Research **33**, 3218 (2018).

[10] J. Varillas, J. Očenášek, J. Torner, and J. Alcalá, Acta Materialia **217**, 117122 (2021).

[11] W. Huang and Y. Chang, Intermetallics **6**, 487 (1998).